University of Sussex

Experiments toward high resolution spectroscopy of N_2^+

Amy A. S. Gardner

Submitted for the degree of Doctor of Philosophy
University of Sussex
September 2015

Declaration

I hereby declare that this thesis has not been and will not be, submitted in whole or in part to another University for the award of any other degree.

Signature:

Amy Anna Stirling Gardner

6th June 2016

UNIVERSITY OF SUSSEX

Amy Anna Stirling Gardner, Doctor of Philosophy

Experiments toward high resolution spectroscopy of N_2^+

Summary

High resolution spectroscopy of molecular nitrogen is a prime candidate for measurement of a potential variation in the electron-to-proton mass ratio. Prerequisites are preparation and non-destructive state detection of the internal states of N_2^+.

An ion trap and molecular beamline system have been set up with the main purpose of progressing towards high resolution spectroscopy of nitrogen ions. While the trap will be employed to conduct spectroscopy, the beamline is used to load the molecular ions into the trap where they are sympathetically cooled by calcium ions.

A separate ionisation spectroscopy experiment has been used to investigate the $a^1\Pi_g(\nu = 10) \longleftarrow X^2\Sigma_g^+(\nu = 0)$ band in N_2 for state preparation via a 2+1 REMPI process. This apparatus has also been used to begin characterising the molecular beamline.

The fluorescence from the laser-cooled ^{40}Ca ions will be used for the state-readout of the co-trapped N_2^+. The non-destructive state detection scheme relies on a weak state-dependent dipole force that is used to resonantly excite the motion of the $^{40}Ca^+$ - N_2^+ Coulomb crystal. In order to make this excitation detectable, a separate pulse scheme has been devised to amplify the motion and extend the period of oscillation, using a rapid change in radiation pressure of the $^{40}Ca^+$ cooling laser to simulate the dipole force. The frequency of the secular motion can then be detected via Doppler velocimetry.

The scheme is sensitive to fluctuations in the frequency of the $^{40}Ca^+$ cooling laser, and so a new laser locking system has been developed. Precision spectroscopy on the $4S_{1/2} \rightarrow 4P_{1/2}$ cooling transition was carried out to determine the full lineshape, while still maintaining a low ion temperature. By repeatedly performing spectroscopy on an ion in a separate ion trap, the laser used for cooling could be frequency locked to perform the required experiments in the molecular ion trap.

Acknowledgements

The work presented in this thesis has been carried out over the four year period from September 2011 to September 2015 under the supervision of Dr. Matthias Keller in the ion trap cavity QED and molecular physics (ITCM) group at the University of Sussex. There are many who have contributed to this work in different ways who I would like to thank for their help, advice, friendship and support.

None of this could have been achieved without the guidance and support of Matthias Keller, who I also want to thank for giving me such an interesting project to work on (and also for giving me the opportunity in the first place!). It has been fantastic to learn so much from Matthias. I am really excited about the future prospects of the experiment.

I am lucky enough to have started off my PhD under the additional supervision of Professor Wolfgang Lange. Not only was Wolfgang a brilliant scientist, but he was an absolute joy to be around. He is sorely missed by all who knew him, and will never be forgotten.

When I first came into the lab I was put in the very capable hands of Kevin Sheridan and Nic Seymour-Smith, both of whom I continued to work closely with for two years. Amongst many other things they taught me how to trap ions and operate the lasers - vital skills in the ITCM group! Thanks guys, it was great working with you. I have really appreciated and enjoyed working with everybody in the ITCM group: Jack Morphew, William Groom, Ezra Kassa, Hiroki Takahashi, Sahar Hejazi, Stephen Begley, Arijit Sharma and Gurpreet Kaur. Thank you so much for all your help and advice over the years.

A lot of the project has involved the development and construction of ultra-high vacuum systems. We are all extremely lucky in the ITCM group to have the very skilled Alan Butler so close at hand. Alan has always had time to squeeze in urgent jobs, as well as advise on the more technical things. If I have one regret it is not stopping to learn more from Alan.

Outside of the lab I have a fantastic support network of family and friends who have always been there to celebrate, but who have also seen me through the tougher times as well. I would especially like to thank my parents and my brother Roo, who have always

supported me in whatever I have wanted to do. My friends are remarkable people, and I cannot wait to catch up with you all.

Finally I have to thank somebody who has played a huge role in all aspects of my life. Not only is he my best friend, but Markus Vogt has also been a fantastic colleague to work with. You have enabled me to find my strength when I needed it most, and without this I doubt this thesis would have ever been written.

Contents

List of Tables **ix**

List of Figures **xvii**

1 Introduction **1**
1.1 Motivations for trapped molecular ions 1
1.2 Experimental techniques for molecular ions 3
1.3 State detection of molecular ions 5
1.4 This thesis 6

2 Theory **8**
2.1 Linear Paul trap 8
2.2 Atom-light interactions 14
2.2.1 Two-level system coupled by a laser 15
2.2.2 Force on a two-level atom 21
2.2.3 Three-level system coupled by two lasers 25
2.2.4 Two-photon processes 28
2.2.5 Doppler velocimetry 31
2.3 Physics with trapped molecular ions 33
2.3.1 Molecular internal structure 33
2.3.2 Resonance enhanced multi-photon ionisation 47
2.3.3 Non-Destructive state detection 51

3 Ion Trap and laser systems for $^{40}Ca^{+}$ **57**
3.1 Ion Trap 57
3.1.1 Trap design and assembly 57
3.1.2 Calcium oven 60
3.1.3 Vacuum system 61
3.1.4 Trap electronics 64
3.1.5 Imaging system 66
3.2 Laser systems 67
3.2.1 Photoionisation lasers for ^{40}Ca 68
3.2.2 Lasers for cooling and detection 69
3.2.3 Arrangement of Lasers around the trap 71
3.3 Micromotion Compensation 72
3.3.1 Coarse compensation 73
3.3.2 Photon correlation method 74
3.4 Ion trap characterisation and crystal weighing 76

4 Spectroscopy on a dipole allowed transition in $^{40}Ca^+$ 80
4.1 Measurement Principle . . . 81
4.2 Experimental setup . . . 82
4.2.1 VCO calibration . . . 83
4.3 Characterisation . . . 85
4.4 Dispersive signal . . . 87
4.5 Lock stability . . . 88

5 Ionisation spectroscopy on the $a^1\Pi_g(\nu = 10) \longleftarrow X^1\Sigma_g^+(\nu = 0)$ band of N_2 92
5.1 2+1 Single-colour resonance enhanced multi-photon ionisation (REMPI) of molecular nitrogen . . . 92
5.2 Measurement principle . . . 93
5.3 Experimental Setup . . . 95
5.3.1 Electronics for signal extraction . . . 96
5.4 Time of flight spectroscopy . . . 98
5.4.1 Tuning the signal . . . 100
5.5 Spectrum of the $a^1\Pi_g \longleftarrow X^1\Sigma_g^+$ band of N_2 . . . 102
5.5.1 Comparison with literature values and PGopher simulation for transition identification . . . 103
5.6 Summary and future spectroscopy for a different band in N_2 . . . 106

6 Trap loading of N_2^+ 108
6.1 Molecular beam dynamics . . . 108
6.2 Molecular beamline . . . 112
6.2.1 Vacuum system and design . . . 114
6.3 Attempted trap loading of N_2^+ . . . 116
6.3.1 Trap parameters . . . 116
6.3.2 Sympathetic cooling of molecular ions . . . 120
6.3.3 Experimental setup . . . 120
6.3.4 Results and conclusions . . . 122
6.4 Characterisation of the beamline using the photoionisation setup . . . 123
6.4.1 Experimental setup . . . 123
6.4.2 Photoionisation spectroscopy of N_2 using a pulse valve . . . 123
6.5 Discussion . . . 124

7 Optical Forces 128
7.1 Optical excitation and amplification . . . 129
7.1.1 Measurement principle . . . 129
7.1.2 Experimental setup . . . 131
7.1.3 Laser switching for optical excitation and amplification . . . 131
7.1.4 Conclusions . . . 132
7.2 Tuned Damping and switching techniques . . . 133
7.2.1 Measurement principle . . . 133
7.2.2 Experimental setup . . . 136
7.2.3 Phonon laser and tuned damping technique . . . 136
7.2.4 Repeated switching technique . . . 139
7.2.5 Adiabatic switching and data analysis: Auto correlation vs. Cross correlation . . . 140
7.3 Summary/Conclusions . . . 144

8 Conclusion **146**
8.1 Summary 146
8.2 Outlook 148

References **150**

List of Tables

3.1 Wavelengths and lifetimes for the transitions in $^{40}Ca^{+}$. The first three transitions in the table are used for cooling and repumping. All the other transitions for $^{40}Ca^{+}$ are shown, including the weak quadrupole transitions occupying the last two rows. 70

List of Figures

2.1 A linear Paul trap with four blade-shaped electrodes for trapping in the x-y plane. Two additional electrodes provide confinement along the z-axis, and each are held at a DC voltage of U_{DC}. Design by Dr. Matthias Keller. . . . 10

2.2 The electric field in a linear Paul trap with four blade-shaped electrodes for trapping in the x-y plane at time t (the spacial coordinates are marked in red). After half an rf cycle the field will switch direction. Simulated by Dr. Matthias Keller. . . . 11

2.3 Stability regions found through stable solutions of the Mathieu equations. These regions have been plotted using the stable solutions quoted in [1]. *Left:* The first stability regions in x and y. The area enclosed by the red lines give stable solutions for x, with the area enclosed by the blue lines giving stable solutions for y. Where the two overlap gives the kite-shaped stable trapping region in terms of the a and q parameters. *Right:* The same region zoomed in. . . . 12

2.4 The slow secular motion, with an amplitude of 1, and fast micromotion of the ion in the trapping field. The displacement from trap centre has been plotted as a function of the periodic secular motion for a q value of 0.1, and for $\Omega = 30\ \omega_r$. . . . 14

2.5 Interaction of a two-level system with a light field that has detuning $\Delta\omega$, the strength of which is described by the Rabi frequency Ω. The spontaneous decay rate from the excited state is given by Γ. . . . 16

2.6 The fraction of population in the excited state ρ_{22} plotted as a function of the detuning. This has been plotted for four different values of the saturation parameter, s_0. For the larger values, the effect of power broadening becomes more extreme, and the excited state population reaches a limit of 0.5. This is made even clearer in fig. 2.7. . . . 19

2.7 The fraction of population in the excited state ρ_{22} plotted as a function of the saturation parameter, when the detuning $\Delta\omega = 0$. The population saturates at a value below 0.5, beyond which there is no further increase or decrease, no matter how much greater the saturation parameter. . . . 20

2.8 The damping coefficient β plotted as a function of the detuning $\Delta\omega$ for four different saturation parameters. . . . 24

2.9 Three-level system with states S and D, and excited state P. Two lasers with frequency ω_C and ω_R are detuned from the transitions S→P and D→P by $\Delta\omega_C$ and $\Delta\omega_R$ respectively. . . . 26

2.10 The excited state probability ρ_{33} of the Λ system as a function of the detuning $\Delta\omega_C$ from the S→P transition, plotted for four different saturation parameters s_C. The detuning from the D→P transition $\Delta\omega_R$ has been set to zero, and the saturation parameter for this transition is equal to 1. . . . 27

2.11 The two-level system has been extended to include a virtual level $|v\rangle$, and the transition between the two states $|1\rangle$ and $|2\rangle$ is made by two photons with total energy $\omega_a + \omega_b$. 29
2.12 The effective detuning seen by the ion is modulated at the secular frequency, this modulation is shown in black. If the laser detuning is set to $\pm\Gamma/2$, the gradient of the lineshape is at its maximum, and gives the largest modulation in fluorescence. For a detuning of zero, the gradient is zero, and there is minimal modulation in the fluorescence. 31
2.13 Illustration of the basic structure of molecules, showing the electronic, vibrational and rotational states relative to each other (not to scale). Also pictured is the vibration and rotation of a diatomic molecule. 34
2.14 The molecular orbital diagram for the ground state of N_2, showing how the atomic orbitals combine [2]. Not to scale. 37
2.15 The hyperfine structure of N_2^+, which comes as a result of the nuclear spin of ^{14}N. 43
2.16 Two potential energy curves for different electronic states A and B. For each of the vibrational states the corresponding wavefunctions have been drawn in light blue. Two examples of transitions with a strong Frank-Condon overlap are illustrated by the red and orange arrows. 46
2.17 The level structure for nitrogen, not including all states. Reprinted from [3] with permission from Elsevier. Reprinted from [4] with the permission of AIP publishing (where a more detailed version can be found). 48
2.18 A possible ionisation scheme for preparing N_2^+ in the $X^2\Sigma_g^+(N = 0, \nu = 0)$ state, using the P_2 transition. 50
2.19 Transitions in N_2^+. Here the energy of each transition within the $A^2\Pi_u(\nu = 2) \longleftarrow X^2\Sigma_g^+(\nu = 0)$ manifold is plotted against the rotational state, N, of the electronic ground state. The different branches ('P', 'Q', and 'R') denote how much the rotational number changes by, as explained in sec. 2.3.1. The most suitable transition for our purposes sits in the R_{21} branch of $A^2\Pi_{u,3/2}(\nu = 2) \longleftarrow X^2\Sigma_g^+(\nu = 0)$, and is the transition from $N = 0$. . . 52
2.20 The calculated probability of spontaneous decay $P_{spont}(t)$ for four different detunings from the excited state $A^2\Pi_{u,3/2}(\nu = 2)$, plotted as a function of the amount of time the laser is applied. The laser power used is 1 mW, with a waist of 50 μm, and has a wavelength of ∼785 nm. 54
2.21 The magnitude of the dipole force as a function of the detuning. For this plot, the laser waist is 50 μm, and the power is 1 mW, with a wavelength of 785 nm. *Inset:* Magnified to show the force when the detuning is on the order of GHz. 55
2.22 The force from the radiation pressure for $^{40}Ca^+$ plotted as a function of the detuning from the $4S_{1/2} \rightarrow 4P_{1/2}$ transition. This has been plotted with typical experimental laser parameters of 50 μm beam waist, 10 μW power and wavelength 397 nm. 56

3.1 Solidworks drawings of the ion trap. Bottom left: Slice through the trap looking down the trap axis. The cuts made into the rf-electrodes and trap frame for mounting are visible, along with the clamps used for securing the dowell pins. Bottom right: view of the trap from the top looking down. In the centre of the electrodes is the collimation hole for calcium effusing from the oven. Also visible is the prism and mount for the dual purpose of reducing laser scatter, and protecting the trap centre from incoming molecules from the beamline. Top: The full trap structure in 3D. 58

3.2 Photographs of the ion trap during construction. (Left) Before the endcap electrodes are inserted. Looking down the trap axis, the four rf blades can be seen. A small screw hole is visible directly below the trap centre - this is where the oven collimation plate is fixed into place. (Right) The electrical connections for the rf electrodes are made with small screws. The oven has been inserted and aligned. 59
3.3 The oven assembly and mounting. (a) The tantalum oven with washers for mounting (b) One of the two assemblies needed for mounting the oven to the trap. (c) How the oven is mounted onto the main trap frame. The oven is aligned so that it points directly up to the trap centre. 60
3.4 Two views of the trap demonstrating the orientation of the important components for the experiment. (A) shows a side view looking along the axis of the trap. Here all of the radial components can be seen: where the radial lasers are aligned with respect to the incoming molecular beam and effusive calcium source. The ions are then imaged from the top. (B) A top view of the trap looking down. Here the position of the deflection prism with respect to the incoming molecular beam and radial lasers is pictured. 62
3.5 Photograph of the vacuum system for the ion trap. The ion trap chamber sits above this on top of the optical breadboard. 63
3.6 The trap electronics for providing a stable trapping field. Two of the electrodes (2 and 4) are held at rf ground, while the other two are driven at radio frequency. Separate DC voltages can be applied to each electrode via an RC circuit. All capacitors have $C = 7\ pF$ and the resistors have $R = 1\ M\Omega$. The addition of an auto-transformer coil creates a resonating circuit (with centre frequency 37.112 MHz) to provide high enough voltages to the electrodes for trapping. 64
3.7 The trap electronics for the axial electrodes that allow for addition of an oscillating signal to the DC voltages applied. 65
3.8 (Left) A schematic of the imaging setup. (Right) A variety of false colour images of calcium ions taken using the CCD. Single ions, strings, and large crystals can be trapped and imaged using this system. 67
3.9 Ionisation scheme for ^{40}Ca. The 423 nm laser can be tuned for addressing different isotopes. 68
3.10 Cooling scheme for $^{40}Ca^{+}$. The cooling and detection takes place on the $4^2S_{1/2} \rightarrow 4^2P_{1/2}$ transition. Two more lasers are required for repumping to avoid population trapping in other states. 69
3.11 Optical setups used for the cooling and repumper lasers. (A) Shows a double-pass AOM configuration for the 397 nm cooling laser, to allow for frequency control as well as control over the amplitude. After being selected from the main laser beam, it is focused down into the AOM. The first order is collimated, retro-reflected, and focused back into the AOM, with the polarisation corrected using a $\lambda/4$ plate. The frequency-shifted beam is then aligned into a single-mode fibre. (B) A single-pass AOM configuration, used as less control over the repumper frequencies are required for the experiments. 850 nm and 854 nm lasers are overlapped using a $\lambda/2$ plate. Both are then focused into the AOM. The first order diffraction is selected and the beams are aligned into a single-mode fibre. 71
3.12 Optics setup around the trap for all of the lasers required. 72
3.13 The alignment of two radial lasers for micromotion compensation using the photon correlation method. 73
3.14 Micromotion setup. 75

3.15 Determination of the voltages required for micromotion compensation. Each data point is a position of minimum micromotion in terms of the voltages applied in each direction (H and V). This has been measured for two lasers in order to probe orthogonal components of the micromotion. The point at which the two lines intercept gives the values that V and H should be set to for micromotion minimisation. 76

3.16 The crystal weighing setup. 77

3.17 The axial secular frequencies for endcap voltages applied. The fit (to the black points) shows that the square of the secular frequency is proportional to the applied voltage, as expected. 78

3.18 The radial secular frequency is proportional to the rf voltage applied. 79

4.1 The switching scheme between probing and cooling. In this example, the probing time is on for 10 μs and is followed by 15 μs of cooling. After some designated amount of time, the probe is stepped to the next detuning. This is repeated until a full spectrum is taken. 81

4.2 Spectrum of the $S_{1/2} \rightarrow P_{1/2}$ transition in calcium. The spectrum obtained by scanning the spectroscopy laser without additional cooling intervals (red open squares) shows a sharp drop close to the linecentre. Employing additional cooling intervals results in a full, undistorted spectral line (blue open circles). A Voigt profile is fit to the undistorted spectrum (blue line). 83

4.3 Experimental setup for spectroscopy on $^{40}Ca^{+}$. Two VCOs for driving the AOM are rapidly switched between using an rf-switch in order to provide the cooling and probing sequence illustrated in fig. 4.1. A computer controlled delay generator (SRS DG645) triggers the rf-switching and also gates the photon counts from the PMT, so that data is only collected during the probe time. 84

4.4 Scanning the frequency of the VCO also changes the power of the laser. The calibration process corrects for this, avoiding a distorted lineshape. . . 85

4.5 (a) The calibration file used to correct for the change in laser power when the VCO frequency is scanned - as seen in fig. 4.4. (b) A frequency scan when the calibration file is used. 86

4.6 (a) R^2 as a function of probe time for a range of pulse sequence repetition rates. For repetition rates of 20 and 40 kHz the value of R^2 drops sharply at small probe times. For repetition rates of 5 and 10 kHz R^2 begins to decrease when the probe time exceeds 35(5) μs. (b) R^2 as a function of duty ratio. As the repetition rate is reduced, a smaller duty ratio is required to sufficiently re-cool the ion. *Inset:* an example of distortion of the line shape. 87

4.7 Spectrum of the $S_{1/2} \rightarrow P_{1/2}$ transition in calcium (top). Over the same range, two probes are used to obtain a dispersion-like signal (bottom). For this 5 MHz resolution scan, the two probes are set at 30 MHz apart. Subtracting the fluorescence count for one of the probes from the other generates the dispersion-like signal. 89

4.8 Measurement of the Allan variance of the spectroscopy signal of a single trapped calcium ion. 90

5.1 The electric field has been simulated using COMSOL for the extraction plate held at 30 V, the drift tube at -30 V, and the detector funnel at -2.6 kV. Two plots have been made for different voltage ranges. Each are 2D plots from the centre of the spectrometer to the outer edge. There are three meshes in each diagram, shown by the dotted lines. (A) is the electric field plotted for a colour range of -30V to 30V to show the field through the whole TOF spectrometer. The fields are particularly strong across the extraction and acceleration regions where the ions are accelerated. Throughout the drift tube the potential gradient is zero to allow for mass separation. (B) gives the field plotted for 30 V to -2.5 kV, so that the field lines can now be seen around the detector funnel. There is a very steep gradient between the final mesh that the ions pass through and the funnel. 94

5.2 Solidworks drawing showing the vacuum setup used for the ionisation spectroscopy experiment. A stream of nitrogen is leaked in from a Swagelock $\longrightarrow$ CF adaptor that is mounted on the flange on the left (not pictured), and is shown as a red arrow. The molecules meet a laser beam, shown as a blue arrow, in the centre of the cylindrical detector. This is mounted on the top flange (not pictured). Optical access for the laser is achieved with viewports that are anti-reflection coated for UV. 96

5.3 The detection setup. At the top is the channel electron multiplier for signal extraction. The funnel of this is held at a high negative voltage V_{CH}. N_2 is shown entering the extraction region as the red arrow, towards the blue cross that demonstrates where the laser passes through for ionisation. Ions are then created in the extraction region, where an extraction plate held at V_{Ex} repels ions up the drift tube (at voltage V_{DT}) towards the channeltron. The insulating parts are shown in black, with the PEEK mount for the channeltron in white. Four dotted lines show the positions of the meshes. . 97

5.4 Circuitry used for amplifying the output of the channel electron multiplier and converting it into a voltage. 98

5.5 An example of what a typical time of flight looks like, for the laser tuned onto a transition (blue) and off a transition (black). 99

5.6 Demonstration of the signals bunching as well as an increase in signal height when the voltage on the extraction plate is increased. Four different voltages have been applied to the extraction plate, 5 V (black), 15 V (red), 30 V (blue) and 60 V (green), while the voltage on the box remains at a constant 8 V. 101

5.7 Similarly to the extraction plate, an increase in voltage applied means the whole TOF spectrum arrives earlier. The extraction plate has been held at 65 V while the box voltage was changed from 1 V (red) to 25 V (blue). . . 102

5.8 The ionisation spectrum obtained for the $a^1\Pi_g \longleftarrow X^1\Sigma_g^+$ band of N_2, with a resolution of 0.001 nm at 300 K. 103

5.9 PGopher simulation for the $a^1\Pi_g \longleftarrow X^1\Sigma_g^+$ band of N_2, showing the O, P, Q, R and S branches, at a temperature of 300 K. The y-axis of the top graph gives the rotational number in which the molecule starts in when in the ground electronic state $X^1\Sigma_g^+$. The bottom graph displays the expected spectrum, showing the relative amplitudes of each transition. 104

5.10 Comparison of the PGopher simulation (blue) to the experimental data (red) shown in fig. 5.8. The experimental data has been normalised to the P_2 transition. After the simulation has been offset by 0.018 nm, the positions of the lines match well, although the relative peak heights in the spectrum do not. 105

5.11 Comparison of three methods for state preparation of N_2^+. In the first panel the 2+1 REMPI scheme used for this chapter is shown, with the main drawback being that it is not completely state selective. In the centre panel is a 2+1' scheme used by the Willitsch group in Basel [5]. The final panel shows the future scheme to be used in the ITCM group at Sussex, which will be fully state-selective, unlike the current scheme shown in the first panel. 106

6.1 Diagram of the flow dynamics during a supersonic expansion. Reprinted from [6] with permission from Oxford University Press. 109

6.2 Location of the Mach disk from the aperture, as a function of the ambient pressure for two different sized apertures. (Top) Mach disk location for a 0.51 mm valve. (Bottom) Mach disk location for a 0.1 mm valve. The inlet on each graph is a zoom-in of the area of most interest, as the pressure during a pulse is expected to become quite high. 111

6.3 A demonstration of how the velocity and translational temperature of the beam changes as it moves away from the aperture, for two different aperture sizes. Collisions within the initially dense beam causes a cooling effect, at the same time there is rapid acceleration caused by the pressure gradient. The terminal values for velocity and the minimum temperature achieved during expansion have almost been reached for both valve sizes: 0.51 mm (top) and 0.1mm (bottom) within 25 mm. 113

6.4 Schematic of the molecular beamline. The stagnation pressure (P_S) behind the pulse valve is adjusted by a regulator on the nitrogen gas cylinder, and can be adjusted from 0.2 bar to 4 bar above atmosphere. The pulse valve can be controlled to make bursts of nitrogen expand out into the primary chamber via a supersonic expansion. The pressure in this chamber is the highest for the whole of the vacuum system (not including P_S), and is pumped by a 400 ls^{-1} turbomolecular pump (TMP). The supersonic beam created by the expansion is skimmed off by the primary skimmer. The divergent beam is re-collimated by the secondary skimmer before entering the ion trap where ionisation takes place. 114

6.5 Top: Schematic showing a cut through of the flange on which the pulse valve is mounted. The inlet in which the valve sits is a tight fit, so as to keep the valve concentric with the flange. The brass ring is threaded and fits into the tapped inlet in order to clamp the valve down and create a vacuum seal with a small o-ring that sits between the valve and the flange. Bottom: One of the skimmer mounts used in the molecular beamline. This enables alignment of the primary and secondary skimmers from outside of vacuum. 115

6.6 Photographs showing the full skimmer mount setup, and the small bellow sealed micrometers for fine adjustment outside of vacuum. The bottom photograph shows the mounting of a 0.3 mm Beam Dynamics skimmer. . . 117

6.7 The molecular beamline. Top: A solidworks drawing showing a slice through of the molecular beamline and ion trap setup. Bottom: A photograph of the beamline and ion trap, facing in the opposite direction to the solidworks drawing. 118

6.8 Stability regions for $^{40}Ca^+$ (red) and N_2^+ (blue). The area where the two overlap gives the region in which the two can be trapped simultaneously. . . 119

6.9 The setup for trap loading of N_2^+ with crystal weighing. The delay generator is used to trigger the pulse laser and pulse valve with the desired delay between the two. Once loading has been completed for the required duration, the delay generator is used to excite the secular motion of the ion crystal in the trap, during which time the modulated fluorescence is collected. This is sent to the p7888 which is a fast counting card for recording the photon arrival times during a measurement. This can then be repeated many times. 121

6.10 Some examples of calcium Coulomb crystals with nitrogen cores. 122

6.11 Experimental setup for the pulsed ionisation spectroscopy for the beamline. 124

6.12 Signal from the channeltron electronics as the delay between the trigger pulses for the pulse valve and the laser was varied. For this delay scan, the system was pulsed at 5 Hz, with the channeltron voltage set to 2.45 kV. The stagnation pressure behind the valve was 0.2 bar (above atmosphere) and the valve was opened for 250 μs, with the actuation voltage set to a maximum. The laser was set to the Q_4 transition in nitrogen. 125

6.13 Spectrum taken of nitrogen spectroscopy setup using just the pulse valve. To completely avoid a build up of pressure, the laser was pulsed at 2 Hz, the pulse width was set to the absolute minimum of 160 μs opening time, and the stagnation pressure was 0.2 bar (above atmosphere). The delay between the dye laser and pulse valve was set to 5 ms, as this is where the maximum signal for the TOF peak sits (fig. 6.12). Each point is the sum over 60 shots. 126

7.1 Experimental setup for optical excitation and amplification. The cooling laser at 397 nm, here seen in blue, is shifted in frequency and amplitude using a double-pass AOM setup. The laser light is then taken to the experiment via a single-mode fibre, overlapped with the repumper light (not shown in this diagram) and aligned through the axis of the ion trap. Two VCOs are used for setting the frequency and amplitude of the laser light for different parts of the sequence, and control is rapidly switched from one to the other using a delay generator triggered rf-switch. Photons are collected via a PMT and counted using a P7888 counting module. 130

7.2 The laser-induced fluorescence of the ion during an optical excitation and amplification sequence. The laser detuning for the cooling stages is -10 MHz and for the amplification region it is set to +10 MHz. 132

7.3 Full experimental setup for applying more complex laser pulse sequences. Two counter-propagating cooling lasers at 397 nm are used, aligned in the axial direction of the ion trap. Control of laser A is switched between two different VCOs which determine the frequency and amplitude of the beam. The AOM for laser B is controlled with one VCO. All three VCOs are frequency controlled with a DAQ (not included in this diagram for clarity), and the amplitude of each is controlled by separate programmable function generators, triggered by the delay generator. As previously, the fluorescence from the ion is collected with a PMT, and the photon arrival times counted with a P7888 counting module, triggered with the delay generator. 134

7.4 The two different sequences used. Both sequences first start with a cooling period using VCO 2, which is switched off adiabatically. VCO 1 is switched on to impart a radiation pressure-induced kick and amplify the motion. (Top) The tuned damping sequence. After some amplification time, VCO 3 is switched on adiabatically for the tuned damping part, shown in purple. (Bottom) The switching sequence. Instead of a tuned damping section, the sequence is switched from amplification to damping many times between VCO 1 and VCO 3 to sustain an oscillation. The switching for these two lasers is also adiabatic. 135
7.5 The motional spectrum amplitude as a function of the blue power when the blue detuning, red power, and red detuning are held constant. The oscillation amplitude is taken to be the mean height of the FFT peak obtained for three separate measurements, with the error bars being the standard deviation. 137
7.6 A cross correlation of photon arrival times between a starting trigger pulse and photon arrival times. This is the tuned damping sequence, which has been extended out for 10 ms. Each of the graphs demonstrate different amounts of damping out of the oscillation. 138
7.7 A cross correlation of photon arrival times with the trigger pulse for the repeated switching sequence, showing 8 ms of the 10 ms duration of the sequence. 140
7.8 The oscillation amplitude as a function of the blue power when the blue detuning, red power, and red detuning are held constant. For this measurement the blue detuning was set at +20 MHz, with the red power and detuning set to 25.5 μ W and -5 MHz respectively. The oscillation amplitude is taken to be the mean height of the FFT peak obtained for three separate measurements, with the error bars being the standard deviation. . 141
7.9 Examples of fast-Fourier transforms to demonstrate the difference between analysis with the cross-correlation and auto-correlation for both *kicking* and *adiabatic* cases. Power and detuning settings were kept constant for each of the measurements. For graphs (a) and (b), the auto-correlation is used. For (c) and (d) the cross-correlation has been used (note that the y-axis changes by a factor of 10 from auto- to cross-correlation). This demonstrates that although a larger signal is obtained for the auto-correlation, the cross-correlation will have to be used for the state detection measurement to avoid exciting the motion regardless of the state. 142
7.10 Fast-Fourier transforms of a cross correlated sequence for when the sequence has a radiation pressure kick (blue) and when it is completely adiabatic (red). 143
7.11 Setup of the proposed walking wave interferometer used to resonantly excite the motion of the Ca^+-N_2^+ Coulomb crystal. 145

Chapter 1

Introduction

Over the past few decades, the fields of atomic and molecular physics have been revolutionised by the invention of the ion trap and the laser. Highly localised atomic ions are routinely trapped and probed by the tunable high-intensity coherent optical fields provided by lasers; as our understanding of the possibilities using these devices grows, so do our goals. This has led to experiments that require a high degree of control over both the motional and internal degrees of freedom of the ions.

Recently, molecular ions have become of particular interest, which has meant development of new techniques required for these more complex entities [7]. The most notable motivations for this are high resolution spectroscopy experiments for improved frequency standards [8; 9], testing fundamental theories [10; 11; 12], and searching for changes in fundamental constants [13; 14]. Additional to this are exciting advances in cold chemistry [15; 16; 17] and proposals for quantum computing [18]. Prerequisites for such experiments are internal state preparation, translational cooling, and identification of loaded species [19; 20].

1.1 Motivations for trapped molecular ions

Research into molecular ions presents a new regime for experimental physics. The development of new technologies and techniques has granted access to species with higher degrees of complexity. The huge variety of different types of transitions within different types of molecules means that a balance can be struck between ease of measurement, precision, and the avoidance of systematics. Fundamental to many experiments within in the field is the ability to precisely measure transition energies for this wide range of transitions for different atomic or molecular species.

Frequency standards have driven the desire for greater meteorological precision, which is vital for global time keeping and modern global navigation satellite systems, and has impacted many of the other fields that require coherent control of internal states [21]. Additionally, there is strong interest in using such high-precision clocks as highly sensitive detectors for the measurement of gravitational and magnetic fields [22]. Although the current record is held by an ^{87}Sr optical lattice clock [21], and many other clock measurements have used atoms [23; 24], there are proposals for using cold molecules [25].

Spectroscopic techniques enable the probing of fundamental physics. There are theories that propose a possible spatial or temporal variation in the fundamental constants α (the fine structure constant) and μ (the proton to electron mass ratio m_p/m_e) [26]. Experiments have already started searching for such drifts, and are either performed under laboratory conditions, or via astronomical observation, with some comparing data from the two, such as experiments by Webb *et. al.* and Wolf *et. al.* [27; 28]. On cosmological time scales of 10^9 years, this has limited the variation of μ to $|\Delta\mu/\mu| < 10^{-7}$ [26]. Recent laboratory measurements using $^{171}Yb^+$ at PTB and NPL have constrained $\dot{\mu}/\mu$ to the order of 10^{-16} yr^{-1} and $\dot{\alpha}/\alpha$ to the order of 10^{-17} yr^{-1} [23; 29].

There are a number of species proposed for detecting drifts [10; 26; 30], which have been chosen due their sensitivity to either α or μ, our ability to measure particular transitions, and the sensitivity to external influences that cause systematic shifts. For instance, electronic transitions in atoms have a sensitivity to α, whereas rovibrational transitions found in molecular internal structure are sensitive to μ [13]. Additional to the study of variations in fundamental constants using molecules is other fundamental physics such as precise measurement of the electric dipole moment of the electron, to which polar molecules have greater sensitivity than atoms [11].

The translational temperatures that can be achieved in ion traps sits within a regime for which the study of chemical reactions is particularly interesting [17]. When temperatures of less than 1 K are reached, the deBroglie wavelength is extended to the point at which the reaction dynamics of the low-energy collisions start to be governed by quantum mechanics [31]. The averaging that generally occurs over many reactions on the macroscopic scale is now scaled down so that a new understanding of collisional dynamics on the order of single reactions can be pursued. As well as this, the precision techniques that are used for trapped ion experiments can be applied to achieve greater control over collisions. Typically parameters that we have control over for chemical reactions are the temperature and pressure, whereas cold chemistry experiments can now be dictated by control over

quantum states of single particles [32]. Experiments probing chemical dynamics under such controlled conditions can lead to a better understanding of fundamental chemistry [16; 33]. Furthermore, better knowledge of how quantum effects dictate reaction pathways can lead to choice over how a reaction will take place. Apparatus similar to the set-up described in this thesis has been used to successfully demonstrate state-dependent charge exchange reactions between N_2^+ and Ar [5].

1.2 Experimental techniques for molecular ions

Depending on the kind of experiment to be carried out, what species are used, and how much control is required, there are a wide variety of techniques for cold molecular ions. The temperature of both the internal (with contributions from the rotational, vibrational and electronic states) and the external (translational) degrees of freedom play a role.

Precise control over the internal states of molecular ions is of utmost importance for trapped ion experiments. In general, molecular ions do not present closed transitions that can be utilised for state manipulation due to their complex structure. However, there has been work that has successfully demonstrated such schemes for specific molecules.

For polar molecules that have a strong interaction with blackbody radiation (BBR), it is possible to laser cool the rotational states so that most of the population is in the ground state. This has been proposed for heteronuclear diatomics MgH^+ and ArH^+ by the Drewsen group [34], where redistribution of the population via the coupling of the rotational states with the blackbody radiation along with optical pumping on particular transitions can achieve a high population in the ground state. This was later demonstrated by the same group for MgH^+ [35], resulting in a thermal distribution equivalent to 20 K. A similar scheme has been used to successfully prepare HD^+ in the rovibrational ground state [36], with a population of 78(4)%.

In general, state selective ionisation uses more than one photon due to the high energy required, and is known as resonance enhanced multiphoton ionisation (REMPI). The REMPI scheme used by Tong *et. al.* is used with the joint purpose of preparing N_2^+ in the rovibrational and electronic ground state, and for loading into an ion trap where they are sympathetically cooled by $^{40}Ca^+$ [5]. REMPI techniques have also been proposed for more complex polyatomic species [37].

Translational cooling of molecular ions in ion traps is also more complex than for atomic ions. This is a similar problem to internal manipulation, as standard direct laser cooling techniques employed in trapping experiments is not applicable to molecular species.

Therefore efforts have been made for the development of various methods for cooling the external degrees of freedom of molecular species.

The method of sympathetic cooling is often used in ion trap experiments as this is fairly robust and easy to implement. An atomic ion species that can be directly laser cooled is loaded into an ion trap before the molecular ion is loaded, the two forming a Coulomb crystal. The Coulomb interaction between the two loaded species means that any kinetic energy gained from some external heating source is shared between the two [17]. If excess energy is taken away from the laser cooled ion, this has the effect of cooling the whole crystal, although problems can occur when the mass of the directly cooled ion differs too much from the mass of the sympathetically cooled ion [38]. Sympathetic cooling has been demonstrated for many different species, but most relevant to this experiment is the cooling of N_2^+ by using $^{40}Ca^+$ [5]. The Doppler cooling limit for $^{40}Ca^+$ is 0.5 mK [17], which is limited by the scattering rate of the transition. The sympathetic cooling technique has been extensively investigated [39; 40], and used for a variety of different experiments [17], which demonstrates how widely used it is. Additionally, sympathetic ground state cooling of molecular ions has been achieved - a vital step towards performing quantum logic spectroscopy [41].

Beamlines can be used for suitable delivery of molecules to traps. Designs for these can range from more simple setups such as supersonic beamlines and quadrupole guides, to systems that require complex switching of fields such as some Zeeman and Stark decelerators. Supersonic beams can be used for internal cooling and precise delivery of neutral molecules for ion trap systems [5]. For such systems, the internal cooling can aid the efficient state-selective loading from REMPI. The Softley group at Oxford University has developed a few beamline systems, one of which uses a bent quadrupole guide for velocity selection in order to select translationally cold molecules for chemical reactions [42], and has been used to successfully study collisions with energies less than 1 K. For a separate experiment a Zeeman decelerator has demonstrated translational cooling of He atoms [43].

Buffer gas cooling and hybrid systems offer alternative techniques to deliver internally and translationally cold molecules. Buffer gas cooling can simultaneously provide cooling for both the internal and translational degrees of freedom, via collisions with a cryogenically cooled buffer gas such as He. This is a technique that has been used successfully to cool the rotational states of trapped molecular ions down to a few Kelvin [44], where sympathetic cooling has been used to cool the translation. Hybrid systems using ion traps and laser cooled atoms have been used for low energy chemical reactions using both large

ion crystals and single-ion reactions [32; 45].

1.3 State detection of molecular ions

So far, mainly destructive state detection techniques have been implemented for molecular ions. Resonance enhanced multi photon dissociation (REMPD) has been used in many of the references in this introduction so far [5; 35; 36; 44], which is a technique that not only destroys the state, but also the molecule itself. More recently, there has been a drive towards non-destructive methods for molecular ions, which has previously been demonstrated with CO^+ in a cryogenically cooled Penning trap [46]. A technique for this in an ion trap setting has been proposed by Koelemeij *et. al.*, where an off-resonant laser is used to impart a state-selective force onto a spectroscopy ion, which can then be read out by a co-trapped control ion that also sympathetically cools the dual species Coulomb crystal [47].

Quantum logic spectroscopy (QLS) is another non-destructive method, by using two ions trapped together which share the requirements for high-precision spectroscopy [48], and has been demonstrated on atomic ions. One is a logic ion used for sympathetic cooling and state readout, and another is the spectroscopy ion - the state of which will be probed. The state information of the spectroscopy ion is transferred to the logic ion via a shared motional mode. This scheme has now been adapted and has been used to successfully perform QLS on trapped MgH^+ [49]. Using this technique, rotational transitions are observed due to the interaction with the BBR.

Mur-Petit *et. al.* propose another technique for non-destructive state detection of molecular ions [50] that reduces the experimental complexity, as ground state cooling is not required, and just sympathetic cooling can be used for a target ion by a laser-cooled control ion. The idea comprises, in its most general form, of a protocol that uses quantum gates that have no sensitivity to the motional state of the ions in order to measure the state of the target ion. Similarly to the previous schemes discussed [47; 48; 49], Mur-Petit *et. al.* propose using state-dependent forces on the ions as part of the protocol, and in their scheme the nature of the force can be changed depending on the type of state to be probed.

An alternative, but similar technique also uses two trapped ions, demonstrated by Hume *et. al.* with atoms, where the logic ion used was $^{25}Mg^+$, and spectroscopy performed on $^{27}Al^+$ [51]. This technique further reduces the experimental requirements, as a less complex routine is used. The coulomb crystal is Doppler cooled via direct cooling of

$^{25}Mg^+$. A walking wave is then used to apply the dipole force, modulated at the COM mode frequency of the crystal, to $^{27}Al^+$. The cooling laser for $^{25}Mg^+$ is then detuned for a short while to the blue side of resonance, amplifying the motion, before returning to optimal cooling. During the sequence, the laser-induced fluorescence is collected, which is modulated by the COM mode frequency only if $^{27}Al^+$ is in the probed state. This is extremely similar to the technique proposed for N_2^+ in this thesis, described in sec. 2.3.3.

1.4 This thesis

The motivation for the research carried out for this thesis is towards high resolution spectroscopy on N_2^+ [30]. In order to reach this goal, methods of state preparation, translational cooling, detection of species and state detection have been either implemented, or progress has been made toward them.

For state preparation of N_2^+, the technique of REMPI has been investigated using an ionisation spectroscopy setup. Furthermore, in order to deliver a rotationally cold beam of neutral molecules to increase the efficiency of the REMPI process, a molecular beamline is being developed. Once loaded into the trap the N_2^+ will be translationally cooled using sympathetic cooling. The N_2^+ is loaded alongside $^{40}Ca^+$ which is directly laser cooled. The successful load of N_2^+ can be determined using a crystal weighing technique for which the atomic ion is used for readout. Work towards a non-destructive state detection technique has been started, with a suitable pulse scheme for state readout investigated.

Chapter 2 gives an overview of the theory required for this thesis. This concentrates mainly on ion trapping of both atomic and molecular ions and atom-light interactions for which laser cooling and the non-destructive state detection scheme are used. The experimental apparatus for trapping and cooling $^{40}Ca^+$ is explained in chapter 3. Next, chapter 4 explains a technique for performing spectroscopy on $^{40}Ca^+$, which extends to use for feedback to the cooling laser for stabilising the frequency. Chapters 5 and 6 explain the REMPI scheme used for loading N_2^+, the setup used for ionisation spectroscopy on N_2 and trap loading of N_2^+ using a molecular beamline. Finally, chapter 7 demonstrates a technique for extending out a motional oscillation within the trapping potential after an excitation, which can be used for state readout for our proposed non-destructive state detection scheme.

Work presented in this thesis has led to the following publications:

- K. Sheridan, N. Seymour-Smith, A. Gardner and M. Keller, **All-optical broad-band excitation of the motional state of trapped ions**, *European Physical Journal D* 66, 289 (2012).

- A. Gardner, K. Sheridan, W. Groom, N. Seymour-Smith and M. Keller, **Precision spectroscopy technique for dipole-allowed transitions in laser-cooled ions**, *Applied Physics B* 117, 755 (2014).

Chapter 2

Theory

The ion-trapping and laser cooling techniques used in this thesis are now commonplace in many atomic and molecular physics (and chemistry) laboratories across the world. This chapter outlines the basic theory required to understand these fundamental tools in the field. Some other techniques that arise from atom-light interactions are also looked at, such as the dipole force interaction which plays a crucial role in the proposed non-destructive state detection technique for molecular ions. There are also ways in which the radiation pressure force (usually used for Doppler laser cooling) can be utilised for excitation and amplification of the secular motion of the ion in the trapping potential.

Molecular ions bring a higher degree of complexity to ion-trapping, mainly due to their internal structure. The main aspects of this are discussed in chapters 5 and 6 - such as cooling the translational motion and the ionisation process required.

2.1 Linear Paul trap

The idea of the Paul trap in 1953 was to revolutionise the field of atomic, molecular and optical physics [52]. In 1980 Wolfgang Paul's invention enabled physicists to accomplish what was previously thought to be the impossible[1]: the confinement of a single Ba^+ ion in the laboratories of Heidelberg [54]. The highly localised nature of ions in these traps has become indispensable for a wide range of experiments that require a high degree of control over the ion's motional degrees of freedom.

The true significance of this invention can be further explained using Earnshaw's theorem, which states that: "a charged particle cannot be held in a stable equilibrium by

[1] Erwin Schrodinger's very famous quote of 1952: *"We never experiment with just one electron or atom or (small) molecule. In thought-experiments we sometimes assume that we do; this invariably entails ridiculous consequences."* [53]

electrostatic forces alone" [55], which is explained further on. The great leap from the impossible trapping of charges in a static DC field to the single-ion confining Paul trap comes from the introduction of a time-varying electric field at radiofrequency (rf).

There are two main categories into which all Paul traps fall. Traps that provide rf confinement in two dimensions, and traps that confine in three dimensions. After this, actual designs can vary widely from using two small endcap electrodes [56], to opening up the whole geometry to form surface ion traps [57]. In this experiment the ion trap used is a linear Paul trap, which has a two dimensional quadrupole field. Therefore this is the category of ion trap that will be reviewed in this thesis.

To understand the dynamics of what happens when a charged particle (ion) is placed into the linear Paul trap, Gauss's law from Maxwell's equations of electrodynamics is the starting point:

$$\nabla \cdot \vec{E} = \frac{\rho}{\epsilon_0}, \tag{2.1}$$

where $\vec{E}$ is the electric field, ρ is the total charge density and ϵ_0 is the permittivity of free space. More specifically, we want to find what the electric potential Φ looks like for our case, and so Poisson's equation has to be used:

$$\nabla^2\Phi = \frac{-\rho}{\epsilon_0}. \tag{2.2}$$

There is no charge, and so as $\rho = 0$, we get to Laplace's equation,

$$\nabla^2\Phi = 0. \tag{2.3}$$

Laplace's equation gives us two important results. Primarily, it allows for the calculation of the potential, which is what we wanted. More subtly, it invokes the previously mentioned Earnshaw's theorem, that shows us why it is not possible to confine charges with static electric fields alone. Equation 2.3 shows that the potential has no local maxima or minima, and thus no ability to provide a potential minimum for the the confinement of charges.

Next, the potential for a quadrupole field $\Phi(x, y, z)$ can be written as:

$$\Phi(x, y, z) = \frac{\Phi_0}{2r_0}(\alpha x^2 + \beta y^2 + \gamma z^2). \tag{2.4}$$

In order to find what the constants α, β and γ are, Laplace's eq. 2.3 has to be used, and so the second differential of the potential goes to zero. This results in:

$$\alpha + \beta + \gamma = 0 \tag{2.5}$$

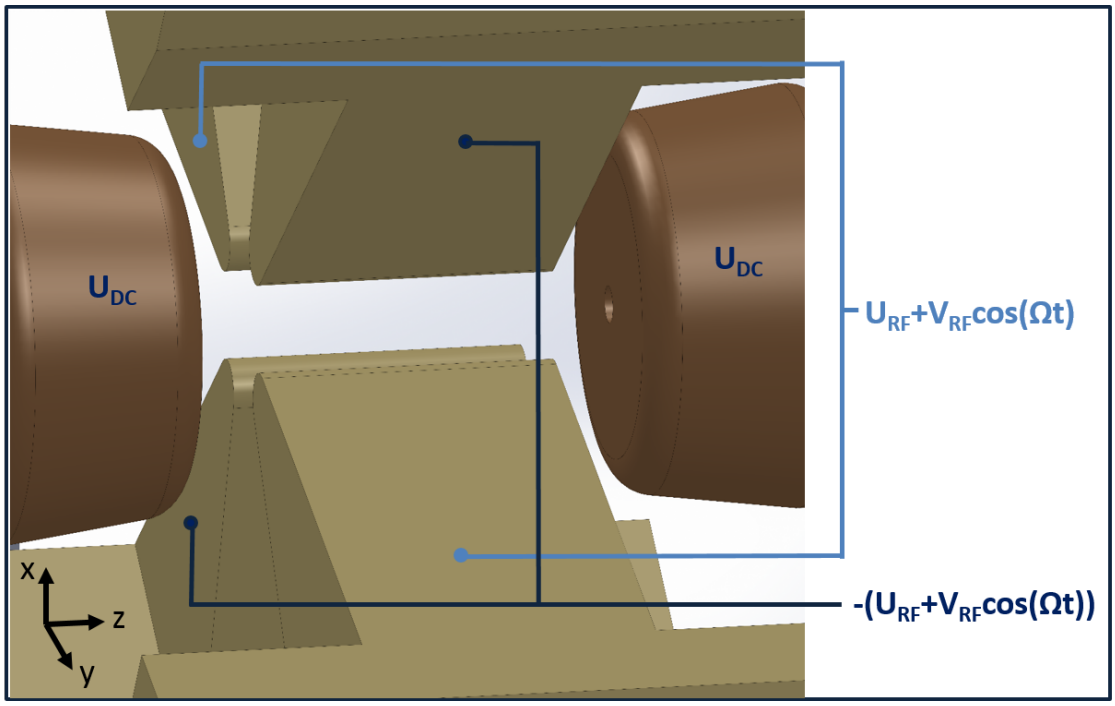

Figure 2.1: A linear Paul trap with four blade-shaped electrodes for trapping in the x-y plane. Two additional electrodes provide confinement along the z-axis, and each are held at a DC voltage of U_{DC}. Design by Dr. Matthias Keller.

(except in the case where $\Phi_0 = 0$).

For the specific case of the two dimensional quadrupole (ie. for a linear Paul trap), $\gamma = 0$ [52]. Therefore $\alpha = -\beta = 1$ can be considered. This gives us a potential of the form:

$$\phi_{Rad} = \frac{\phi_{RF}}{r_0^2}(x^2 - y^2) \tag{2.6}$$

in the radial direction for ideal, hyperbolic electrodes, with r_0 being the ion-electrode distance. In the axial direction we apply a harmonic DC potential of the form:

$$\phi_{Ax} = \frac{\phi_{DC}}{z_0^2}(z^2)\eta, \tag{2.7}$$

where z_0 is the distance between the axial electrodes, and η describes the geometry. To describe the whole potential we add the two components $\phi_{tot} = \phi_{Rad} + \phi_{Ax}$ and express everything in terms of x and y:

$$\phi_{tot} = \frac{\phi_{RF}}{r_0^2}(x^2 - y^2) + \frac{\phi_{DC}}{z_0^2}(x^2 + y^2)\eta. \tag{2.8}$$

Laplace's eq. 2.3 showed us that there is no potential minimum in space for static fields,

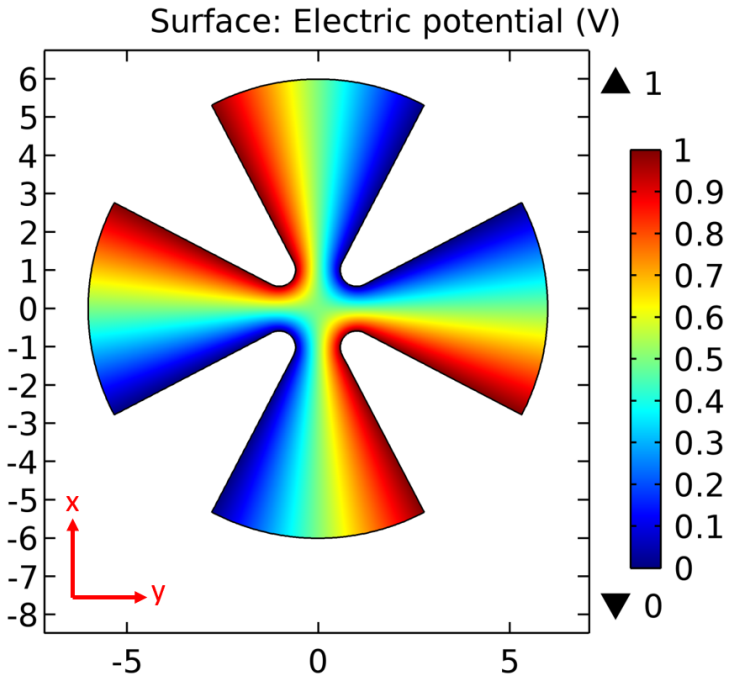

Figure 2.2: The electric field in a linear Paul trap with four blade-shaped electrodes for trapping in the x-y plane at time t (the spacial coordinates are marked in red). After half an rf cycle the field will switch direction. Simulated by Dr. Matthias Keller.

therefore the voltage applied to the radial electrodes is an oscillating field at a frequency Ω. For there to be a confining effect, it is required at time t that two of the electrodes are at a positive potential - specifically a pair of diagonally facing electrodes (fig. 2.1). Meanwhile the other two are held at rf ground. The electrodes onto which we apply a potential then oscillate between positive and negative (The field at a moment in time has been simulated in fig. 2.2). This oscillating voltage looks like $\phi_{RF} = U_{RF} + V_{RF}cos(\Omega t)$, where V_{RF} is the amplitude of the rf voltage, and U_{RF} is a DC quadrupole offset that can be applied to the radial electrodes. The DC potential in the z-direction in eq. 2.7 comes simply from an applied DC voltage $\phi_{DC} = U_{DC}$.

The equations of motion that describe the behaviour of the ion for the potential in eq. 2.8 are now found. This is done simply by finding the force induced by the potential $\left(F_x = -e\frac{d\phi_{tot}}{dx}\right)$ in the x direction and equating with $F_x = m\ddot{x}$ to give:

$$\ddot{x} + \frac{e}{m}\left(\frac{U_{DC}\eta}{z_0^2} + \frac{U_{RF}}{r_0^2} + \frac{V_{RF}cos(\Omega t)}{r_0^2}\right)x = 0 \tag{2.9}$$

and similarly for y:

$$\ddot{y} + \frac{e}{m}\left(\frac{U_{DC}\eta}{z_0^2} - \frac{U_{RF}}{r_0^2} - \frac{V_{RF}cos(\Omega t)}{r_0^2}\right)y = 0. \tag{2.10}$$

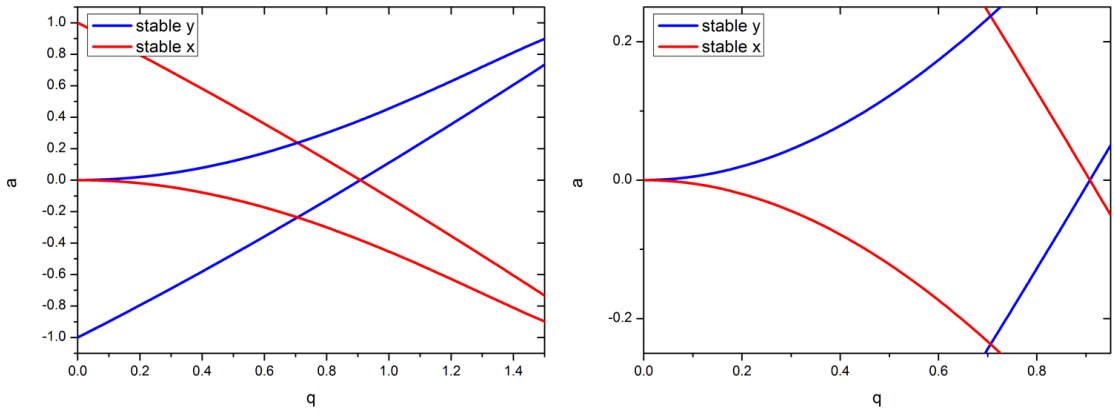

Figure 2.3: Stability regions found through stable solutions of the Mathieu equations. These regions have been plotted using the stable solutions quoted in [1]. *Left:* The first stability regions in x and y. The area enclosed by the red lines give stable solutions for x, with the area enclosed by the blue lines giving stable solutions for y. Where the two overlap gives the kite-shaped stable trapping region in terms of the a and q parameters. *Right:* The same region zoomed in.

The stable solutions to these equations can be found if they can be put into the form of the canonical Mathieu equations, for which the stable solutions are known:

$$\frac{d^2x}{d\zeta^2} - (a - 2q\cos(2\zeta))\,x = 0, \tag{2.11}$$

$$\frac{d^2y}{d\zeta^2} - (a + 2q\cos(2\zeta))\,y = 0. \tag{2.12}$$

This can be achieved by introducing:

$$q = \frac{2V_{RF}e}{mr_0^2\Omega^2}, \tag{2.13}$$

$$a = -\frac{4e}{m\Omega^2}\left(\frac{U_{DC}\eta}{z_0^2} \pm \frac{U_{RF}}{r_0^2}\right), \tag{2.14}$$

where $\zeta = \frac{\Omega t}{2}$ has also been introduced. In general, the trap is not operated with the extra DC quadrupole U_{RF}, and so the a parameter can be written:

$$a_{Ax} = -\frac{4e}{m\Omega^2}\frac{U_{DC}\eta}{z_0^2}, \tag{2.15}$$

and is negative due to the anti-confining effect in the radial direction.

The stable solutions to the Mathieu equations are known, and can now be used to find out for what values of the parameters a and q the ion is stable in the trap. The first

stability region has been plotted in fig. 2.3, using solutions given in [1]. Where the areas enclosed for x and y stability overlap gives the kite-shaped stable trapping region for a linear Paul trap. From eq. 2.13 and eq. 2.14 we can see that where the ion sits in the stability diagram depends on the voltages applied to the electrodes, the trap geometry η, the drive frequency Ω and the charge to mass ratio of the ion being trapped.

An approximate solution to the Mathieu equations can be found which demonstrates an interesting result. If the approximation $|a|$, $|q| \ll 1$ is made, then the solutions

$$x(t) = x_0 \left(1 - q\cos(\Omega t)\right)\cos(\omega_r t), \tag{2.16}$$

and

$$y(t) = y_0 \left(1 - q\cos(\Omega t)\right)\cos(\omega_r t), \tag{2.17}$$

are found. An additional oscillating term is revealed along with the trap drive frequency Ω. This is the secular frequency of the ion in the radial potential, ω_r, and is given in terms of the a and q parameters by:

$$\omega_r = \frac{\sqrt{q^2/2 \pm a}}{2}\Omega. \tag{2.18}$$

As a result, we describe the trapping potential generated in the radial direction as a harmonic 'pseudo potential' in which the ion has oscillation frequency ω_r, also known as the radial secular frequency. Additional to this, the ion undergoes another oscillation due to the trapping field which has frequency Ω and is called micromotion.

The resulting motion of the ion as it is displaced from the trap centre has been plotted in fig. 2.4. When at the trap centre, the contribution from the trap drive is at a minimum, and so this is where it is best to place the ion. As the ion is displaced from the trap centre by the secular motion within the trapping potential, the driven trap-drive motion, also known as the micromotion, increases until a turning point is reached. Stray fields or patch potentials can displace where the ion sits, and so micromotion minimisation techniques are used to bring it back to the trap centre, as demonstrated in sec. 3.3.2.

The ion is also confined in the axial direction due to the potential from the DC electrodes held at U_{DC} (eq. 2.7). The equation of motion for the ion in the axial z-direction is:

$$\ddot{z} + z\frac{a_{Ax}}{2}\Omega^2 = 0, \tag{2.19}$$

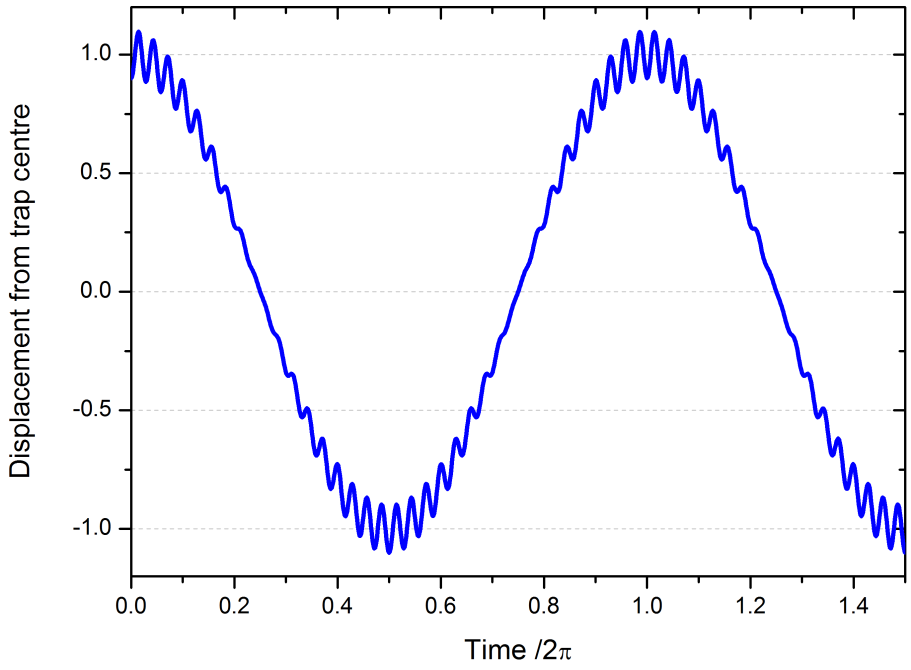

Figure 2.4: The slow secular motion, with an amplitude of 1, and fast micromotion of the ion in the trapping field. The displacement from trap centre has been plotted as a function of the periodic secular motion for a q value of 0.1, and for $\Omega = 30\ \omega_r$.

which has the simple solution:

$$z(t) = z_0 \cos(\omega_z t), \tag{2.20}$$

with

$$\omega_z = \Omega \sqrt{\frac{-a_{Ax}}{2}}, \tag{2.21}$$

which describes the secular motion of the ion in the axial direction.

2.2 Atom-light interactions

The invention of the laser has had far-reaching consequences throughout the physical sciences. The ability to trap ions and then tune lasers to probe specific internal transitions has revolutionised the field of atomic and molecular physics. This atom-laser system gives rise to a new regime for atom-light interactions - lasers providing highly intense narrow-band radiation present some interesting effects that are very advantageous to the ion

trapper.

When an ion is placed in a laser field that has some detuning $\Delta\omega$ from its internal transition, it feels a force. This force can be split into two parts:

- A dissipative force arising from absorption and spontaneous decay, also known as radiation pressure, which is used for laser Doppler cooling.
- A conservative force that comes from the intensity gradient of the field, the dispersive dipole force. This is often used as a technique for confinement of neutral atoms.

Although both are present when applying a laser to an ion, generally one will dominate depending on the parameters used; for instance, as will be seen in sec. 2.2.2, the dipole force goes to zero when the detuning is zero, and the radiation pressure dominates [58].

Doppler cooling is vital to keeping the ion well localised in the ion trap, where the kinetic energy of the ion has to be less than the energy required to leave the trap. The methods for cooling and trapping atoms with laser light earned Steven Chu, Claude Cohen-Tannoudji and William D. Phillips the Nobel prize for physics in 1997 [59]. The Doppler cooling of atomic ion species $^{40}Ca^{+}$ is central to all of the ion trap experiments in this thesis. The molecular species used, N_2^+, cannot be directly laser cooled, but is always trapped alongside calcium, which has the effect of sympathetically cooling its external motion. This is discussed further on in chapter 6.

The dipole force is the basis for the non-destructive state detection technique presented in this thesis. It will be used to provide a state-dependent resonant force on the ion's translational motion, which can then be read out using the Doppler velocimetry technique that is also discussed in this chapter.

2.2.1 Two-level system coupled by a laser

To understand the basics of both laser Doppler cooling and the dipole force interaction, a two level system will be considered. To describe the full atom-laser system a semi-classical approach will be taken, with the laser field treated as a classical oscillating electric field. This interaction picture is then fully described by the time evolution of the elements of the density matrix. Figure 2.5 shows the two-level system, with states that have wavefunctions ψ_1 and ψ_2 with energies $\hbar\omega_1$ and $\hbar\omega_2$ respectively. The laser applied is detuned by $\Delta\omega$ from the transition which has frequency $\omega_0 = \omega_2 - \omega_1$. The study of the time evolution of such a system will require us to use the time-dependent Schrödinger equation:

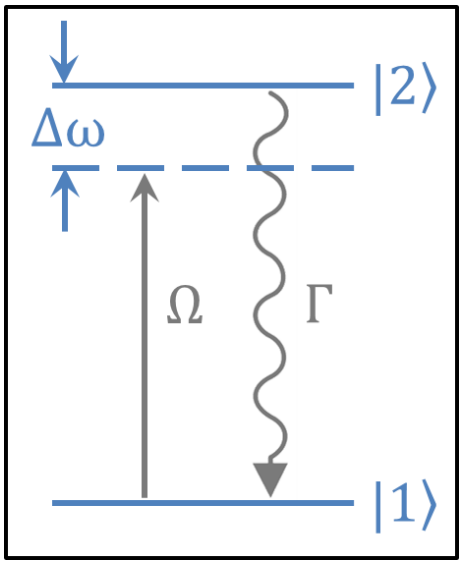

Figure 2.5: Interaction of a two-level system with a light field that has detuning $\Delta\omega$, the strength of which is described by the Rabi frequency Ω. The spontaneous decay rate from the excited state is given by Γ.

$$\hat{H}\Psi\left(\vec{r},t\right)=i\hbar\frac{\partial\Psi}{\partial t}, \tag{2.22}$$

which is a differential equation where $\hat{H}$ is the hamiltonian and $\Psi\left(\vec{r},t\right)$ is the wavefunction which is dependent on time and space.

The two-level atom that we wish to investigate has the following Hamiltonian and total wavefunction:

$$\hat{H}=\hat{H}_A+\hat{V}(t), \tag{2.23}$$

$$\Psi\left(\vec{r},t\right)=\psi_1\left(\vec{r}\right)e^{-i\omega_1 t}C_1(t)+\psi_2\left(\vec{r}\right)e^{-i\omega_2 t}C_2(t), \tag{2.24}$$

where the total wavefunction has been written as the sum of wavefunctions for state 1 and state 2. The amplitudes $C_1(t)$ and $C_2(t)$ have been introduced, and when squared give the measurement probability of each state. Therefore, $|C_1(t)|^2+|C_2(t)|^2=1$ is required for normalisation. The atomic part of the Hamiltonian is $\hat{H}_A$, and $\hat{V}(t)$ is a time-dependent interaction part of the Hamiltonian, defined as:

$$\hat{V}(t)=\hat{\mu}\cdot\vec{E}(t), \tag{2.25}$$

$$\vec{E}(t)=\frac{1}{2}\vec{E}_0\left(e^{i\omega t}+e^{-i\omega t}\right), \tag{2.26}$$

with the applied electric field $\vec{E}(t)$ of the laser having amplitude $\vec{E}_0$ and oscillating at frequency ω. The transition dipole moment operator of the two level system is given by:

$$\hat{\mu} = -e \int \Psi^*(\vec{r}, t) r \Psi(\vec{r}, t) dV, \tag{2.27}$$

and can now be used to calculate the dipole moment of the atom using the wavefunction in eq. 2.24. Terms with μ_{11} and μ_{22} go to zero, giving [60]:

$$\hat{\mu} = \left(C_2^*(t) C_1(t) \mu_{21} e^{i\omega_0 t} + C_1^*(t) C_2(t) \mu_{12} e^{-i\omega_0 t} \right). \tag{2.28}$$

By substituting the wavefunction eq. 2.24 into the time-dependent Schrödinger equation (eq. 2.22), and using the rotating wave approximation [61], two coupled equations are found for the amplitudes $C_1(t)$ and $C_2(t)$:

$$i \frac{dC_1}{dt} = C_2 e^{-i\Delta\omega t} \frac{\Omega_0}{2}, \tag{2.29}$$

$$i \frac{dC_2}{dt} = C_1 e^{i\Delta\omega t} \frac{\Omega_0^*}{2}, \tag{2.30}$$

where the detuning of the laser from the transition $\Delta\omega$ has been introduced and is given by $\Delta\omega = \omega - \omega_0$. The on-resonance Rabi frequency Ω_0 is:

$$\Omega_0 = \frac{\vec{\mu}_{12} \cdot E_0}{\hbar}, \tag{2.31}$$

where the generalised Rabi frequency is given by $\Omega = \sqrt{(\Delta\omega)^2 + \Omega_0^2}$. When eq. 2.30 is integrated from time $t = 0$ to time t, and initial conditions of $C_1(t = 0) = 1$ and $C_2(t = 0) = 0$ set, an equation for the excited state amplitude is found:

$$C_2(t) = \frac{\Omega_0^*}{2} \left[\frac{1 - e^{i\Delta\omega t}}{\Delta\omega} \right]. \tag{2.32}$$

So far, this has not considered the effect of spontaneous decay. In order to investigate this, the density operator is introduced:

$$\rho = \sum_i P_i \left| \psi_i \right\rangle \left\langle \psi_i \right|. \tag{2.33}$$

For the two-level system considered here, the density operator becomes a 2x2 matrix, the trace of which is equal to one. The diagonal elements give the populations in state $|1\rangle$ and state $|2\rangle$, with the off-diagonal elements being *coherences* between the two states, which first appeared in eq. 2.28:

$$\rho = \begin{pmatrix} \rho_{11} & \rho_{12} \\ \rho_{21} & \rho_{22} \end{pmatrix} = \begin{pmatrix} |C_{11}|^2 & C_1 C_2^* \\ C_2 C_1^* & |C_{22}|^2 \end{pmatrix}. \tag{2.34}$$

It is the time evolution of these elements that describe the evolution of the system. The time evolution of the density matrix is given by the Liouville equation:

$$\frac{d\rho(t)}{dt} = \frac{i}{\hbar}\left[\rho(t), \hat{H}\right]. \tag{2.35}$$

This equation does not take the effect of spontaneous emission into account. To truly describe the full system another term has to be added to the Liouville equation, now forming it into what is known as the master equation [62]:

$$\frac{d\rho(t)}{dt} = \frac{i}{\hbar}\left[\rho(t), \hat{H}\right] + \Lambda\rho, \tag{2.36}$$

$$\Lambda\rho = -\frac{\Gamma}{2}\left[\sigma_+\sigma_-\rho - 2\sigma_-\rho\sigma_+ + \rho\sigma_+\sigma_-\right], \tag{2.37}$$

with Γ being the rate of spontaneous decay of the excited level. It is also known as the Einstein A coefficient. The operators $\sigma_+ = |2\rangle\langle 1|$ and $\sigma_- = |1\rangle\langle 2|$ are the atomic raising and lowering operators respectively.

Either by using the master equation, or by using the coupled equations found in eq. 2.29 and eq. 2.30 (when an extra spontaneous emission term has been added), the time evolution of each of the elements of the density matrix can now be found. They are:

$$\frac{d\rho_{11}}{dt} = \Gamma\rho_{22} - i\frac{\Omega_0}{2}\left[e^{i\Delta\omega t}\rho_{21} - e^{-i\Delta\omega t}\rho_{12}\right], \tag{2.38}$$

$$\frac{d\rho_{22}}{dt} = -\Gamma\rho_{22} + i\frac{\Omega_0}{2}\left[e^{i\Delta\omega t}\rho_{21} - e^{-i\Delta\omega t}\rho_{12}\right], \tag{2.39}$$

$$\frac{d\rho_{12}}{dt} = -\frac{\Gamma\rho_{12}}{2} + i\frac{\Omega_0}{2}e^{i\Delta\omega t}\left(\rho_{11} - \rho_{22}\right), \tag{2.40}$$

$$\frac{d\rho_{21}}{dt} = -\frac{\Gamma\rho_{21}}{2} - i\frac{\Omega_0}{2}e^{-i\Delta\omega t}\left(\rho_{11} - \rho_{22}\right), \tag{2.41}$$

and are known as the optical Bloch equations (OBEs), assuming Ω_0 is real. By making the substitution $\tilde{\rho}_{21} = \rho_{21}e^{i\Delta\omega t}$ these are simplified to:

$$\frac{d\rho_{11}}{dt} = \Gamma\rho_{22} - i\frac{\Omega_0}{2}\left(\tilde{\rho}_{21} - \tilde{\rho}_{12}\right) = -\frac{d\rho_{22}}{dt} \tag{2.42}$$

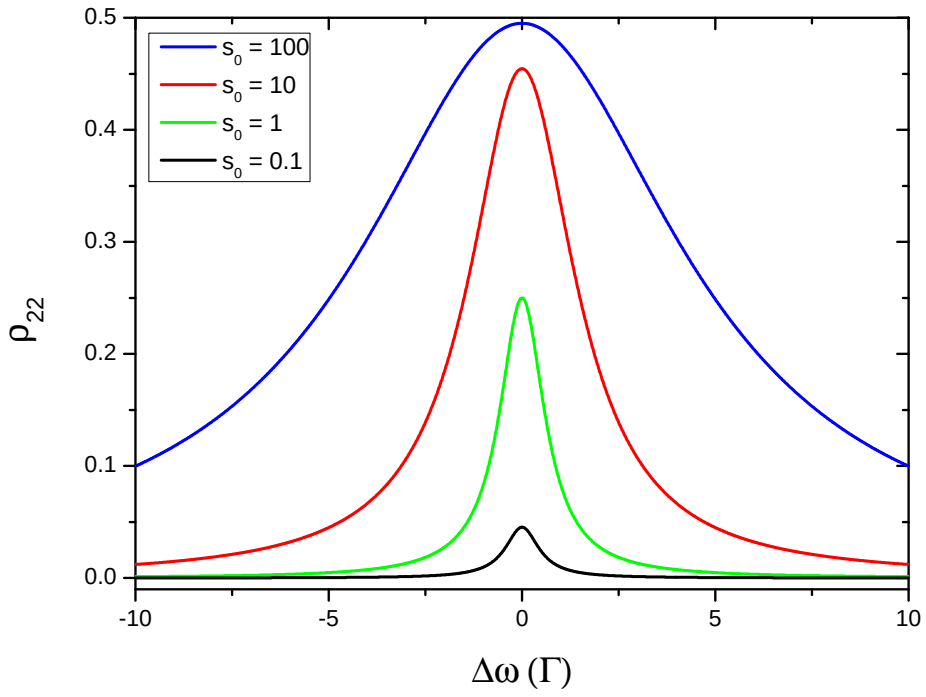

Figure 2.6: The fraction of population in the excited state ρ_{22} plotted as a function of the detuning. This has been plotted for four different values of the saturation parameter, s_0. For the larger values, the effect of power broadening becomes more extreme, and the excited state population reaches a limit of 0.5. This is made even clearer in fig. 2.7.

$$\frac{d\tilde{\rho}_{12}}{dt} = -\frac{\Gamma\tilde{\rho}_{12}}{2} + i\frac{\Omega_0}{2}\left(\rho_{11} - \rho_{22}\right) - \tilde{\rho}_{12}i\Delta\omega = \frac{d\tilde{\rho}^*_{21}}{dt}. \tag{2.43}$$

By using the relation $\tilde{\rho_{12}} = \tilde{\rho}^*_{21}$, conservation of population $\rho_{11} + \rho_{22} = 1$, and finding the steady-state solutions to these coupled equations (ie. when $d\rho/dt = 0$), the population in the excited state when the system is in equilibrium is given by [58]:

$$\rho_{22} = \frac{s_0/2}{1 + s_0 + \left(2\Delta\omega/\Gamma\right)^2}, \tag{2.44}$$

where $s_0 = 2\Omega^2/\Gamma^2 = I/I_s$ is the on-resonance saturation parameter, which is also defined as the ratio of the intensity to the saturation intensity I_s:

$$I_s = \frac{2\pi^2 hc\Gamma}{3\lambda^3}. \tag{2.45}$$

Additionally an expression for the coherences can be found [58],

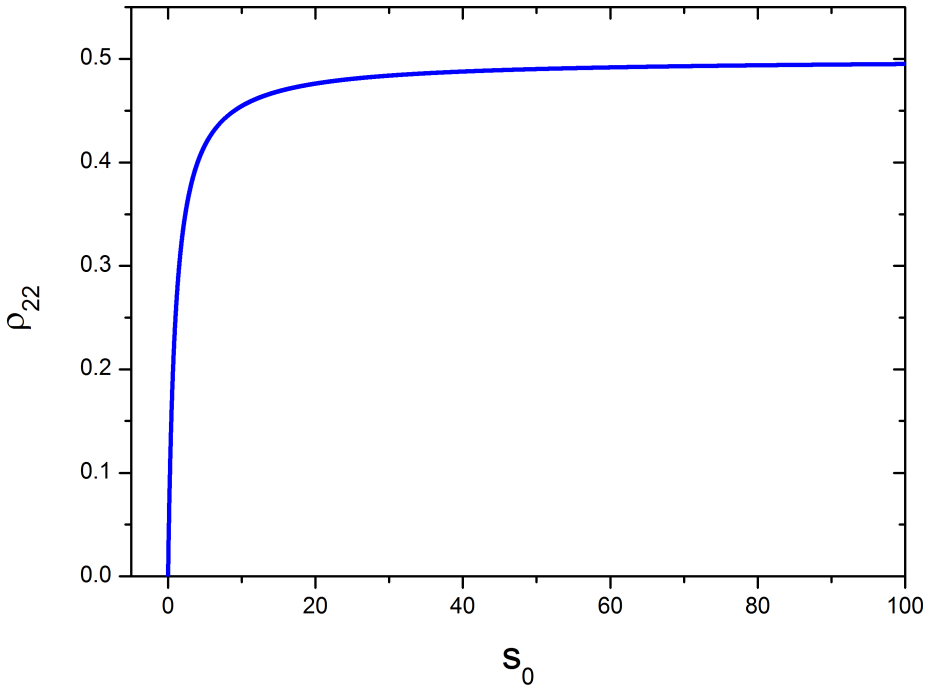

Figure 2.7: The fraction of population in the excited state ρ_{22} plotted as a function of the saturation parameter, when the detuning $\Delta\omega = 0$. The population saturates at a value below 0.5, beyond which there is no further increase or decrease, no matter how much greater the saturation parameter.

$$\tilde{\rho}_{21} = \frac{i\Omega_0}{2\left(\frac{\Gamma}{2} - i\Delta\omega\right)\left(1 + \frac{2\Omega_0^2}{\Gamma^2 + 4\Delta\omega^2}\right)}. \tag{2.46}$$

The excited state population as a function of the detuning has been plotted in fig. 2.6, for a set of different saturation parameters. When resonant ($\Delta\omega = 0$) light of a high intensity ($s_0 \gg 1$) is applied to the two-level system, the excited state population approaches half of the total population. As the applied intensity is reduced, the population of the excited state reduces, with the majority being in the ground state at any given time. This is illustrated further in fig. 2.7, where ρ_{22} has been plotted as a function of the saturation parameter for a detuning $\Delta\omega = 0$. As the power is increased, the transition saturates and the excited state population approaches a limit of 0.5.

For the higher applied intensities the broadening of the transition becomes more extreme. This is a result known as power broadening, where the width of the power broadened line is given by:

$$\Gamma' = \Gamma\sqrt{1+s_0}. \tag{2.47}$$

2.2.2 Force on a two-level atom

By using the results found for a two-level atom in sec. 2.2.1, it is now possible to consider the total force that arises from the interaction of a laser when applied to an atom. First, the time differential of the momentum operator $\hat{p}$ is considered, as this will result in the force [58]:

$$\vec{F} = \frac{d\langle\hat{p}\rangle}{dt} = \frac{i}{\hbar}\left\langle\left[\hat{H},\hat{p}\right]\right\rangle, \tag{2.48}$$

where the commutation relation between the Hamiltonian of the system $\hat{H}$ and the momentum operator $\hat{p}$ is given by $\left[\hat{H},\hat{p}\right] = i\hbar\frac{d\hat{H}}{dz}$, and so the resulting equation when this is substituted into eq. 2.48 can be used to find the force in the z direction:

$$F_z = \left\langle -\frac{d\hat{H}}{dz}\right\rangle, \tag{2.49}$$

for which the interaction part of the Hamiltonian $\hat{V}(t)$ is used from eq. 2.25 [58]. By substituting the expression found in eq. 2.28 into the above, and expressing it in terms of the density matrix elements, a force of the form:

$$F_z = -\mu_{12}\left(\tilde{\rho}_{21}e^{-i\omega t} + \tilde{\rho}_{12}e^{i\omega t}\right)\frac{d\vec{E}}{dt} \tag{2.50}$$

is found. Next the electric field defined in eq. 2.26 is used to get:

$$F_z = \frac{-\mu_{12}}{2}\left(\left(\tilde{\rho}_{12}+\tilde{\rho}_{21}\right)\frac{\partial E_0}{\partial z} + E_0 ki\left(\tilde{\rho}_{12}-\tilde{\rho}_{21}\right)\right). \tag{2.51}$$

When split into its real and imaginary parts, this now reveals an expression for the total force on the atom that has two components. The steady-state solutions to the OBEs for the coherence term $\tilde{\rho}_{12}$ is used (see eq. 2.46) along with the definition of the saturation parameter (used in eq. 2.44) to get a final expression of:

$$F_z = \frac{s_0\mu_{12}/\Omega_0}{1+s_0+\left(\frac{2\Delta\omega}{\Gamma}\right)^2}\left(-\Delta\omega\frac{\partial E_0}{\partial z} + \frac{\Gamma}{2}E_0 k\right) \tag{2.52}$$

for the two level atom.

The second term is dependent on the scattering rate Γ which comes from the spontaneous decay of the excited state. It is this term that gives us the radiation pressure

force. The proportionality to Γ means that the scattering force is limited; the excited state eventually saturates and the force will reach a maximum.

The radiation pressure force is what is used for Doppler laser cooling of atomic ions, and so it is important to explore further the origins of this force separately from eq. 2.52. Considering an atom at rest and initially in the ground state, and a photon of momentum $\vec{p} = \hbar\vec{k}$, one absorbed photon will result in the atom receiving a momentum kick in the direction of the k-vector. Once in the excited state, the atom can undergo one of two emission processes; either stimulated or spontaneous emission. The former will result in an equal and opposite momentum kick to the first received during absorption, and so the net force goes to zero. But if the atom spontaneously decays instead, the photon is emitted in a random direction. Therefore, if many absorption-spontaneous emission cycles are considered, there is a force of zero due to the spontaneous decay, but overall a total force in the direction of the k-vector due to absorption. The force from the absorption-spontaneous emission process can then be written:

$$\vec{F}_{RP} = \frac{d\vec{p}}{dt} = \hbar\vec{k}\Gamma\rho_{22}. \tag{2.53}$$

Considering the two-level system excited state population given in eq. 2.44, the radiation pressure force then becomes:

$$\vec{F}_{RP} = \hbar\vec{k}\Gamma\frac{s_0/2}{1 + s_0 + \left(\frac{2\Delta\omega}{\Gamma}\right)^2}. \tag{2.54}$$

This equation gives the radiation pressure force when the atom is at rest, and agrees with the second term in eq. 2.52.

The first term is dependent on the detuning of the laser from the transition $\Delta\omega$, and results in the dipole force. This arises when there is a spatial gradient in the light intensity. The electric field induces energy shifts of the states, and so if there is a spatial gradient to this shift, there is a resulting force. Conversely to the scattering force, this is not limited by the saturation of the excited state, and can be arbitrarily increased by introducing a steeper intensity gradient.

It is this detuning-dependent force (see the first term in eq. 2.52) that is utilised for resonantly exciting the motion of the N_2^+ in the molecular state detection scheme. For the purposes of this scheme the parameters have to be carefully chosen in order to avoid exciting the molecule during detection and losing the state.

The first term of eq. 2.52 gives the form of the dipole force part of the total force that acts on the atom. This leads to the expression (in the z-direction):

$$F_{dipole} = -\frac{\hbar\Delta\omega}{\Omega_0}\left(\frac{s_0}{1+s_0+\left(\frac{2\Delta\omega}{\Gamma}\right)^2}\right)\frac{\partial\Omega_0}{\partial z}. \tag{2.55}$$

As mentioned previously, it can now be seen that when the laser is tuned to resonance, ie. the detuning $\Delta\omega = 0$, the dipole force also goes to zero. And so in this limit, the only force that can act on the atom is from the radiation pressure. For the case that $\Delta\omega \gg \Gamma$, the dipole force becomes (in all directions):

$$F_{dipole} = -\nabla\left(\frac{\hbar\Omega^2}{4\Delta\omega}\right), \tag{2.56}$$

which is also known as the gradient of the AC stark shift. The term $\frac{\hbar\Omega^2}{4\Delta\omega}$ is equal to the magnitude of the energy shift of each of the states in the two level system, and so the spatial gradient of this leads to a force. In terms of the intensity, this can be written:

$$F_{dipole} = -\frac{\mu_{12}^2\nabla I}{c\epsilon_0\Delta\omega\hbar}, \tag{2.57}$$

where $I = \frac{1}{2}c\epsilon_0 E_0^2$, and c is the speed of light. Now the dependence of this force on the intensity gradient of the applied laser becomes apparent. Additionally, in this form we can see that the dipole force is inversely proportional to the detuning of the laser from the transition. Further on in this chapter, in sec. 2.3.3, the dipole force has been calculated for a transition in N_2^+, and the dependence of the force on the detuning for the limit $\Delta\omega \gg \Gamma$ is illustrated.

Laser Doppler cooling

The expression in eq. 2.54 gives the radiation pressure force from a laser field on an atom. However, this is not the full picture, and does not yet describe the laser cooling principle. When the atom is no longer at rest, and has motion that has a component in the direction of the laser, there is a shift in the frequency in the atom's frame due to the Doppler effect. The detuning is then shifted so that: $\Delta\omega \to \Delta\omega + \delta$, where the additional frequency shift is dependent on the velocity of the atom in the direction of $\vec{k}$: $\delta = v_k\vec{k}$. Substituting this back into eq. 2.54 gives:

$$\vec{F}_{RP}(v_k) = \hbar\vec{k}\Gamma\frac{s_0/2}{1+s_0+\left(\frac{(2\Delta\omega+v_k\vec{k})}{\Gamma}\right)^2}. \tag{2.58}$$

In order to get a better picture of how the Doppler shift now affects the force, it is useful to separate the force into two parts, with one being dependent on the atom's velocity in

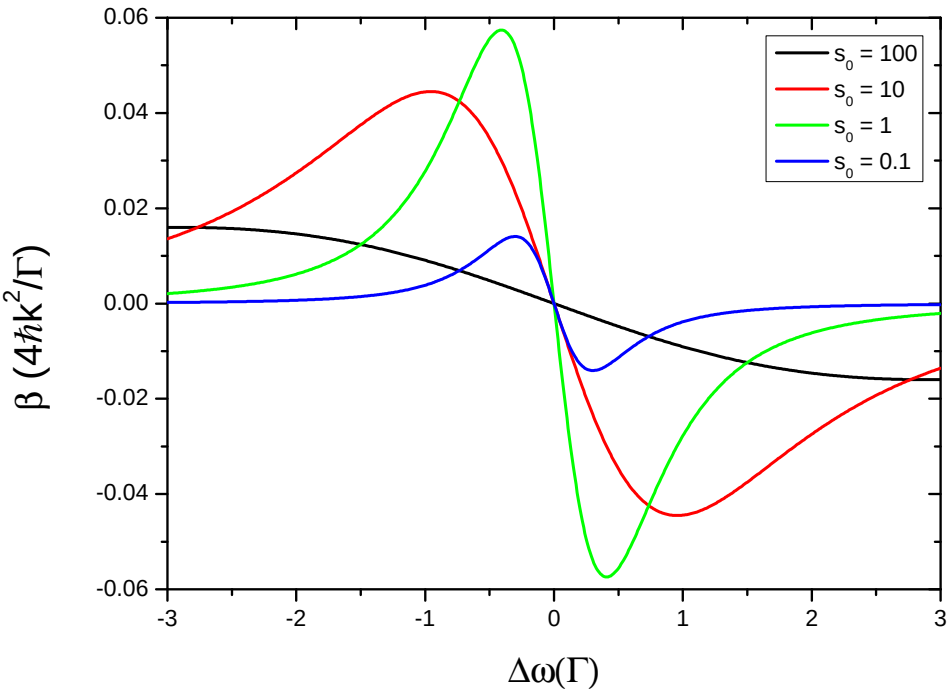

Figure 2.8: The damping coefficient β plotted as a function of the detuning $\Delta\omega$ for four different saturation parameters.

the $\vec{k}$ direction. This can be achieved by approximating the force by the first two terms of a Taylor expansion around $v_k = 0$:

$$\vec{F}_{RP}(v_k) = \vec{F}_0 + \beta v_k \tag{2.59}$$

(for small velocity). Here:

$$\vec{F}_0 = \hbar\vec{k}\frac{s_0\Gamma/2}{1 + s_0 + \left(\frac{2\Delta\omega}{\Gamma}\right)^2}, \tag{2.60}$$

and

$$\beta = -\frac{4\hbar k^2\Delta\omega}{\Gamma} \cdot \frac{s_0}{\left(1 + s_0 + \left(\frac{2\Delta\omega}{\Gamma}\right)^2\right)^2}. \tag{2.61}$$

Immediately it can be seen that the velocity-dependent β term is in the opposite direction to the the velocity. As the magnitude of the velocity increases, so does the force - but in the opposite direction. This is the damping force that is used for laser cooling of atoms. The β damping coefficient has been plotted for four different saturation parameters as shown in fig. 2.8. For negative detunings (red-detuned) of the laser from the transition,

the damping force is positive, and opposes the motion of the atom. The opposite is true for the blue-detuned case. There is also a saturation effect due to the limit on the scattering rate of the transition. For saturation parameters $s_0 \leq 1$, the damping force increases with saturation parameter. After this, the damping force starts to decrease again. The optimum Doppler cooling parameters for which the damping force is maximised are $s_0 = 2$, at a detuning of $-\Gamma/2$.

Although the net momentum that the atom acquires from spontaneous emission is zero, the recoil force from each individual event is not, and imparts some kinetic energy that contributes to heating. The Doppler cooling process is therefore limited by the scattering rate of the excited state. Taking the kinetic energy $(\hbar k)^2/2m$ and the scattering rate, $\Gamma\rho_{22}$ into account, a total heating rate of $R = \Gamma\rho_{22}(\hbar k)^2/m$ is found [63]. Equating the heating rate to the cooling rate, which is $\left\langle \vec{F} \cdot \vec{v} \right\rangle = \beta \left\langle v_k^2 \right\rangle$ gives a limit to the Doppler cooling temperature of:

$$T_{limit} = \frac{\hbar\Gamma}{2k_B}, \tag{2.62}$$

where k_B is the Boltzmann constant. This gives a Doppler cooling limit of 0.5 mK for ^{40}Ca ions [17].

2.2.3 Three-level system coupled by two lasers

The two-level system has so far illustrated the main dynamics of atom-light interactions. However, in general, we are not lucky enough to work with simply a two-level system and a more realistic setup would include a third state. The $^{40}Ca^+$ level scheme can be approximated as three levels, called a Λ system, which it is possible to use for Doppler laser cooling. In the Λ system, the cooling transition used is the S$\rightarrow$P transition with frequency ω_{SP}, shown in fig. 2.9. The cooling laser has detuning $\Delta\omega_C = \omega_{SP} - \omega_C$ from the transition, where ω_C is the frequency of the applied laser. The extra complexity now comes from the probability of decay Γ_R from the P state down into a third state, which is D. If this occurs then the S$\rightarrow$P transition can no longer be addressed and cooling stops due to population being shelved in D, which is a long lived metastable state [64]. Therefore a second laser field that addresses the D$\rightarrow$P transition with frequency ω_{DP} should be applied, which we call a repumper laser with frequency ω_R. This has detuning $\Delta\omega_R = \omega_{DP} - \omega_R$ from the transition.

First of all the Hamiltonian of the system is defined as before to consist of an atomic part, but this time there are two interaction parts:

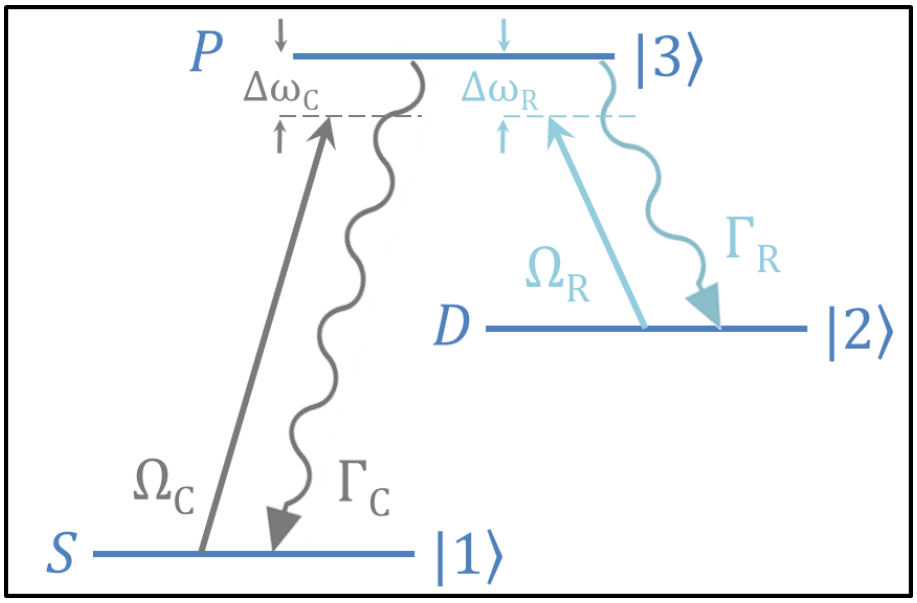

Figure 2.9: Three-level system with states S and D, and excited state P. Two lasers with frequency ω_C and ω_R are detuned from the transitions S→P and D→P by $\Delta\omega_C$ and $\Delta\omega_R$ respectively.

$$\hat{H} = \hat{H}_A + \hat{V}_{SP}(t) + \hat{V}_{DP}(t), \tag{2.63}$$

which are given by:

$$\hat{V}_{DP}(t) = \hat{\mu}_{DP} \cdot \vec{E}_R(t), \tag{2.64}$$

$$\hat{V}_{SP}(t) = \hat{\mu}_{SP} \cdot \vec{E}_C(t), \tag{2.65}$$

with the assumption that the two transitions are well separated enough in energy so that laser $\vec{E}_C(t)$ does not interact with the D→P transition and vice versa. For the system there are five OBEs that describe the time evolution of the density matrix, which are given by [64; 65]:

$$\frac{d\rho_{11}}{dt} = i\frac{\Omega_C}{2}\left(\tilde{\rho}_{13} - \tilde{\rho}_{31}\right) + \Gamma_C\rho_{33}, \tag{2.66}$$

$$\frac{d\rho_{22}}{dt} = i\frac{\Omega_R}{2}\left(\tilde{\rho}_{23} - \tilde{\rho}_{32}\right) + \Gamma_R\rho_{33}, \tag{2.67}$$

$$\frac{d\tilde{\rho}_{12}}{dt} = i\left(\Delta\omega_D - \Delta\omega_C\right)\tilde{\rho}_{12} + i\frac{\Omega_R}{2}\tilde{\rho}_{13} - i\frac{\Omega_C}{2}\tilde{\rho}_{32}, \tag{2.68}$$

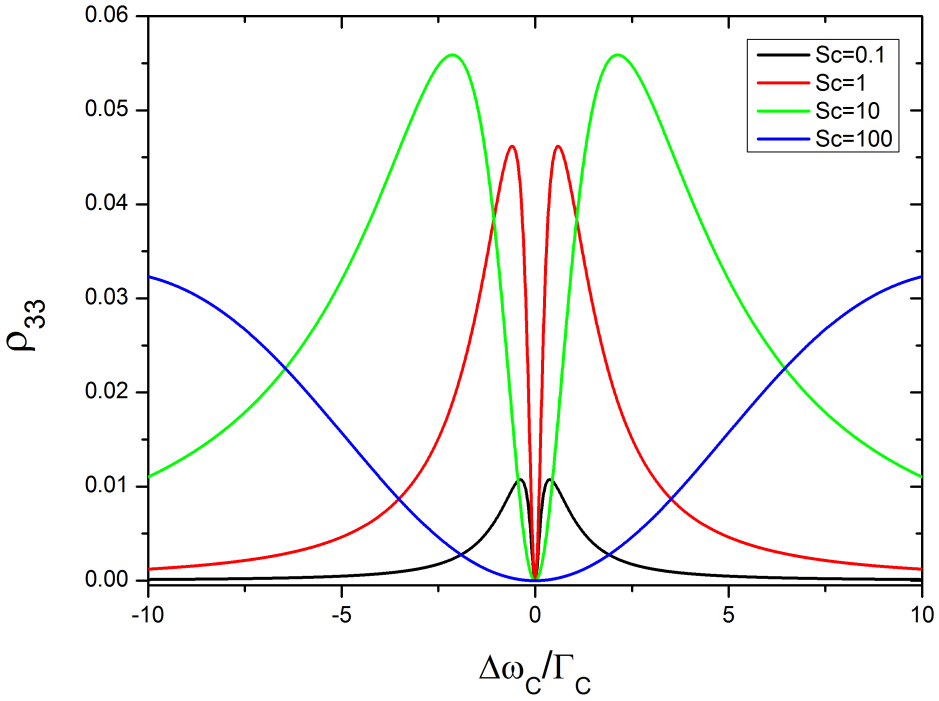

Figure 2.10: The excited state probability ρ_{33} of the Λ system as a function of the detuning $\Delta\omega_C$ from the S→P transition, plotted for four different saturation parameters s_C. The detuning from the D→P transition $\Delta\omega_R$ has been set to zero, and the saturation parameter for this transition is equal to 1.

$$\frac{d\tilde{\rho}_{13}}{dt} = i\frac{\Omega_C}{2}\left(\rho_{11} - \rho_{33}\right) + i\frac{\Omega_R}{2}\tilde{\rho}_{12} - i\Delta\omega_C\tilde{\rho}_{13} - \frac{\Gamma_C + \Gamma_R}{2}\tilde{\rho}_{13}, \tag{2.69}$$

$$\frac{d\tilde{\rho}_{23}}{dt} = i\frac{\Omega_R}{2}\left(\rho_{22} - \rho_{33}\right) + i\frac{\Omega_C}{2}\tilde{\rho}_{21} - i\Delta\omega_R\tilde{\rho}_{23} - \frac{\Gamma_C + \Gamma_R}{2}\tilde{\rho}_{23}, \tag{2.70}$$

where the Rabi frequencies are Ω_C and Ω_R for transitions S→P and D→P respectively. The steady state solution for the excited state population is then [65]:

$$\rho_{33} = \frac{4\left(\Delta\omega_C - \Delta\omega_R\right)^2\Omega_C^2\Omega_R^2\left(\Gamma_D + \Gamma_R\right)}{Z} \tag{2.71}$$

with

$$
\begin{aligned}
Z = & \, 8\left(\Delta\omega_C - \Delta\omega_R\right)^2 \Omega_C^2 \Omega_R^2 \left(\Gamma_D + \Gamma_R\right) \\
& + 4\left(\Delta\omega_C - \Delta\omega_R\right)^2 \left(\Gamma_D + \Gamma_R\right)^2 \left(\Omega_C^2 \Gamma_R + \Omega_R^2 \Gamma_C\right) \\
& + 16\left(\Delta\omega_C - \Delta\omega_R\right)^2 \left(\Delta\omega_C^2 \Omega_R^2 \Gamma_C + \Delta\omega_R^2 \Omega_C^2 \Gamma_R\right) \\
& - 8\Delta\omega_C \left(\Delta\omega_C - \Delta\omega_R\right) \Omega_R^4 \Gamma_C + 8\Delta\omega_R \left(\Delta\omega_C - \Delta\omega_R\right) \Omega_C^4 \Gamma_R \\
& + \left(\Omega_C^2 + \Omega_R^2\right)^2 \left(\Omega_C^2 \Gamma_R + \Omega_R^2 \Gamma_C\right).
\end{aligned}
\tag{2.72}
$$

The excited state probability has been plotted in fig. 2.10 as a function of the detuning $\Delta\omega_C$ from the transition S→P. This has been plotted for four different values of the saturation parameter for this transition $s_C = 2\Omega_C^2/\Gamma_C^2$. The detuning from the D→P transition has been set to $\Delta\omega_R = 0$, and the saturation parameter $s_R = 1$. When this is compared to the plot for the excited state population of the two-level system in fig. 2.6, there are a few main differences between them. For the three level system, the population drops to zero at a detuning $\Delta\omega_C = 0$. This occurs when $\Delta\omega_C = \Delta\omega_R$, and is due to the coherent trapping of the population in a superposition between S and D. This reveals an issue with using a Λ system for cooling, as no population in the excited state means that there are also no scattering events, and so there is no cooling effect at these settings.

Additional to this is the excited state population for the three level system. Compared to the two level system in fig. 2.6, there is around an order of magnitude reduction in the excited state probability for the Λ system, which means a large reduction in the scattering events required for cooling. Another interesting difference is that there is not a saturation effect as there was for two levels. As the saturation parameter is increased, the lineshape becomes broader and starts to reach a maximum as before. However, in fig. 2.10, the excited state population starts to come down again, as can be seen for a saturation parameter of $s_C = 100$.

This demonstrates that the two-level system is not completely adequate for describing the full dynamics of atom-light interactions for all systems. It also reveals the shortcomings of using a Λ system for laser Doppler cooling. In this experiment the full five level system of calcium is actually used, and requires two repumpers instead of one to form a closed system. This system is described further in sec. 3.2.2.

2.2.4 Two-photon processes

In some circumstances, transitions between two states can be driven by more than one photon. For cases like this, the sum of the photon energies equals the difference in energy between the two states. Transitions such as this have to be considered when the energy

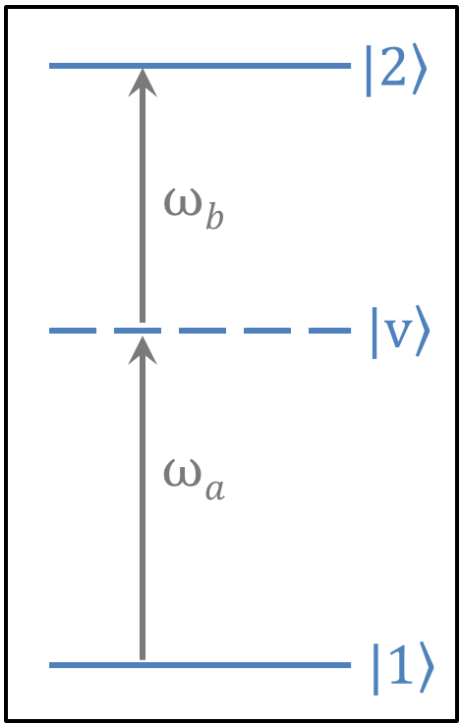

Figure 2.11: The two-level system has been extended to include a virtual level $|v\rangle$, and the transition between the two states $|1\rangle$ and $|2\rangle$ is made by two photons with total energy $\omega_a + \omega_b$.

between the two states is too high to be accessed by just a single photon, for example for excitation and ionisation of molecular species (see sec. 5.1). Multiphoton processes also provide important techniques for high resolution spectroscopy, for instance Raman spectroscopy can be used to address those transitions that are disallowed. The high resolution spectroscopy scheme proposed for N_2^+ uses such a technique [30].

First of all a two-level system is considered, with the ground state having energy $\hbar\omega_1$ and the excited state having energy $\hbar\omega_2$, and is shown in fig. 2.11. This time there are two photons to make the transition, with frequencies ω_a and ω_b. A third state has also been included in the diagram, and this represents a 'virtual' state $|v\rangle$ that has energy $\hbar\omega_v$. The system will never physically be in this state, but it is useful as a description. In reality the $|v\rangle$ state represents a real state from which ω_a is far detuned [66]. This description also makes it clearer as to how this applies to Raman transitions: in this case the state $|2\rangle$ would sit (in terms of energy) in between the ground state $|1\rangle$, and the intermediate state $|v\rangle$ which always has a population of zero. This condition also demonstrates the fundamental difference between a two-photon transition, and two single-photon transitions [60].

The electric field applied to the two level system now has two frequency components, and takes the form:

$$\vec{E}(t) = \vec{E}_a \left(e^{i\omega_a t} + e^{-i\omega_a t}\right) + \vec{E}_b \left(e^{i\omega_b t} + e^{-i\omega_b t}\right), \tag{2.73}$$

which can be substituted into eq. 2.25 to give the interaction part of the Hamiltonian. The total Hamiltonian for a two-level system interacting with a field is given in eq. 2.23. Now the effective transition that takes place between $|1\rangle$ and $|v\rangle$ has to be taken into account in order to find the effective amplitude C_v:

$$C_v = \frac{\Omega_{1va}}{2}\left(\frac{1 - e^{i(\omega_v - \omega_1 - \omega_a)t}}{\omega_v - \omega_1 - \omega_a}\right) + \frac{\Omega_{1vb}}{2}\left(\frac{1 - e^{i(\omega_v - \omega_1 - \omega_b)t}}{\omega_v - \omega_1 - \omega_b}\right), \tag{2.74}$$

this is via the same method used to find eq. 2.32, except that two processes have to be considered. The first is that photon ω_a effectively excites $|1\rangle \rightarrow |v\rangle$. But it is also possible for ω_b to excite this transition. For each of these cases there is a different effective Rabi frequency, Ω_{1va} and Ω_{1vb} respectively.

Next the effective transition from $|v\rangle$ to $|2\rangle$ can be derived to find the amplitude C_2 for the excited level:

$$\begin{aligned} C_2 = &\left(\frac{\Omega_{2va}\Omega_{1va}}{4\delta_a} + \frac{\Omega_{2va}\Omega_{1vb}}{4\delta_b}\right)\left(\frac{1 - e^{i(\omega_2 - \omega_v - \omega_a)t}}{\omega_2 - \omega_v - \omega_a}\right) \\ &+ \left(\frac{\Omega_{2vb}\Omega_{1va}}{4\delta_a} + \frac{\Omega_{2vb}\Omega_{1vb}}{4\delta_b}\right)\left(\frac{1 - e^{i(\omega_2 - \omega_v - \omega_b)t}}{\omega_2 - \omega_v - \omega_b}\right), \end{aligned} \tag{2.75}$$

where $\delta_a = \omega_v - \omega_1 - \omega_a$ is the detuning of the laser with frequency ω_a from $|1\rangle \rightarrow |v\rangle$ and $\delta_b = \omega_v - \omega_1 - \omega_b$ is the detuning of the laser with frequency ω_b from the same transition. When squared, C_2 gives the probability ρ_{22} for the two-level atom to undergo a two-photon transition from $|1\rangle$ to $|2\rangle$.

Spontaneous decay has not been considered for this transition. There can't be any spontaneous decay from the virtual state $|v\rangle$, but there certainly can be from the excited state $|2\rangle$. However, it has not been included as the two photon transition used for exciting N_2 in the ionisation scheme for this experiment is very quickly succeeded by the stage after excitation, which is ionisation to N_2^+.

For the case where there is a single laser applied to the two-level atom, eq. 2.75 simplifies to:

$$C_2 = \frac{\Omega_{2v}\Omega_{1v}}{\delta_{1v}}\left(\frac{1 - e^{i\delta_{2v}t}}{\delta_{2v}}\right), \tag{2.76}$$

where $\omega_a = \omega_b = \omega$, $\Omega_{2va} = \Omega_{2vb} = \Omega_{2v}$, $\Omega_{1va} = \Omega_{1vb} = \Omega_{1v}$ and $\delta_a = \delta_b = \delta_{1v}$. This is due to the fact that the laser frequency has only one component now, ω, and so there

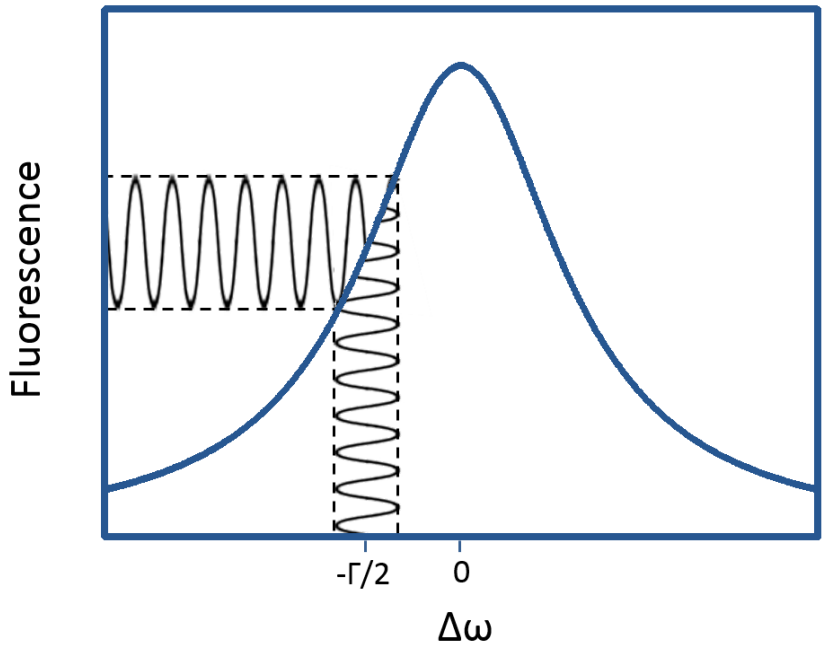

Figure 2.12: The effective detuning seen by the ion is modulated at the secular frequency, this modulation is shown in black. If the laser detuning is set to $\pm\Gamma/2$, the gradient of the lineshape is at its maximum, and gives the largest modulation in fluorescence. For a detuning of zero, the gradient is zero, and there is minimal modulation in the fluorescence.

are only two effective Rabi frequencies, one for $|1\rangle \rightarrow |v\rangle$ which is Ω_{1v} and the other for $|v\rangle \rightarrow |2\rangle$ which is Ω_{2v}. The term $\omega_2 - \omega_v - \omega = \delta_{2v}$ has also been introduced. And so now the excited state probability ρ_{22} is expressed in only the detunings and the effective Rabi frequencies of each virtual transition.

2.2.5 Doppler velocimetry

The technique of Doppler velocimetry allows for precise determination of the resonance frequency of the ions in the trapping potential. This is how the state-dependent motion of the ^{40}Ca-N_2 ion crystal is detected. When the motion of the ion in the trapping potential is excited, it undergoes oscillations at the secular frequency (see sec. 2.1 and in particular eq. 2.18). An interaction laser can be aligned so that the propagation direction is parallel to the ion's oscillation.

As the ion oscillates, it will experience a shifted frequency of the laser due to the Doppler effect (sec. 2.2.2), the magnitude of which depends on the velocity of the ion. Therefore, as the effective detuning of the laser is modulated at the frequency of the ion's motion, so is the laser-induced fluorescence, as demonstrated in fig. 2.12. When the ion

moves in the same direction as the laser propagates, the frequency is red-shifted, and so the effective detuning becomes larger. This means that the laser-induced fluorescence will decrease. For the other part of the oscillation cycle, the ion moves in the opposite direction of the laser propagation and so there is instead a blue shift, which means an increase in the laser induced fluorescence. Therefore the oscillation of the ion can be detected and the frequency of oscillation determined by measuring the fluorescence of the trapped ion. From fig. 2.12 it can be quite clearly seen that the detuning of the laser from linecentre is critical for maximising the modulated fluorescence signal. If the detuning is set, for example, at $\pm\Gamma/2$, the slope of the lineshape is at a maximum. Therefore a modulation in $\Delta\omega$ gives the largest modulation amplitude. If $\Delta\omega = 0$, the modulation in fluorescence is at a minimum, as the gradient is zero. For the ion-trap experiments in this thesis, the cooling laser for $^{40}Ca^{+}$ is used for Doppler velocimetry, with a detuning of $-\Gamma/2$. Therefore, the motion of the ion is damped out as the fluorescence is collected and the secular frequency determined. If small ion velocity $\vec{v}$ is considered, with small oscillation amplitude, the modulation amplitude of the laser induced fluorescence Fl can be written:

$$Fl = \Gamma \left.\frac{d\rho_{22}}{d\Delta\omega}\right|_{\Delta\omega_0} \vec{k}\cdot\vec{v}, \tag{2.77}$$

where $\Delta\omega_0$ is the detuning of the laser from linecentre, ρ_{22} is the excited state population from eq. 2.44, Γ is the decay rate, and $\vec{k}\cdot\vec{v}$ gives the component of the ion oscillation in the direction of the applied laser.

If the detuning is instead set to $+\Gamma/2$, the ion's oscillation can be amplified instead of being damped out [51; 67]. By approximating the change in fluorescence rate as linear with the changing detuning Δ, and the velocity-dependent term $\vec{\beta}\cdot\vec{v}$ in the expression for the radiation pressure induced force in eq. 2.59 is considered, the increase in oscillation amplitude A can be written:

$$A = \exp\left(\frac{\pi h}{m\lambda^2}\left.\frac{d\mathcal{F}}{d\Delta}\right|_{\Delta_0} t\right), \tag{2.78}$$

where λ is the wavelength of the laser, m is the mass of the ion, and $\mathcal{F}$ is the fluorescence rate which is proportional to $\Gamma\rho_{22}$. When the blue-detuned laser is applied for a time t, there is an exponential increase in the oscillation amplitude A of the ion. It has been experimentally determined that increasing the oscillation amplitude is limited to around 150 μs. For longer periods of time than this, the ion becomes de-localised and the phase of the oscillations becomes random.

As well as being critical for the state detection scheme, this measurement technique

is also particularly important for 'crystal weighing' measurements. The dependence of the secular frequency on the charge to mass ratio of the ion crystal means that a precise measurement of the frequency is a precise measurement of the average mass of the trap contents (assuming all are singly ionised). This can then be used to find the mass of 'dark ions' loaded alongside the ^{40}Ca ions. For instance, during trap loading of N_2^+ this method can be used to measure if a nitrogen ion has been successfully loaded or not.

2.3 Physics with trapped molecular ions

Experiments with trapped molecular ions suffer from the vastly more complex nature of molecules in comparison to atomic ions. For the experiments described in this thesis the main challenges lie in the ionisation of nitrogen, internal state preparation, cooling of the translational motion, and state readout. Our solutions to these problems are outlined in this section, which include the techniques of resonance enhanced multi-photon ionisation, which both ionises the molecule for ion-trapping, and prepares the internal state. Once trapped, the molecular ion is sympathetically cooled by a separate species which can be directly laser cooled, which is $^{40}Ca^+$ for our experiments. Finally, a non-destructive state detection technique is outlined, which, along with the other techniques mentioned, will enable a scheme for high resolution spectroscopy on N_2^+.

Additionally in this section the basic structure and notation for diatomic molecules is explained so as to give a basis for the molecular spectroscopy outlined in this thesis.

2.3.1 Molecular internal structure

The complexity of molecular internal structure can be appreciated when we consider the many bodies involved, and how this influences the energy of the system. For the simplistic case in which we have a diatomic molecule, we can start by considering the motion of the two nuclei with respect to the bond between the two atoms, as illustrated in the first part of fig. 2.13. First of all we can consider the rotation of the molecule. For the case of a diatomic, we can see that there is only one mode of rotation possible, as shown in the figure. For more complex molecules, the number of rotational modes will depend on the relative positions of the nuclei.

Additional to this is the vibrational modes, which is the change in energy when the two nuclei are moving apart/closer together. Again, this motion can only occur along one direction when we have only two nuclei, but there will be many more vibrational modes for more nuclei. So, in addition to the electronic structure that we recognise from atomic

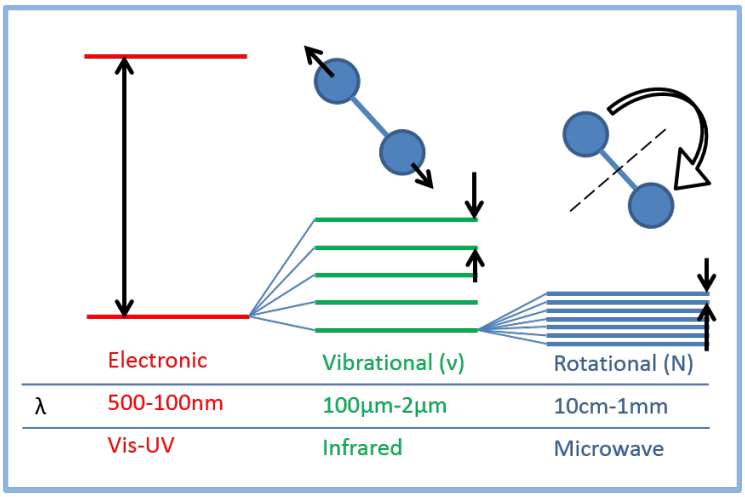

Figure 2.13: Illustration of the basic structure of molecules, showing the electronic, vibrational and rotational states relative to each other (not to scale). Also pictured is the vibration and rotation of a diatomic molecule.

physics, there are additional molecular states which arise from the rotation and vibration of the molecule.

It is important to note that in general, transitions in energy for rotations, vibrations, and the electronic structure are on very different magnitude scales, shown in fig. 2.13. And so we find that the molecular structure is principally made up of an electronic manifold within which lies vibrational states. Each of the vibrational states then splits into the rotational structure. In the schemes outlined in this thesis, state preparation will prepare the molecule in a specific electronic, vibrational, and rotational state.

Born Oppenheimer approximation

Finding analytic solutions of the Schrödinger equation for a molecule is not possible for even the simplest systems [68], and so an approximation has to be made from the start. The Born-Oppenheimer approximation treats electrons and the much more massive nuclei of a molecule in different ways. The electrons are assumed to adapt instantaneously to changes in the positions of the nuclei. This means that the Schrödinger equation can first be solved for the nuclei in a fixed position. The coordinates of the nuclei then may be changed and solutions found again. By using this method, the potential energy that arises from the nuclear positions may be plotted.

For the Born-Oppenheimer approximation, the total wavefunction is proposed to have the form:

$$\Psi_{tot} = \Psi_{el}\Psi_{nuc} \tag{2.79}$$

where the electronic wavefunction Ψ_{el} and nuclear wavefunction Ψ_{nuc} are dependent on the coordinates of the electrons and the two nuclei. The Hamiltonian of the system is a function of the kinetic energy of the electrons T_{el} and of the nuclei T_{nuc}, as well as the total potential energy of the system V:

$$H_{mol} = T_{el} + T_{nuc} + V, \tag{2.80}$$

and so by substituting the wavefunction Ψ_{tot} and the Hamiltonian H_{mol} into the Schrödinger equation $H_{mol}\Psi_{tot} = E\Psi_{tot}$, we get:

$$\Psi_{el}T_{nuc}\Psi_{nuc} + (T_{el}\Psi_{el} + V\Psi_{el})\Psi_{nuc} = E\Psi_{el}\Psi_{nuc}. \tag{2.81}$$

This has been written in a way so that it is clear to see where the energy from the electronic contribution comes from - the kinetic energy of the electrons T_{el} and the potential energy of the system at fixed nuclear positions V, along with the electronic part of the wavefunction Ψ_{el}. Re-writing the bracketed term out gives the Schrödinger equation for the electrons with fixed nuclear positions:

$$T_{el}\Psi_{el} + V\Psi_{el} = E_{el}\Psi_{el}. \tag{2.82}$$

This equation can now be used to find the eigenvalues E_{el} for different nuclear positions. This results in what is called a molecular potential energy curve.

Additionally, we also have the Schrödinger equation for Ψ_{nuc} for the total energy E:

$$T_{nuc}\Psi_{nuc} + E_{el}\Psi_{nuc} = E\Psi_{nuc}, \tag{2.83}$$

where E_{el} is the potential energy curve derived from eq. 2.82. This can now be used to find the total energy of the system when nuclear vibrations and rotations are considered.

Electronic, vibrational and rotational structure

As can be expected, there are many similarities between the electronic structure of atoms and diatomic molecules which can be drawn upon. The main issues that make diatomic molecules so much more complex are to do with the symmetry and thus how angular momentum couples together. Atoms have spherical symmetry, whereas diatomics have axial symmetry about the internuclear axis. Where for atoms, we consider electronic spin

S, orbital angular momentum **L**, and the total angular momentum **J**, we instead have the projections of these quantities on the internuclear axis, which are Σ, Λ, and Ω respectively for diatomic molecules. Another quantity that must be taken into account is the nuclear spin **I** of each of the nuclei.

Molecular orbital theory can be used to understand the electronic structure of molecules. For this, it is assumed that when two atoms are brought together to form a molecule, we can use the atomic orbitals that we already know as a basis [2]. The method of linear combination of atomic orbitals (LCAO) is used to describe the process. The molecular orbitals are thus approximately formed as so [68]:

$$\Psi_+ \approx X_A + X_B$$
$$\Psi_- \approx X_A - X_B,$$

where X_A and X_B are the atomic orbitals from atoms A and B which form the diatomic molecule. The wavefunction Ψ_+ represents what is called the bonding orbital, with Ψ_- being the anti-bonding orbital. Whether a molecular orbital is bonding or not depends on the electron density in the region between the two nuclei, with the bonding orbital having a high electron density, and the anti-bonding orbital having a low density. When the atomic orbitals are combined in this way there are always bonding and anti-bonding orbitals formed, although in this example the weighting of the atomic basis orbitals have not yet been considered. The resulting molecular orbitals Φ are actually more formally expressed as a linear sum of atomic orbitals X_i:

$$\Phi = \sum_i C_i X_i, \tag{2.85}$$

weighted with coefficients C_i, where the functions X_i should form a complete basis set. Optimum values of the coefficients C_i can then be found by using the variational principle in order to determine the final molecular orbitals [68].

Figure 2.14 demonstrates the energy change when the atomic orbitals of two nitrogen atoms go on to form the molecular orbitals of N_2^+. The atomic orbitals from atoms A and B are depicted on the left and right hand side of the diagram. The levels in between show the molecular orbitals that are formed, where the π and σ labelling denote the symmetry type of the orbital. For instance, the two atomic 2s orbitals come together to give a bonding orbital $2\sigma g$, and an anti-bonding orbital $2\sigma u$, where u and g denote the parity. The complete ground state for N_2 is labelled as $X^1\Sigma_g^+$, using the notation explained below.

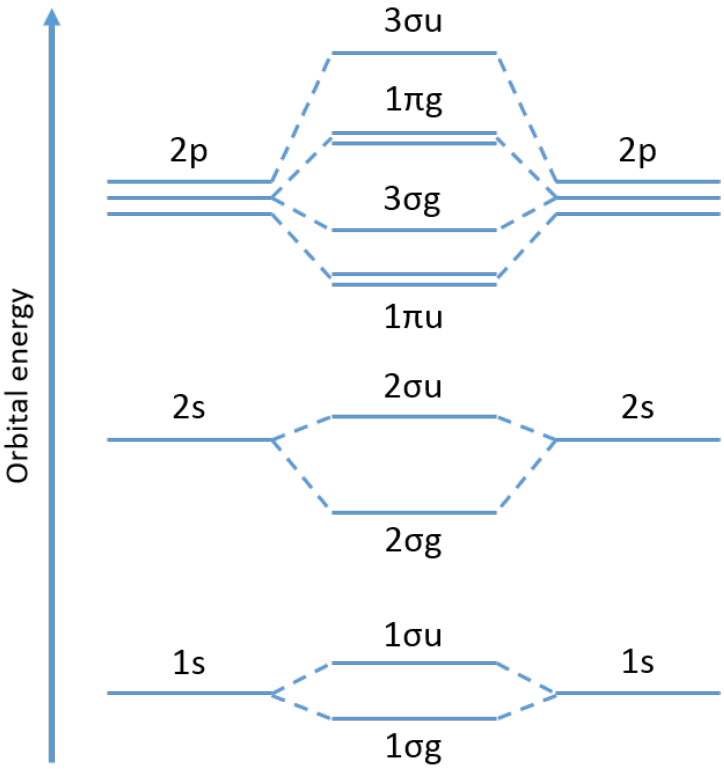

Figure 2.14: The molecular orbital diagram for the ground state of N_2, showing how the atomic orbitals combine [2]. Not to scale.

The molecular term symbol which is used for labelling the electronic state is:

$$M^{(2S+1)}\Lambda^{+/-}_{u/g,\Omega} \tag{2.86}$$

where M is the principal quantum number, which starts from the ground state labelled X, and then continues as A, B, C... , with the superscript on this number being the spin multiplicity. If the principal quantum number has been changed to a lower-case letter, then this indicates a change in the multiplicity compared to the ground state[2]. Next the orbital angular momentum as projected onto the internuclear axis is given by Λ. Similarly to the atomic spectroscopic term symbol, this quantum number goes up like S, P, D... - although the equivalent letters from the Greek alphabet are used, so that it goes like Σ, Π, Δ... , with values 0, 1, 2... respectively. The +/- superscript gives the reflection symmetry, with u/g denoting the parity where g stands for *gerade*, which means even parity, and u being *ungerade* for odd. Finally, Ω gives the total angular momentum as projected along the internuclear axis. How the angular momenta couple together for different cases are

[2]For historical reasons, this is not always true. For instance, the excited state $a^1\Pi_g$ in N_2 uses a lower case letter, even though it has the same multiplicity as the ground electronic state.

governed by Hund's coupling cases, the details of which can be found in [68].

The symbols for the rotational and vibrational quantum numbers in this thesis are N and ν respectively. Generally, these are quoted in brackets after the molecular term symbol if relevant. For example, the state in which N_2^+ needs to be prepared for the experiments outlined in this thesis is the electronic, vibrational and rotational ground state: $X^2\Sigma_g^+(N = 0, \nu = 0)$.

The LCAO provides a means to calculate the energy of the electronic states. Now the energy contributions from the motion of the nuclei must be considered, as this will give the total energy of the molecule as in eq. 2.83. First of all the vibration of the nuclei along their bond can be looked at, so that E_{vib} can be found. For the diatomic molecule, there is only one vibrational mode - the stretch mode - in which case the nuclei move towards and away from each other. The vibrational energy is then a function of the displacement of the nuclei from their equilibrium positions. For small vibrational energies, ie. at the bottom of the potential energy curve, it can be approximated as a harmonic potential. Therefore we can treat the vibration of the nuclei as an oscillator undergoing simple harmonic motion, with the solutions to such a problem being well known.

First of all this vibrational motion can be thought of in a classical sense to find the energy of the system. For this, the two nuclei in the diatomic molecule are thought of as point-like particles, with each nucleus having mass m_1 and m_2. The total separation between the masses is r, and the distances from each nuclei to the centre of mass of the system are r_1 and r_2, so that $r = r_1 + r_2$. The kinetic energy of the system is written:

$$E_{kin} = \frac{1}{2}m_1 v_1^2 + \frac{1}{2}m_2 v_2^2, \tag{2.87}$$

where v_1 and v_2 are the velocities of the masses m_1 and m_2 respectively. To simplify the problem further, we introduce the reduced mass of the system, which is:

$$\mu = \frac{m_1 m_2}{m_1 + m_2}. \tag{2.88}$$

As well as this, we call the total displacement of the nuclei from their equilibrium positions q, which is the sum of the displacement of mass m_1 and the displacement of mass m_2 ($q = q_1 + q_2$). Using this and the reduced mass simplifies eq. 2.87 to:

$$E_{kin} = \frac{1}{2}\mu \dot{q}^2, \tag{2.89}$$

where the substitution $p = \mu\dot{q}$ can be made to reform the kinetic energy in terms of the vibrational momentum. Next, the potential energy for a harmonic oscillator can be

written:

$$E_{pot} = \frac{1}{2}k_1 q_1^2 + \frac{1}{2}k_2 q_2^2, \tag{2.90}$$

and similarly this can be written in the simpler form:

$$E_{pot} = \frac{1}{2}kq^2. \tag{2.91}$$

Summing the energy contributions from kinetic and potential energy gives:

$$E_{tot} = \frac{1}{2}\frac{p^2}{\mu} + \frac{1}{2}kq^2, \tag{2.92}$$

which is the reduced mass form of the vibrational energy of a diatomic molecule. Now, in order to cast this into a quantum mechanical form, the Hamiltonian of the system should be written down in the form of quantum mechanical operators:

$$H_{vib} = -\frac{\hbar^2}{2\mu}\frac{d^2}{dq^2} + \frac{1}{2}kq^2, \tag{2.93}$$

where p has now been written as the momentum operator: $-i\hbar\partial/\partial q$. Using the Hamiltonian and the vibrational wavefunction Ψ_{vib}, the Schrödinger equation becomes:

$$E_{vib}\Psi_{vib} = -\frac{\hbar^2}{2\mu}\frac{d^2\Psi_{vib}}{dq^2} + \frac{1}{2}kq^2\Psi_{vib}, \tag{2.94}$$

for which the eigenvalues will give the vibrational energies E_{vib}. The well-known solutions to the quantum harmonic oscillator are $\Psi_{vib}(\nu) = e^{-\sqrt{k\mu}q^2/2\hbar}H_\nu(q)$, with the normalised Hermite polynomials $H_\nu(q)$. This leads to the eigenvalues:

$$E_{vib} = \hbar\omega_{vib}(\nu + 1/2), \tag{2.95}$$

where ω_{vib} is the frequency of vibration, and ν is the vibrational quantum number. In this case, it can be seen that the separation of vibrational states is evenly spaced. In fact, there is an additional correction to this due to the nature of the potential energy curves, which become anharmonic for higher vibrational states. The anharmonic correction reveals that the vibrational energy is actually represented by a series:

$$E_{vib} = \hbar\omega_{vib}(\nu + 1/2) - \hbar\omega_{vib}x_e(\nu + 1/2)^2 + \hbar\omega_{vib}y_e(\nu + 1/2)^3 + ..., \tag{2.96}$$

where the constants $\omega_{vib}, \omega_{vib}x_e$ and $\omega_{vib}y_e$ are generally determined empirically from vibrational spectra [68], and x_e and y_e are dimensionless quantities.

Now we can consider the rotational structure of the molecule. The diatomic molecule can be thought of as two masses connected together as shown in fig. 2.13. If this structure rotates about its centre of mass, which for a homonuclear molecule will be equidistant between the nuclei, the rotational energy E_{rot} can be simply written in terms of the moment of inertia I:

$$E_{rot} = \frac{1}{2} I \omega^2, \tag{2.97}$$

where ω is the angular velocity of the rotor, and the moment of inertia is defined by $I = \mu r^2$, which uses the reduced mass μ from eq. 2.88. This is now the classical energy of a rotor, and must be re-written in terms of quantum mechanical operators to find the quantised energy of the system. For this, eq. 2.97 can first be expressed in terms of classical angular momentum:

$$E_{rot} = \frac{1}{2} \frac{L^2}{I}, \tag{2.98}$$

where the angular momentum $L = I\omega$. The classical angular momentum now needs to be replaced with a quantum mechanical operator, $\hat{L}$, which has units $\hbar$, and its known eigenvalues to get:

$$E_{rot} = \frac{\hbar^2}{2I} \hat{L}^2 = \frac{\hbar^2}{2I} N(N+1), \tag{2.99}$$

where N is the rotational quantum number. Therefore, the spacing between the rotational levels is determined by the coefficient $B = \hbar^2/2I$. It can also been seen that as N increases, so does E_{rot}, and so the spacing between rotational levels increases with the rotational state.

So far, this formulation for the energy in rotational states works well, particularly for lower rotational energy [2]. However, there is an additional consideration that must be taken into account especially for faster rotation, and this is known as centrifugal distortion. The bond between the two nuclei is not completely rigid, and so as the rotation is faster, they can move apart, increasing the moment of inertia. Rather than modelling the diatomic molecule as a rigid structure, it should instead be thought of as two masses connected by a stiff spring that has spring constant k. The restoring force comes from Hooke's law:

$$F = -k\Delta r, \tag{2.100}$$

where $\Delta r = r_{CD} - r$ is the change in distance between the nuclei from separation at equilibrium r to a separation due to centrifugal distortion r_{CD}. Equating this to the centripetal force gives:

$$k\Delta r = \mu r\omega^2, \tag{2.101}$$

which can be solved to find an expression for the bond length r_{CD}:

$$r_{CD} = \frac{r}{1 - \mu\omega^2/k}, \tag{2.102}$$

where $\mu\omega^2/k$ is small for small variations to the bond length.

As the bond is stretched, both the potential and kinetic energy of the system changes. As the distance between the two nuclei increase, so will the moment of inertia due to the equation $I = \mu r^2$. And so, as a result of conservation of momentum the angular velocity will decrease, as will the kinetic energy in eq. 2.98. The potential energy will increase due to the effective stretching of the 'spring' joining the two nuclei. Calculating the contribution from these changes in energy will allow us to make a correction to eq. 2.99 in order to find the total rotational state energies.

First of all, to find the change in kinetic energy we can substitute the expression for r_{CD}, found in eq. 2.102, into eq. 2.98, so that:

$$\begin{aligned} \frac{1}{2}\frac{L^2}{I} &= \frac{1}{2}\frac{L^2}{\mu r_{CD}^2} = \frac{1}{2}\frac{L^2(1-\mu\omega^2/k)^2}{\mu r^2} \\ &= \frac{1}{2}\frac{L^2}{\mu r^2} - \frac{\mu L^4}{I^3 k} + ..., \end{aligned} \tag{2.103}$$

where the first term is the kinetic energy for the rigid rotor, the second term is the centrifugal distortion correction, and the final term containing $(\mu\omega^2/k)^2$ has been neglected as it is very small for small changes to the bond length. The contribution to the potential energy is:

$$\begin{aligned} E_{pot} &= \frac{1}{2}k\Delta r^2 = \frac{1}{2}k\left(\frac{\mu r\omega^2}{k}\right)^2 \\ &= \frac{\mu L^4}{2I^3 k}, \end{aligned} \tag{2.104}$$

which gives the total centrifugal distortion contribution:

$$\begin{aligned} E_{CD} &= -\frac{\mu L^4}{2I^3 k} \\ &= -\frac{\hbar^4}{2I^3 k/\mu} N^2(N+1)^2. \end{aligned} \tag{2.105}$$

Now that this correction has been found, the total rotational energy can be written as the sum of eq. 2.99 and eq. 2.105:

$$E_{rot} = BN(N+1) - DN^2(N+1)^2, \tag{2.106}$$

where the rotational properties of the molecule are defined by the rotational coefficient $B = \hbar^2/2I$ and the centrifugal distortion constant $D = \hbar^4/(2I^3k/\mu)$.

So now the total energy of the molecule can be determined from plotting the potential energy curves using the linear combination of atomic orbitals, and by considering the vibrational and rotational energy (E_{vib} and E_{rot}) of the molecule using equations 2.96 and 2.106.

Nuclear spin and statistical weighting

So far the effects of the spin of the nuclei, **I**, have been neglected. There are two main effects of the nuclear spin on the molecular structure; the first being the appearance of hyperfine structure, in which there is additional splitting of the rotational states. The nuclear spin can also have the effect of determining if some rotational states actually exist or not - and so contributes to a statistical weighting of accessible states. Therefore the nuclear spin of N_2 is going to play a role in the non-destructive state detection scheme for N_2^+ (which is explained in further detail in sec. 2.3.3). Additional structure means the possibility of addressing more than one state, and so should certainly be considered.

The hyperfine structure of N_2^+ is shown in fig. 2.15. Each of the nuclei in N_2^+ have spin equal to 1, which has two consequences for the structure. First of all, it means that N_2 is bosonic, and so the total molecular wavefunction has to be symmetric under parity inversion: $P\Psi_{tot} = \Psi_{tot}$ (where P is the parity operator). If the wavefunction in eq. 2.79 is further decomposed into the different nuclear components, we can write it as:

$$\Psi_{tot} = \Psi_{el}\Psi_{vib}\Psi_{rot}\Psi_I, \tag{2.107}$$

where Ψ_{vib} and Ψ_{rot} are the vibrational and rotational wavefunctions, the total nuclear wavefunction is given by $\Psi_{nuc} = \Psi_{vib}\Psi_{rot}\Psi_I$, and Ψ_I is the nuclear spin wavefunction. And so, in order to make Ψ_{tot} symmetric, we must consider the symmetry of each of the different wavefunctions in eq. 2.107. We begin by examining the vibrational wavefunction Ψ_{vib}. As discussed in the previous section, this is just a function of the nuclear separation. Therefore if the nuclei are exchanged, this will have no effect on Ψ_{vib}, and so it is symmetric.

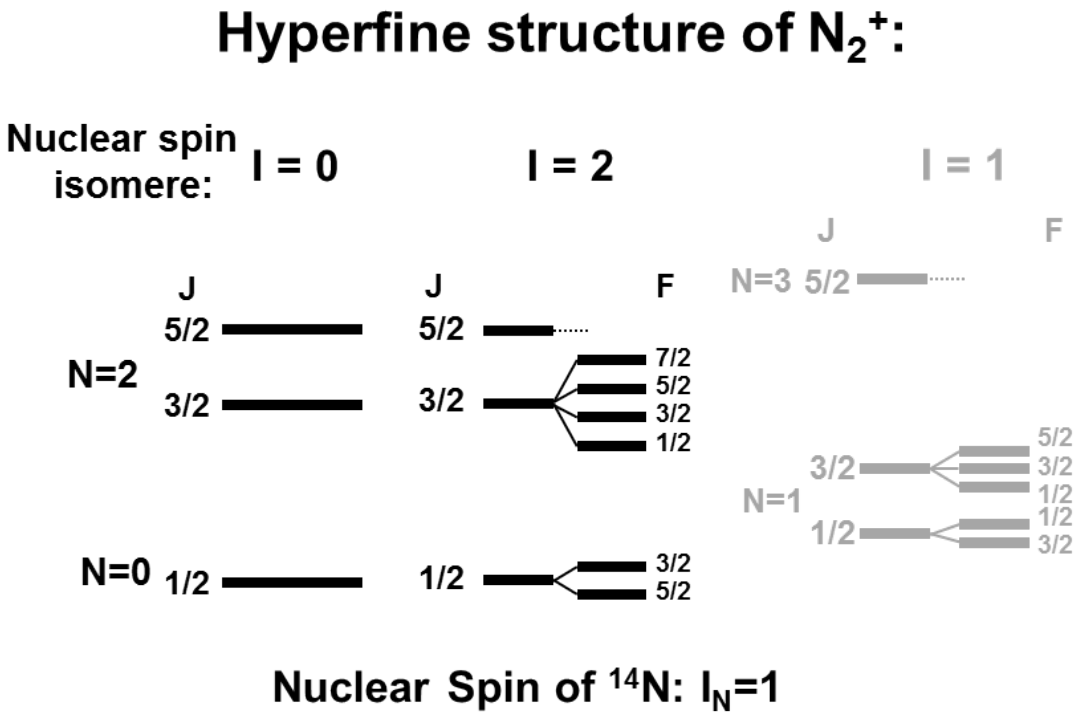

Figure 2.15: The hyperfine structure of N_2^+, which comes as a result of the nuclear spin of ^{14}N.

The symmetry of Ψ_{el} will depend on the electronic state. If we just consider the ground state of N_2 as an example, we have a Σ_g^+ state, which is symmetric under inversion.

Now there is the symmetry of the Ψ_{rot} and Ψ_I wavefunctions to find. For this, we must look back at the spin of each nucleus, $\mathbf{I} = 1$, and the different spin state combinations for the N_2 molecule. For each nucleus, there are two possible spin states, which for now we shall call α and β. Therefore, for the two nuclei, there are four possible spin states, $\alpha\alpha$, $\beta\beta$, $\beta\alpha$ and $\alpha\beta$, for which we can find the symmetry:

$$\begin{aligned} P\alpha\alpha &= \alpha\alpha \\ P\beta\beta &= \beta\beta \\ P(\alpha\beta + \beta\alpha)\frac{1}{\sqrt{2}} &= (\alpha\beta + \beta\alpha)\frac{1}{\sqrt{2}} \\ P(\alpha\beta - \beta\alpha)\frac{1}{\sqrt{2}} &= -(\alpha\beta + \beta\alpha)\frac{1}{\sqrt{2}}, \end{aligned} \tag{2.108}$$

where the first three states form a triplet, and are symmetric, and the final spin combination is the singlet state, which is antisymmetric. There are three values in total for this, $I_{tot} = 0, 1, 2$, where the even nuclear spin states are the triplet states $I_{tot} = 0, 2$, which are symmetric. The singlet spin state $I_{tot} = 1$ is anti-symmetric under inversion.

The final contribution to the symmetry comes from the rotational wavefunction Ψ_{rot}, which is dependent on if the rotational quantum number N is even or not. For $N = 0, 2, 4, ...$, the rotational wavefunction is symmetric, and for $N = 1, 3, 5, ...$ it is antisymmetric, according to $P\Psi_{rot} = (-1)^N \Psi_{rot}$.

So if we now combine all of these results, there are two situations that can occur with regards to getting the total wavefunction to be symmetric:

- The nuclear spin state is even ($I = 0, 2$), and so the rotational states within the ground electronic state can only be even ($N = 0, 2, 4, ...$).
- The nuclear spin state is odd ($I = 1$), and so the rotational states within the ground electronic state can only be odd ($N = 1, 3, 5, ...$).

It is important to also note that the weighting of these results (Even nuclear spin state: Odd nuclear spin state) is 2:1, which will have an effect on the rotational spectra.

Looking back at the hyperfine structure for N_2^+ in fig. 2.15, the consequences for the three spin combinations $I = 0, 1, 2$ are illustrated. For the $I = 1$ case, which is greyed out, $N = 0$ does not exist, and so the state-selective ionisation scheme (described in sec. 2.3.2) will not even address this configuration. State-selective loading into $N = 0$ for $I = 0$ is the ideal case, as there is no splitting and so there is only one transition to be addressed. The main problem occurs for $I = 2$, where splitting occurs in $N = 0$. The current proposed state-detection scheme will not address these two states separately.

Selection rules

Transitions between different states in an atom or molecule will be dependent on the dipole moment operator, which for a two-level system is given in eq. 2.27. There are three main different types of transitions in molecules. First of all there are pure rotational transitions, which occur with a change in the rotational quantum number. Similarly are pure vibrational transitions. Finally, there are electronic transitions, in which case it is possible for there to also be a change in rotational or vibrational quantum number. For a molecule, the dipole moment operator is given by [69]:

$$\hat{\mu}_{mol} = e\left(\sum_i Z_i \hat{R}_i - \sum_j \hat{r}_j\right), \tag{2.109}$$

where the first term is the sum over the positions $\hat{R}_i$ and the charges of the nuclei $Z_i e$, and the second term is the sum over the positions of the electrons $\hat{r}_j$. The transition moment can be written [2]:

$$\begin{aligned}&\int\int\int \Psi'_{el}\Psi'_{vib}\Psi'_{rot}\hat{\mu}_{mol}\Psi''_{rot}\Psi''_{vib}\Psi''_{el}dV_{rot}dV_{vib}dV_{el}\\&=\int \Psi'_{rot}\hat{\mu}_{rot}\Psi''_{rot}dV_{rot}\int\int \Psi'_{el}\Psi'_{vib}\hat{\mu}_{\alpha}\Psi''_{vib}\Psi''_{el}dV_{vib}dV_{el},\end{aligned} \tag{2.110}$$

where Ψ_{rot} is the rotational wavefunction, dV_{rot} is the volume integral over the rotational coordinates, and so on. The $''$ and $'$ denote the initial and final state. The rotational parts have been factored out according to the Born-Oppenheimer approximation. The rotational dipole moment μ_{rot} and the electronic/vibrational dipole moment μ_{α} have also been factored out from the total dipole moment μ_{mol}. For the case of pure rotational transitions, there is no change in the electronic state or the vibrational state, therefore $\Psi'_{el} = \Psi''_{el}$ and $\Psi'_{vib} = \Psi''_{vib}$. Therefore the second part of the right hand side of eq. 2.110 is equal to the permanent dipole moment of the molecule. For a homonuclear molecule such as N_2, there is no permanent dipole moment and so the transition moment goes to zero. For heteronuclear diatomics the rotational selection rule for pure rotational transitions is $\Delta N = \pm 1$.

Now for the case of vibrational transitions for a diatomic molecule, the transition dipole moment is the second part of the right hand side of eq. 2.110. Because the dipole moment depends on the bond length, it can be expanded in a Taylor series to give [2]:

$$\mu_{vib} = \mu_0 + \frac{\partial \mu_{vib}}{\partial q}q + ... \tag{2.111}$$

which is a function of the changing distance between the nuclei q. The first term μ_0 is the dipole moment when $q = 0$. This has to be non-zero in order to allow a pure vibrational transition. Therefore, ignoring both the electronic and rotational parts, the vibrational transition dipole moment is:

$$\int \Psi'_{vib}\mu_{vib}\Psi''_{vib} = \int \Psi'_{vib}\mu_0\Psi''_{vib} + \int \Psi'_{vib}\frac{\partial \mu_{vib}}{\partial q}q\Psi''_{vib} + ... \tag{2.112}$$

where the first term goes to zero as μ_0 is a constant and Ψ'_{vib} and Ψ''_{vib} are orthogonal to each other. Therefore, for an allowed pure vibrational transition, $\partial\mu_{vib}/\partial q$ must be non-zero, and the dipole moment must vary with internuclear distance. Again, for a homonuclear molecule with no permanent dipole moment, this does not happen and so there is no pure vibrational spectrum.

Now we can consider the selection rules that govern a transition in which there is a change in both the rotation and vibration of the molecule. In this case the selection rules are:

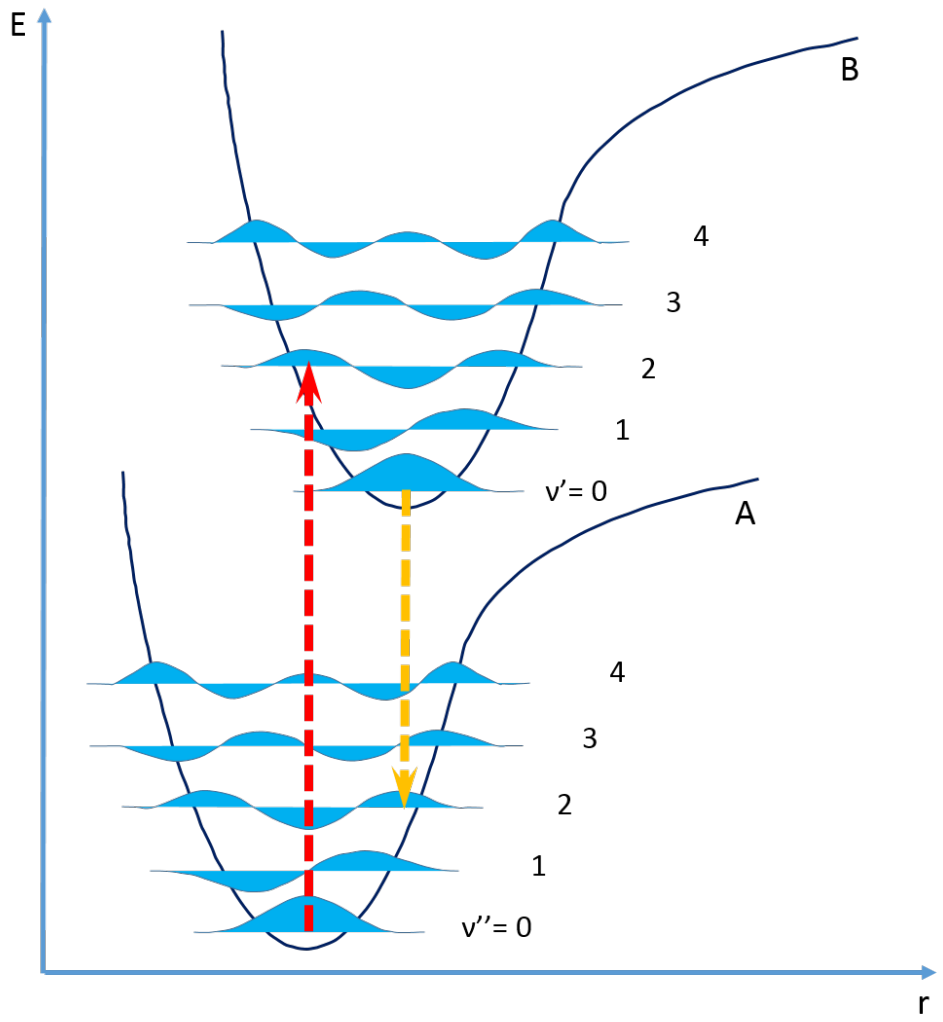

Figure 2.16: Two potential energy curves for different electronic states A and B. For each of the vibrational states the corresponding wavefunctions have been drawn in light blue. Two examples of transitions with a strong Frank-Condon overlap are illustrated by the red and orange arrows.

$$\begin{aligned} &\Delta\nu = \pm 1 \text{ (where 2, 3, ... are allowed but weaker)} \\ &\Delta N = 0, \pm 1 \\ &+ \longleftrightarrow - \end{aligned} \tag{2.113}$$

For electronic transitions there are further considerations to be made. Both the rotational and vibrational state can also change, which is true even for homonuclear molecules. The rules for electronic transitions are as follows:

$$\begin{aligned} &\Delta\Lambda = 0, \pm 1 \\ &\Delta N = 0, \pm 1 \\ &g \longleftrightarrow u \\ &+ \longleftrightarrow - \text{ (except for } \Sigma^+ - \Sigma^+ \text{ and } \Sigma^- - \Sigma^-) \end{aligned} \tag{2.114}$$

The change in rotational number ΔN has three values, which are often referred to as the P, Q and R branches, which is a change in $\Delta N = -1$, 0 and $+1$ respectively[3].

For the vibrational band structure of electronic transitions there are no selection rules. Instead the strength of different transitions within a band is dictated by the vibrational wavefunction overlap, calculated from $\int \Psi'_{vib}\Psi''_{vib}dV_{vib}$. The square of this overlap integral gives the strength of the vibrational transition, which is called the Frank-Condon overlap.

The reason for this is that when an electronic transition takes place, it is on a very short timescale, and so the distance between the comparatively slow nuclei will remain the same. This means that the strongest vibrational transition between electronic states will be where there is the largest overlap between the Ψ''_{vib} and Ψ''_{vib} wavefunctions, with no change in the nuclear separation r. Figure 2.16 illustrates two strongly overlapped electronic-vibrational transitions.

For the case where the initial state is $A(\nu'' = 0)$, and there is a transition between electronic states A and B, the strongest transition is shown in red, which is $B(\nu' = 2) \leftarrow A(\nu' = 0)$. Another example of a transition with a strong Frank-Condon overlap is shown by the orange arrow, which is the $B(\nu' = 0) \leftarrow A(\nu'' = 2)$ transition. For each of these cases there is no change in the internuclear separation r, and a strong overlap between the vibrational wavefunctions. Other vibrational transitions which do not exhibit such a strong overlap are also possible, but will be much weaker as the overlap is reduced.

2.3.2 Resonance enhanced multi-photon ionisation

The ionisation process for loading nitrogen molecules is complicated by the requirement for state-preparation, the higher complexity of molecular structure, and the large energy required to ionise (as seen in fig. 2.17, it requires ∼16 eV to ionise molecular nitrogen). As a result of the latter, high-energy photons are used (∼ 237 nm) and ionisation is a two-stage process of resonant excitation and then ionisation. The first stage excitation

[3]In other cases, such as two photon transitions, it may also be possible to see rotational spectra with $\Delta N = \pm 2$. Therefore the branches are labelled as the O, P, Q, R and S branches, where ΔN has changed by -2, -1, 0, $+1$ and $+2$ respectively.

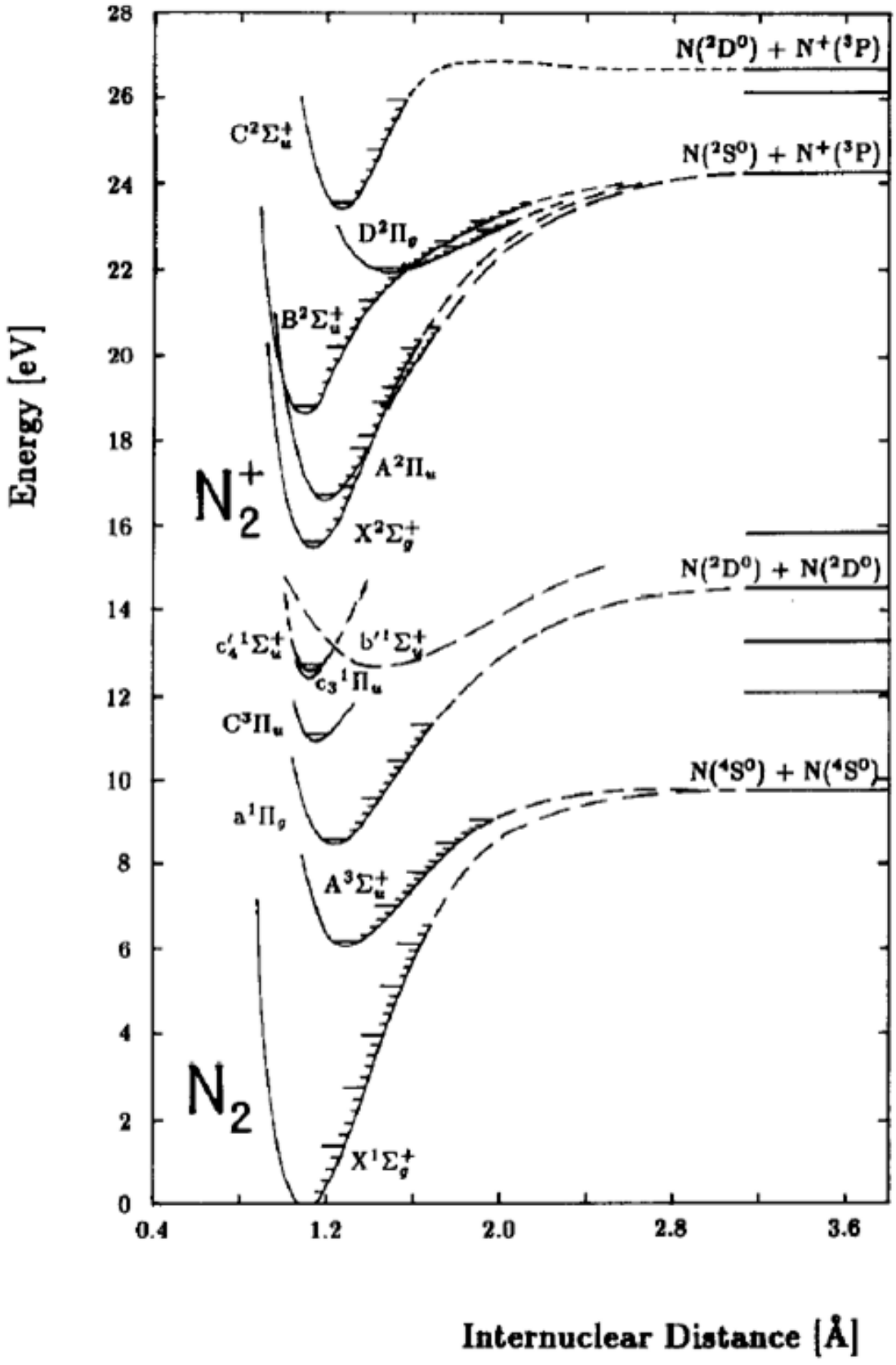

Figure 2.17: The level structure for nitrogen, not including all states. Reprinted from [3] with permission from Elsevier. Reprinted from [4] with the permission of AIP publishing (where a more detailed version can be found).

is a two-photon process, the outline of which is described in sec. 2.2.4. For this case in particular, the two photons will come from the same source, and so the excited state amplitude can be calculated from eq. 2.76.

The second stage ionises the N_2 and also prepares the ion in the desired electronic, vibrational, and rotational state. The current ionisation process used is not fully state-selective as the final state can be one of two that are allowed, but benefits from the simplicity of requiring only one laser, as it is a same-colour 2+1 scheme. This scheme has also been investigated by Opitz *et. al.* [3], who mainly investigated the S_0 and S_1 transitions, as these were strongest for their low temperature source. Despite not being able to investigate the P_2 transition fully, Opitz proposed it as being a strong candidate for preparing N_2^+ in the ground state. Other schemes, which instead use two-colour 2+1' REMPI processes, include that of Pratt *et. al.* [70], who investigated the intermediate Rydberg states c_3 and c_4', and the Willitsch group [5] who use $a''^1\Sigma_g^+$ (not included in fig. 2.17) for the intermediate excitation stage to achieve ion trap loading.

The neutral nitrogen molecules start off in the ground electronic and vibrational state, $X^2\Sigma_g^+(\nu = 0)$. Although N_2 is an apolar molecule and so does not couple to background blackbody radiation (BBR) [71], the rotational states begin in a distribution that indicates their internal temperature, due to collision dynamics. This initial temperature can be room temperature, as in the experiment in chapter 5, or can be cooled in a supersonic expansion as is being worked towards in chapter 6. The initial internal temperature is important as it strongly determines how much of the population will finish in the desired final state.

The two-photon excitation for this scheme takes the nitrogen molecule into an excited electronic, vibrational state, and, depending on which branch the excitation goes through, causes a change in the rotational state[4] of $\Delta N = 0, \pm 1, \pm 2$. The transition is $a^1\Pi_g(\nu = 10) \longleftarrow X^1\Sigma_g^+(\nu = 0)$, with the vibrational number[5] changing by 10. The excited electronic state is the lowest-lying singlet state in N_2 [3], as seen in fig. 2.17.

The final desired state for this experiment is the ground electronic, vibrational and rotational state $X^2\Sigma_g^+(N = 0, \nu = 0)$. There are a few different branches through which this can be achieved, with the P_2 branch, suggested by Opitz *et. al.*, shown as an example in fig. 2.18. Another possible example would be the O_3 transition. For the excitation stage

[4] In general, the selection rule for an electronic transition in a diatomic molecule is $\Delta N = 0, \pm 1$, with $\Delta N = \pm 2$ being disallowed. But, for the case of a two-photon transition, the rotational number can go through a change of ± 2.

[5] The vibrational selection rule for this is governed by the Frank Condon overlap of the two vibronic states.

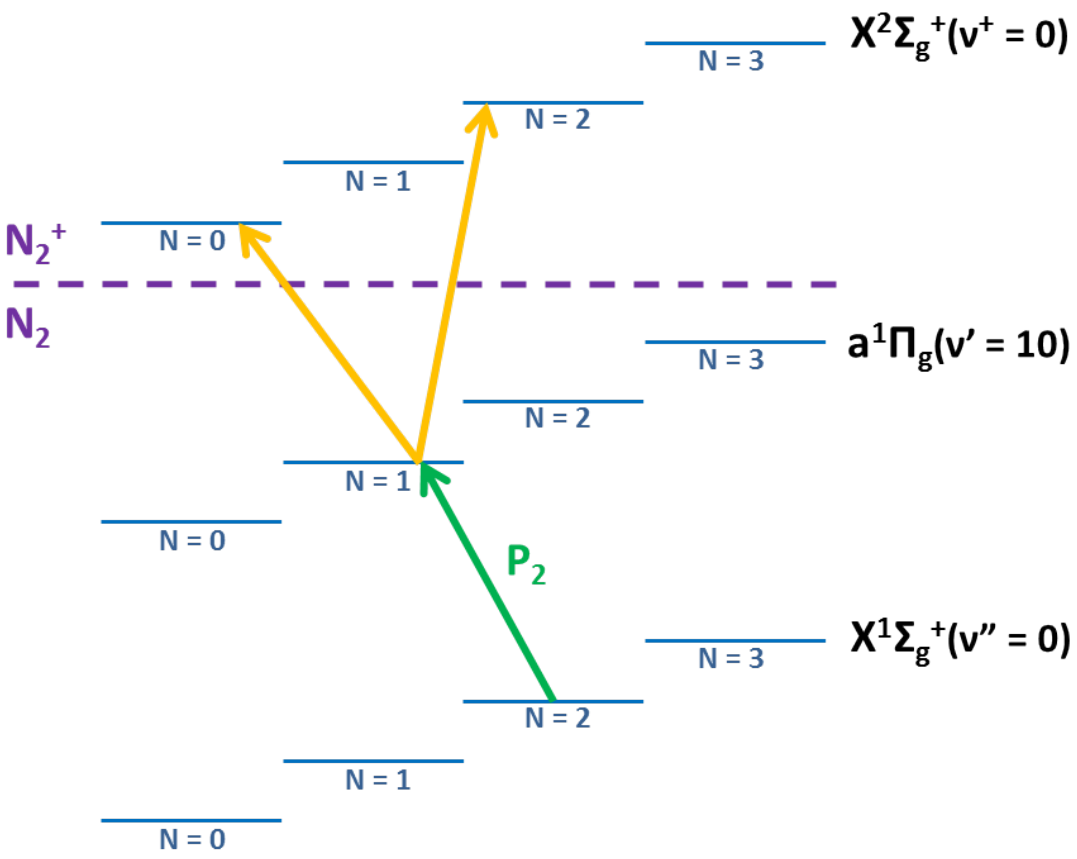

Figure 2.18: A possible ionisation scheme for preparing N_2^+ in the $X^2\Sigma_g^+(N=0,\nu=0)$ state, using the P_2 transition.

of the neutral molecule, the P_2 transition takes the state from rotational number $N=2$ to $N=1$ with $\Delta N=-1$. As previously mentioned, the final ionisation stage does not necessarily prepare the molecule in the ground rotational state. It is, in fact, energetically allowed for the molecule to also be prepared in the $N=2$ state of $X^2\Sigma_g^+(\nu=0)$. It is not possible, however, for the molecule to be prepared in the $N=1$ final state. This is governed by Hund's rule (b) [3]:

$$N_+ - N_i + l + p_+ + p_i = odd \tag{2.115}$$

where N is the rotational quantum number, p = 0 for states Σ^+ and Π^+, and p = 1 for states Σ^- and Π^-, and l is the angular momentum of the liberated electron. The indices + and i refer to the ionised and intermediate states. l is always odd. Therefore, there are two main outcomes for $N_2^+(X^2\Sigma_g^+) \longleftarrow N_2(a^1\Pi_g)$. If in the Π^+ component of the intermediate state, then $\Delta N = even$ to maintain the rule. And, if in the Π^- component, $\Delta N = odd$. So if the P_2 transition is used, the Π^- component of the intermediate transition is populated,

and so $\Delta N = odd$, which means that only the even rotational states of the ion can be populated, as indicated in fig. 2.18.

Therefore spectroscopy has to be performed on molecular nitrogen to find the transitions of interest. A suitable experiment for resonant creation and detection of ions has been setup using this ionisation scheme and a mass spectrometer for detection using time-of-flight (TOF) mass spectrometry, described in chapter 5.

2.3.3 Non-Destructive state detection

The experiments described in this thesis are aimed towards performing high-resolution spectroscopy on N_2^+. A prerequisite for this is the development of techniques for state readout. For high-resolution spectroscopy we wish to use a non-destructive state detection scheme.

For the non-destructive state detection scheme to work there are a number of considerations to be made. The scheme has to be state-dependent, avoid loss of state information from the ion and also be detectable. For this, a single N_2^+ will be trapped alongside a single $^{40}Ca^+$. The two form a coulomb crystal, and so share a centre of mass mode (COM) of motion at the secular frequency of the dual-species crystal. A state-selective resonant excitation of the COM mode will be applied to the N_2^+. As a result, the motion of the crystal will only be excited if the nitrogen ion is in the prepared state. For this, the laser-induced dipole force will be utilised (sec. 2.2.2).

Transition separation

From inspection of the dipole force equation, eq. 2.57, repeated here:

$$F_{dipole} = -\frac{\mu_{12}^2 \nabla I}{c\epsilon_0 \Delta\omega \hbar}, \tag{2.116}$$

we see that the two parameters that can be changed are the detuning from the transition $\Delta\omega$, and the gradient of the applied laser intensity ∇I. It is the detuning that allows the force to be state selective, and so relies on having well separated transition energies within the molecule. Figure 2.19 is a plot of all of the transitions in N_2^+ within the electronic transition $A^2\Pi_u(\nu = 2) \longleftarrow X^2\Sigma_g^+(\nu = 0)$, on which the state will be probed, plotted using the experimentally determined values by Wu *et. al.* [72]. Here the initial rotational state N is plotted against transition energy for different rotational branches in the electronic-vibrational transition $A^2\Pi_u(\nu = 2) \longleftarrow X^2\Sigma_g^+(\nu = 0)$. The molecular band structure is revealed in this plot, with the allowed P, Q and R branches that correspond to

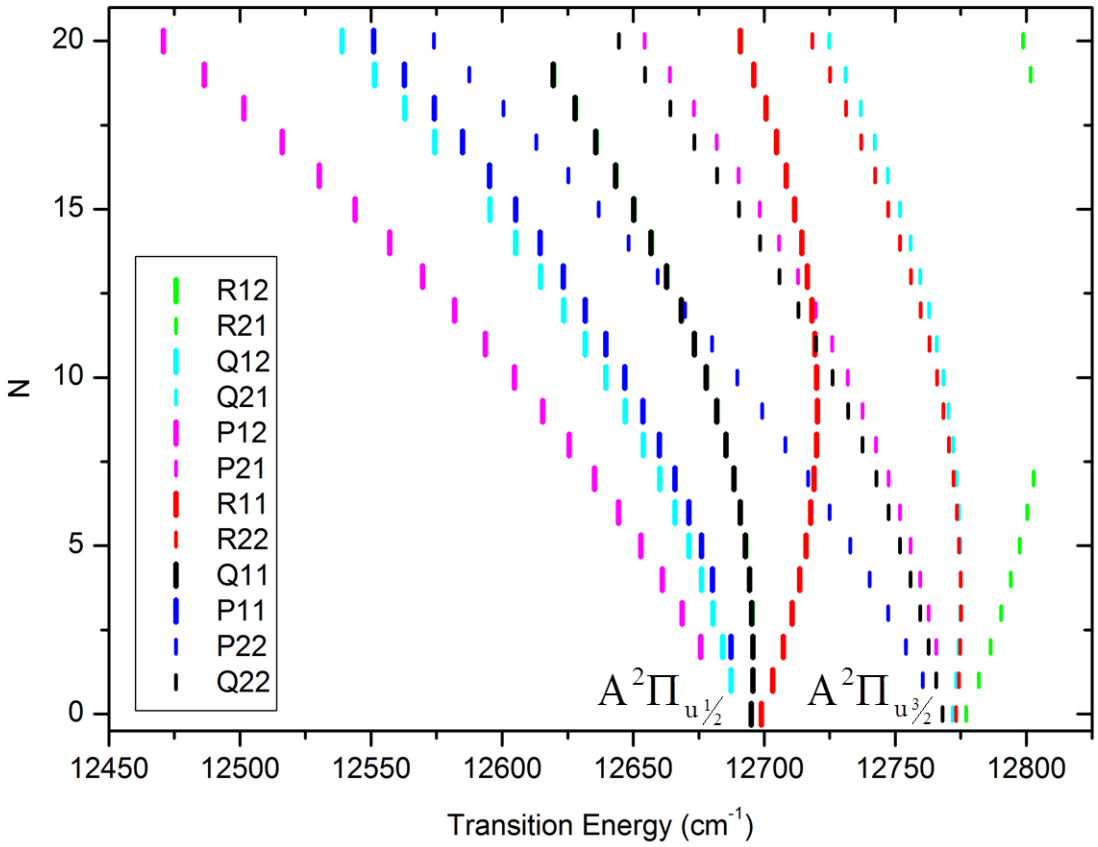

Figure 2.19: Transitions in N_2^+. Here the energy of each transition within the $A^2\Pi_u(\nu = 2) \longleftarrow X^2\Sigma_g^+(\nu = 0)$ manifold is plotted against the rotational state, N, of the electronic ground state. The different branches ('P', 'Q', and 'R') denote how much the rotational number changes by, as explained in sec. 2.3.1. The most suitable transition for our purposes sits in the R_{21} branch of $A^2\Pi_{u,3/2}(\nu = 2) \longleftarrow X^2\Sigma_g^+(\nu = 0)$, and is the transition from $N = 0$.

$\Delta N = -1, 0, +1$ respectively. The chosen transition for probing the $X^2\Sigma_g^+(N = 0, \nu = 0)$ state of N_2^+ is the $R_{21}(N = 0)$ transition, which is well separated from other close-lying transitions, for rotational numbers up to $N = 20$.

Motional excitation

In order to make the force induced by the dipole laser detectable, it must excite the COM mode of motion of the ion crystal within the trapping potential. Then, by using Doppler velocimetry (sec. 2.2.5), the motional spectrum can be determined, and hence the state detected.

Therefore the dipole force has to be modulated at the secular frequency of the COM mode. This way, the dipole force will be able to resonantly excite the secular motion. The gradient of the applied laser intensity is what determines the strength of the force, and is also how the motional COM mode is resonantly driven.

Instead of using a single laser, two lasers will be applied simultaneously, counter-propagating to one another, by using an interferometer setup. Each will be detuned such that the difference in frequency between the two is equal to the secular frequency of the ion crystal, ω_z, so that the intensity gradient oscillates at the secular frequency, which can then drive the motion.

Both the detuning, $\Delta\omega$ and the applied intensity of the field I, have to be tuned so that the maximum force is applied, while avoiding excitation of the transition. If this occurs, the state is lost via spontaneous decay. The more intense the laser beams, and the longer they are applied for, the higher the probability of this occurring. Also with the detuning - the closer the lasers are tuned to be resonant with the transition, the larger the force, but the higher the probability of spontaneous decay. In order to calculate the probability of spontaneous decay, first the excited state population has to be calculated using eq. 2.44, where the laser applied has power 1 mW and a waist of 50 μm. The rate of spontaneous decay is taken to be $\Gamma = 42000\ \mathrm{s}^{-1}$. Next, to find the probability of spontaneous decay $P_{spont}(t)$ from the excited state after time t:

$$P_{spont}(t) = \Gamma\rho_{22}t, \tag{2.117}$$

is calculated. In fig. 2.20 the probability of spontaneous decay has been calculated for four different laser detunings. As the laser is detuned from 2 GHz to 100 MHz, the probability of decay rapidly increases. Therefore the proposed detuning will be on the order of GHz. If the laser is applied for 1 ms with a detuning of 1 GHz, the probability of spontaneous

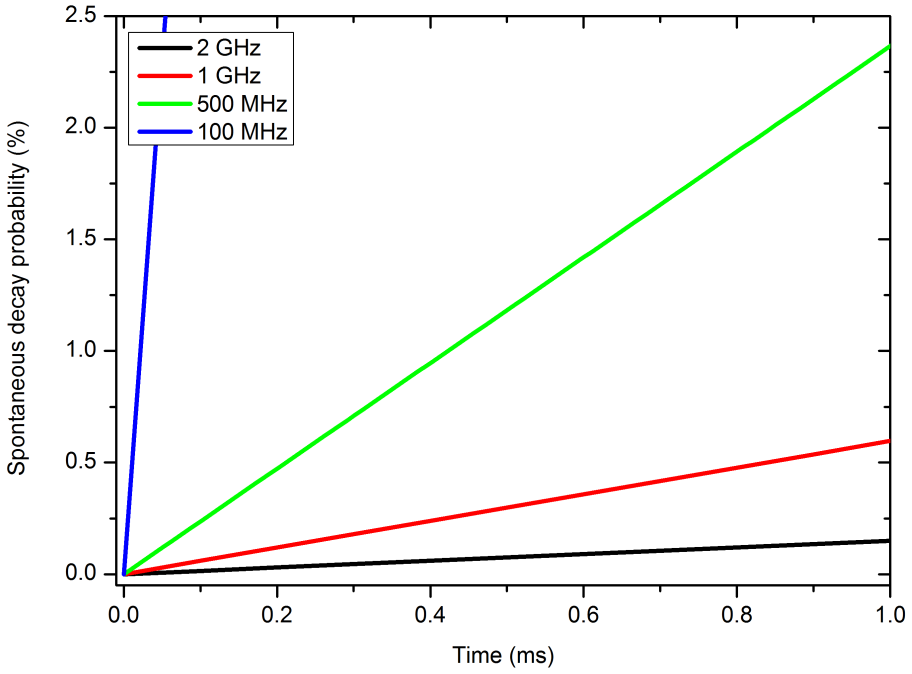

Figure 2.20: The calculated probability of spontaneous decay $P_{spont}(t)$ for four different detunings from the excited state $A^2\Pi_{u,3/2}(\nu = 2)$, plotted as a function of the amount of time the laser is applied. The laser power used is 1 mW, with a waist of 50 μm, and has a wavelength of $\sim$785 nm.

decay will be below 0.6 %.

The force exerted using the same laser now has to be calculated. In fig. 2.21 the magnitude of the dipole force has been calculated and plotted with the detuning. From a detuning of 100 MHz to 2 GHz the force decreases by an order of magnitude from 3.32 zN to a value of 0.17 zN (where 1 zN = 1 zepto Newton = 10^{-21}N). For the proposed detuning of 1 GHz, the expected force is 0.33 zN. The order of magnitude decrease when going from a detuning of order MHz to GHz is outweighed by the probability of spontaneous decay coming down from 100 % (for 100 MHz) to below 0.6 % (for 1 GHz) when the laser is applied for 1 ms.

The dipole force induced is particularly weak, as can be seen in fig. 2.21 and so an additional technique must be used in order to make this force more easily detectable. An amplification and tuned damping scheme on $^{40}Ca^+$ is explored in chapter 7. For development of this scheme, the radiation pressure force on $^{40}Ca^+$ has been used in order to simulate the dipole force, and so the magnitude of the two has to be comparable. In

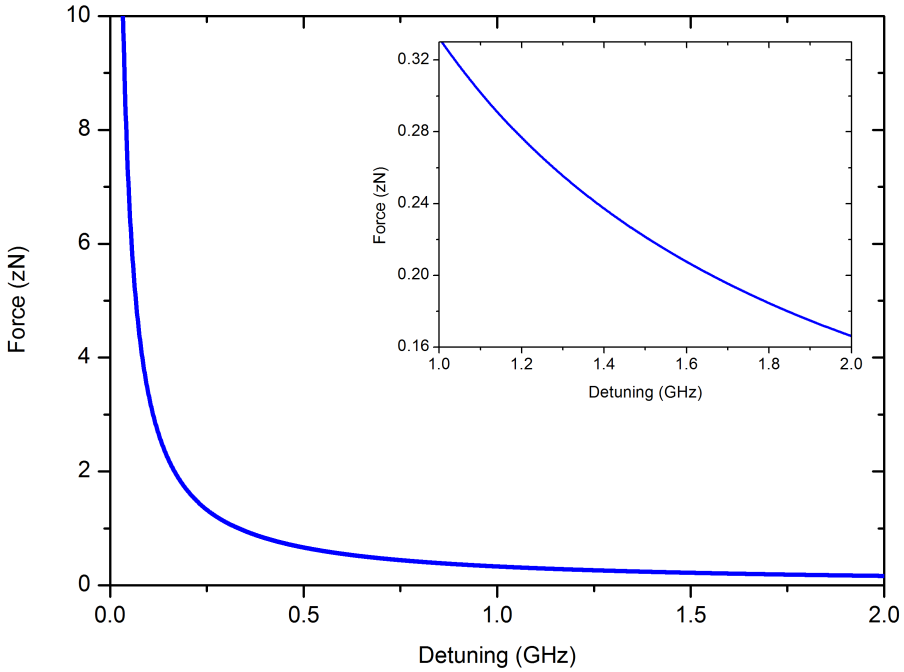

Figure 2.21: The magnitude of the dipole force as a function of the detuning. For this plot, the laser waist is 50 μm, and the power is 1 mW, with a wavelength of 785 nm. *Inset:* Magnified to show the force when the detuning is on the order of GHz.

fig. 2.22 the radiation pressure has been plotted as a function of the detuning from the transition. In general, this laser would be tuned somewhere between 10 MHz and 20 MHz for optimal laser cooling (this is at the ideal detuning of $-\Gamma/2$ for the cooling transition used in $^{40}Ca^{+}$, as explained in sec. 2.2.2). This is equivalent to a force between 84 zN and 85 zN. Although this is a larger force than that of the dipole force interaction on N_2^+, it will not drive the motion in the same way. The resonant excitation from the dipole force means that it will be a driven harmonic oscillator. Therefore the radiation pressure force with a larger magnitude of ∼85 zN should be a good way to simulate the overall effect of applying the weaker, but resonant dipole force of magnitude 0.33 zN.

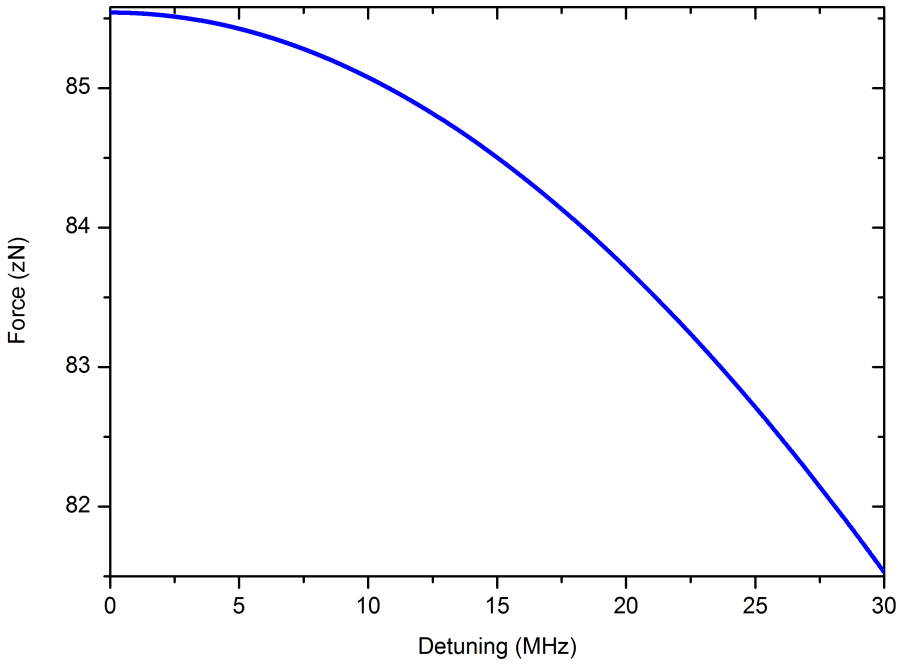

Figure 2.22: The force from the radiation pressure for $^{40}Ca^{+}$ plotted as a function of the detuning from the $4S_{1/2} \rightarrow 4P_{1/2}$ transition. This has been plotted with typical experimental laser parameters of 50 μm beam waist, 10 μW power and wavelength 397 nm.

Chapter 3

Ion Trap and laser systems for $^{40}Ca^{+}$

The main apparatus used for the experiments outlined in this thesis consists of an ion trap to provide confinement for highly localised atomic and molecular ions. While an atomic source of calcium is relatively easy to integrate into the main design, the source for state-selectively ionised N_2 is not, and so a molecular beamline is also required. The ion trap will be discussed in this chapter, whereas a description of the molecular beamline can be found in chapter 6. Also within this chapter is a description of the laser systems required for ionisation, cooling and detection of $^{40}Ca^{+}$, along with the characterisation of the system.

3.1 Ion Trap

3.1.1 Trap design and assembly

The trap used for all experiments in this thesis is an rf linear Paul trap, shown in fig. 3.1. For radial confinement, four blade-shaped stainless steel rf electrodes sit close to the main trapping region, with the ion-electrode distance $r_0 = 460\ \mu$m, and are brass-coloured in the diagram. Two endcap electrodes are required to confine the ions in the axial direction, and sit 6 mm apart either side of the radial electrodes, seen in brown. Both sets of electrodes have been designed to provide good optical access to the ions: the blade shaped electrodes allow for laser access in the radial plane, as well as imaging the trap centre from above. The axial electrodes have apertures through which it is possible to address the axis of the trap with lasers.

The machining process used for building the trap makes it self-aligning when it comes

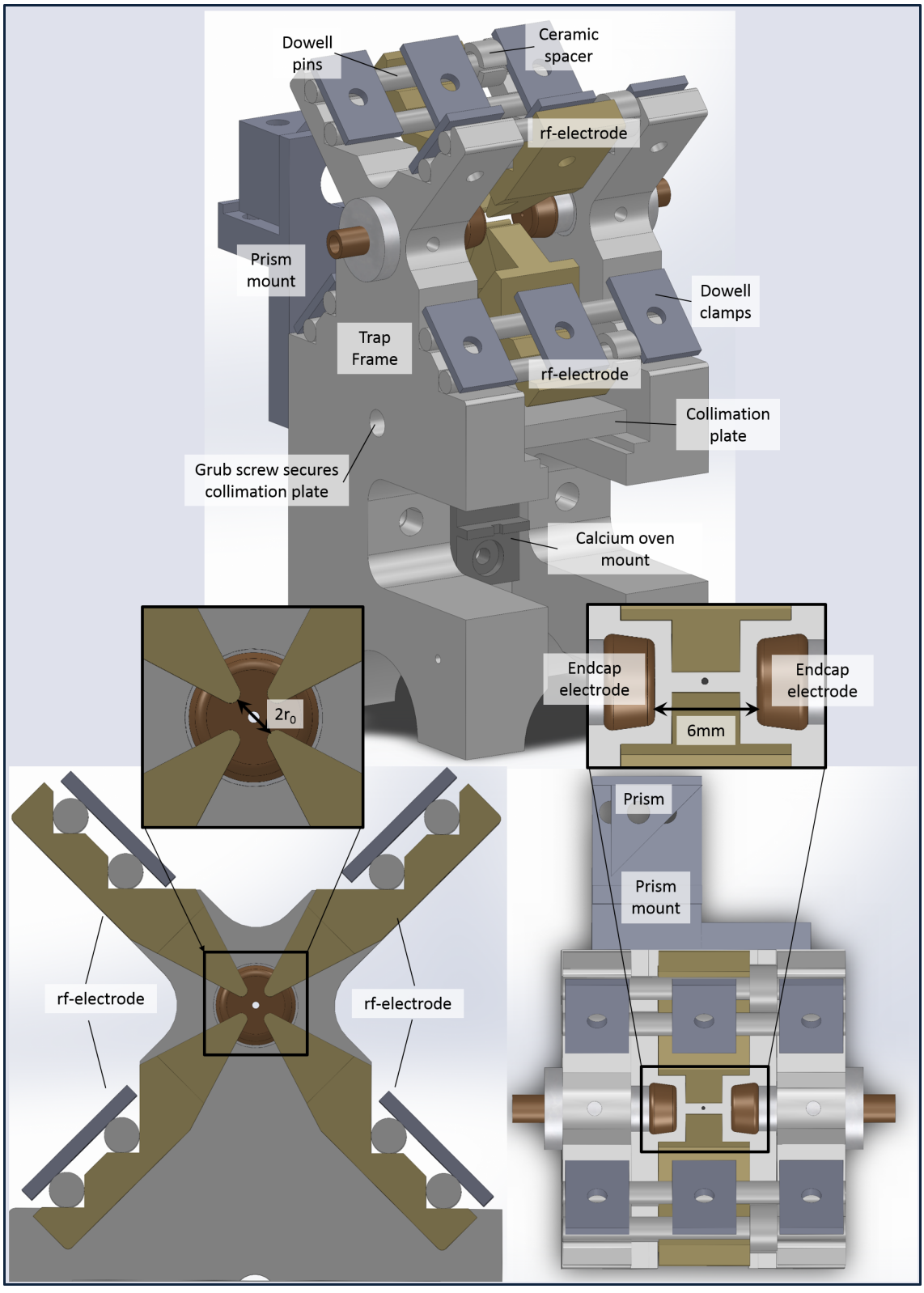

Figure 3.1: Solidworks drawings of the ion trap. Bottom left: Slice through the trap looking down the trap axis. The cuts made into the rf-electrodes and trap frame for mounting are visible, along with the clamps used for securing the dowell pins. Bottom right: view of the trap from the top looking down. In the centre of the electrodes is the collimation hole for calcium effusing from the oven. Also visible is the prism and mount for the dual purpose of reducing laser scatter, and protecting the trap centre from incoming molecules from the beamline. Top: The full trap structure in 3D.

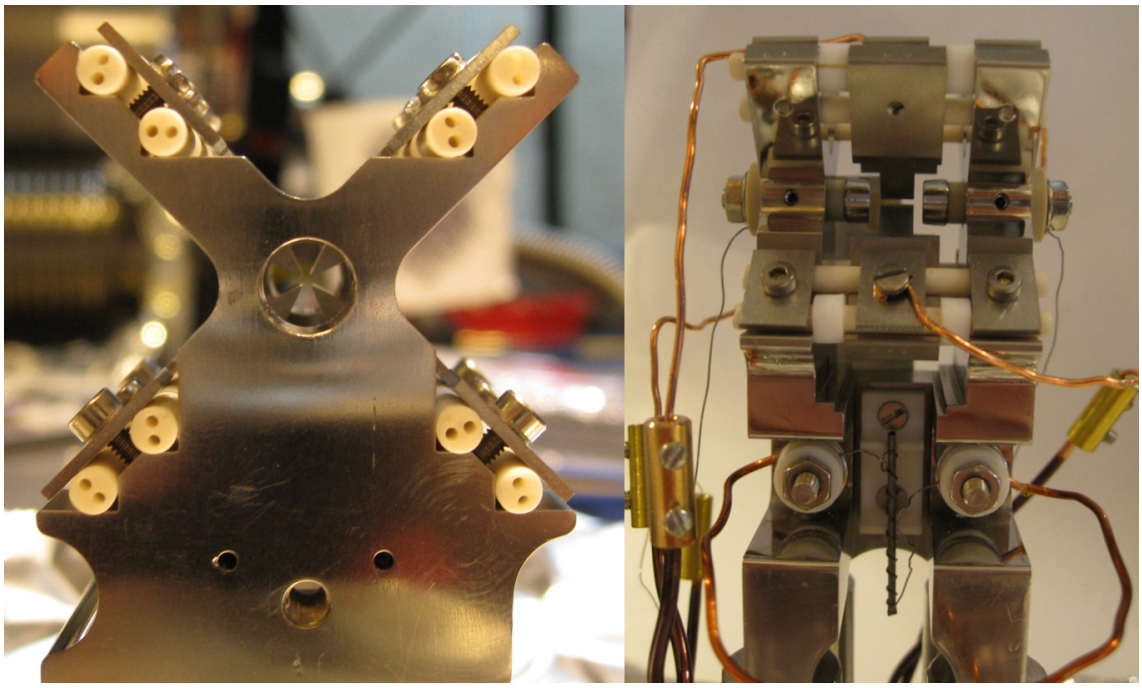

Figure 3.2: Photographs of the ion trap during construction. (Left) Before the endcap electrodes are inserted. Looking down the trap axis, the four rf blades can be seen. A small screw hole is visible directly below the trap centre - this is where the oven collimation plate is fixed into place. (Right) The electrical connections for the rf electrodes are made with small screws. The oven has been inserted and aligned.

to assembly. The whole structure is wire-eroded from a single block of stainless steel. First of all cuts are made into the block so that the four main arms of the structure are defined. A pair of grooves are also cut into each of the arms so that the positions of the dowell pins in the structure are marked. This means that when it comes to assembly, the dowell pins simply fit into the grooves that have been made in the trap structure and the rf-electrodes, and no alignment process has to take place. Ceramic spacers are then used to keep the electrodes in the centre of the structure and insulate them from the main frame of the trap. The electrodes have small tapped holes drilled into the centre of them, in between the dowell pin pairs. Along with screws, a small rectangular clamp is used to secure the electrodes to the dowell pins and thus to the trap frame, as seen in fig. 3.1. This is also how electrical connections are made with the radial electrodes, as shown in the photographs of the trap during construction in fig. 3.2.

The endcap electrodes pass right through the trap frame, and the electrical connections are made with small nuts. The electrodes are insulated from the main frame using ceramic spacers, into which the electrodes are mounted.

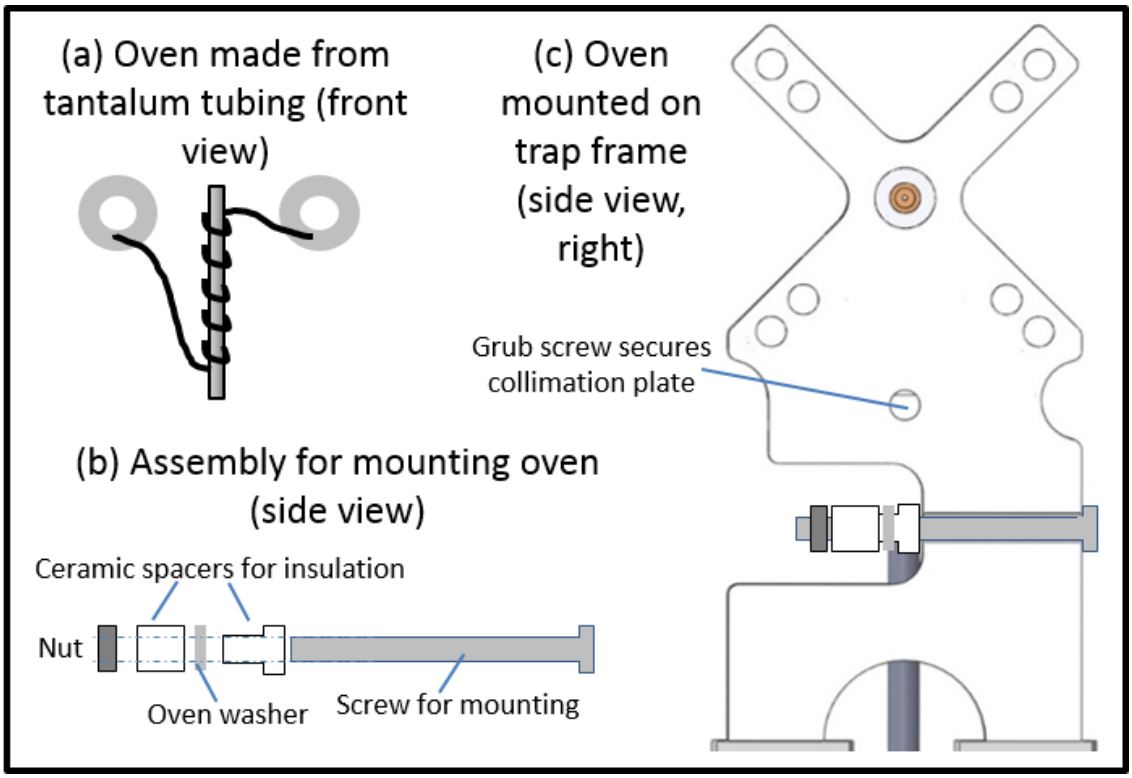

Figure 3.3: The oven assembly and mounting. (a) The tantalum oven with washers for mounting (b) One of the two assemblies needed for mounting the oven to the trap. (c) How the oven is mounted onto the main trap frame. The oven is aligned so that it points directly up to the trap centre.

The whole trap structure is mounted via four posts that sit on a cross flange. This is bolted onto the underside of a breadboard which mounts onto a customised optical bench.

3.1.2 Calcium oven

The calcium oven for ion-loading is mounted beneath the rf electrodes. This is made from small-diameter tantalum tubing that has been crimped at one end. Tantalum wire is spot-welded around the tubing to allow for the oven to be resistively heated. Small washers are spot-welded to the wires to make the required electrical connection, as can be seen in fig. 3.3 (a). The oven-mounting assembly includes two screws that bolt through the trap frame for mounting the washers, with ceramic spacers used for insulation (fig. 3.3). A small nut is used to keep the assembly in place. A collimation plate is placed above the oven as a measure to protect the trap electrodes from calcium deposits, which can alter the trapping fields and contribute to micromotion in the trap (see sec. 3.3 for more detail). A small ceramic mount with two notches for keeping the oven in place is attached beneath the collimation plate, and can be seen in the top drawing in fig. 3.1.

The oven is aligned so that it clearly points directly upwards toward the trap centre, and kept in place through tension in the wires and also the ceramic mount. The collimation plate is aligned by viewing the trap from above and adjusting until the collimation hole can be seen in between the rf electrodes, also seen in fig. 3.1, in the bottom-left image. This plate is then fixed into place with a small grub screw, which is indicated on the 3D drawing of the same figure, and also fig. 3.3. Currents typically around 1.6 A - 2 A are applied across the oven to produce an effusive calcium beam across the trap centre, where the atoms are then ionised with lasers.

3.1.3 Vacuum system

Ultra-high vacuum (UHV) conditions are required for ion trapping experiments and so the whole experiment has to be contained within a suitable vacuum system. The trap is housed in a main chamber of cubic geometry, with four windows for optical access: one at the top for imaging and the others placed on three vertical faces of the cube. The fourth face of the chamber is used for access for the molecular beamline, which is described in chapter 6. The direction from which the molecular beam enters the system can be seen in fig. 3.4. The three side windows are standard off-the-shelf vacuum windows - the seals with the trap chamber are copper gaskets. The windows provide optical access for lasers along the trap axis and also in the radial direction, as seen in fig. 3.4 (B). The top window that is used for imaging the ions is a custom-made re-entrant window, and is indium sealed.

As well as providing optical access, the design has to allow for laser beams to escape the vacuum chamber. The purpose of this is to reduce scatter in the trapping region, which can produce an unwanted extra background count of photons as detected by the imaging system. Therefore a small prism is incorporated into the trap design, which can be seen in the drawings in fig. 3.1, and also in fig. 3.4. This means that radial cooling lasers aligned through the axis of the trap can be reflected out of one of the axial viewports. The prism is also used to protect the trap centre from the incoming molecular beam, shown in fig. 3.4 (B). This is to avoid interaction of incoming neutral molecules with those that have already been loaded into the trap.

Beneath the main trap chamber is a feed-through chamber, which is bolted onto the underside of the optical breadboard, as shown in fig. 3.5. It consists of six CF40 flanges, each with its own purpose: one has four high-voltage (HV) feed-throughs for the rf electrodes, another has two HV connections for the endcaps. The third feed-through flange

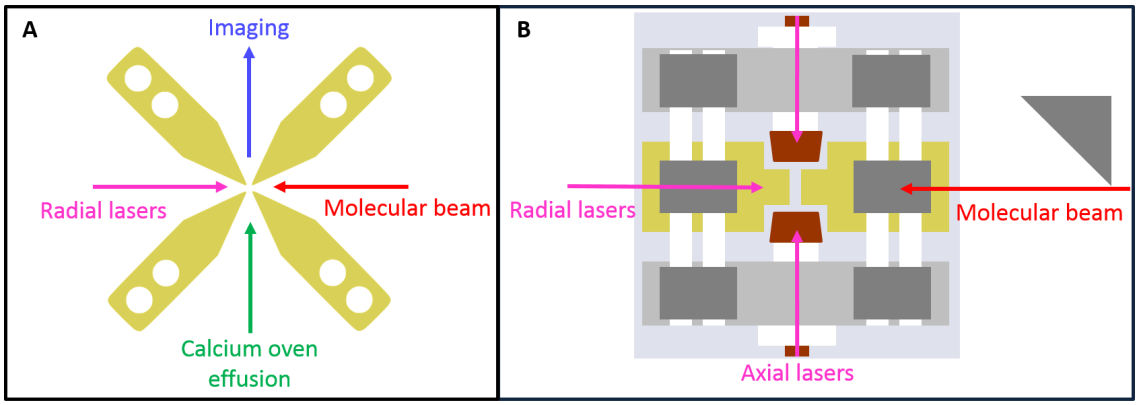

Figure 3.4: Two views of the trap demonstrating the orientation of the important components for the experiment. (A) shows a side view looking along the axis of the trap. Here all of the radial components can be seen: where the radial lasers are aligned with respect to the incoming molecular beam and effusive calcium source. The ions are then imaged from the top. (B) A top view of the trap looking down. Here the position of the deflection prism with respect to the incoming molecular beam and radial lasers is pictured.

provides connections for the oven. Two of the CF40 ports are reserved for the ion gauge and a leak valve. Finally the sixth port is a spare blanked off flange.

Beneath the feed-through chamber are bellows to vibration isolate the trap from the pumps required to keep the system at UHV. The system is pumped by a turbomolecular pump[1] (TMP), the pumping speed of which is 400 ls^{-1} for nitrogen. Additionally, an ion pump[2] is used, which has a pumping speed of 125 ls^{-1} for nitrogen. The TMP is backed by a dual stage rotary vane pump, and can be isolated from the vacuum system by way of a gate valve, leaving just the ion pump to maintain the pressure. The typical pressure in the trap chamber as measured by an ion gauge in the feed-through flange is $\sim 3 \times 10^{-10}$ mbar.

The whole vacuum system is supported by struts that affix to the underside of the optical table. This supports the system when at atmosphere, and prevents the bellow collapsing in on itself when the system is pumped down.

In order to reach a low pressure, every part of the trap and vacuum system was cleaned to UHV standards. Upon the initial assembly the whole system was baked to temperatures between 80 °C and 200 °C (depending on local vulnerability to higher temperatures) for over a week.

[1] Oerlikon Leybold vacuum TURBOVAC 361 DN 160 CF
[2] Agilent Starcell 150

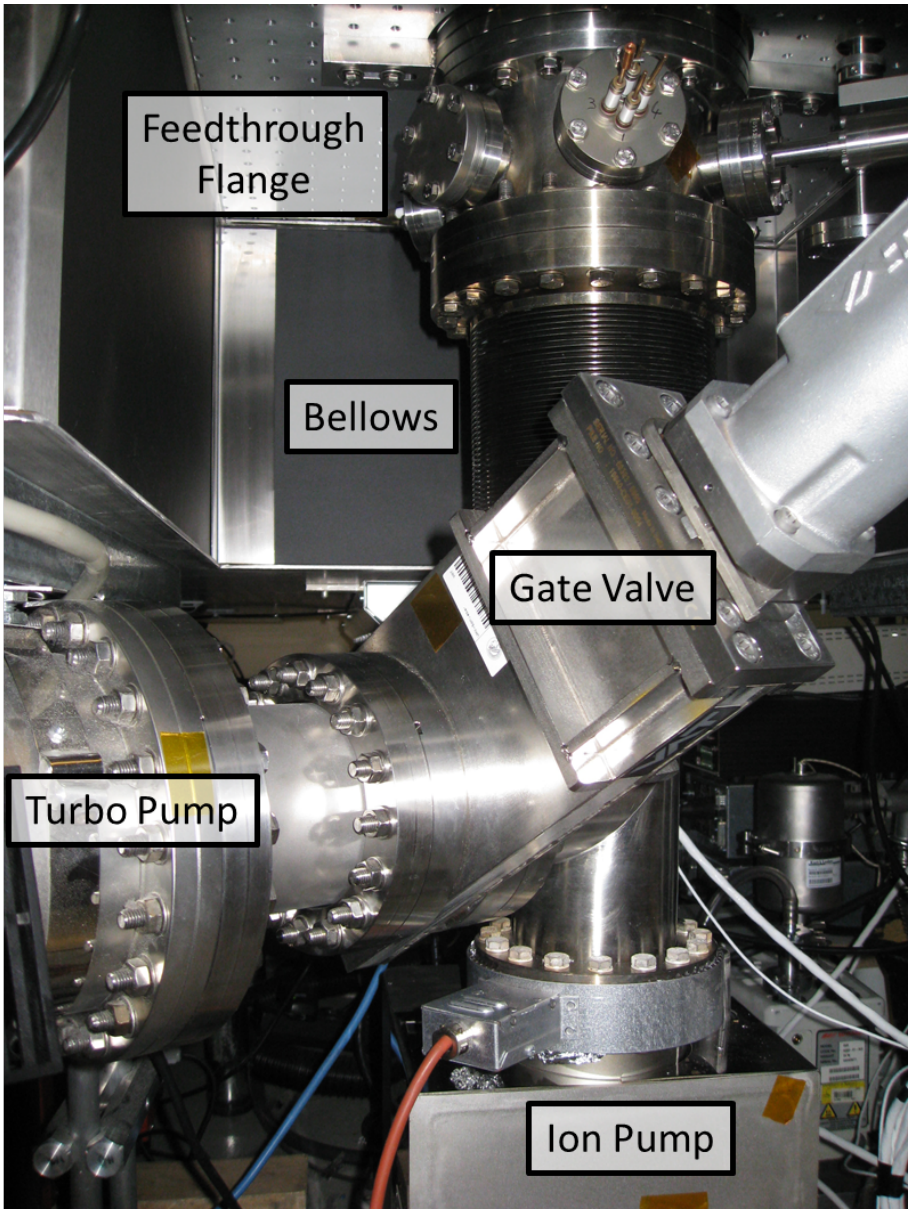

Figure 3.5: Photograph of the vacuum system for the ion trap. The ion trap chamber sits above this on top of the optical breadboard.

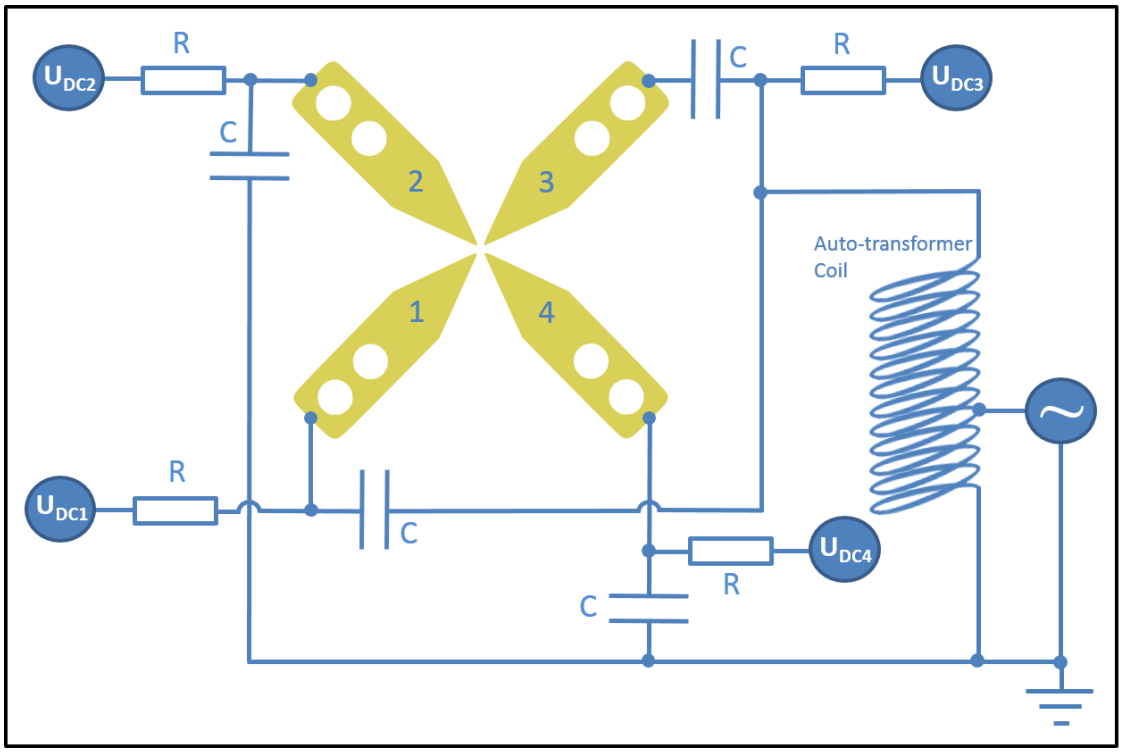

Figure 3.6: The trap electronics for providing a stable trapping field. Two of the electrodes (2 and 4) are held at rf ground, while the other two are driven at radio frequency. Separate DC voltages can be applied to each electrode via an RC circuit. All capacitors have $C = 7\ pF$ and the resistors have $R = 1\ M\Omega$. The addition of an auto-transformer coil creates a resonating circuit (with centre frequency 37.112 MHz) to provide high enough voltages to the electrodes for trapping.

3.1.4 Trap electronics

Radial electrodes

The radial electrodes in a linear Paul trap have rf-voltages applied to them in order to provide a stable trapping potential for experiments with ions, for which an rf resonator is required for generation of trapping fields of a high enough amplitude. The output from a function generator[3] is enhanced using an auto-transformer coil and capacitors to form an LC circuit, the electronics of which are shown in fig. 3.6.

A diagonal pair of electrodes have rf voltages applied to them (electrodes 1 and 3), with the other two held at rf ground. Resistors and capacitors are used to add individual DC voltages ($U_{DC\#}$) to each electrode for micromotion compensation using analogue outputs from the main data acquisition device (DAQ)[4] for computer control of the experiment.

[3] BK Precision 4055

[4] National Instruments SCB-68

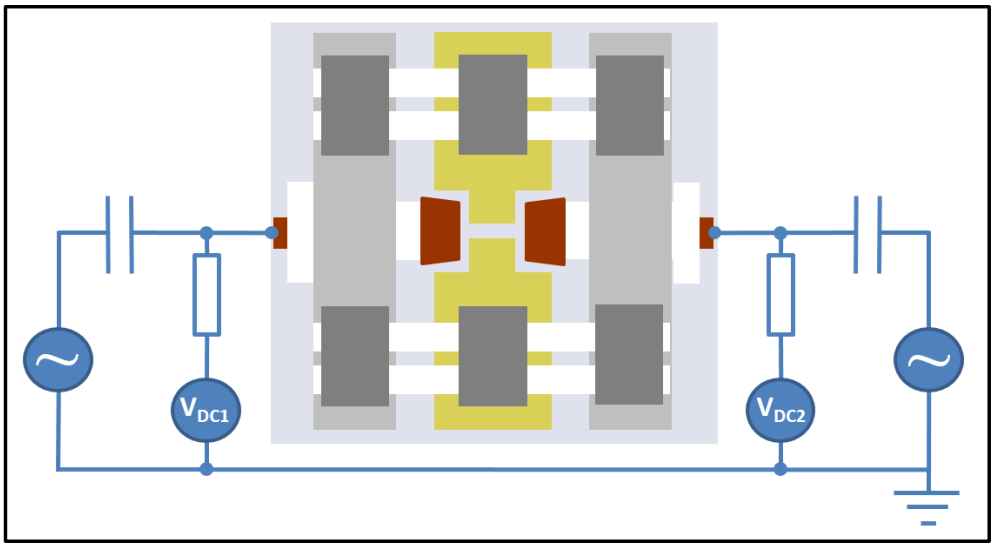

Figure 3.7: The trap electronics for the axial electrodes that allow for addition of an oscillating signal to the DC voltages applied.

Not indicated on the diagram is a monitor coil that sits near the auto-transformer coil, which is used for finding the resonance frequency and impedance matching.

The trap itself has some capacitance which contributes to the behaviour of the circuit. It is possible to empirically determine the value of the trap capacitance by replacing the trap with capacitors of different values, and monitoring the response of the circuit [64].

All of the electronics are housed in an aluminium box that is fixed onto a CF40 feed-through flange with four high-voltage feed-throughs, one for each electrode.

The contact made between the function generator and the auto-transformer coil has been made so that it can be moved smoothly along the coil. This allows for the process of impedance matching. The reflection as monitored using an rf-reflectometer has been minimised to $< 1\%$ as the contact was moved into the optimum position. For this system the optimum position gives a Q-factor of $\sim$90 with a trap frequency of 37.112 MHz.

Axial electrodes

An additional aluminium box mounted onto the feed-through flange for the axial electrodes houses the endcap electronics. Each of the endcap electrodes are held at typically hundreds of volts using high voltage power supplies[5], to provide confinement in the axial direction.

In order to excite the secular motion of the ions in the trapping field, it is useful to be able to apply additional oscillating fields at the trap frequency, or even pulse trains for crystal weighing measurements (see section 3.4). An RC circuit is used for this purpose,

[5]SRS PS350

and is shown in fig. 3.7.

3.1.5 Imaging system

The imaging system is used for detection of the ion's fluorescence in the trap, and is placed above the ion trap looking downwards toward the trap centre, and shown in fig. 3.8. The top window is a re-entrant window in order to allow the lens to get closer to the trapping region and so increasing the numerical aperture of the imaging system.

The lens is custom-made, with a working distance that is suitable for the chamber dimensions. It has a large diameter to allow for more fluorescence to be captured. The lens is mounted on adjustable lens tubing for focusing. This is mounted onto an x-y micrometer stage so that the position of the focus in the x-y plane can also be adjusted. The x-y stage is screwed onto an aluminium support. A slit is placed at the focus of the image in order to reduce any scatter from the radial electrodes. As well as this, a notch filter[6] blocks out the the light from unwanted sources, so that the majority of light detected is fluorescence from the ions at 397 nm.

There are two methods of detecting ions using this system: a charge-coupled device (CCD) camera[7], and a photo-multiplier tube (PMT). For the majority of the experiments in this thesis, fluorescence is collected using the more sensitive PMT, although it is extremely useful to have the option of the CCD for some parts of the experiment (for instance, determining how many dark ions are present in the crystal during N_2 loading to determine a successful load using the 'crystal weighing' technique. See chapter 6).

The PMT is placed directly above the system. Just below the PMT sits an optics cube into which different optical elements can be placed. A mirror can be inserted to reflect light away from the PMT and into the camera instead. It is possible to have a semi-reflective mirror so that only some of the light is reflected into the CCD, enabling the PMT and camera to be used in tandem. Generally the system is not operated in this way as all the fluorescence is required for the PMT to get maximum signal.

The whole imaging system is mounted on a frame which is made from four optic mount posts, and two aluminium stages.

[6] Semrock BrightLine FF01-395/11-25

[7] Andor Luca S

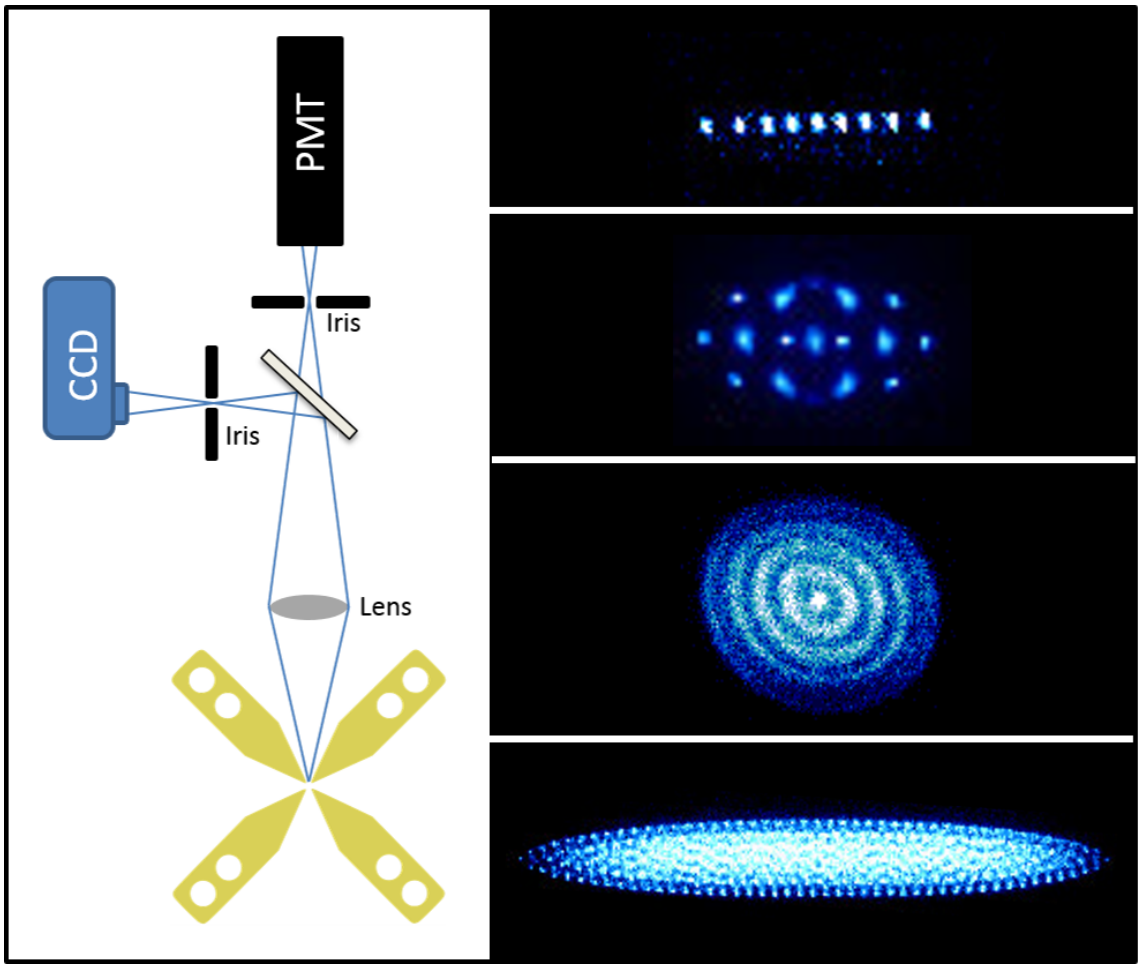

Figure 3.8: (Left) A schematic of the imaging setup. (Right) A variety of false colour images of calcium ions taken using the CCD. Single ions, strings, and large crystals can be trapped and imaged using this system.

3.2 Laser systems

The majority of the lasers used in this thesis are home-built external-cavity diode lasers in the Littrow configuration, allowing for a long tunable range using a piezo for adjusting the angle of the diffraction grating. One optics bench in the centre of the lab is dedicated to the main laser systems, with optic fibres taking beams to the required parts of the lab. This means that many of the systems are generally used in tandem by two main ion-trap experiments.

The lasers are frequency stabilised by using a wavelength meter[8] and feedback system to re-adjust the wavelength when it drifts. The measured wavelength is compared to a set wavelength, and the difference is used by a labview program to provide feedback using a virtual PI circuit. The required voltage for correcting any drifts is fed back to

[8] Angstrom HighFinesse model WS7

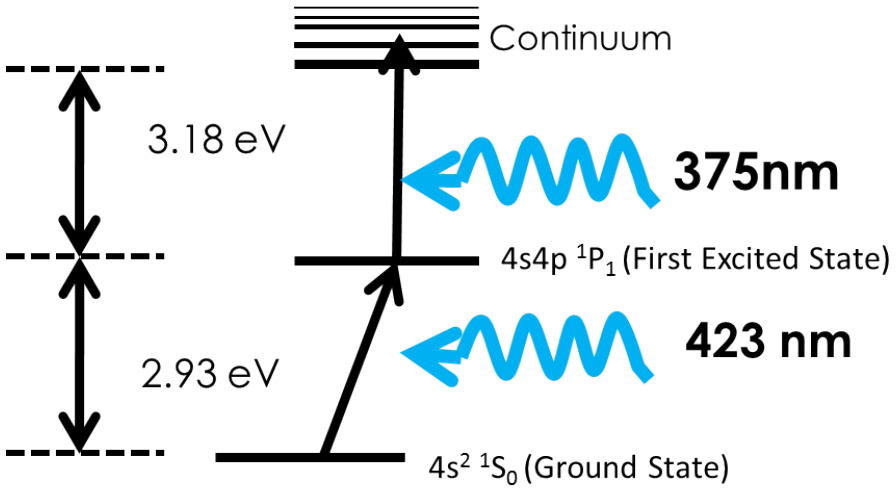

Figure 3.9: Ionisation scheme for ^{40}Ca. The 423 nm laser can be tuned for addressing different isotopes.

the diffraction grating piezos to change the angle and adjust the output frequency. The voltages are supplied by analogue outputs from a data acquisition device (DAQ)[9]. In some circumstances, this feedback system is not precise enough for a particular application, for instance the experiments found in chapter 7. In this case another laser stabilisation system was devised using trapped calcium ions, for further detail see section 4.5.

3.2.1 Photoionisation lasers for ^{40}Ca

We use an isotope-selective resonant ionisation process for calcium-ion production. This requires two photons, the first of which is at 423 nm and is a resonant excitation from the $4S_0$ ground state to the $4P_1$ excited state in ^{40}Ca. This laser can be tuned to address different isotopes of calcium, although the subsequent trap-loading efficiency depends on the natural abundance, which is 96.9% for ^{40}Ca [73]. The 423 nm laser has a typical output power of 20 mW.

The second photon ionises the calcium out of the $4P_1$ state to the continuum. The laser used for this is at 375 nm, and as this is not a resonant process, does not require frequency stabilisation.

High precision control over the frequency and amplitude of these lasers is not necessary, and so the optic setups are kept to a minimum. Rotation of the polarisation using $\lambda/2$ plates allows for splitting of the beams into different 'arms' for each of the experiments, which are then aligned into optic fibres.

[9] Redlabs

3.2.2 Lasers for cooling and detection

The $^{40}Ca^{+}$ level structure can be approximated to a lambda system with S, P and D states. There is further fine-structure splitting in the P and D states. The calcium ions are cooled on the $4^2S_{1/2} \rightarrow 4^2P_{1/2}$ transition, the fluorescence of which is collected via the imaging system and used for detection. Once in the $4^2P_{1/2}$ state the ion can then decay into $3^2D_{3/2}$, and as a result, a repumper at 850 nm is needed to re-populate the ground state so that cooling can continue. The calcium ion can also decay into $3^2D_{5/2}$, and so a second repumper at 854 nm on the $3^2D_{5/2} \rightarrow 4^2P_{3/2}$ transition is used. These three lasers are all that are required for cooling and detection of calcium ions, as a closed system is formed between the states with the lasers. The wavelengths[10] and linewidths[11] for each transition in this system are given in table 3.1, with a diagram of the cooling scheme shown in fig. 3.10.

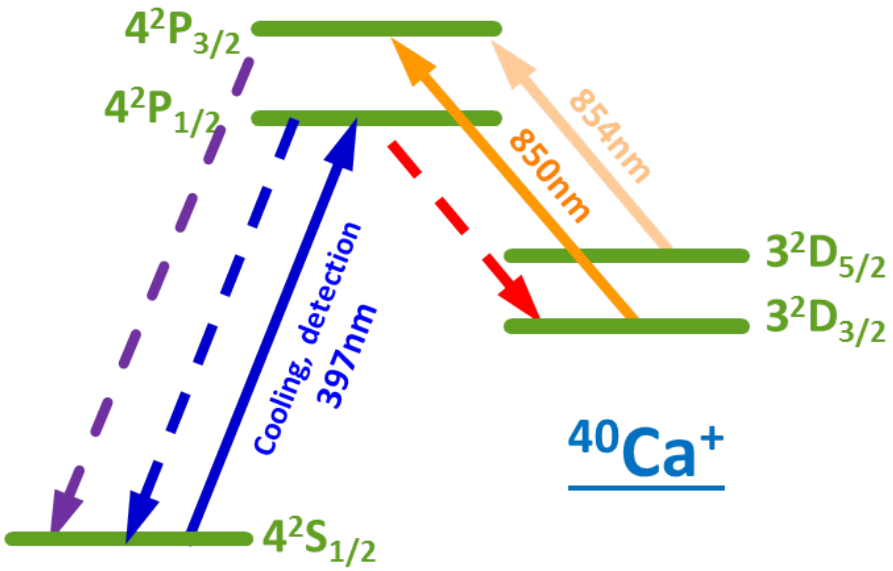

Figure 3.10: Cooling scheme for $^{40}Ca^{+}$. The cooling and detection takes place on the $4^2S_{1/2} \rightarrow 4^2P_{1/2}$ transition. Two more lasers are required for repumping to avoid population trapping in other states.

The 397 nm cooling laser is a commercial laser diode system[12] which supplies two ion-trap experiments. The optics for this laser are set up so that the total laser power (approximately 3 mW) is shared between six different arms - four of which are used for the experiments described here. The frequency and amplitude of each of the arms can be

[10] Wavelengths from: `http://physics.nist.gov/cgi-bin/ASD/lines1.pl`

[11] Transition rates calculated from lifetimes given in [74]

[12] Toptica series DL100

Transition	Wavelength (air) /nm	Decay Rate /2π MHz
$4^2S_{1/2} \rightarrow 4^2P_{1/2}$	396.847	20.67
$3^2D_{3/2} \rightarrow 4^2P_{3/2}$	849.802	0.18
$3^2D_{5/2} \rightarrow 4^2P_{3/2}$	854.209	1.58
$3^2D_{3/2} \rightarrow 4^2P_{1/2}$	866.214	1.69
$4^2S_{1/2} \rightarrow 4^2P_{3/2}$	393.366	21.51
$4^2S_{1/2} \rightarrow 3^2D_{5/2}$	729.147	15.23 x 10^{-8}
$4^2S_{1/2} \rightarrow 3^2D_{3/2}$	732.389	14.74 x 10^{-8}

Table 3.1: Wavelengths and lifetimes for the transitions in $^{40}Ca^+$. The first three transitions in the table are used for cooling and repumping. All the other transitions for $^{40}Ca^+$ are shown, including the weak quadrupole transitions occupying the last two rows.

independently controlled, making the system extremely versatile.

The 854 nm and 850 nm repumpers are two home-built lasers. For this system only two different arms are required; with one for each experiment. To provide more space around the ion-trap experiments, the two repumpers are overlapped before being coupled into each of the optic fibres that bring the laser light to each of the experiments. The power output of each laser is around 20 mW.

Precise control over the frequency and amplitude of these lasers (particularly the cooling laser) is required. For this, acousto-optic modulators (AOMs)[13] driven by voltage controlled oscillators (VCOs)[14] are used in two different configurations depending on the degree of control required, illustrated in fig. 3.11.

The frequency of the repumper beams does not need to be varied for any of the experiments. It is, however, useful to be able to change the amplitude, or switch the repumpers off completely. Therefore, only a single pass configuration is used as shown in fig. 3.11(B). Independent control over the frequency of each of the 397 nm arms is vital for many of the experiments, and therefore a double-pass setup is used (fig. 3.11(A)). As the frequency of the VCO is varied, the pointing of first pass diffraction shifts. But, this is retro-reflected and passes through the AOM for a second pass. The shift in laser pointing effectively cancels out after a double-pass, and so the laser alignment is maintained.

[13]Crystal Technologies model 3200

[14]Crystal Technologies model 1200AF-AEFO-1.0W

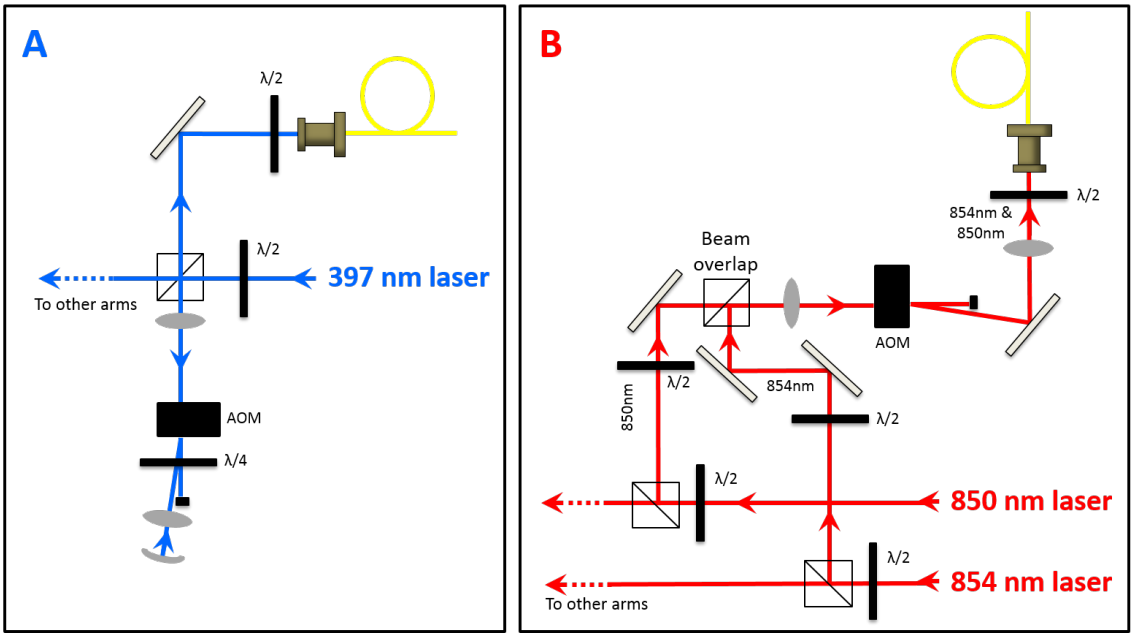

Figure 3.11: Optical setups used for the cooling and repumper lasers. (A) Shows a double-pass AOM configuration for the 397 nm cooling laser, to allow for frequency control as well as control over the amplitude. After being selected from the main laser beam, it is focused down into the AOM. The first order is collimated, retro-reflected, and focused back into the AOM, with the polarisation corrected using a $\lambda/4$ plate. The frequency-shifted beam is then aligned into a single-mode fibre. (B) A single-pass AOM configuration, used as less control over the repumper frequencies are required for the experiments. 850 nm and 854 nm lasers are overlapped using a $\lambda/2$ plate. Both are then focused into the AOM. The first order diffraction is selected and the beams are aligned into a single-mode fibre.

3.2.3 Arrangement of Lasers around the trap

Due to the experiments described in this thesis, there are many laser beams that need to be aligned into the trap, with the axial or radial directions being critical for many of the lasers. Therefore space around the trap is at a premium, and the setup has to be carefully considered to be as compact as possible. Many of the beams are overlapped to preserve the use of space. Figure 3.12 shows the laser configuration into the trap.

The photoionisation beams for calcium-ion production are overlapped using a polarisation beam splitter (PBS) and aligned radially into the trap. The orientation in this case is not so critical, and so these beams could really be placed anywhere around the trap. For the main 397 nm cooling beams, however, the positioning is more critical. There are, in fact, four different beams needed for the main experiments: two counter-propagating axial beams for the tuned damping (see chapter 7) and state-detection schemes, and two

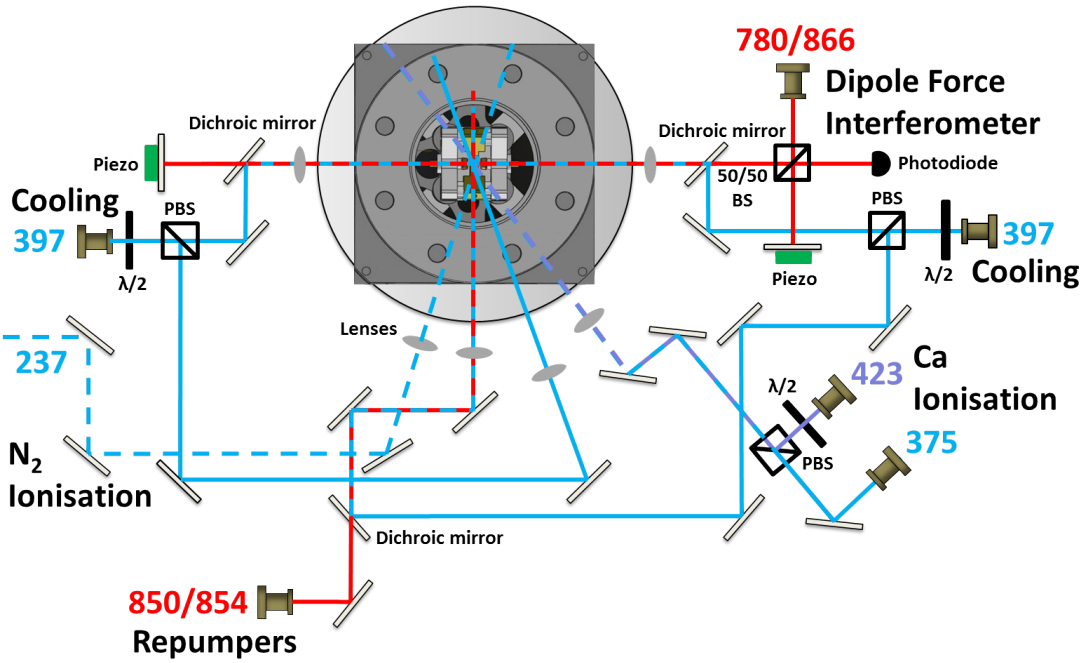

Figure 3.12: Optics setup around the trap for all of the lasers required.

radial beams which are required for the micromotion photon-correlation method (see sec. 3.3.2). The two axial beams need to also be aligned with the dipole force interferometer for nitrogen spectroscopy, as this also needs to be aligned axially.

There is no space left in the axial direction for any more lasers, and so the rest need to be aligned into the trap in the radial direction. The 850 nm and 854 nm repumper lasers are overlapped with one of the radial 397 nm lasers using a dichroic mirror. The final laser is the pulse laser at 237 nm which is used for state-selective photoionisation of nitrogen molecules (see chapters 5 and 6).

3.3 Micromotion Compensation

Aside from the secular motion of the ion within the trap potential, there is another higher frequency motion due to the trap drive, discussed in sec. 2.1. This is referred to as the micromotion. In the trap centre the RF electric field is zero; whereas elsewhere the field oscillates at the trap drive frequency. When placed directly into the trap centre there will still be some intrinsic micromotion felt by the ion due to its secular motion, although this can be minimised by laser cooling.

Excess micromotion arises when the position of the ion deviates from the trap centre, which can be due to a build up of charges or patch potential somewhere close to the trapping region. This can be minimised by applying extra voltages to place the ion back

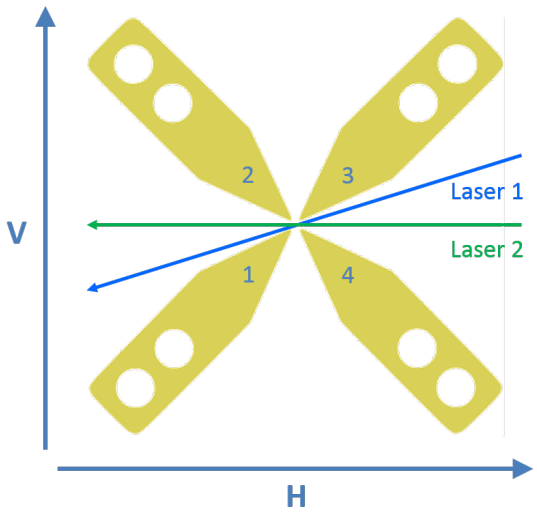

Figure 3.13: The alignment of two radial lasers for micromotion compensation using the photon correlation method.

into the trap centre. The micromotion will also increase when the secular motion is excited, as the ion's motional amplitude probes trap regions of larger micromotion. If 3D ion crystals are loaded into the trap, heating will occur due to the micromotion. This is due to the fact that only some of the ions will sit exactly at the trap centre, with the other ions sitting in regions of higher micromotion amplitude.

In the case of the blade-trap used, extra DC voltages are superimposed on the rf trap drive onto each electrode individually using an RC circuit (fig. 3.6). The ion can be pushed back into the trap centre this way. First the trap centre has to be found - there are two methods presented here that can be used to do this. One is a coarse method, which gives a good idea of the region in which the trap centre is; the other uses a more precise photon correlation technique.

3.3.1 Coarse compensation

For this method, the ions are imaged by the CCD (see fig. 3.8), and the rf trap amplitude is controlled. The amplitude is scanned while the trapped ions are imaged. In the case of a high-amplitude rf drive there is a steep trapping potential which will push the ions closer to the true rf trap centre. For a shallower potential, and in the case of having poorly compensated ions, the crystal will move away from the trap centre as the strength of the extra micromotion-inducing field takes over.

The ion position in the trap can be expressed in terms of the voltages that are applied to the rf blades, defining H as the horizontal direction and V the vertical direction, shown

in fig. 3.13. A combination of voltages on the four electrodes can be applied to push the ion along these axes and back to the rf centre:

$$H = (U_1 + U_2) - (U_3 + U_4) \tag{3.1}$$

$$V = (U_1 + U_4) - (U_2 + U_3). \tag{3.2}$$

The micromotion can be easily compensated in the horizontal direction with the CCD camera, as the ions can be seen moving from the true trap centre as the RF amplitude is reduced. In the vertical direction, however, this becomes a judgment of how unfocused the ions become as they move towards/away from the imaging system. Ideally, two CCD cameras looking into the trap perpendicular to each other would be most effective for seeing the micromotion in both directions, although is not practical for this setup.

3.3.2 Photon correlation method

The photon correlation method is an effective way of precisely minimising the micromotion of the ions in both the V and H directions. The scheme for this is reliant on the Doppler effect. As the ions move into and away from the cooling laser, the effective detuning from the transition is shifted, resulting in a modulation of the laser-induced fluorescence (This is the same effect used for Doppler velocimetry, section 2.2.5). Therefore, for an ion that has micromotion parallel to a cooling laser (397 nm), the fluorescence collected will be modulated at the trap frequency Ω. To detect this, photons from the ion are collected via a PMT, with their arrival times recorded by a time to digital converter (TDC)[15]. Micromotion leads to a modulation of the cross-correlation between the trap drive and fluorescence. For small amplitudes the modulation amplitude of the correlation signal is proportional to the micromotion amplitude.

If the ion is displaced along the V axis, then the ion will undergo oscillations due to micromotion in the H direction, and vice-versa. This is due to the direction of the electric field that is being driven at Ω. As the ion moves parallel to the laser, the fluorescence decreases due to redshift. In the next half cycle the fluorescence increases as the ion moves in the other direction: anti-parallel to the laser. Any micromotion with a component orthogonal to the laser propagation remains undetected, and so two radial lasers with a large angle between them are required to fully minimise the effect in a 2D trap.

[15] ACAM GP2

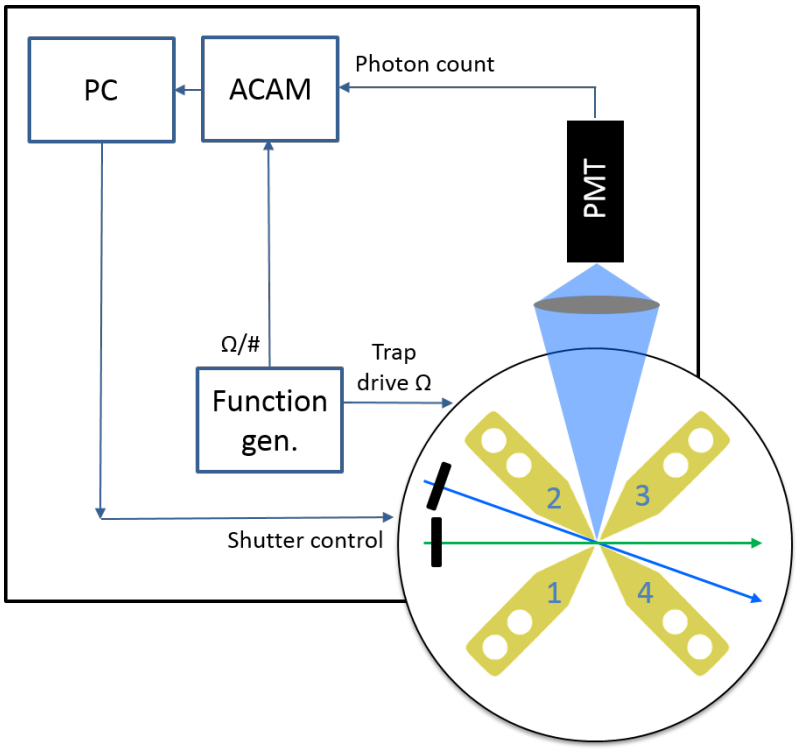

Figure 3.14: Micromotion setup.

The full experimental setup for this method is shown in fig. 3.14. There are two lasers in the radial plane, each of which can be blocked via computer-controlled shutters. The function generator has two outputs: the first is used for the rf trap drive. The second output, which is in phase with the first, is a TTL pulse, the frequency of which is a multiple of the trap drive frequency $\Omega/\#$. The fluorescence collected by the PMT and the TTL pulse from output 2 on the function generator are correlated using the counting card. If the TTL output has a frequency of $\Omega/5$, five cycles of micromotion would be seen in the correlation. A sine wave is fit to this, and the amplitude of the micromotion determined for the particular H and V voltages.

For laser 1 a region of H-space is scanned whilst holding V constant. The amplitude is measured for each of the H voltages. As the ion crosses through a micromotion minima the amplitude reduces, until the minima is crossed, after which the phase of the sine wave changes by 180 deg. The value of V is then changed and held constant for another range in H, and repeated. Using this a range of H and V voltages are found for which the micromotion amplitude is zero. These are the data points in fig. 3.15. Using this method a line of minimum micromotion for laser 1 can be plotted in H-V space. The first laser is then blocked, and the same measurement is taken with laser 2. The result is a line of minimum micromotion for each laser: the crossing point of which gives the values that V

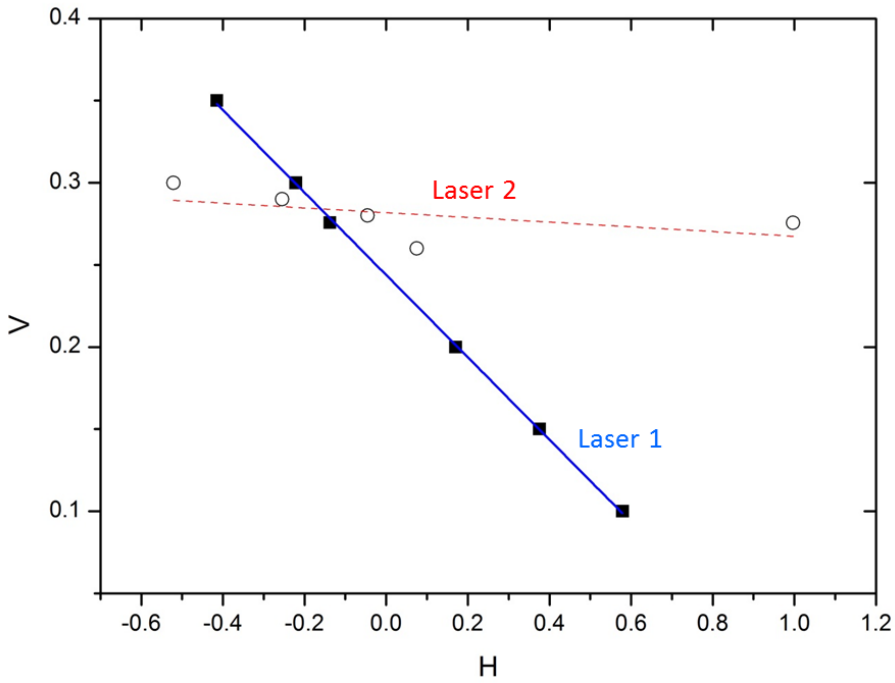

Figure 3.15: Determination of the voltages required for micromotion compensation. Each data point is a position of minimum micromotion in terms of the voltages applied in each direction (H and V). This has been measured for two lasers in order to probe orthogonal components of the micromotion. The point at which the two lines intercept gives the values that V and H should be set to for micromotion minimisation.

and H should be set to in order to minimise the micromotion (fig. 3.15).

3.4 Ion trap characterisation and crystal weighing

The working parameters of the ion trap system need to be characterised. For this, secular frequency measurements in both the radial and axial directions are taken for a range of applied voltage amplitudes. The secular frequencies can then be related to the a and q trapping parameters via eq. 2.21 and eq. 2.18. For the setup used, the trap drive frequency is $\Omega = 2\pi$ 37.112 MHz, with values $Q = 1$ e and $m = 40$ amu for calcium.

In order to excite the axial secular motion, two approaches can be taken. The first is to image the ions on the CCD while scanning an applied rf signal to one of the endcap electrodes using the RC circuit in fig. 3.7. The frequency is scanned until the crystal visibly heats up, indicating resonance between the driving field and the ions, and so the secular frequency is determined.

For higher resolution, a different approach can be used, the setup of which is shown in fig. 3.16. Instead of applying rf to one of the endcap electrodes, a square pulse is used

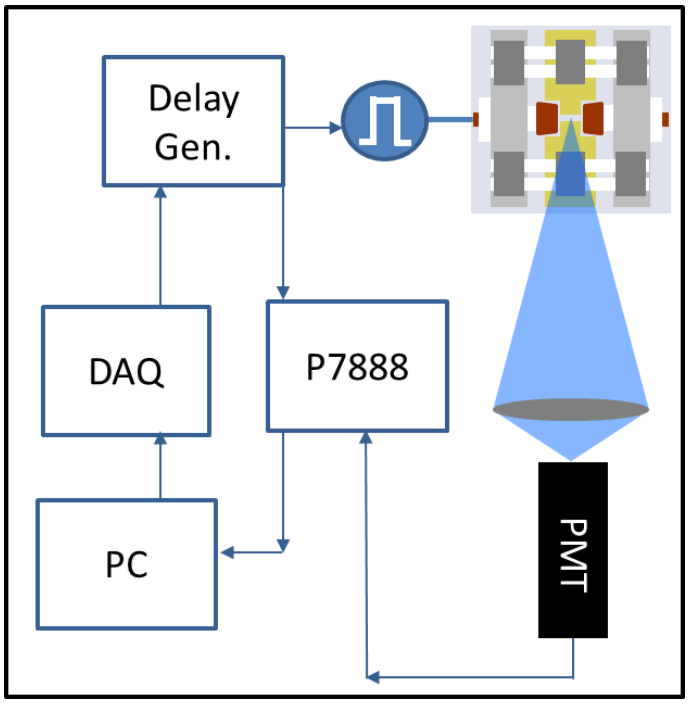

Figure 3.16: The crystal weighing setup.

instead. The square pulse contains a wide spectrum of frequencies which can interact with the ion. If the centre-of-mass (COM) mode frequency of the ion crystal is within this packet, the secular motion is excited. The frequency of the COM mode can then be measured using Doppler velocimetry. This is known as a crystal weighing technique [19]. The measurement of the frequency relies on the laser used having some component aligned parallel to the motion of the ions. Other important parameters for this are the detuning and power of the cooling laser.

The fluorescence detected on the PMT will be modulated at the secular frequency of the ion. To extract the motional spectrum, the arrival times of the photons at the PMT are binned in a histogram. Similarly to the technique used for micromotion minimisation, the binned times are correlated to the excitation pulse. After this has been performed, a fast-Fourier transform (FFT) is used to extract the motional spectrum and the COM mode frequency of the ion crystal is determined. In the axial direction, confinements are typically at hundreds of kHz. Measurements for a range of voltages applied onto the endcap electrodes were taken, ranging from around 100 V to 600 V, fig. 3.17.

For exciting the secular motion in the radial direction, the first method is applied. Rf frequencies are applied to one of the endcaps, although for confinement in the radial direction the frequencies are now on the order of MHz. The ions are imaged on the CCD and the frequency scanned until the ions become hot. The expected linear relationship

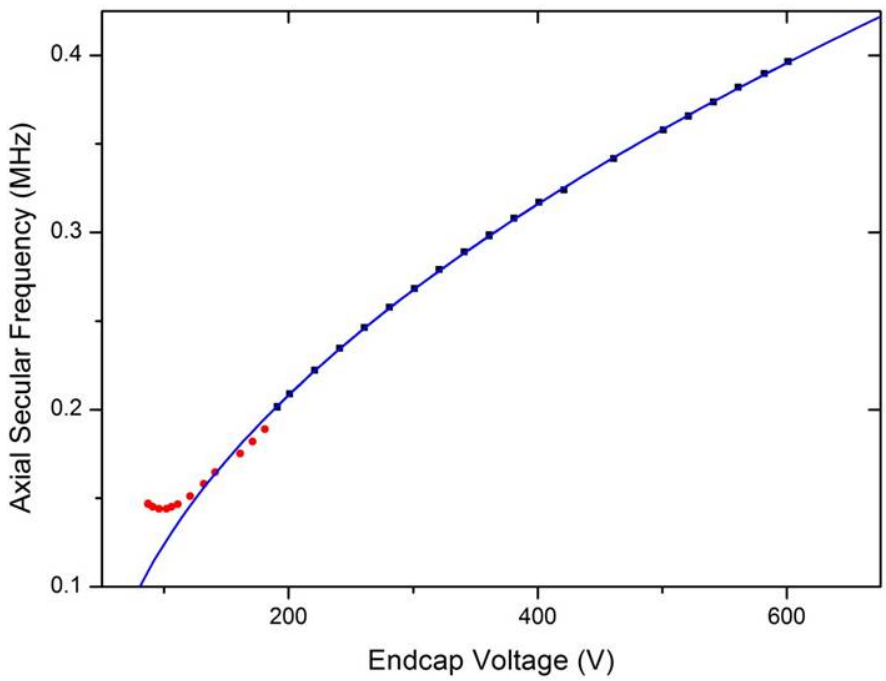

Figure 3.17: The axial secular frequencies for endcap voltages applied. The fit (to the black points) shows that the square of the secular frequency is proportional to the applied voltage, as expected.

between the radial secular frequency and the voltage applied was obtained (fig. 3.18).

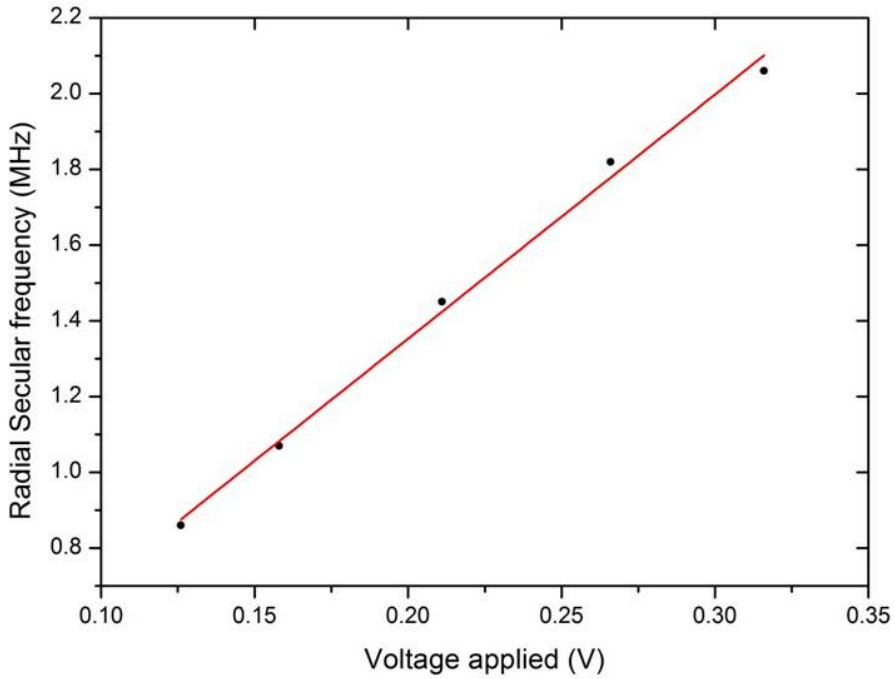

Figure 3.18: The radial secular frequency is proportional to the rf voltage applied.

Chapter 4

Spectroscopy on a dipole allowed transition in $^{40}Ca^{+}$

Stabilisation of the Doppler cooling laser used for $^{40}Ca^{+}$ is of particular importance for the non-destructive state detection technique for N_2^+ which is proposed in this thesis. Due to the strong dependence of the state readout scheme on the radiation pressure force on the dual-species ion crystal, the laser used for cooling must have good power and frequency stability. By rapidly performing spectroscopy on the cooling transition in a separate ion trap system, feedback can be provided to stabilise the frequency of the laser for the main experiment.

In general, determination of the lineshape and the position of linecentre for dipole-allowed transitions is an important tool for trapped-ion experiments. Measurement of the transition lineshape gives rise to precise determination of the central frequency, and also provides information as to where the ideal detuning for Doppler cooling sits. Analysis of the lineshape can reveal sources of broadening, and can be decomposed into Lorentzian and Gaussian contributions. For example, the degree of power broadening and also the temperature of the ion can be determined. This can be used to check if there is any excess heating in the trap [75; 76] (for example, from excess micromotion). A precise measurement of the lineshape of the $4S_{1/2} \rightarrow 4P_{1/2}$ transition in Calcium is also particularly useful for experiments where the levels of radiation pressure are critically tuned - for example the experiments described in chapter 7 in this thesis.

While high resolution spectroscopy on forbidden transitions has been very successful [8; 9; 77; 78], spectroscopy of transitions with high scattering rates is particularly challenging, as scanning the frequency across the line strongly affects the cooling dynamics of the ion. For instance, probing some regions of the line will actively heat the ion. This can not only

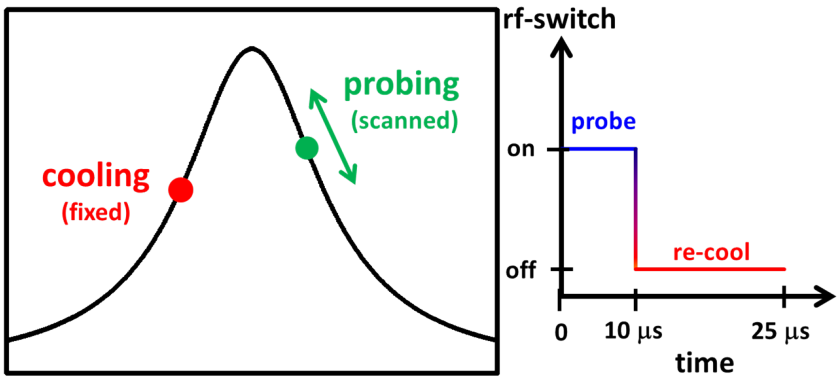

Figure 4.1: The switching scheme between probing and cooling. In this example, the probing time is on for 10 μs and is followed by 15 μs of cooling. After some designated amount of time, the probe is stepped to the next detuning. This is repeated until a full spectrum is taken.

cause possible ion loss, but also a complete alteration of the lineshape found - preventing the determination of a symmetric lineshape.

There have been a few different approaches to this problem, for instance Wan *et. al.*. have recently devised a scheme to transfer the scattering rate of a spectroscopy ion to a co-trapped readout ion to measure the full, undisturbed spectrum of a single ^{40}Ca-ion [79]. Other approaches include using single-photon scattering [80; 81], using separate probe and cooling lasers [82; 83], or scanning over the resonance to produce a half-Lorentzian lineshape [84].

4.1 Measurement Principle

The standard procedure for determining the central frequency of a transition is to scan the frequency of a probe laser, and collect the fluorescence from the ion. There are some problems associated with this, the most notable effect seen being a sharp drop in fluorescence when the frequency is near linecentre. This is due to the changing cooling dynamics. With the optimum cooling being at the steepest slope, the system starts off being inefficiently cooled, as the laser is far red-detuned. As the laser is scanned the cooling efficiency reaches the optimum - and swiftly after this point there is a rapid drop from efficient cooling to heating of the ion. In order to prevent this it is necessary to cool the ion and probe the transition simultaneously.

The principle behind improving on the spectroscopy technique is similar to that of Wolf *et. al.*, where two cooling lasers are used; one is left cooling the ions, while the frequency of a probe laser is scanned across resonance [28]. The fluorescence is collected and a Voigt (or Lorentzian) profile can be fit.

In the scheme demonstrated here, a single laser is used for both the probing and cooling. Fast switching between these two modes enables determination of the lineshape for the transition in a short amount of time. The PMT used for fluorescence collection is gated so that fluorescence is only collected during the probing part of the sequence. Figure 4.1 demonstrates the pulse sequence. The cooling pulse that follows the probe pulse is held at the same frequency, whereas the probe is scanned across resonance.

Figure 4.2 shows a comparison of the results of the two techniques to demonstrate this improvement - in both the frequency has been scanned from negative to positive detuning. The red squares demonstrate the standard way of scanning across the transition. Just before linecentre the fluorescence starts to drop off very slightly, indicating the decrease in cooling efficiency. Eventually cooling turns to heating and the fluorescence count drops down to background for the rest of the scan. In comparison is the result after introducing cooling periods during the spectroscopy scan (blue circles). There is very little distortion to the full scan, and results in a symmetric Lorentzian line.

This scheme can be extended to include a second probe interval, during which the frequency is slightly detuned from the first probe frequency. Thus the ion's fluorescence is probed at two laser detunings in quick succession by consecutive probe pulses interrupted only by a short cooling interval. Subtracting the fluorescence rates during both probe intervals results in a dispersion-like signal for the ion's transition. This scheme is robust against drifts of the laser power and directly provides an error signal to precisely determine the line centre of the transition and stabilise the probe laser.

4.2 Experimental setup

The scheme uses a double-pass AOM setup for scanning the frequency and cooling the ion, and is shown in fig. 4.3. Two voltage controlled oscillators (VCOs) drive the AOM, and are used to control the frequency shifts required and also the amplitude of the output. Analogue outputs from the data acquisition device (DAQ)[1] are used for computer control of the VCOs. An rf switch is used to quickly alternate between the two VCOs, the timing

[1]National Instruments USB-6009

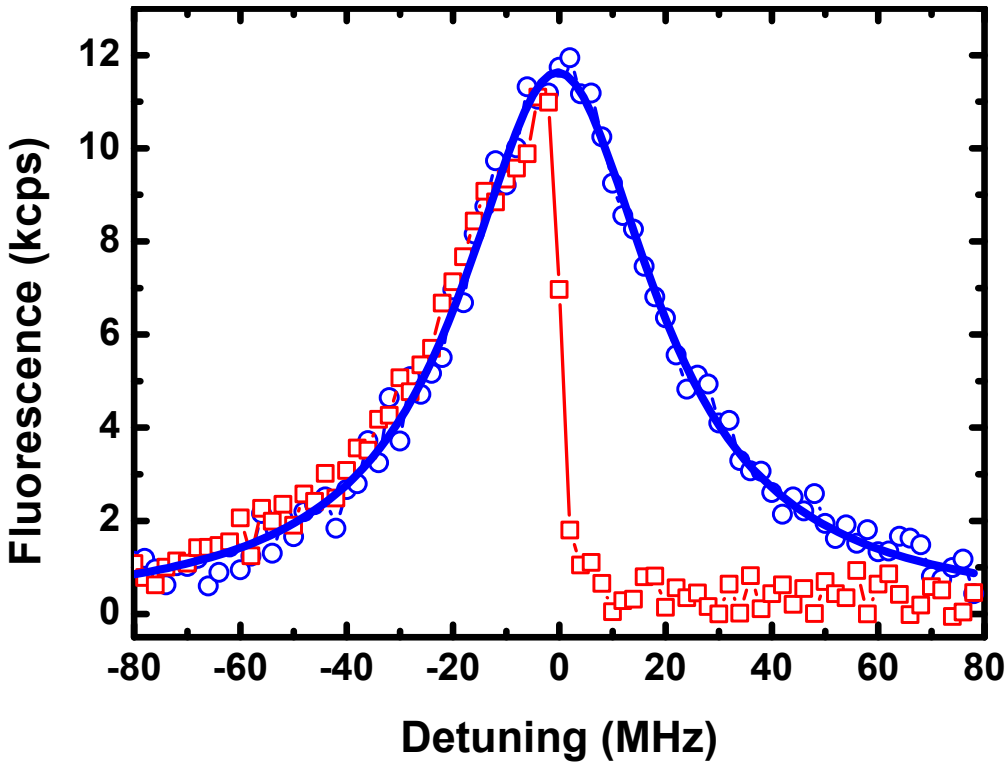

Figure 4.2: Spectrum of the $S_{1/2} \rightarrow P_{1/2}$ transition in calcium. The spectrum obtained by scanning the spectroscopy laser without additional cooling intervals (red open squares) shows a sharp drop close to the linecentre. Employing additional cooling intervals results in a full, undistorted spectral line (blue open circles). A Voigt profile is fit to the undistorted spectrum (blue line).

of which is controlled by a delay generator[2]. Photons are counted with a photomultiplier tube (PMT), and the signal is recorded with another DAQ[3]. The rf switch and the PMT counts are gated by the same delay generator output so that only counts from the probing part of the sequence are recorded.

A second rf switch and third VCO may also be added to this setup in order to provide a second probe section in the pulse sequence. This can be used to give a dispersion-like signal as demonstrated in sec. 4.4.

4.2.1 VCO calibration

The cooling VCO needs to be kept at a constant frequency and amplitude that is suitable for cooling efficiently for the duration of the scan. The probe VCO is scanned over a range typically of around 160 MHz in order to get the full lineshape. As scanning the

[2]SRS DG645

[3]National Instruments SCB-68

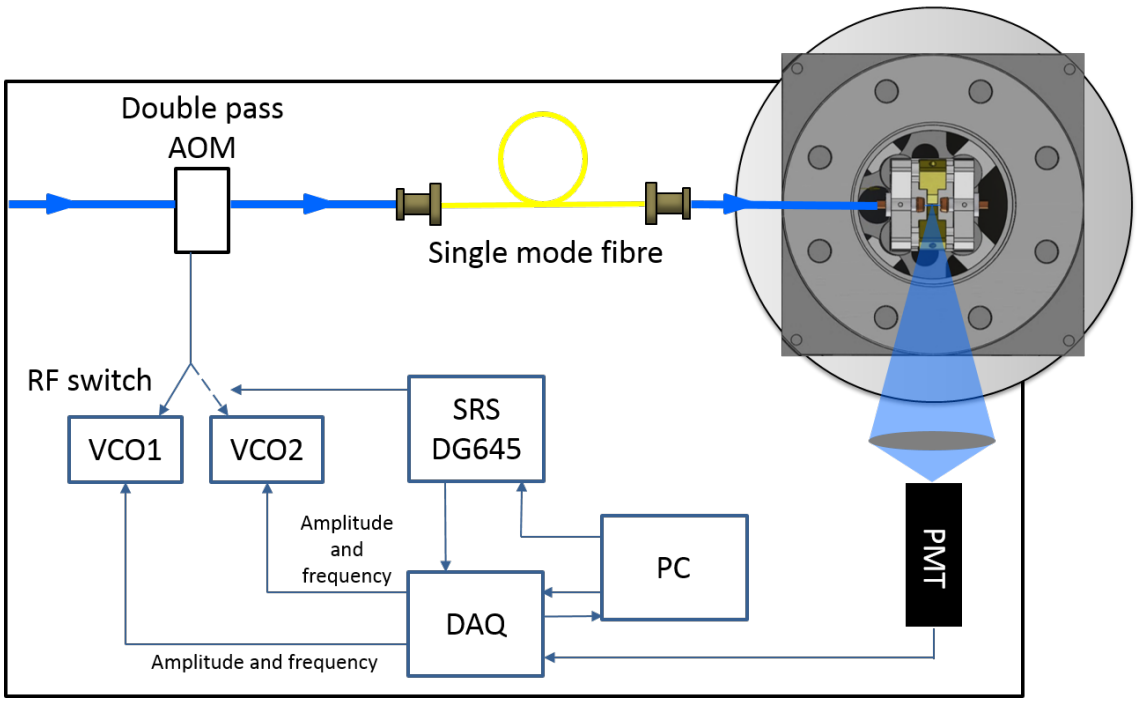

Figure 4.3: Experimental setup for spectroscopy on $^{40}Ca^{+}$. Two VCOs for driving the AOM are rapidly switched between using an rf-switch in order to provide the cooling and probing sequence illustrated in fig. 4.1. A computer controlled delay generator (SRS DG645) triggers the rf-switching and also gates the photon counts from the PMT, so that data is only collected during the probe time.

frequency of the VCO also changes the amplitude, it is important to compensate for this by simultaneously scanning the amplitude input of the VCO with the frequency.

Figure. 4.4 shows what happens to the background fluorescence as the frequency of the probe VCO is scanned. If the change in power is not corrected for during scanning, different parts of the lineshape would be probed by a different power, leading to a deformed lineshape. In order to calibrate for this, the frequency is stepped over the necessary range, and for each step the laser power is measured. For each point in the scan, a linear interpolation is fit to a small region, and the necessary voltage amplitude required to correct for the change in power is found.

A calibration file is generated as a result of this procedure. Figure 4.5(a) shows an example of a typical calibration file. This can now be tested by making a frequency scan with no ions in the trap and watching the background laser scatter - the same as fig. 4.4, but this time using the calibration file to compensate the amplitude on the VCO. Figure 4.5(b) now shows the resulting background when the frequency is scanned at the same time as the amplitude.

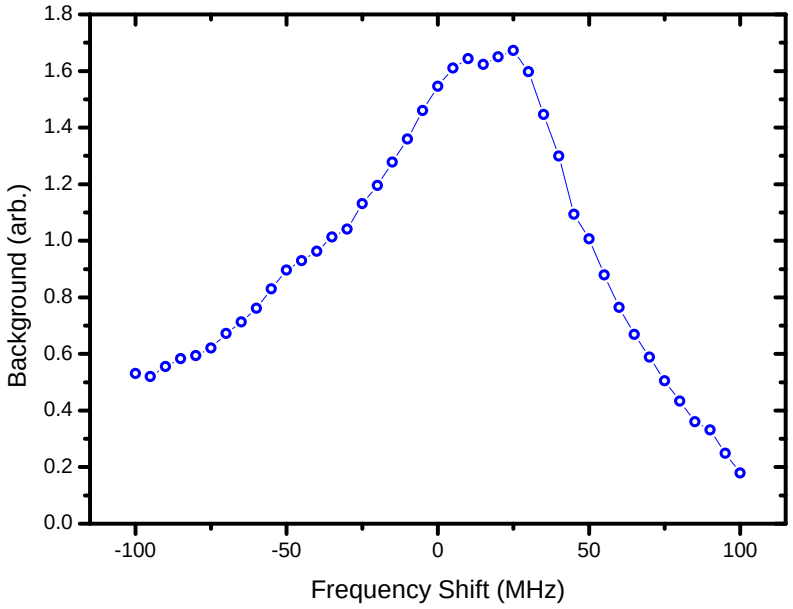

Figure 4.4: Scanning the frequency of the VCO also changes the power of the laser. The calibration process corrects for this, avoiding a distorted lineshape.

4.3 Characterisation

The most important parameter for determining a non-distorted lineshape is the duty ratio (probe time/period). This is the ratio of probe time to cooling time during the pulse sequence. A well-cooled, highly localised ion is required to get a narrow, symmetric lineshape.

First of all the cooling pulse that directly follows each probe pulse can be considered. This needs to be long enough so that all of the thermal energy that the ion gains through the probe pulse duration is taken away during the cooling time. If the ion is not completely re-cooled during this time, the excess energy is carried through to the next probe point in the sequence. This can result in a build-up of energy, so that there is a heating effect throughout the whole scan. This would be enough to distort the lineshape and needs to be avoided. Additionally, the probe pulse length must be sufficiently short to reduce the heating of the ion during the probe time.

In order to determine a suitable duty ratio, the timings are varied, and the asymmetry is measured by using the coefficient of determination R^2 of the Lorentzian fit to the resulting line. For a spectrum with N measured fluorescence values $y_i(x_i)$ at frequency x_i, the coefficient if defined as:

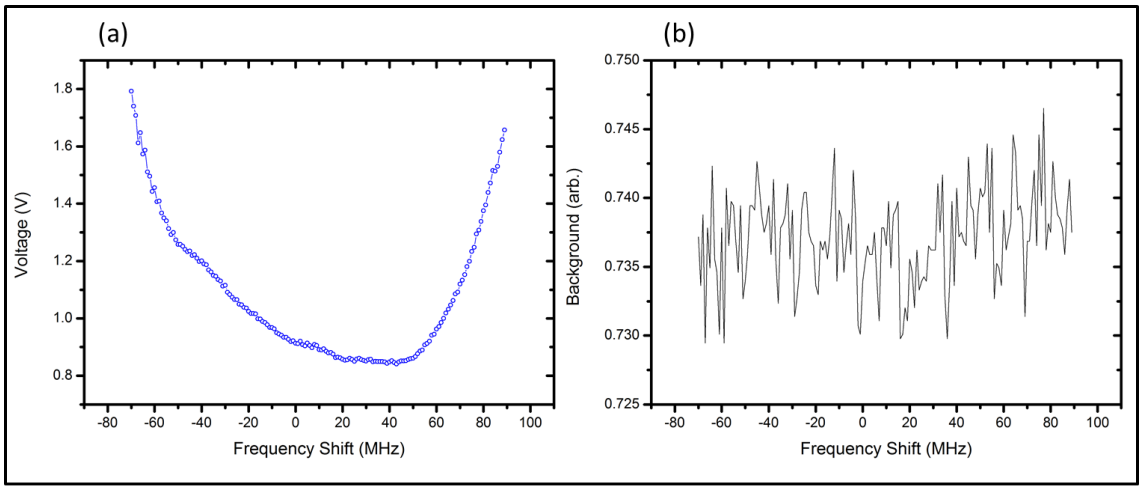

Figure 4.5: (a) The calibration file used to correct for the change in laser power when the VCO frequency is scanned - as seen in fig. 4.4. (b) A frequency scan when the calibration file is used.

$$R^2 = 1 - \frac{\sum_{i=0}^{N} \{y_i(x_i) - f(x_i)\}^2}{\sum_{i=0}^{N} \{y_i(x_i) - \bar{y}\}}, \tag{4.1}$$

where the fitting function is $f(x_i)$ and $\bar{y}$ is the mean value of the data points. As the fit residuals approach zero, R^2 approaches 1.

Figure 4.6 shows the value of R^2 as the probe and cooling timings are varied. The data shown in 4.6(a) and 4.6(b) are the same set, but are displayed differently in order to demonstrate how R^2 varies with probe duration and duty ratio.

In fig. 4.6(a), it is clear to see that at longer probe durations, the coefficient of determination starts to decrease. How quickly this drops off is dependent on the repetition rate used. For the slower 5 kHz rate, R^2 comes down very slowly, whereas for the highest repetition rate of 40 kHz, a dramatic drop off is seen at fairly low probe durations. This effect can be attributed to a build-up of heating during the frequency scan. For the low repetition rates, the cooling time is still long enough even for fairly high probe times of 40 μs, although this is not true for higher probe times. At the higher probe times, there is a heating effect during the probe section itself, and so even if the cooling time is long enough to re-cool, the spectrum becomes deformed due to the large heating build-up during the probe pulse.

This effect is also clearly observed in fig. 4.6(b). For the same duty ratio of 0.2, there is already quite a large difference in R^2 between the 5 kHz and 40 kHz cases. In this case,

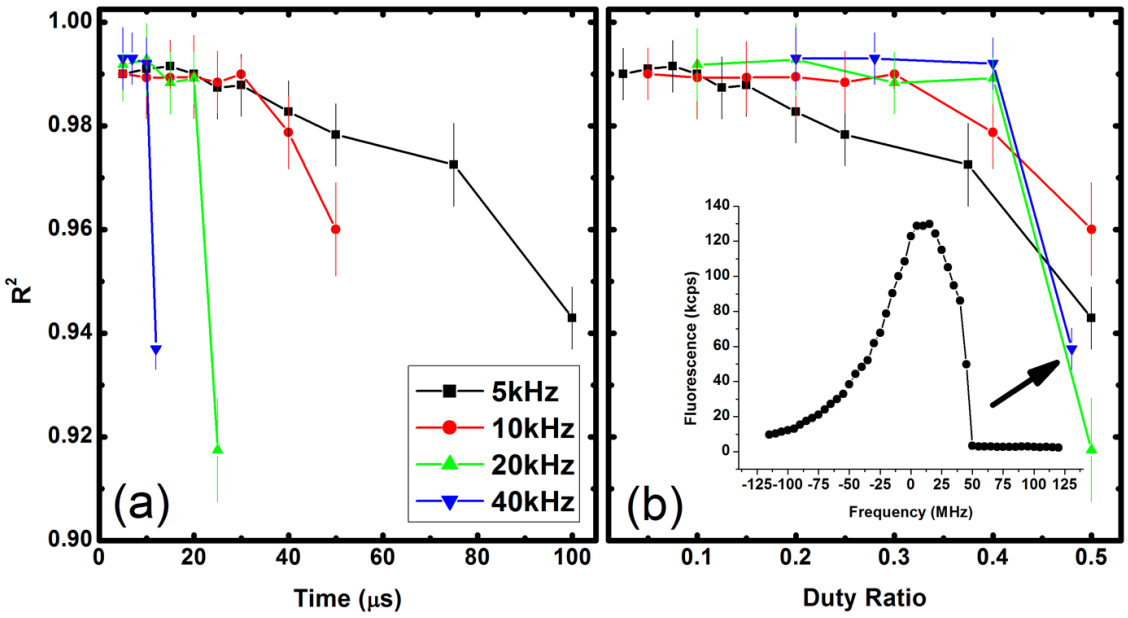

Figure 4.6: (a) R^2 as a function of probe time for a range of pulse sequence repetition rates. For repetition rates of 20 and 40 kHz the value of R^2 drops sharply at small probe times. For repetition rates of 5 and 10 kHz R^2 begins to decrease when the probe time exceeds 35(5) μs. (b) R^2 as a function of duty ratio. As the repetition rate is reduced, a smaller duty ratio is required to sufficiently re-cool the ion. *Inset:* an example of distortion of the line shape.

the higher repetition rate has a better coefficient, which is due to the fact that although the probe/cooling ratio is the same, the actual probe duration is larger for a rate of 5 kHz.

4.4 Dispersive signal

A third VCO is added to the set-up to measure a dispersion-like signal. The same cooling/probing sequence is used but now the probe laser is switched between two frequencies by an additional rf-switch. Two independent fluorescence counters are used to measure the fluorescence rate during both probe intervals separately and the resulting rates are subtracted. The parameters of the sequence are the same as for the previous measurement. After collecting a data point, the probe frequencies are changed synchronously and the process is repeated until the entire fluorescence profile has been measured. Figure 4.7 shows a 5 MHz resolution spectrum. The top graph shows the fluorescence spectrum measured simultaneously with the dispersion-like signal. The bottom graph shows the dispersion-like signal with its characteristic zero crossing at the resonance frequency. A single calcium ion is probed over a 120 MHz range by a scan with a total run-time of 40

s with a laser power of 6(2) μW in each laser beam.

The measured Lorentzian linewidth of 29.6 MHz is in good agreement with the expected saturation broadening. Other contributions to the line broadening are expected to be significantly smaller than the power broadening. A detailed discussion of line broadening and systematic shifts is presented in the last section.

By probing two parts of the transition simultaneously in this manner, it is possible to measure the position of the line centre constantly over time. This method is robust against fluctuations in laser power and can be used to stabilise the frequency of the 397 nm laser (sec. 4.5).

4.5 Lock stability

In order to determine the long-term stability of the spectroscopy signal, two independent ion trap systems are employed. The first system is employed to generate a dispersion-like signal by measuring the transition at two frequencies equally detuned either side of line centre. This signal is used to stabilise the spectroscopy laser. To maintain low ion temperature, the red detuned laser is applied for 175 μs while the blue probe laser is applied only for 25 μs. This sequence is repeated with a frequency of 5 kHz. By feeding back the error signal to the laser through digital PID control, the laser is stabilised to the atomic resonance. The feedback bandwidth is a compromise between the statistical fluctuation of the measured count rate and the drift of the free running laser. We have determined the optimal interrogation time to be 300 ms. The laser is stabilised to the line centre of the transition.

To measure the absolute frequency stability of the system we performed a long-term spectroscopic measurement in an independent ion trap with the stabilised 397 nm laser. The $4S_{1/2} \rightarrow 4P_{1/2}$ transition is probed by the same method as used in the first trap. The dispersion-like error signal generated is employed to measure any changes in the laser detuning with respect to the ion's resonance. The two identical traps are about 5 m apart on separate benches and both systems have independent control systems for the spectroscopy laser beams.

Figure 4.8 shows the Allan variance for the spectroscopy signal. The Allan variance gives a measure of how stable the frequency of an oscillator is, and is the time average of how much the frequency has deviated from the set point. The value of the Allan variance depends on the sample time τ, and so gives a measure of the performance of the oscillator over different time domains. In order to get fig. 4.8 the error signal generated from probing

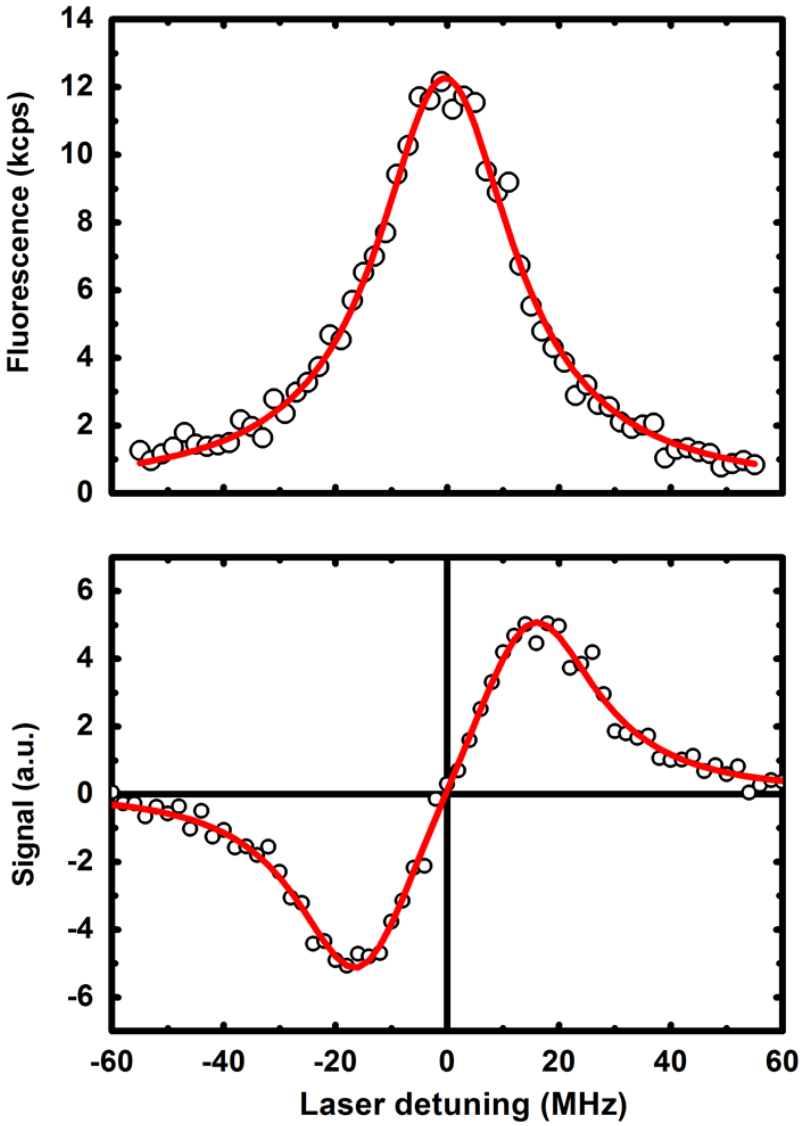

Figure 4.7: Spectrum of the $S_{1/2} \rightarrow P_{1/2}$ transition in calcium (top). Over the same range, two probes are used to obtain a dispersion-like signal (bottom). For this 5 MHz resolution scan, the two probes are set at 30 MHz apart. Subtracting the fluorescence count for one of the probes from the other generates the dispersion-like signal.

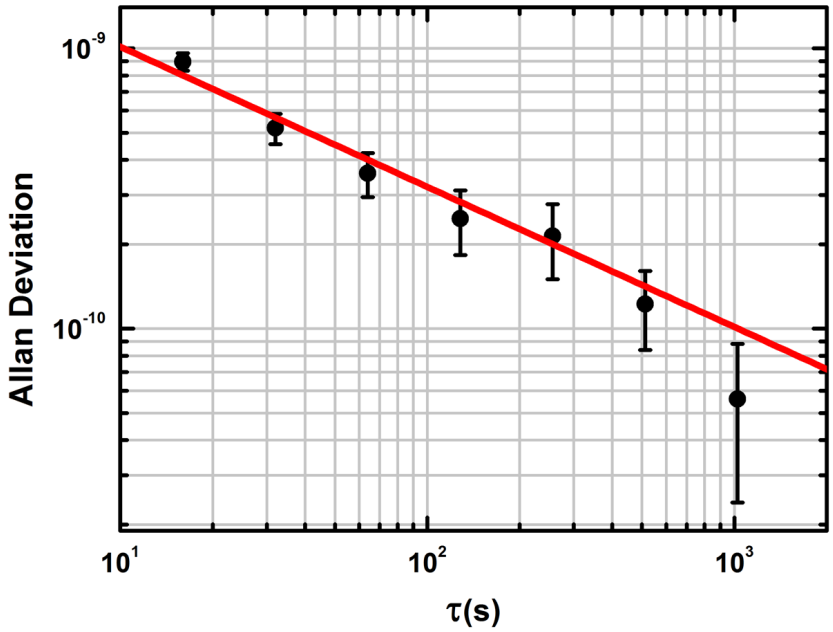

Figure 4.8: Measurement of the Allan variance of the spectroscopy signal of a single trapped calcium ion.

the $4S_{1/2} \rightarrow 4P_{1/2}$ transition was recorded for a long duration. This data could then be sampled over different time periods τ, up to a maximum of 10^3 s. From a linear fit to the data in fig. 4.8 we obtain an instability of our spectroscopy signal of $\sigma(\tau) = 3.5 \cdot 10^{-9}\sqrt{s/\tau}$, and thus a statistical frequency uncertainty of $1 \cdot 10^{-10}$ within 1000 s. This is in keeping with the recent work by Wan *et al.*, who obtained an instability of $\sigma(\tau) = 5.1 \cdot 10^{-9}\sqrt{s/\tau}$ for the same calcium transition [79].

The systematic shift of the transition frequency is governed by the Zeeman shift (<450(10) kHz) and the ac Stark shift of the $P_{1/2}$ level due to the repump lasers (45(5) kHz), while other shifts arising from the line shape and experimental controls are below 10 kHz. Utilising only linearly polarised laser light for cooling and re-pumping, Zeeman splitting should only contribute to the line broadening rather than the systematic level shift. Thus, we expect the line shift to be significantly smaller than the Zeeman splitting of <450(10) kHz. To determine the systematic shift due to the experiment control, we carefully measured the timings of the electronic pulses and determined the response of the laser modulators. Due to the short response times and comparable long probe times, these effects are estimated to be below 10 kHz. For shorter probe times the contribution of these shifts to the error budget increases. Therefore, the optimal probe time is a compromise between systematic shifts due to the experiment control and the shift of the line due to heating induced asymmetry of the line shape. Furthermore, the total interrogation time

to obtain a sufficient signal-to-noise ratio and the intrinsic stability of the laser are also important factors to determine the optimal settings. In our system, a probe time of 25 μs at a repetition rate of 5 kHz has been found to be optimal.

Chapter 5

Ionisation spectroscopy on the $a^1\Pi_g(\nu = 10) \longleftarrow X^1\Sigma_g^+(\nu = 0)$ band of N_2

For both the non-destructive state detection scheme, and the high precision vibrational spectroscopy in nitrogen ions, it is important that the required state can be prepared efficiently. A suitable ionisation scheme has to be implemented before this. A 2+1 resonance enhanced multi-photon ionisation (REMPI) scheme can be used. A separate ionisation spectroscopy experiment has been set up to investigate the transition required.

5.1 2+1 Single-colour resonance enhanced multi-photon ionisation (REMPI) of molecular nitrogen

The scheme for ionising N_2 so that it is prepared in the $X^2\Sigma_g^+(N = 0, \nu = 0)$ is a resonant process that uses two photons to initially excite the molecule, and then a third that ionises it. In this particular case, a single laser is used for both the excitation and the ionisation. The excitation uses the transition $a^1\Pi_g(\nu = 10) \longleftarrow X^1\Sigma_g^+(\nu = 0)$, where the rotational branch of the transition has to be carefully chosen in order to fulfil the requirement of preparing in the ground rotational state. The full scheme is described in sec. 2.3.2, where there is more information on the requirements for the REMPI process.

5.2 Measurement principle

Time of flight mass spectrometers are devices used to determine the charge to mass ratio of ions, and so can be used to identify differing species in a sample. Electric fields are used to manipulate the trajectory of the ions so that the different species can be separated out in time according to mass. If the charge of the ions is assumed to be the same, then the kinetic energy gained for for each species is the same due to the applied field. However, the difference in mass means that the velocity distribution for each ion changes for the same field. Therefore, if the time it takes for all of the ions to take the path through the TOF spectrometer is recorded, the mass can be determined.

In general, there are three main regions used for this. There is an extraction region, where the path of the ions begin, an acceleration region, where the ions are accelerated for mass separation, and a field free drift tube zone. At the end of this there is a detector. Each of these regions have a different potential gradient. Interference between the well-defined regions is significantly reduced by introducing meshes for shielding. These meshes are also held at potentials to form the electric fields, while at the same time allowing ions to pass through to the next zone.

For extraction, a potential difference is applied so that the ions are guided in the correct direction. After this the acceleration region is entered: in this part, lighter ions will be accelerated at a faster rate than the heavier ions, and so the differing masses begin to be separated out. This means that upon entering the field-free region, the heavy ions have a smaller velocity than the light ions. Therefore, as the drift tube is traversed, the distance in time between differing masses becomes larger. Once the ions reach the detector, there should be well defined arrival times for each mass, so that different species can be resolved.

For the case of this experiment, neutral N_2 enters the mass spectrometer at the extraction region. The laser for the 2+1 REMPI scheme is overlapped with the stream of N_2 so that ions are created within the centre of the extraction region. Figure 5.1 shows the gradient of the potential throughout the spectrometer, simulated using COMSOL[1], for two different ranges. Each of the regions are separated by meshes.

The extraction and acceleration regions have a steep potential gradient across them, as shown in fig. 5.1(A). As soon as the ions are created, they follow this gradient, and are accelerated into the drift tube, where there is no field. Figure 5.1(B) demonstrates that there is an even steeper gradient between the final mesh and the detector which is held at a large negative potential with respect to the rest of the spectrometer.

[1]Simulation provided by Matthias Keller

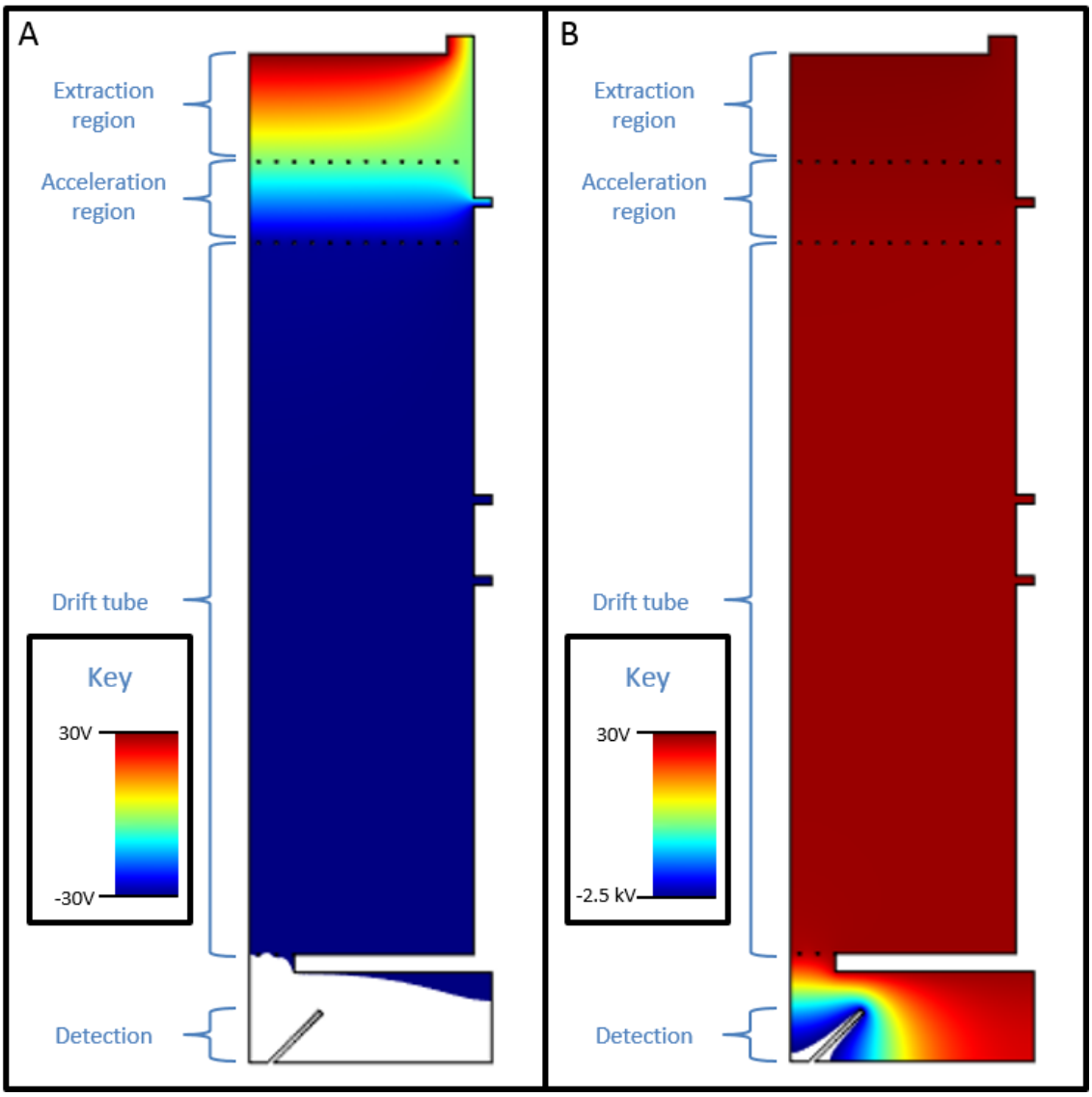

Figure 5.1: The electric field has been simulated using COMSOL for the extraction plate held at 30 V, the drift tube at -30 V, and the detector funnel at -2.6 kV. Two plots have been made for different voltage ranges. Each are 2D plots from the centre of the spectrometer to the outer edge. There are three meshes in each diagram, shown by the dotted lines. (A) is the electric field plotted for a colour range of -30V to 30V to show the field through the whole TOF spectrometer. The fields are particularly strong across the extraction and acceleration regions where the ions are accelerated. Throughout the drift tube the potential gradient is zero to allow for mass separation. (B) gives the field plotted for 30 V to -2.5 kV, so that the field lines can now be seen around the detector funnel. There is a very steep gradient between the final mesh that the ions pass through and the funnel.

5.3 Experimental Setup

The whole ionisation spectroscopy setup is housed in a vacuum chamber with flanges for high voltage feed-throughs, gas inlet, and viewports for laser access. Figure 5.2 shows a cut-through drawing of the ion detection setup. The gas inlet and optical access for the laser run perpendicular to each other, crossing in the centre of the extraction region. The trajectory of the neutral molecules is shown as a red arrow passing through the extraction region, with the blue arrow being the ionisation laser that meets the molecules in the centre. Directly beneath this is an extraction plate, which is held at a positive voltage V_{Ex} and is used to extract the ions created up into the acceleration region. A close-up diagram of the detection system is shown in fig. 5.3. The extraction plate is glued to an insulating ring, which in turn is glued to the extraction 'box', onto which a separate voltage V_{Box} can be applied for acceleration. At the top of the extraction box is a mesh which is held at the same voltage V_{Box}, and defines the boundary between the extraction and acceleration regions, at the same time allowing ions to pass through. A second mesh which is at the same voltage as the drift tube V_{DT} is positioned at the end of the acceleration region. After this, the ions pass into the field-free drift tube.

At the end of the drift tube is the detector, a spiral shaped channel electron multiplier (channeltron), shown in fig. 5.3. The ions are collected in the channeltron funnel which is held at a large negative voltage with respect to its output, in order to generate a current. Because of this, two more meshes are required. One of them sits at the end of the drift tube, and is held at V_{DT}. The final mesh is placed between the drift tube and the channeltron funnel, and is held at V_{CH}. This is so the channeltron funnel is shielded from the drift tube region. Without this, there is a risk that the secondary electrons induced by the incoming ions are drawn back up into the drift tube, instead of contributing to the current output for detection.

The drift tube/extraction box/extraction plate assembly is mounted on a PEEK piece (coloured in white in fig. 5.3) that houses the channeltron. The entire assembly is then mounted onto a CF100 flange which sits on top of a five-way cross. On this flange a CF40 tube is welded to allow for a feedthrough flange with 7 high-voltage feedthroughs, five of which are used for this setup. Connections for the extractor plate, extractor box, drift tube, channeltron funnel and the channeltron output are made by spot-welds with tantulum wire, and using the connections already provided by the channeltron funnel and output. The tantalum wire is then connected to the feed-throughs using barrel connectors.

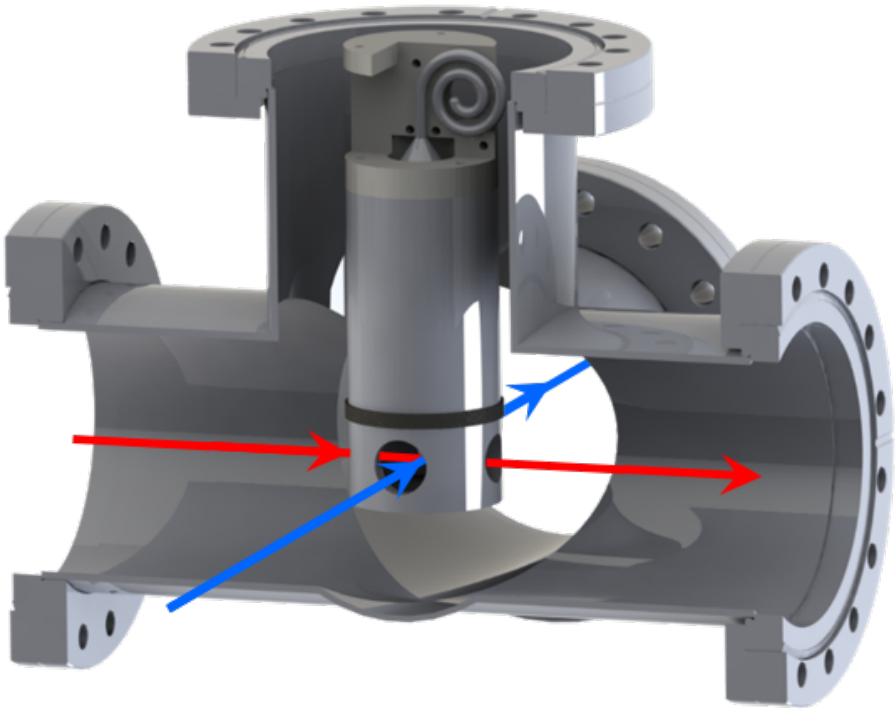

Figure 5.2: Solidworks drawing showing the vacuum setup used for the ionisation spectroscopy experiment. A stream of nitrogen is leaked in from a Swagelock $\longrightarrow$ CF adaptor that is mounted on the flange on the left (not pictured), and is shown as a red arrow. The molecules meet a laser beam, shown as a blue arrow, in the centre of the cylindrical detector. This is mounted on the top flange (not pictured). Optical access for the laser is achieved with viewports that are anti-reflection coated for UV.

The laser used for ionisation is a frequency doubled pulsed dye laser[2] pumped by a frequency tripled Nd:YAG laser[3]. The typical energy per pulse is 2 mJ at a wavelength of 237 nm, with a repetition rate of up to 10 Hz and a pulse length of 9 ns.

5.3.1 Electronics for signal extraction

A current spike is output from the channeltron when a burst of ions hit the funnel. It is this output that is used as the TOF signal. The current is converted to a voltage, which is then amplified.

A fast transimpedence amplifier was used for both amplification and conversion to a voltage. This could then be measured with an oscilloscope. The time-of-flight of the ions collected is then visible, and the region of interest (the nitrogen ion signal) can be selected. The initial time of flight measurement is shown in fig. 5.5. A Labview routine was then

[2]Radiant dyes narrow scan

[3]Coherent

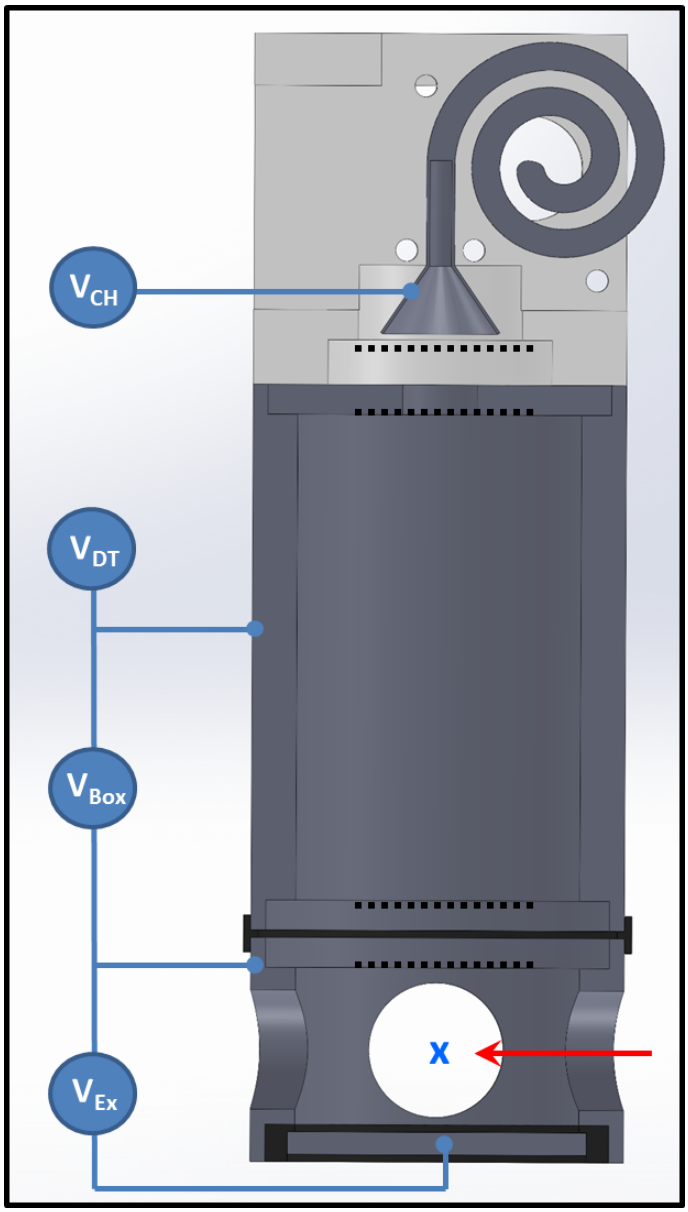

Figure 5.3: The detection setup. At the top is the channel electron multiplier for signal extraction. The funnel of this is held at a high negative voltage V_{CH}. N_2 is shown entering the extraction region as the red arrow, towards the blue cross that demonstrates where the laser passes through for ionisation. Ions are then created in the extraction region, where an extraction plate held at V_{Ex} repels ions up the drift tube (at voltage V_{DT}) towards the channeltron. The insulating parts are shown in black, with the PEEK mount for the channeltron in white. Four dotted lines show the positions of the meshes.

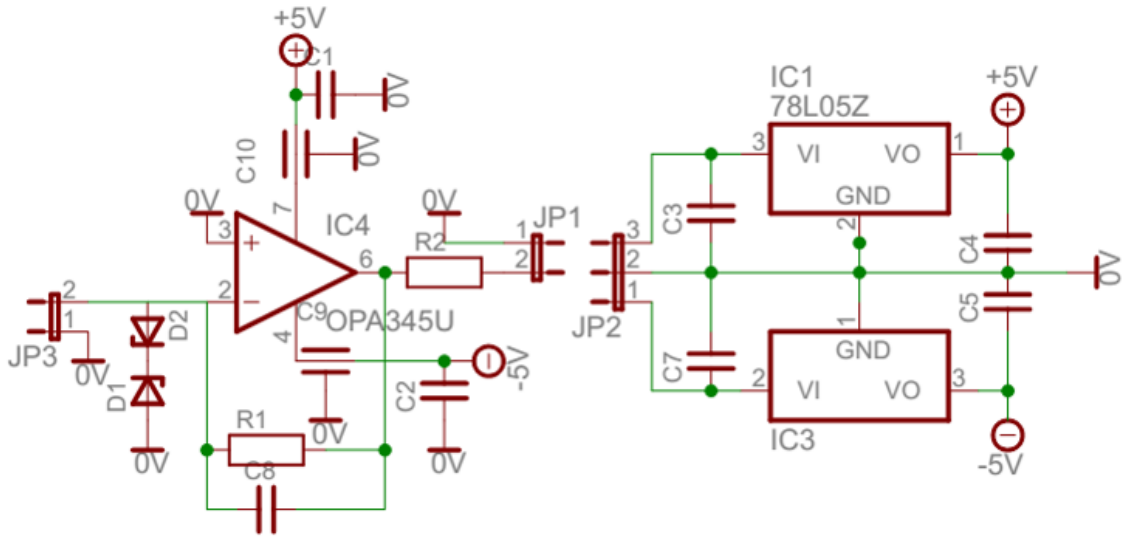

Figure 5.4: Circuitry used for amplifying the output of the channel electron multiplier and converting it into a voltage.

used to extract the amplitude of the nitrogen signal as the laser wavelength was scanned, producing a spectrum.

The electronics are shown in fig. 5.4, and are similar to photodiode circuitry. The current from the channeltron output enters the circuit at terminal JP3. The operational amplifier used is an OPA657, which is a fast high-gain amplifier. The most important components are labelled R1 and C8, which have values of 110 kΩ and 1 pF respectively. These components determine the speed of the amplifier, which therefore determine the resolution of detection. The selected values give a suitable resolution in the time-of-flight (TOF) measurements for the experiments carried out. Two Zener diodes, D1 and D2, are used to protect the operational amplifier from voltage spikes.

5.4 Time of flight spectroscopy

The time of flight spectrum is used to identify resonant N_2 ionisation through mass spectrometry. An example of the TOF signal is shown in fig. 5.5, which demonstrates a TOF spectrum with (blue) and without (black) a resonant ionisation peak. This peak only appears when the laser is tuned to certain wavelengths, in this case 474.155 nm. When detuned away from here (to 474.171 nm), this peak disappears, although the other peaks remain. This suggests that these other peaks are from ion creation via non-resonant processes, such as the creation of photo-electrons that are then accelerated in the electric fields.

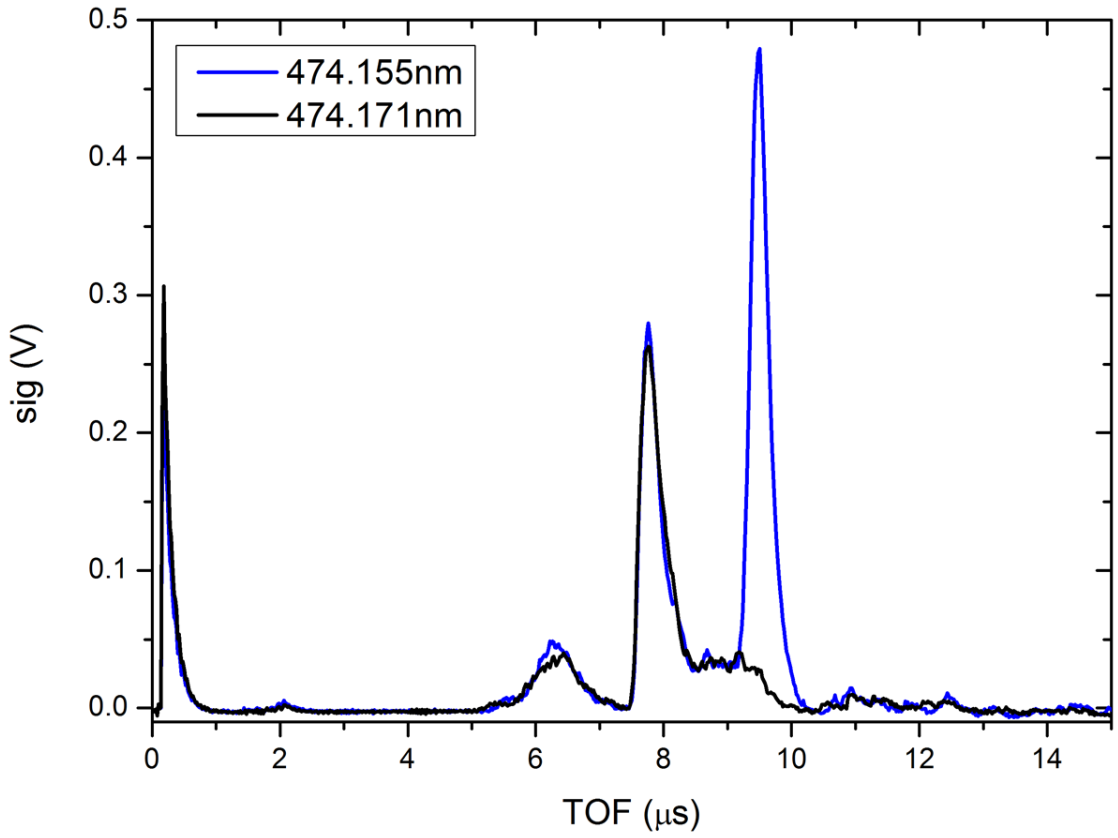

Figure 5.5: An example of what a typical time of flight looks like, for the laser tuned onto a transition (blue) and off a transition (black).

The arrival times of these peaks are dependent on the voltages that are applied to the extraction plate, chamber, and drift tube, and also the mass of the ion. In fig. 5.5, the laser has been positioned somewhere near the centre of the ionisation region, with the extraction chamber at 12 V and drift tube held at ground. The extraction plate was held at 28.4 V.

Aside from the main resonant N_2^+ signal in the TOF spectrum, there are a few other non-resonant peaks. As long as these are well separated from the N_2^+ peak they should not interfere with the ionisation spectroscopy experiment, although it is useful to know what their origin could be. By taking measurements at different settings, more information could be gained. For example, the arrival time of the resonant N_2^+ peak should have some dependence on the vertical position of the laser as it passes through the extraction region, as this will change the starting position of the ions. However, if the other peaks are caused by a different ionisation process, then this may not be the case. For instance, the high energy photons from dye laser scatter at 237 nm can liberate electrons from the stainless steel that the experimental setup is made from via the photoelectric effect. These

electrons can then be accelerated in the electric fields and ionise other species that may be contaminating the vacuum. As long as the laser does not start to actually clip the setup in some way, any peaks from this should arrive at the same time, even if the laser alignment is changed.

Figure. 5.5 shows an example TOF spectrum when the laser has been tuned to resonance. The resonant N_2^+ peak arrives just before 10 μs. The first peak in the spectrum in fig. 5.5 is a noise peak that always occurs just after t = 0 μs, regardless of the settings used. This is probably generated by the large field induced by the flash-lamp in the pump laser when it is triggered. The largest peak also always appears in the spectrum. When the laser position is scanned, it remains in the same position, and is also present when the laser is tuned off resonance, as seen in fig. 5.5. This is a peak that also grows larger as N_2 is leaked in. There are therefore a few suspects for this peak. It could be that it is simply H_2O from the atmosphere that enters the system along with the nitrogen stream. The mass of H_2O would just about match the arrival time from simulations. With a similar mass to this is nitrogen atoms. There are possible dissociative processes that can occur when using the 2+1 REMPI scheme [3]. Or it is possible that it is in fact N_2^+ that has been ionised with photoelectrons, but much closer to the detector than the resonant N_2^+, as they arrive faster.

5.4.1 Tuning the signal

Separate connections on the extraction plate, extraction box and drift tube allow for good control over the time of flight spectrum. In order to fully optimise the signal of interest, these three parameters were tuned. The main aim is, of course, to have as large a signal as possible - but another important consideration has been taken into account. This is the time of flight resolution - and overlapping signals have to be avoided. For instance, increasing the capacitor voltage leads to a larger signal - but also bunches together the times of arrival for different masses. So a compromise has to be struck between these two effects to maximise the signal, whilst keeping any background signal as low as possible.

In fig. 5.6, this bunching effect is demonstrated. For this measurement, the extraction box was held at a constant 8 V, while the drift tube was grounded. The lowest voltage applied to the extractor plate was 5 V (black), with the resonant nitrogen signal at around 16 μs. When compared to the highest voltage of 65 V (green), it is clear that the amplitude of the signal, which is now found just below 8 μs, has increased in height. As well as this, the peak has become more defined, with a much reduced width. The change in these

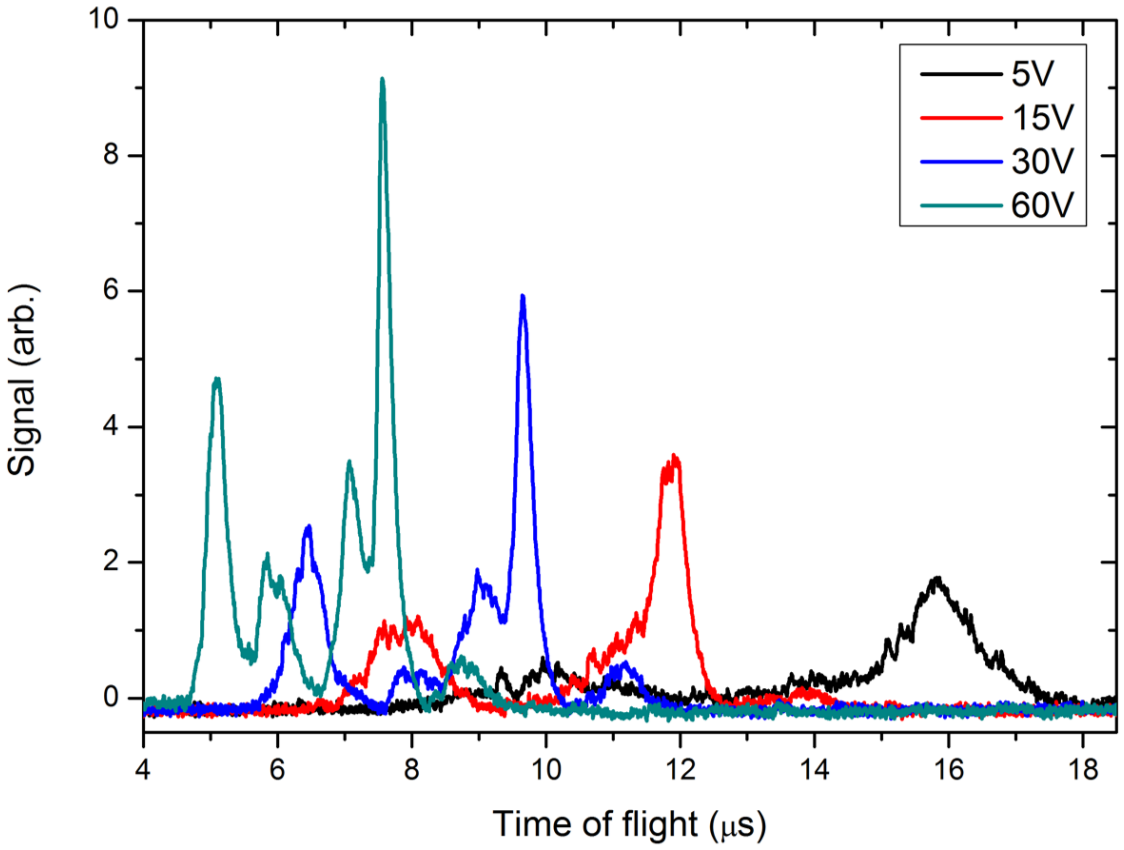

Figure 5.6: Demonstration of the signals bunching as well as an increase in signal height when the voltage on the extraction plate is increased. Four different voltages have been applied to the extraction plate, 5 V (black), 15 V (red), 30 V (blue) and 60 V (green), while the voltage on the box remains at a constant 8 V.

features is also confirmed when 15 V (red) and 30 V (blue) are applied to the extractor plate.

Figure 5.7 gives an example of how the TOF spectrum is affected when the voltage on the extraction box is increased from 1 V to 25 V, while the extraction plate is held at 65 V. Similarly to the extraction plate, an increasing voltage on the extractor box causes a bunching effect on the entire TOF signal, with an overall increase in height of the main signal of interest. For even the maximum voltages used in fig. 5.6 and fig. 5.7, the bunching does not appear to cause any more of an overlap than for the lower voltages used. Therefore, for the voltage range investigated the maximum voltages of $V_{Ex} = 65$ V and $V_{Box} = 25$ V would be suitable for extracting the resonant N_2 signal.

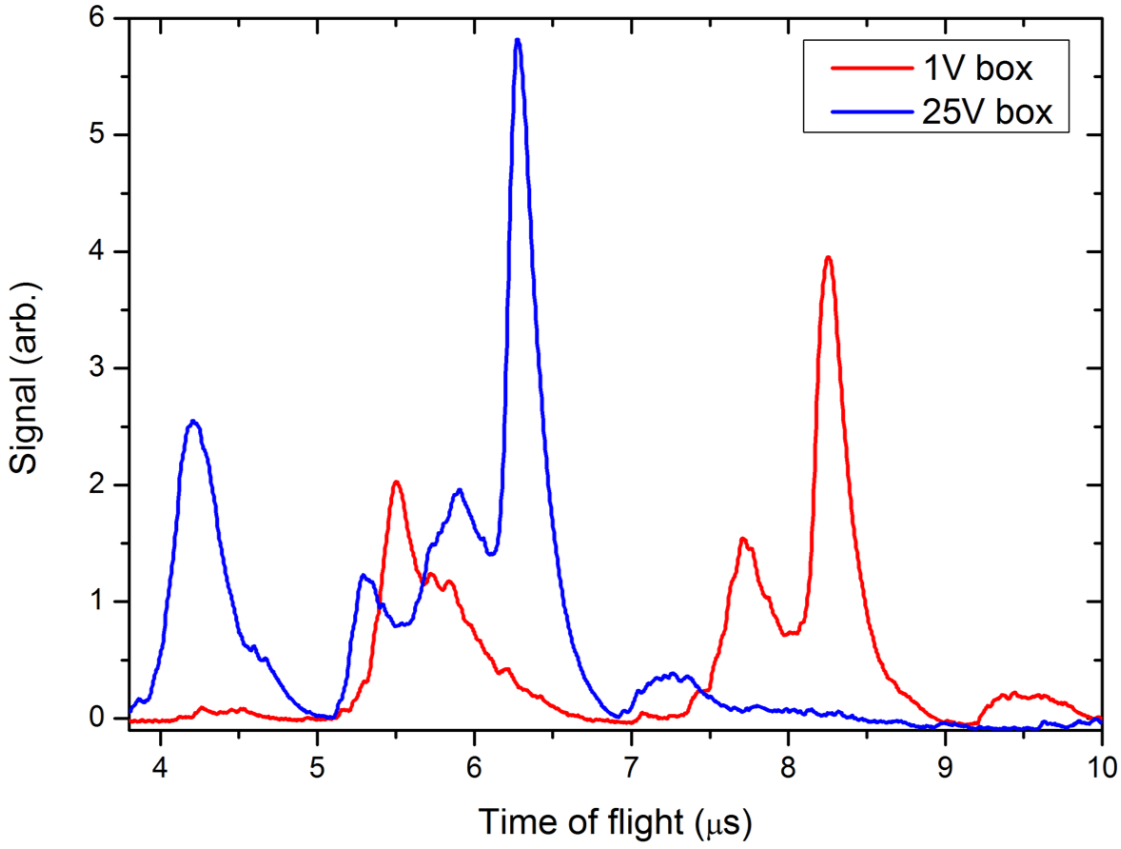

Figure 5.7: Similarly to the extraction plate, an increase in voltage applied means the whole TOF spectrum arrives earlier. The extraction plate has been held at 65 V while the box voltage was changed from 1 V (red) to 25 V (blue).

5.5 Spectrum of the $a^1\Pi_g \longleftarrow X^1\Sigma_g^+$ band of N_2

The precise transition wavelengths for the $a^1\Pi_g \longleftarrow X^1\Sigma_g^+$ band of N_2 were experimentally determined so that a suitable transition to prepare the nitrogen ions into the $X^2\Sigma_g^+(N = 0, \nu = 0)$ could be identified. For this, just the resonant ionisation peak for nitrogen in the TOF spectrum was considered. The resonant peak in the TOF spectrum was identified by tuning the laser through different wavelengths. This peak was then zoomed in on, so that it is the only part of the TOF signal taken into account to perform spectroscopy.

The dye laser was scanned from 474.236 nm to 473.974 nm in incremental steps of 0.001 nm. For each step in the scan, the wavelength was measured and the zoomed-in signal was integrated and summed over 600 shots (60 s @ 10 Hz).

The pulse energy of the dye laser was optimised at the start of the scan to ~ 2 mJ per pulse. However, when the frequency of the dye laser is scanned, the power starts reducing. In order to compensate for this, the scan was stopped every 0.05 nm and the power re-

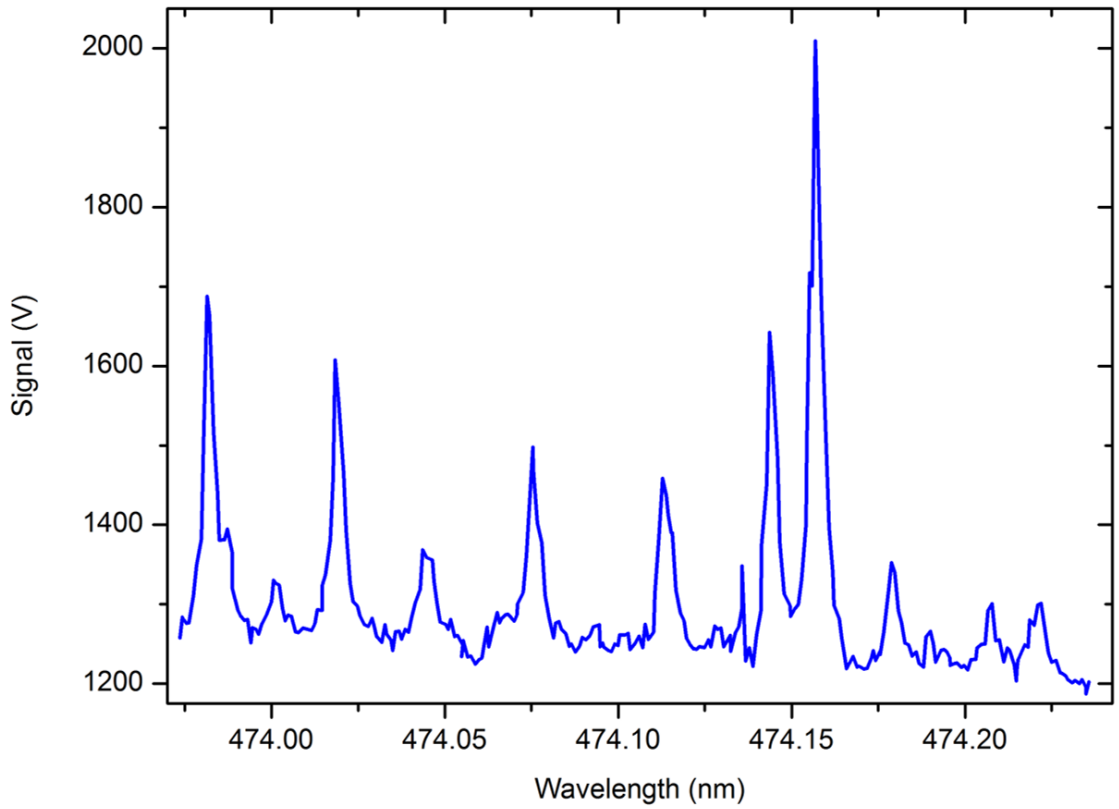

Figure 5.8: The ionisation spectrum obtained for the $a^1\Pi_g \longleftarrow X^1\Sigma_g^+$ band of N_2, with a resolution of 0.001 nm at 300 K.

optimised. Figure 5.8 shows the spectrum obtained. During the scan (from higher to lower wavelength) there is a drift of the offset, which steadily increases as the wavelength comes down. This has been attributed to a change in the gain of the channeltron directly after it has been switched on, although this effect has not been fully investigated.

5.5.1 Comparison with literature values and PGopher simulation for transition identification

The lines were identified using two methods; from the literature values [3; 4], and also using a simulation tool called PGopher[4]. After inputting the rotational and vibrational constants for the electronic states $a^1\Pi_g$ and $X^1\Sigma_g^+$ as found in the NIST Chemistry web book[5], the full rotational spectrum, including relative intensities, was plotted.

In fig. 5.9, the $a^1\Pi_g \longleftarrow X^1\Sigma_g^+$ band has been simulated for the O, P, Q, R and S branches, at a temperature of 300 K. The expected spectrum in the bottom graph has

[4]PGopher is open source software for calculating rotational, vibrational and electronic spectra that can be obtained from: `http://pgopher.chm.bris.ac.uk/`

[5]`http://webbook.nist.gov/cgi/cbook.cgi?ID=C7727379&Units=SI&Mask=1000#Dia64`

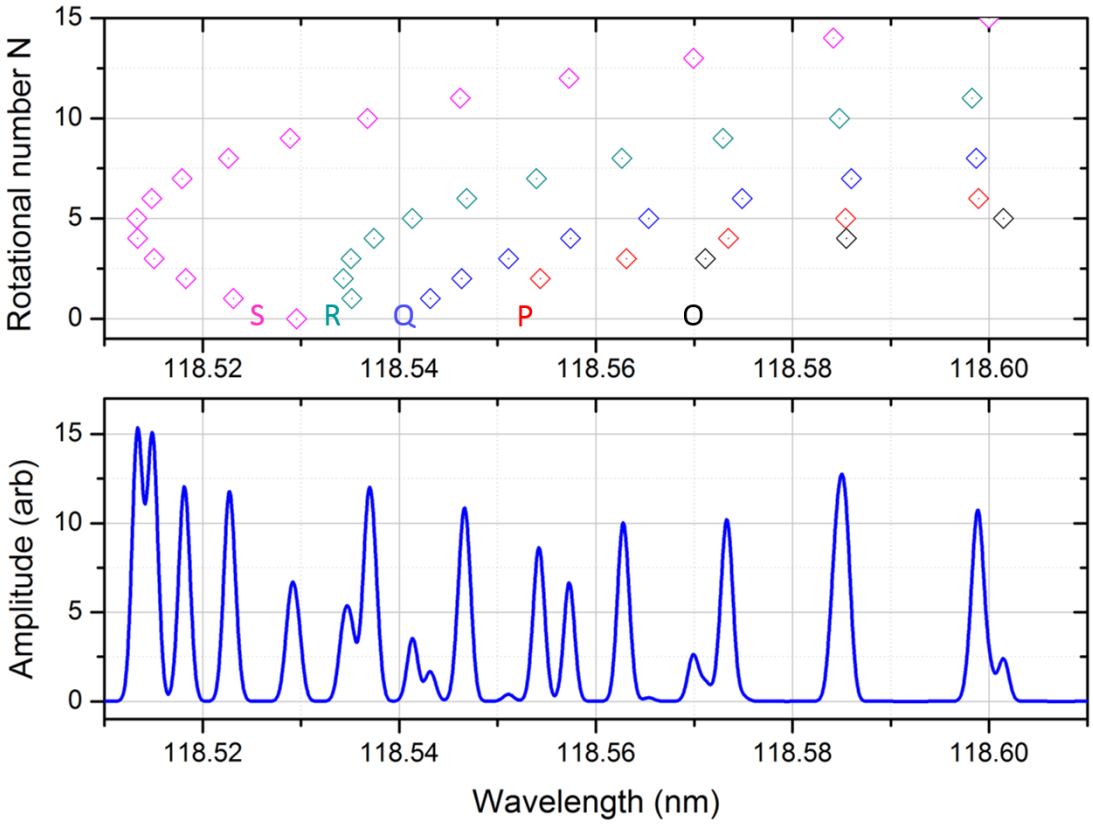

Figure 5.9: PGopher simulation for the $a^1\Pi_g \longleftarrow X^1\Sigma_g^+$ band of N_2, showing the O, P, Q, R and S branches, at a temperature of 300 K. The y-axis of the top graph gives the rotational number in which the molecule starts in when in the ground electronic state $X^1\Sigma_g^+$. The bottom graph displays the expected spectrum, showing the relative amplitudes of each transition.

been plotted so that the linewidth is similar to the width found in the experimental data (the large laser linewidth being the main contribution). The scale on the x-axis shows the actual energy of the transition, ie. the total energy of the two photon transition, so it is half the laser wavelength used.

The top graph demonstrates how overlapped many of the transitions are, particularly at the band heads of each band. The width of the laser further reduces the available resolution.

In fig. 5.10 the simulated results (blue) have been compared to the experimental data (red). The experimental data has been normalised to the P_2 transition in the simulation. The positions of the lines match well, although this is after subtraction of an offset of 0.018 nm from the simulated data - the two different scales for the x-axis have been included in the figure. Another, very noticeable difference is the relative peak heights for each

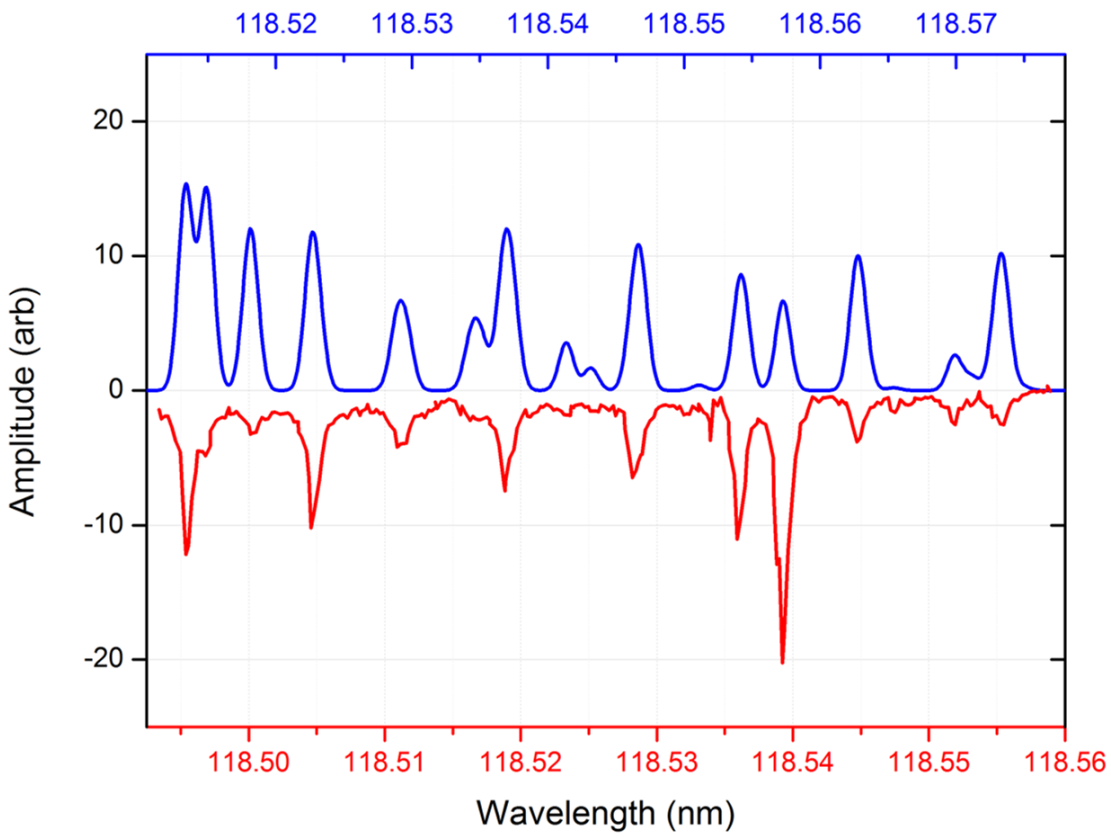

Figure 5.10: Comparison of the PGopher simulation (blue) to the experimental data (red) shown in fig. 5.8. The experimental data has been normalised to the P_2 transition. After the simulation has been offset by 0.018 nm, the positions of the lines match well, although the relative peak heights in the spectrum do not.

spectrum. Many peaks are much smaller than they should be in the experiment, or not there at all. It is not clear what this is down to as the neutral molecules in the experiment should be at room temperature, 300 K.

Although the reason for such a large offset is also not clear, our experimental data (for the positions of the lines) appear to agree with the results from the Opitz group [3]. An additional comment is that the relative peak heights for the transitions found by Opitz *et. al.*, at a temperature of 8 K, do not quite match up with the 8 K PGopher simulation either.

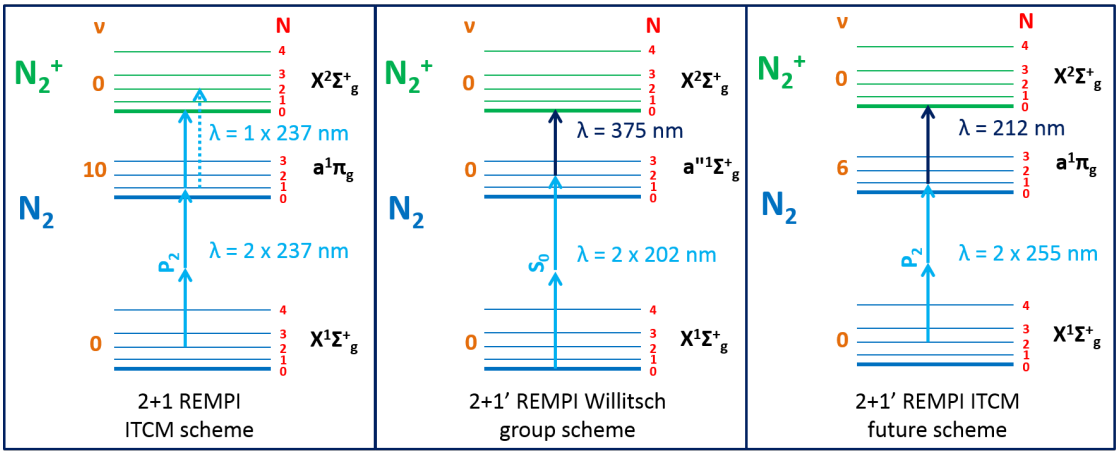

Figure 5.11: Comparison of three methods for state preparation of N_2^+. In the first panel the 2+1 REMPI scheme used for this chapter is shown, with the main drawback being that it is not completely state selective. In the centre panel is a 2+1' scheme used by the Willitsch group in Basel [5]. The final panel shows the future scheme to be used in the ITCM group at Sussex, which will be fully state-selective, unlike the current scheme shown in the first panel.

5.6 Summary and future spectroscopy for a different band in N_2

An experimental apparatus suitable for determination of the different transitions in the $a^1\Pi_g \longleftarrow X^1\Sigma_g^+$ band of N_2 was set up and a spectrum obtained using time-of-flight spectroscopy. The purpose being to identify transitions suitable for state preparation of the nitrogen ions for state sensitive experiments in an ion trap. The current ionisation setup for preparation of N_2^+ in the $X^2\Sigma_g^+(N=0,\nu=0)$ state is possible, but relies on having a source of neutrals of a low rotational temperature. Although one of the possible transitions for state preparation, the P_2 transition, appears to have a large transition amplitude, this is only due to the strong overlap with the S_{12} transition. At room temperature, the population of the $N=12$ transition would be expected to be much larger than that of the $N=2$ state. The molecular beamline (sec. 6.2) used for trap loading has been designed to supply a rotationally cold beam to the ion trap experiment.

The 2+1 REMPI scheme used also has a drawback, as it is not fully state-selective. As discussed in sec. 5.1, more than one final state is energetically allowed - this goes for all of the suitable transitions investigated. This can only be improved upon by using a two-colour 2+1' REMPI scheme. The current 2+1 scheme used is shown alongside two 2+1' schemes in fig. 5.11, one of which is used by the Willitsch group [5] and is shown

in the centre panel, and the other is our proposed improved scheme in the panel on the right. The REMPI from the Willitsch group uses two photons at ∼202 nm to excite the molecule to an entirely different vibronic state from our scheme, using the transition $a''^1\Sigma_g^+(\nu = 0) \longleftarrow X^1\Sigma_g^+(\nu = 0)$. A third photon at a wavelength of 375 nm then state selectively ionises the molecule, making this an improvement to the 2+1 same-colour scheme. However, a slight drawback to this scheme is that the excitation photons have a higher energy than the final ionisation photon. This means that it is possible to instead have a 2+1 process occurring instead, using the 202 nm photons for ionisation as well as excitation. To reduce the 2+1 probability, the 202 nm intensity would need to be reduced [5].

The third panel shows our newly proposed scheme for nitrogen ionisation. Like the Willitsch technique, it is a 2+1' REMPI, meaning that it is fully state selective, which would be an improvement on our current setup. The excitation stage will use two photons at 255 nm, using the transition $a^1\Pi_g(\nu = 6) \longleftarrow X^1\Sigma_g^+(\nu = 0)$, which will excite the molecule to the same electronic state as our current scheme, although there is a change to the vibrational state, which will now be $\nu = 6$ instead of $\nu = 10$. The third photon for state selective ionisation will be at 212 nm. This scheme avoids a 2+1 same-colour process occurring instead, as the final ionisation stage requires a higher energy than the energy of one photon at 212 nm. There are currently two Ti:Sapphire lasers being set up in the lab for this purpose. An additional benefit to these lasers is that the expected linewidth (10's of MHz [85]) will be two orders of magnitude narrower than the dye laser linewidth of ∼3 GHz.

The photoionisation setup used is versatile enough so that it can be used in conjunction with the molecular beamline for full characterisation of the beam. Before attachment to the ion trap, the beamline settings can be optimised and also its alignment. By performing spectroscopy on the beam in a similar way as outlined in this chapter, the rotational temperature can be determined via comparison with PGopher simulations.

Chapter 6

Trap loading of N_2^+

The efficiency of trap loading of nitrogen molecules in the desired internal state $X^2\Sigma_g^+(N = 0, \nu = 0)$ relies on having a source of internally cold neutral molecules (see sec. 5.1). Additional to this is the desire to keep the nitrogen pressure in the trapping region as low as possible, so as to avoid charge exchange reactions occurring, as this is the mechanism for loss of a prepared state. To meet these two requirements a molecular beamline has been set up, with trap loading trials carried out. Resulting low loading efficiencies has required full characterisation of the system, which has started with the simplest configuration using just the pulse valve.

Use of a molecular beamline for the purpose of state-selectively loading N_2^+ has successfully been demonstrated by the Willitsch group in Basel [5]. Similarly to the setup described in this chapter, a pulse valve is used to synchronise a pulse of nitrogen gas to arrive with the lasers used for ionisation in the trapping region, with two skimmers used to extract the supersonic beam and for collimation. The main difference between the two setups is the ionisation scheme used, described in detail in sec. 5.6.

6.1 Molecular beam dynamics

The requirement for keeping a low trap pressure is solved immediately by use of a pulse valve aligned to the trap centre. This would provide a pulse of a high density that can be timed with a pulse laser for efficient loading of molecular ions, without formation of a high nitrogen background. However, it is also important that the internal temperature of the neutral molecules is low so that the efficiency of loading into the correct internal state is enhanced. Production of a cold beam of molecules is achieved via expansion of a high pressure thermal source into a low pressure vessel via a small diameter aperture.

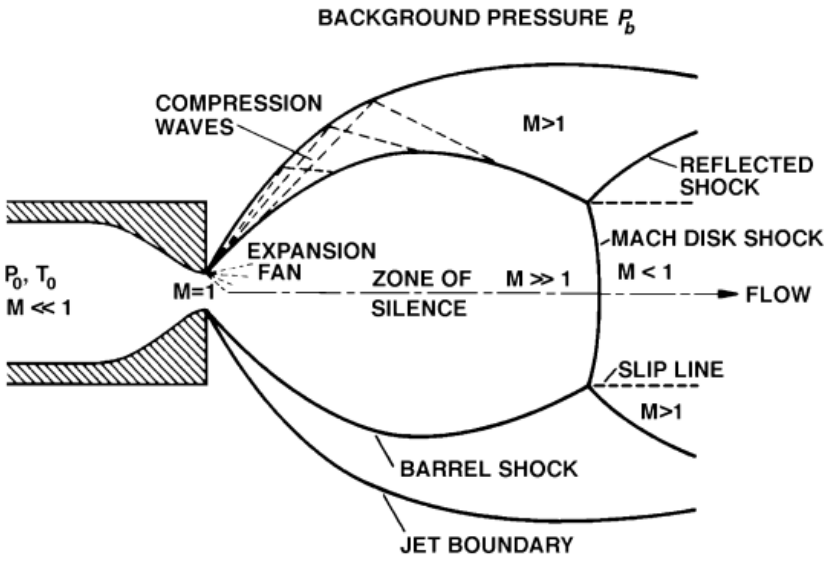

Figure 6.1: Diagram of the flow dynamics during a supersonic expansion. Reprinted from [6] with permission from Oxford University Press.

It is the flow through the aperture that separates the high and low pressure regions that determines the expansion properties, a full discussion of which is given in [86]. For the desired supersonic case, the expansion is said to be *underexpanded* and occurs in the regime where the stagnation pressure, P_0 (the high pressure reservoir) is much greater than the ambient pressure, P_b of the vessel into which the gas expands. Figure 6.1 illustrates the dynamics of a supersonic expansion, which occurs when $P_0 \ll P_b$. The ratio between these pressures for supersonic flow is given by the inequality [6]:

$$\frac{P_0}{P_b} > \left(\frac{\gamma+1}{2}\right)^{\gamma/(\gamma-1)}, \tag{6.1}$$

where γ is the heat capacity ratio of an ideal gas, which for the diatomic molecule N_2 is 7/5. So for supersonic flow across the aperture a pressure ratio $P_0/P_b > 1.9$ is required. When in this regime, the gas is accelerated from the high pressure region into the region of ambient pressure.

It is important at this stage to define the Mach number M, as this will describe the dynamics at various stages of the expansion, as can be seen in fig. 6.1. The Mach number is a dimensionless quantity given by the ratio of the the particle velocity (v) to the speed of sound of the particular gas looked at $M = v/v_S$, where the speed of sound v_S is given by [86]:

$$v_S = \sqrt{\frac{\gamma RT}{W}}, \tag{6.2}$$

which has been defined in terms of the molar mass of the gas W, the gas constant R, and the temperature T.

When in the high-pressure reservoir, the Mach number is much less than 1. However, as the gas accelerates, driven by the large pressure gradient, the Mach number increases and is equal to one at the aperture, provided that eq. 6.1 holds. As the flow expands out into the vacuum, the gas continues to accelerate and so $M > 1$. Due to the flow velocity being larger than the speed of sound, and the fact that the incoming gas is at a higher pressure than the ambient pressure P_b, shock waves are created, and indicated in fig. 6.1. The *zone of silence* which is defined by these boundaries now contains the gas with the properties that are required by the experiment. In order to extract a beam, without changing its properties, a skimmer is positioned within the zone of silence.

So it is therefore important to locate the position of the Mach disk, to make sure that the skimmer will sit within the zone of silence. In fig. 6.2 the position of the Mach disk with respect to the valve for a range of different ambient pressures has been plotted . Two separate plots have been made to demonstrate the difference between using a 0.1 mm valve (bottom) and a 0.51 mm valve (top). This has been plotted using the known equation for the position of the Mach disk [6]:

$$Z_{Mach} = 0.67 \left(\frac{P_0}{P_b}\right)^{1/2} d, \tag{6.3}$$

which is only a function of the ratio between the stagnation and ambient pressures.

For both of the valves, for fairly high ambient pressures between 0.01 mbar and 0.10 mbar, the Mach disk sits quite far away from the valve, between 25 mm and 50 mm. So if the skimmer is placed within 25 mm of the valve, it should sit in the shock-free zone of silence if either valve is used.

During the rapid expansion, due to the large density of the beam, a high rate of collisions occur. This causes cooling of the internal states of the molecules. The velocity along the beam flow, and also the decrease in temperature can be calculated using:

$$v = M\sqrt{\frac{\gamma R T_0}{W}} \left(1 + \frac{\gamma - 1}{2} M^2\right)^{-0.5}, \tag{6.4}$$

$$T = T_0 \left(1 + \frac{\gamma - 1}{2} M^2\right)^{-1}, \tag{6.5}$$

both of which are given in terms of γ, the initial temperature of the source T_0, the molar mass W, the ideal gas constant R, and the Mach number M, the importance of which has been demonstrated in fig. 6.1, and which is given by:

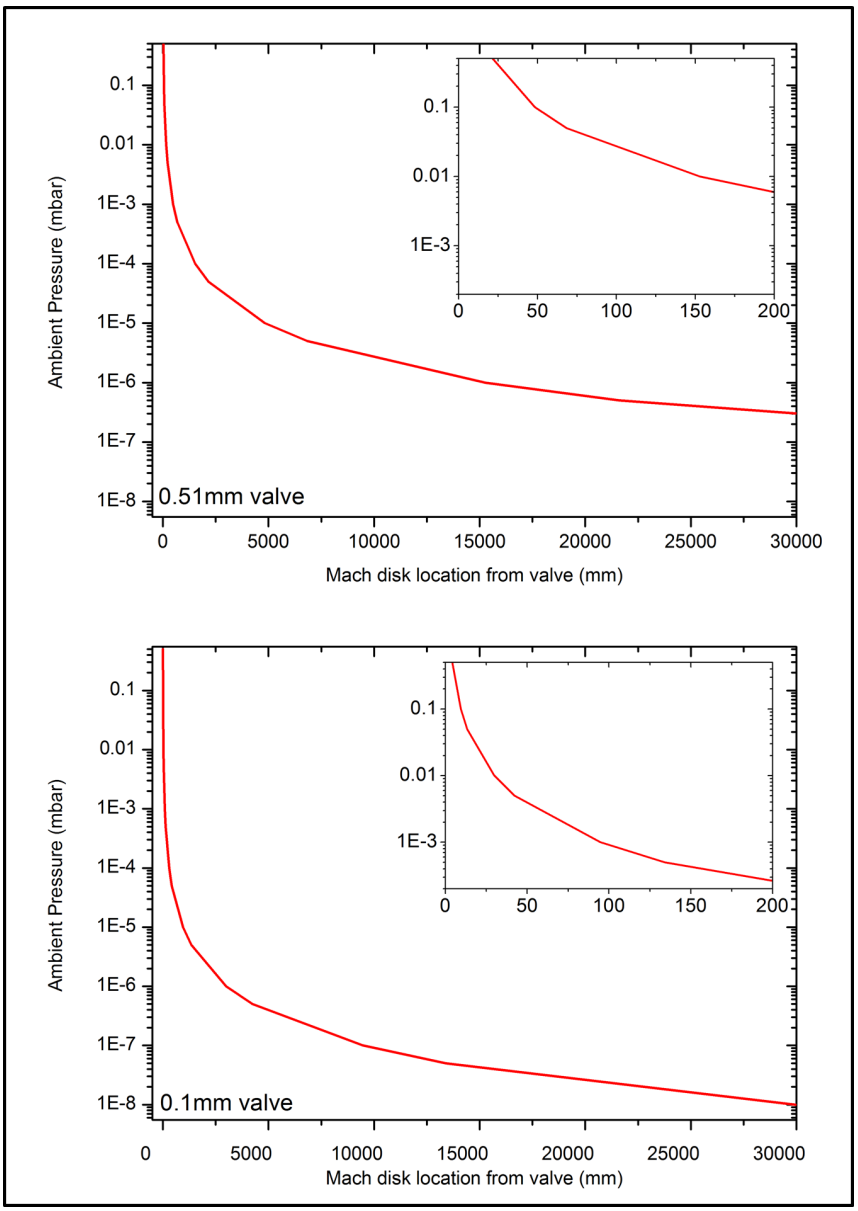

Figure 6.2: Location of the Mach disk from the aperture, as a function of the ambient pressure for two different sized apertures. (Top) Mach disk location for a 0.51 mm valve. (Bottom) Mach disk location for a 0.1 mm valve. The inlet on each graph is a zoom-in of the area of most interest, as the pressure during a pulse is expected to become quite high.

$$M = A\left(\frac{z - z_0}{d}\right) - \frac{\frac{1}{2}\left(\frac{\gamma+1}{\gamma-1}\right)}{A\left(\frac{z-z_0}{d}\right)^{\gamma-1}}. \tag{6.6}$$

This is a fitting function that has been found empirically [6]. The expected temperature and velocity along the flow for an initial temperature of $T_0 = 300$ K and a source pressure of $P_0 = 2$ bar is plotted in fig. 6.3, for both valve sizes. For the species of gas used the particular parameters of interest can be looked up in [6]. Here the parameters $z_0 = 0.4$, and $A = 3.65$ have been used. The top graph in fig. 6.3 is for the 0.51 mm valve and the bottom graph corresponds to the 0.1 mm valve. For both valves there is a minimum temperature and maximum velocity that the beam reaches. This is at the point at which the expansion has led to a decrease in collision rate as the beam flows away from the valve. For the smaller valve the terminal velocity is reached faster, compared to the the 0.51 mm valve.

From the Mach disk location calculated in fig. 6.2 and the translational temperature in fig. 6.3, an ideal distance at which the skimmer should be placed can be decided. If both valves are to be tested on the same setup, it looks as though a skimmer distance of around 20 mm would be suitable for placing the skimmer in the zone of silence, while being far enough away from the valve to have had sufficient cooling.

6.2 Molecular beamline

The molecular beamline is a differentially pumped vacuum system that attaches to the main ion trap experiment. It consists mainly of an induction actuated pulsed valve, and two skimmers[1] with the main purpose of producing a collimated beam of nitrogen. The skimmers also act as pressure barriers to reduce the background in the trap. This very basic description of the system is illustrated in fig. 6.4.

The collimated molecular beam enters the trapping region radially, aligned just off from the trapping region. A small prism (fig. 6.4) protects the trap centre from the incoming beam of molecules, to prevent charge exchange reactions between the neutral molecules and previously loaded molecular ions. The nitrogen ionisation laser is aligned counter-propagating to the molecular beam, aligned to the same region in the trap.

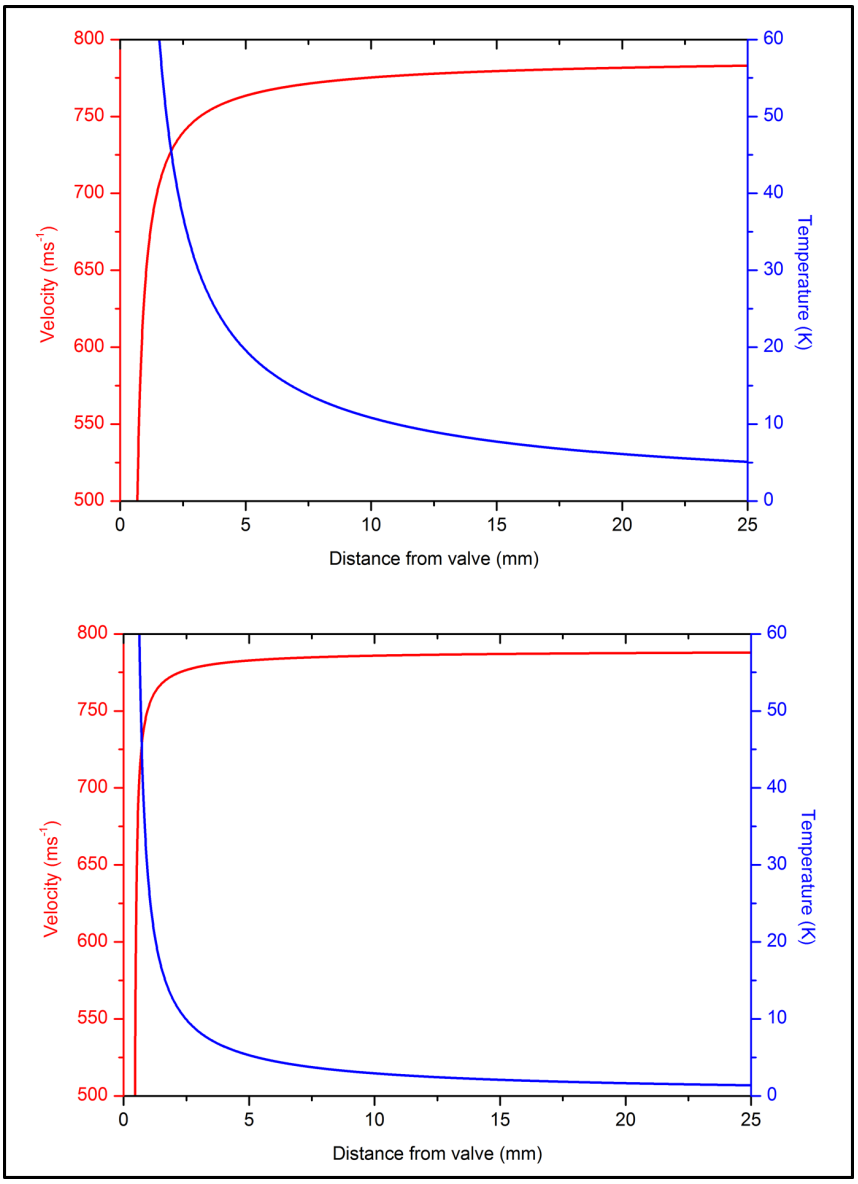

Figure 6.3: A demonstration of how the velocity and translational temperature of the beam changes as it moves away from the aperture, for two different aperture sizes. Collisions within the initially dense beam causes a cooling effect, at the same time there is rapid acceleration caused by the pressure gradient. The terminal values for velocity and the minimum temperature achieved during expansion have almost been reached for both valve sizes: 0.51 mm (top) and 0.1mm (bottom) within 25 mm.

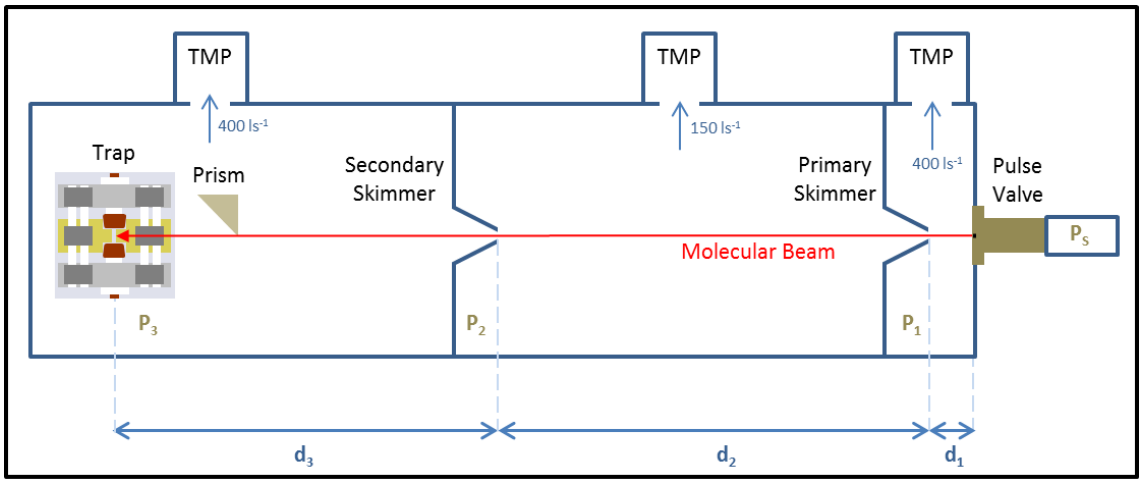

Figure 6.4: Schematic of the molecular beamline. The stagnation pressure (P_S) behind the pulse valve is adjusted by a regulator on the nitrogen gas cylinder, and can be adjusted from 0.2 bar to 4 bar above atmosphere. The pulse valve can be controlled to make bursts of nitrogen expand out into the primary chamber via a supersonic expansion. The pressure in this chamber is the highest for the whole of the vacuum system (not including P_S), and is pumped by a 400 ls^{-1} turbomolecular pump (TMP). The supersonic beam created by the expansion is skimmed off by the primary skimmer. The divergent beam is re-collimated by the secondary skimmer before entering the ion trap where ionisation takes place.

6.2.1 Vacuum system and design

The induction actuated pulsed valve[2] used for injecting nitrogen molecules into the beamline system is mounted onto a custom CF63 flange, the design of which is shown in fig. 6.5 (top). The valve sits on the flange face, through which a conical hole has been machined to allow nitrogen into the vacuum system. This is then vacuum sealed by use of a small O-ring that sits in-between the flange and the pulse valve, which is clamped down by a brass ring that screws into the flange.

In fig. 6.5 (top), there are two concentric inlets that have been drilled into the flange face, which are centred by the conical hole for leaking in nitrogen. The larger diameter inlet is tapped, and this is how the brass ring clamps down onto the valve. The pulse valve snugly fits into the smaller inlet, and guarantees that the valve is concentric to the conical hole and the flange.

[1]Both home-built conical skimmers and also ideal skimmers supplied by Beam Dynamics have been used.

[2]Parker series 9 valve with a minimum opening time of 160 μs

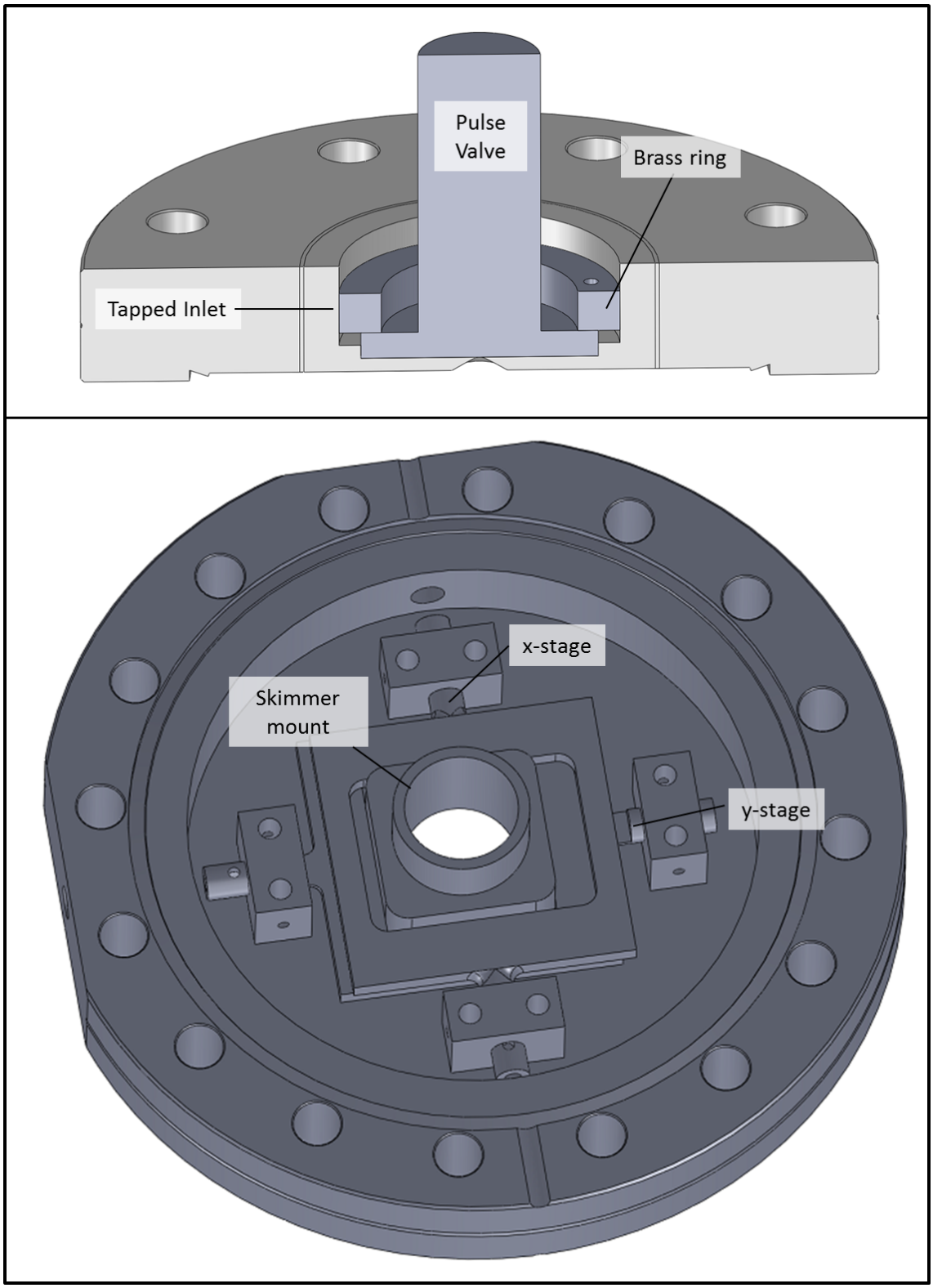

Figure 6.5: Top: Schematic showing a cut through of the flange on which the pulse valve is mounted. The inlet in which the valve sits is a tight fit, so as to keep the valve concentric with the flange. The brass ring is threaded and fits into the tapped inlet in order to clamp the valve down and create a vacuum seal with a small o-ring that sits between the valve and the flange. Bottom: One of the skimmer mounts used in the molecular beamline. This enables alignment of the primary and secondary skimmers from outside of vacuum.

The pulse valve flange is bolted onto the primary chamber, which is pumped by a turbomolecular pump[3] (TMP) with a pumping speed of 400 ls^{-1} for nitrogen. The primary skimmer is positioned around 2 cm after the valve. The x-y alignment of this skimmer is critical, and so is mounted on a 2D stage, which can be aligned from outside of the vacuum. Figure 6.5 (bottom) gives a Solidworks drawing of this[4].

The two stages have rectangular sections machined out of them that guide the tapped skimmer mount without blocking the molecular beam. The stages are then mounted onto the flange via four teflon guides that allow for smooth movement in the required direction. Not shown on the drawing is the method of translating the stages, or how they are vacuum sealed. This can be seen in better detail in the photograph in fig. 6.6. Each of the stages are attached to shafts that are actuated via micrometers that are mounted on the outside of the flange on two frames. The vacuum seal is made with small bellows that have been welded onto the micrometers.

The region between the primary and secondary skimmer is pumped by a second TMP, with a pumping speed of 150 ls^{-1}. The pumping speed for this TMP does not need to be as high, as the pressure in this secondary chamber is much lower than the primary chamber. Each of the TMPs are backed with a separate two-stage rotary vane pump.

The secondary skimmer position is also mounted on a fully adjustable flange, and has exactly the same design as for the primary skimmer. Behind this skimmer is a gate valve that can be used to isolate the beamline from the ion trap if required. The beamline is attached to the ion trap chamber by way of short CF63 bellows with a rotatable flange at one end.

The full beamline and ion trap setup is shown in fig. 6.7, using a solidworks drawing and a photograph of the setup.

6.3 Attempted trap loading of N_2^+

6.3.1 Trap parameters

First of all the trapping parameters required for trapping molecular nitrogen ions simultaneously with atomic calcium ions have been considered. As shown in section 2.1, the a and q parameters, and therefore where the stability region lies in $a-q$ space are dependent on the charge-to-mass ratio of the ions to be trapped (see eq. 2.13 and eq. 2.14). To trap both, the separate stability regions have to be found. The overlap of the two will

[3] Oerlikon Leybold vacuum TURBOVAC 361 DN 160 CF

[4] Design by Dr. Matthias Keller

Figure 6.6: Photographs showing the full skimmer mount setup, and the small bellow sealed micrometers for fine adjustment outside of vacuum. The bottom photograph shows the mounting of a 0.3 mm Beam Dynamics skimmer.

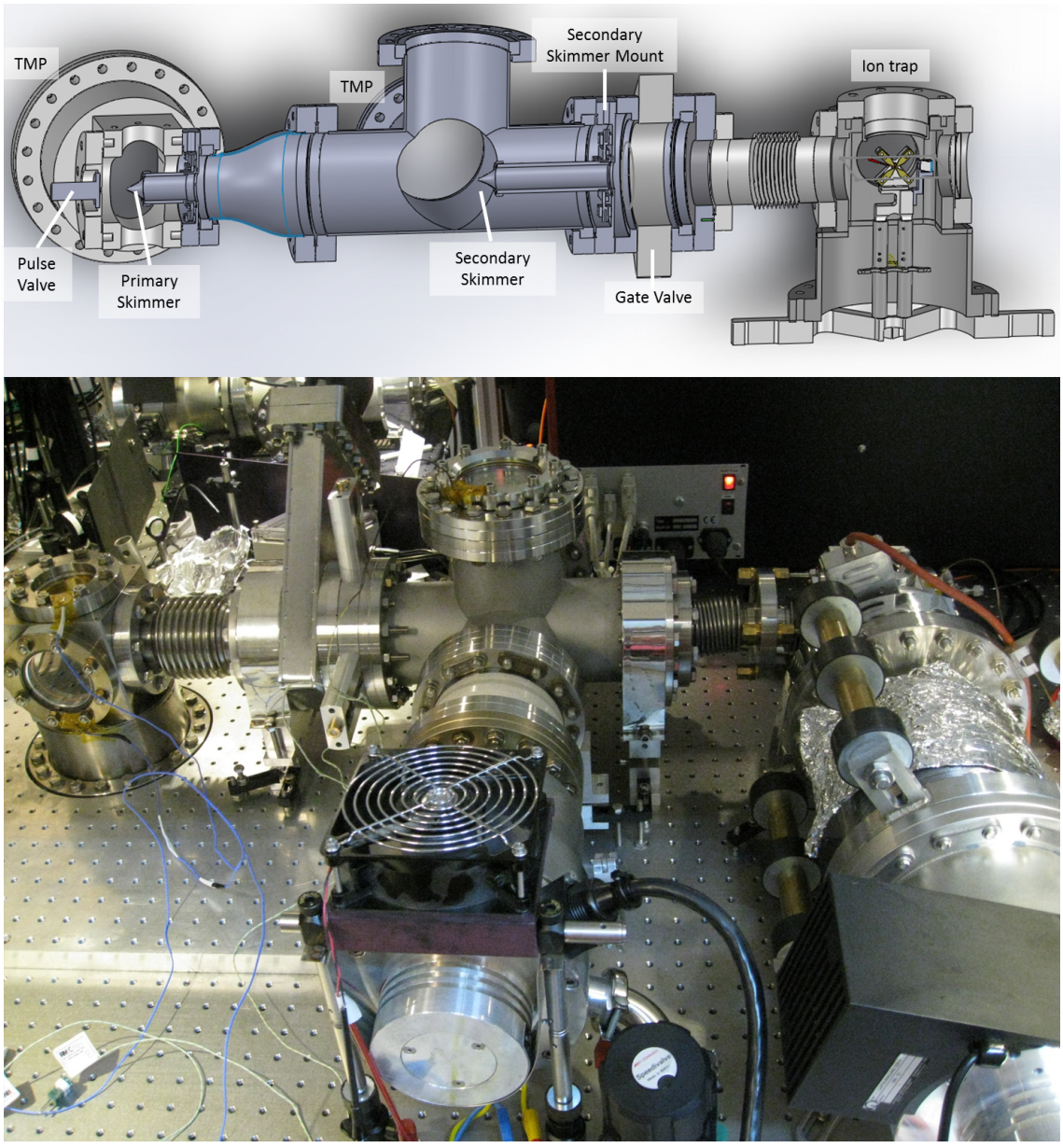

Figure 6.7: The molecular beamline. Top: A solidworks drawing showing a slice through of the molecular beamline and ion trap setup. Bottom: A photograph of the beamline and ion trap, facing in the opposite direction to the solidworks drawing.

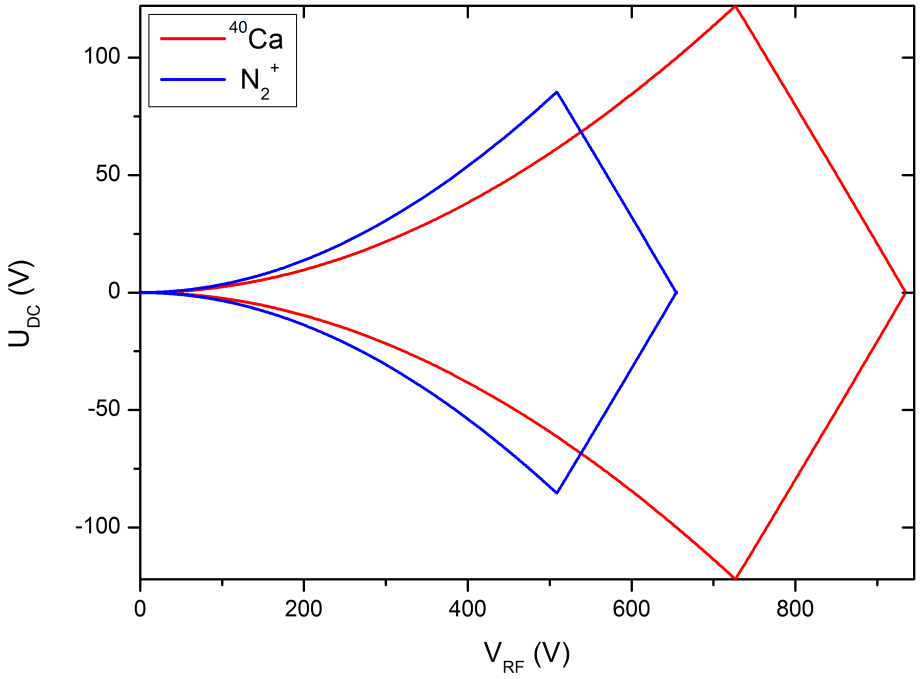

Figure 6.8: Stability regions for $^{40}Ca^+$ (red) and N_2^+ (blue). The area where the two overlap gives the region in which the two can be trapped simultaneously.

demonstrate the region in which the trap has to be operated in.

A difference in the charge to mass ratio means that the two species will sit at two different places on the stability diagram. Therefore the stability diagram can be re-plotted, this time in terms of the rf voltage amplitude V_{RF} and the DC axial voltage U_{DC} for the particular charge-to-mass ratio of the ion species we wish to trap. Figure 6.8 shows an example of two stability regions: one for $^{40}Ca^+$ and the other for molecular nitrogen, and where the two overlap in terms of the voltages applied onto the electrodes. If the charge to mass ratio of the two separate species differs too much, then it may not be possible to trap the two simultaneously.

An additional effect of simultaneous trapping of multiple ion species is that the relative positions of ions within a 3D crystal also depends on the charge-to-mass ratio of each [87]. For a micromotion compensated Coulomb crystal consisting mainly of $^{40}Ca^+$ along with N_2^+, the ions will arrange so that the nitrogen ions will form an inner core to the ion crystal. With the correct trapping parameters, this effect manifests itself as a dark band across the middle of an otherwise normally shaped pure ion crystal. If the total potential minimum of the ion trap does not overlap with the rf minimum (ie. not micromotion

compensated), this band will appear off-centre [45].

6.3.2 Sympathetic cooling of molecular ions

As well as being stably trapped the nitrogen molecules have to have their translational motion cooled effectively. Direct laser cooling has been demonstrated on other types of molecules, sometimes taking advantage of the more complex interactions that molecules undergo with the environment, such as the interaction of polar molecules with blackbody radiation [35; 36]. Another technique is buffer-gas cooling [44], which also cools the internal degrees of freedom. Still, the simplicity of sympathetic cooling means that it is widely used for trapped-ion experiments.

Sympathetic cooling is a technique that relies on the Coulomb interaction of the ions in the trapping potential. If there is a two-species ion crystal in the trap, kinetic energy is transferred between the two species due to their Coulomb interaction. If one of the species is directly laser cooled, the energy of the whole system is taken away, and both types of ions are effectively cooled. The kinetic energy transfer between the trapped ions is so effective (for ions of similar mass) that it is still possible to cool the crystal close to the Doppler cooling limit, to mK temperatures [17].

6.3.3 Experimental setup

Both the beamline valve used and the laser for ionisation are pulsed devices. Trap loading is carried out by pulsing both at the same time, with the aim of hitting the densest part of the molecular beam with the laser. A diagram of the experimental setup for trap loading of N_2^+ is given in fig. 6.9. Before any loading attempts begin, a pure calcium crystal is loaded and imaged simultaneously on the PMT and CCD camera, the setup of which shown in fig. 3.8. This means that if any nitrogen molecules are loaded, they are sympathetically cooled by the calcium ions, and their presence can be detected within the crystal by using the crystal weighing technique (see sec. 3.4 for a description of how crystal weighing is carried out).

For trap loading the pulse valve used has an inlet diameter of 0.1 mm, and was controlled by a home-built pulse valve controller[5]. Using this, the opening time of the valve can be varied from a minimum of 160 μs up to hundreds of ms. The actuation voltage can also be adjusted from 100 V to 500 V, which also has a contribution to the actual opening time of the valve.

[5]Kindly supplied by the Softley group at Oxford University

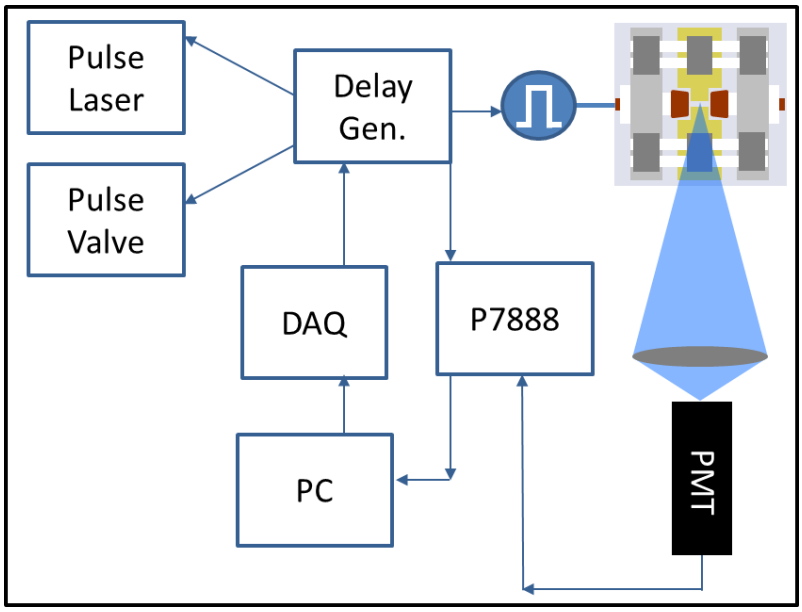

Figure 6.9: The setup for trap loading of N_2^+ with crystal weighing. The delay generator is used to trigger the pulse laser and pulse valve with the desired delay between the two. Once loading has been completed for the required duration, the delay generator is used to excite the secular motion of the ion crystal in the trap, during which time the modulated fluorescence is collected. This is sent to the p7888 which is a fast counting card for recording the photon arrival times during a measurement. This can then be repeated many times.

An important parameter for trap loading is the delay between triggering the pulse valve and the ionisation laser. Using the expected velocity distribution of the beam, appropriate timing could be used. This is a parameter that was later scanned in order to check if the trap was indeed being loaded from the beam, rather from just diffusion through the beamline system.

A Labview routine was used to carry out nitrogen ion loading. Along with this a delay generator was used for triggering the pulse valve, laser, and to excite the COM mode motion of the ion crystal. First, a calcium crystal was loaded in the trap. The routine could then begin, and a crystal weighing measurement performed. From this, the secular frequency of the pure calcium crystal is determined. Next, loading begins for some set amount of shots, with the chosen important parameters of pulse length, valve actuation voltage and delay between the valve and the laser. The loading process is then stopped so that another crystal weighing measurement can be taken, to check if a nitrogen ion has been loaded. The routine then carries on for the number of iterations set.

These loading attempts were carried out for a range of different set parameters, and

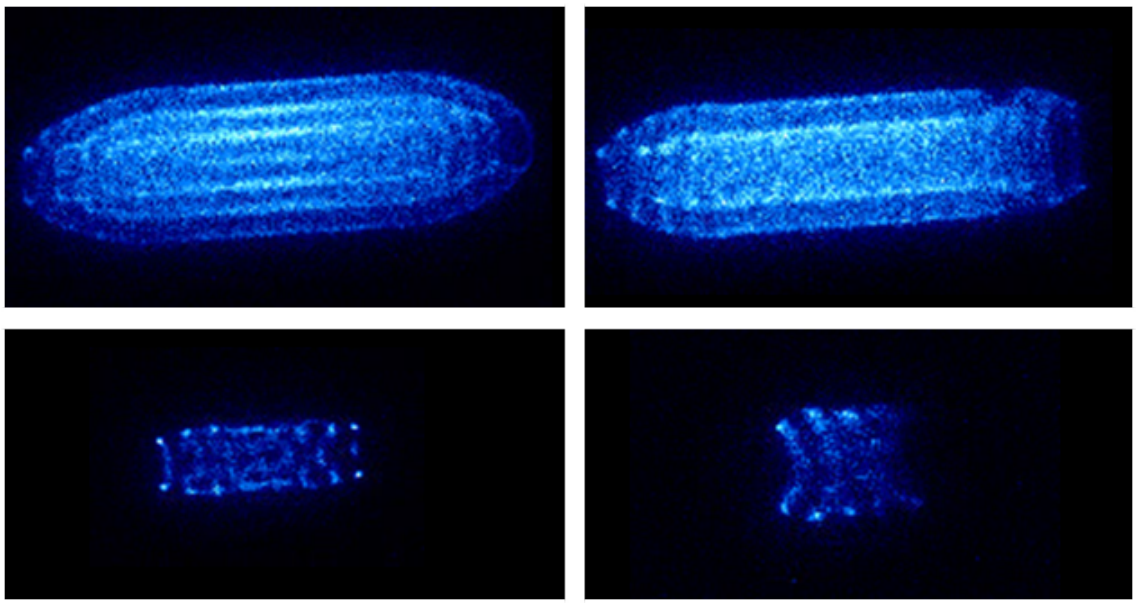

Figure 6.10: Some examples of calcium Coulomb crystals with nitrogen cores.

also for different calcium crystal sizes. The laser was also tuned to different transitions in nitrogen using the spectrum found in fig. 5.8.

6.3.4 Results and conclusions

Results from some of the more successful loads are shown in fig. 6.10, in the form of CCD false-colour images. These all started with large ion crystals loaded into the trap. The laser and beamline were then operated for a minute or more at 10 Hz repetition rate, and then repeated again, until a dark core could be seen forming in the centre of the crystal. Although the cores in these images look quite large, it would take many attempts at loading to see a core forming. For instance, it took over 600 shots to get to the top right image in fig. 6.10, and even longer for the subsequent images.

If starting with a smaller calcium ion crystal or string, it became more apparent that the loading efficiency was extremely low. For long loading durations on the order of 100 s, only one or two nitrogen ions would be loaded. During this stage, the delay between the pulse valve and laser was scanned in order to look for the time-resolved beam. If a supersonic beam was formed with the molecular beamline, there should be a peak if the delay is scanned. These experiments revealed that no such peak could be found. For a large range of delay times, the number of successful nitrogen loads remained the same. This strongly suggested some fundamental problem with the molecular beamline, and so further tests had to be carried out on this separately as a result.

6.4 Characterisation of the beamline using the photoionisation setup

In order to fully characterise the system and understand its dynamics, it was taken back to its simplest form, consisting of just the pulse valve and a detector - in this case the photoionisation setup used in chapter 5. In this configuration, the timing of the molecular beam could be found, and characterised by varying parameters such as the stagnation pressure and set opening time of the valve. This is as far as the characterisation has gone, but in future work the system will be fully characterised.

In future iterations of the characterisation, the system will be built up to gain more information from each of the stages. First, the primary skimmer can be placed in front of the pulse valve and its position optimised to get the best alignment through to the photoionisation setup. Finally the secondary skimmer can be placed in the system, and again optimised before connecting back to the ion trap.

6.4.1 Experimental setup

The detection setup is exactly the same as in chapter 5, but this time the gas source used is pulsed, and is further away from the detector. The main purpose of this characterisation is to perform TOF spectroscopy in order to see the pulse of molecules from the time-resolved beam. Therefore, the most important aspect of this new setup was the delay between the ionisation laser and the pulse valve. The experimental setup is shown in fig. 6.11

6.4.2 Photoionisation spectroscopy of N_2 using a pulse valve

First of all the delay that is set between the pulse valve and the laser has to be scanned in order to make sure the timing is correct, and that the valve is working as it should. Figure 6.12 shows how the signal varies as the delay between the valve and the laser is scanned.

For such a large diameter valve, the pulse width was kept to a minimum. The stagnation pressure and repetition rate also had to be kept low in order to avoid a large build-up of pressure in the system. For this scan the repetition rate used was 5 Hz, although it is evident from the height of the signal at delays of 0 ms and 200 ms that this is not quite enough time to allow for the system to recover and the pressure to come down to zero between each pulse. For each data point the signal was summed over 20 shots. In between every data point is a period of 40 s dead time to allow for the nitrogen to be pumped away. The first narrow peak is nitrogen that arrives directly from the pulse valve. The

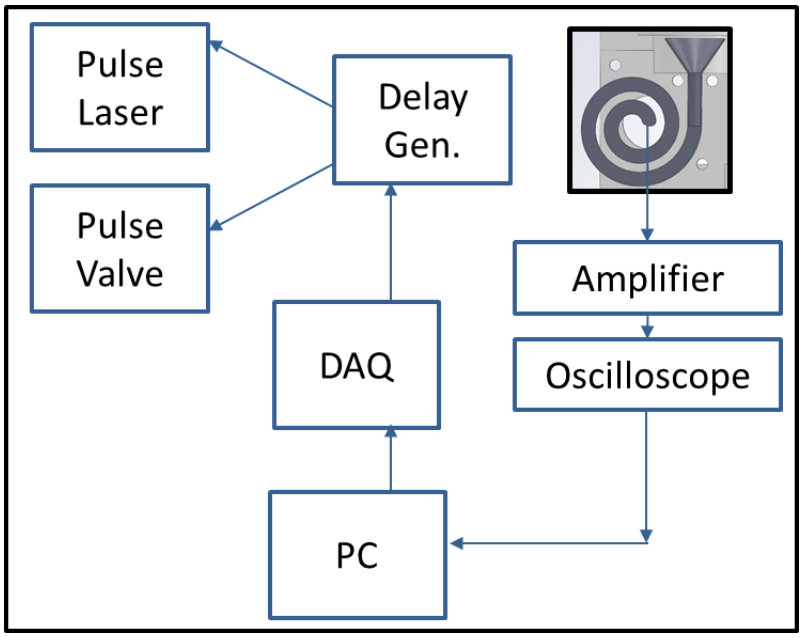

Figure 6.11: Experimental setup for the pulsed ionisation spectroscopy for the beamline.

second, spread-out peak that comes afterwards is due to a general build up of pressure in the entire chamber. Nitrogen that has hit the surfaces and taken a much longer path to get to the detection is part of this distribution.

The spectrum that is shown in fig. 6.13 is very similar to the one taken with a continuous nitrogen flow, as shown in chapter 5 - a main difference being that fewer shots were required to get a much larger signal in the case of having a pulsed source (600 shots were used to get the spectrum in fig. 5.8 compared to 60 shots for fig. 6.13). Another improvement to the spectrum taken before is that the peaks are narrower than before - for instance the two peaks at the lowest wavelength in the spectrum are well defined, whereas in the previous spectrum the smaller peak was just a shoulder on the much larger one. The main result that this spectrum shows is that the relative peaks heights across the spectrum have not changed at all from the continuous nitrogen flow spectrum.

6.5 Discussion

This chapter has described results gained so far from efforts that have been made toward producing a supersonic molecular beam of cold nitrogen molecules for the high resolution experiments proposed in this thesis. When the system was initially built, successful nitrogen loads were confirmed via the technique of crystal weighing. As well as this, the expected alignment for a lighter species of ion within the crystal was observed, with the nitrogen ions appearing as a dark core in the centre of the calcium ion crystal.

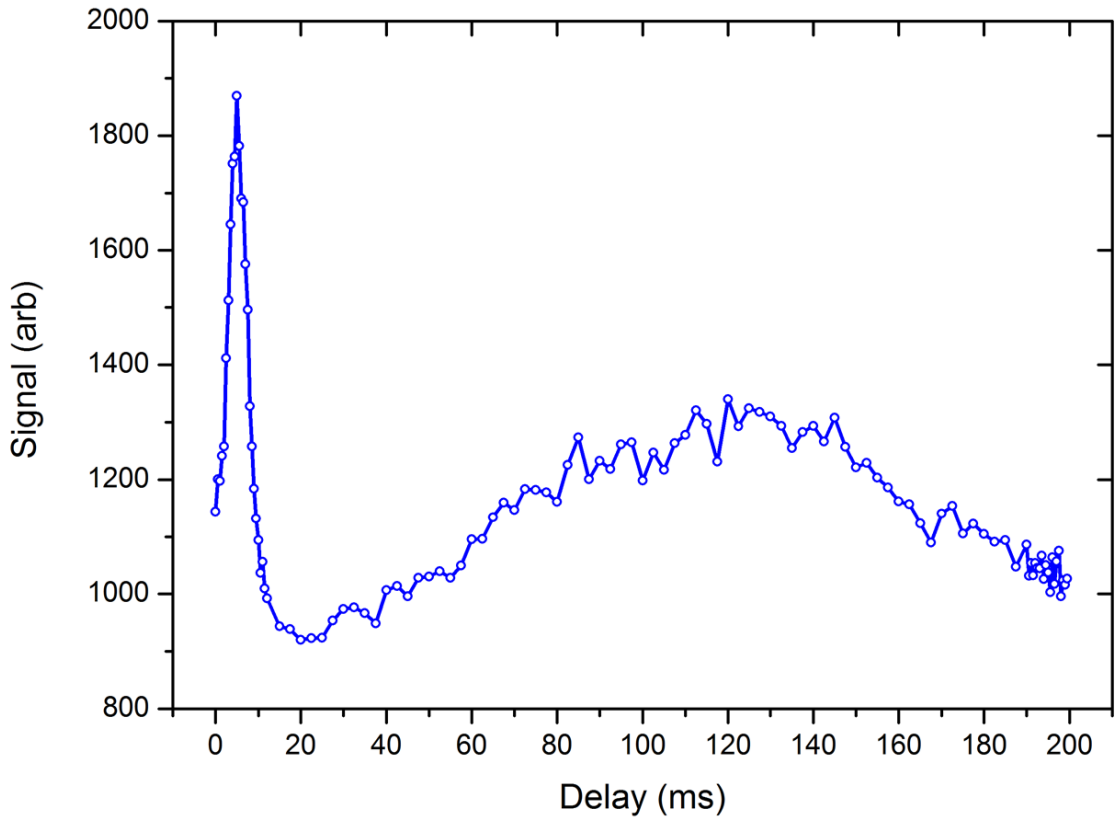

Figure 6.12: Signal from the channeltron electronics as the delay between the trigger pulses for the pulse valve and the laser was varied. For this delay scan, the system was pulsed at 5 Hz, with the channeltron voltage set to 2.45 kV. The stagnation pressure behind the valve was 0.2 bar (above atmosphere) and the valve was opened for 250 μs, with the actuation voltage set to a maximum. The laser was set to the Q_4 transition in nitrogen.

However, the efficiency of the loading process meant that nitrogen loading took a considerable amount of time. Attempts to measure a change in the efficiency with a change in the delay between the laser and the pulse valve showed no measurable variation. This confirms that no beam had made it through to the ion trap, and that any loading success was simply due to a nitrogen background.

As a result of this further characterisation of the beamline has been started. TOF spectroscopy has been used to study the molecular beam produced, which so far has been seen for the simplest setup consisting of just the pulsed valve. A nitrogen spectrum has been taken, and it has been found that the beam produced from just the pulse valve has an internal temperature of 300 K, as the relative transition amplitudes are the same as for the spectrum in chapter 5.

Future work will involve extending the characterisation by placing the primary skimmer in the beamline system. The temperature of the produced beam can then be measured by

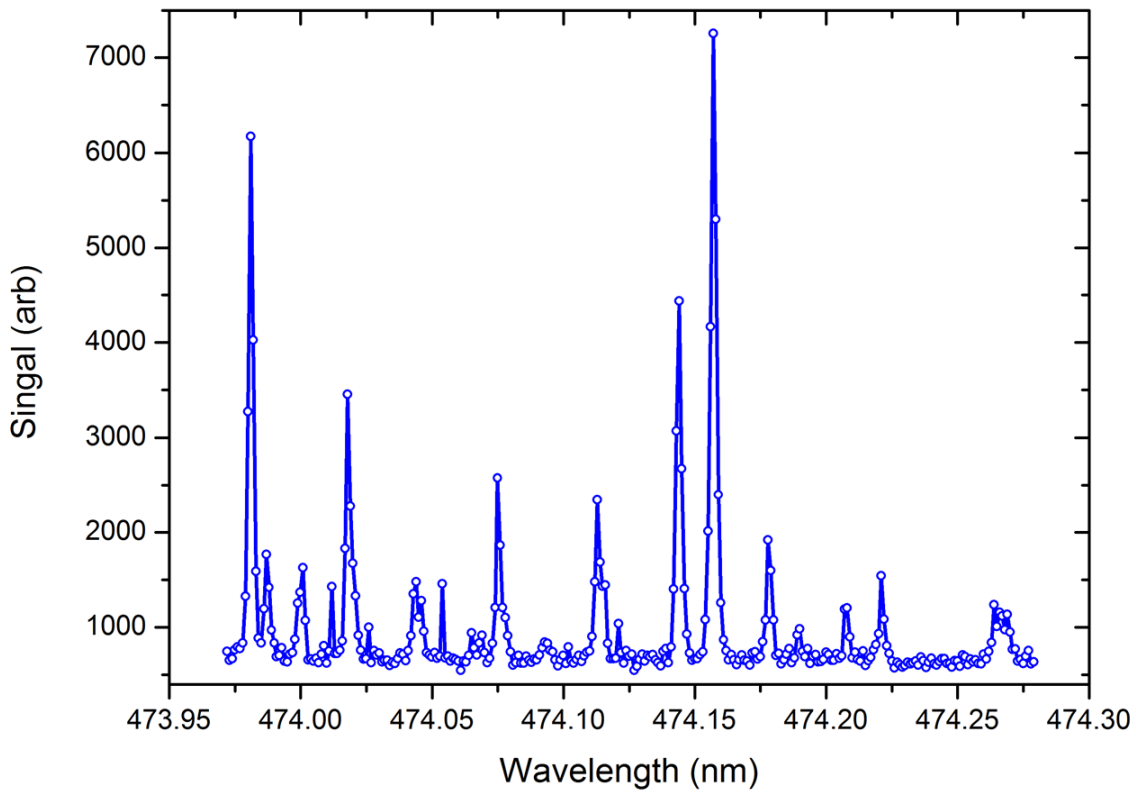

Figure 6.13: Spectrum taken of nitrogen spectroscopy setup using just the pulse valve. To completely avoid a build up of pressure, the laser was pulsed at 2 Hz, the pulse width was set to the absolute minimum of 160 μs opening time, and the stagnation pressure was 0.2 bar (above atmosphere). The delay between the dye laser and pulse valve was set to 5 ms, as this is where the maximum signal for the TOF peak sits (fig. 6.12). Each point is the sum over 60 shots.

taking another nitrogen spectrum. Further to this, the secondary skimmer can then be placed in the system, and the beam dynamics checked again. By using the spectroscopy signal the alignment of the skimmers can be optimised before the beamline is added onto the ion trap.

Once the beamline and trap system are reassembled, measurements using the crystal weighing technique and watching for a dark core can be used to assess the loading efficiency and compare this to the previous loading. After full characterisation, this efficiency should improve. Finally, it is important to be able to identify if N_2^+ is being efficiently loaded in the correct internal state, as the scheme used is not fully state-selective (see sec. 5.1). A destructive state detection technique could be used to initially check the loading efficiencies. Tong *et. al.* have a similar trap and beamline system for loading state-selected nitrogen ions alongside laser cooled $^{40}Ca^+$, and use charge exchange reactions between the

loaded nitrogen and neutral argon that is leaked into the trap system [5]. Once the N_2^+ is loaded, a spectroscopy laser is used to induce a transition from the chosen rovibrational state in $X^2\Sigma_g^+$ to an excited state $A^+\Pi_{u,3/2}(\nu = 2)$. If the ions are excited (ie. if they start in the loaded state), then they can decay back down to an excited vibrational state in the ground electronic state. Once the population is in this state, it is possible for the N_2^+ to undergo charge exchange reactions with Ar, and so the dark core of nitrogen is depleted. Not only would this be a good way to test if the REMPI scheme efficiently loads into the ground state, but it could also be used to find how long-lived the loaded state is.

Additionally trap loading could be tested with a new 2+1' REMPI scheme using Ti:sapphire lasers, as explained in sec. 5.6.

Chapter 7

Optical Forces

The proposed scheme for non-destructive state detection of molecular ions relies on the force that arises when a far-detuned laser is applied to an ion, known as the dipole force (see sec. 2.2.2). As shown in chapter 2, this force increases linearly with intensity without saturation due to the conservative nature of the force. But, in order to reduce the probability of exciting the transition being probed and subsequently causing spontaneous emission and the loss of the ion's state, the intensity has to be kept as low as possible. Therefore a compromise between how detectable the state is, and probability of losing the state during probing has to be found.

In order to enhance the detection efficiency of the state, an additional optical force can be used that does not increase the probability of state loss for the N_2^+. This is a force that is always acting on the species that sympathetically cools the N_2^+, which, in this scheme is $^{40}Ca^+$ and is the laser-induced radiation pressure force from the cooling laser. In this chapter, schemes using the radiation pressure force are investigated for the purpose of amplifying an initial small motional excitation from the state-dependent dipole force. As well as this, the oscillation that results from such an excitation can also be extended for a longer period of time. This way, the probability of state loss can be reduced by using a lower intensity dipole force laser.

Another aspect to this is the method of detecting the secular motion after the ion has been excited resonantly by the dipole force laser. Excitation of the centre-of-mass (COM) mode of the two-species two ion crystal means that the calcium ion that sympathetically cools the molecule's external degrees of freedom also oscillates at the secular frequency due to the Coulomb-interaction of the ions in the ion crystal. State readout of the molecular ion can therefore be performed with the calcium ion. The technique of Doppler velocimetry (sec. 2.2.5) is used for the detection of the COM mode motion via the cooling laser used

on the calcium ion.

As detection occurs via the cooling laser on the calcium ion, and the magnitude of the dipole force laser on the molecular ion is constrained, some extra techniques can be used involving the manipulation of the atom-light interactions between the calcium ion and its cooling laser. When the red-detuned laser used for cooling is switched onto the blue side of resonance, heating effects will occur, which can be taken advantage of for amplifying any residual motion the ion already has. The technique of full optical excitation and coherent amplification on calcium ions using the cooling transition has been demonstrated in [88]. These implementations can be adjusted so as to instead create a 'tuned damping' technique, which can sustain the oscillation of the ion for a much longer period of time. Or alternatively, the cooling laser can be switched repeatedly from amplification to damping to create a similar effect.

For this chapter, to effectively simulate the magnitude expected for the dipole force excitation, radiation pressure is used to optically kick calcium ions. In the first section, a scheme for excitation, amplification and damping using a single cooling laser on $^{40}Ca^{+}$ is described and demonstrated. In the next section, the scheme is extended to include a far longer damping period, which reduces the number of excitations needed to acquire enough signal for a measurement of the secular frequency. Two potential sequences are explored and discussed, each of which require an additional cooling laser for greater control over the parameters.

7.1 Optical excitation and amplification

7.1.1 Measurement principle

First of all a sequence is used to demonstrate excitation of the secular motion of $^{40}Ca^{+}$ using optical forces alone. The cooling laser for $^{40}Ca^{+}$ at 397 nm is employed to excite the secular motion via a rapid change in radiation pressure that occurs when the laser is rapidly switched off or on.

This laser is also used for measurement of the secular frequency after it has been excited. If the detuning from the cooling transition in $^{40}Ca^{+}$ is tuned to negative detuning (ie. to the red side of resonance) when the laser is switched on, the excited motion is damped out by the cooling. Alternatively, the laser can be tuned to the blue side of resonance, in which case the motion is instead amplified. For either of these cases, the oscillatory motion of the ion within its potential causes a modulation of the laser induced

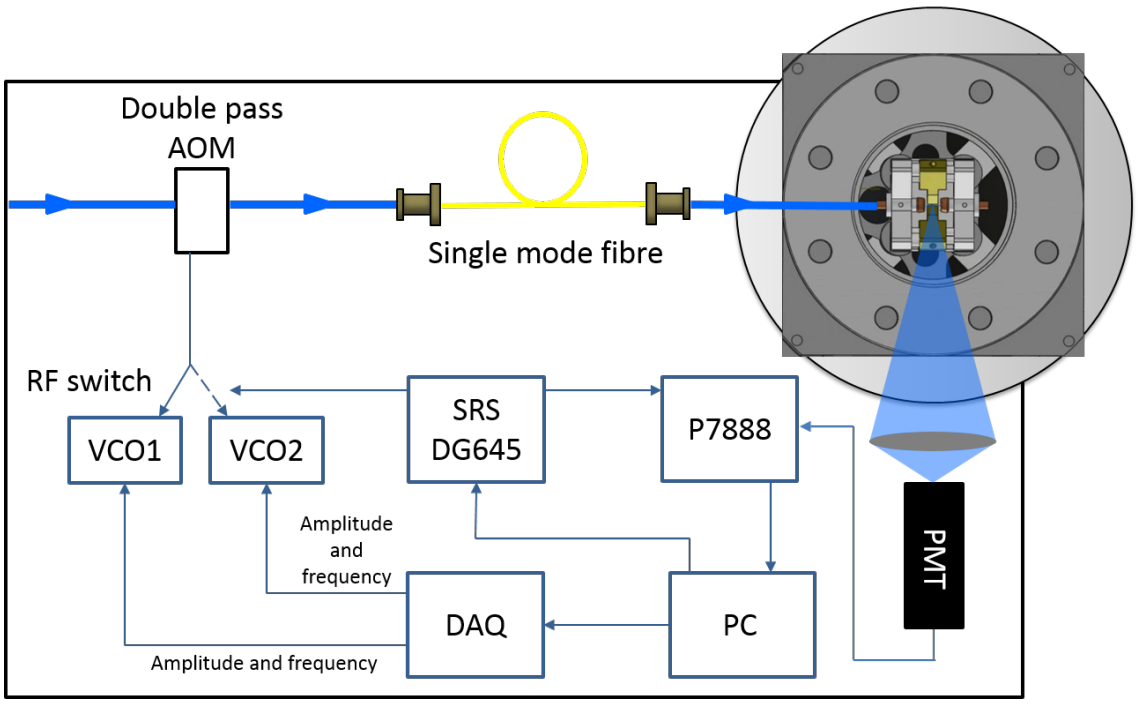

Figure 7.1: Experimental setup for optical excitation and amplification. The cooling laser at 397 nm, here seen in blue, is shifted in frequency and amplitude using a double-pass AOM setup. The laser light is then taken to the experiment via a single-mode fibre, overlapped with the repumper light (not shown in this diagram) and aligned through the axis of the ion trap. Two VCOs are used for setting the frequency and amplitude of the laser light for different parts of the sequence, and control is rapidly switched from one to the other using a delay generator triggered rf-switch. Photons are collected via a PMT and counted using a P7888 counting module.

fluorescence at the same frequency (if the motion has a component in the direction of the laser propagation). This detection technique is Doppler velocimetry, and is explained further in sec. 2.2.5.

From these concepts a full excitation, amplification and damping sequence can be used to excite the secular motion, measure the secular frequency, and cool the ion back to its initial temperature. First of all, $^{40}Ca^{+}$ is cooled by an optimally tuned cooling laser. Next, the laser is adiabatically switched off, and so the fast change in radiation pressure induces an optical 'kick' that excites the motion of the ion in the trapping potential. When the laser is switched back on, it has been tuned to the blue side of resonance, and so the motion will be amplified. This is applied for a short period before switching back to the parameters for laser cooling (red detuned). After a period the motion will be damped out and the temperature of the ion returns to its previous value. Throughout the sequence,

the laser-induced fluorescence is collected so that the secular frequency is determined using Doppler velocimetry.

7.1.2 Experimental setup

The cooling laser is set up as described in sec. 3.2.2, so that the frequency and amplitude of the laser can be precisely and quickly controlled using a VCO controlled double-pass AOM. The frequency and amplitude of the VCOs are controlled via an analogue output from the DAQ, as shown in fig. 7.1. Two lasers at 850 nm and 854 nm are used as part of the cooling scheme for repumping.

The sequence for this scheme requires fast switching of the cooling laser so it can be turned off and on rapidly to impart a radiation pressure 'kick'. Additional to this, the frequency of the laser also has to be switched quickly from the red-detuned cooling part of the sequence, to the blue-detuned amplification part. For this, an rf-switch[1], triggered by a delay generator[2], is used to change control from one of two VCOs that are set to the correct amplitude and frequency via a computer-controlled DAQ.

Fluorescence from the ions is collected via a PMT. The arrival times of the photons are recorded and binned using a fast counting module[3]. A trigger pulse from the delay generator that controls the laser sequence starts the counting. The photon arrival times can then be cross-correlated with the trigger pulse and a fast-Fourier transform (FFT) performed on the correlated data in order to determine the frequency and oscillation amplitude of the ion's motion in the trapping potential.

7.1.3 Laser switching for optical excitation and amplification

Figure 7.2 demonstrates the resulting cross-correlated fluorescence trace for an 800 μs sequence. This is the result of having repeated the sequence at a rate of 1 kHz, collecting the laser-induced fluorescence from the ion, and binning the photon arrival times with respect to the trigger. Each sequence is then summed to give the total profile, on which an FFT can be performed in order to find the secular frequency.

For the first 350 μs the laser detuning is set to the red side of resonance, so that the ion is cooled. The laser is then rapidly switched off which imparts an optical 'kick' to the ion: the fast change in radiation pressure means that the equilibrium position of the ion has changed, and so starts oscillating within the trapping potential. This can be seen as

[1] Mini-Circuits ZASWA-2-50DR

[2] SRS DG645

[3] FAST ComTec four-input multiscalar p7888 counting module

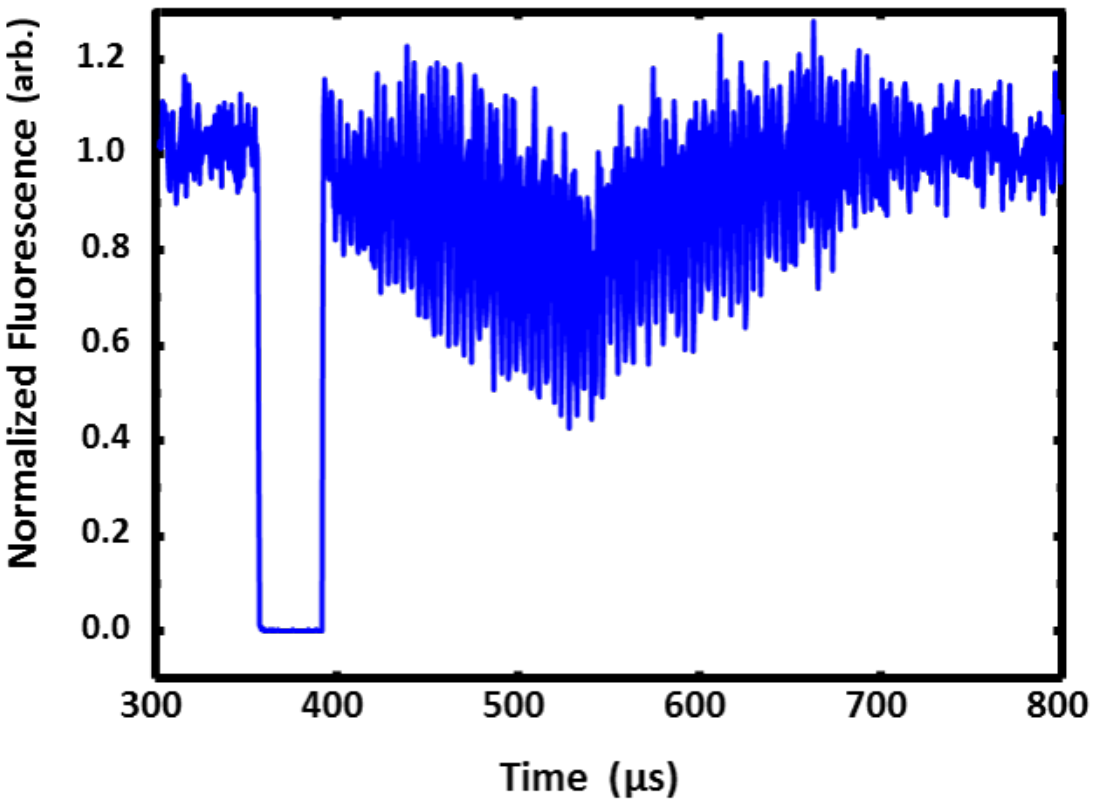

Figure 7.2: The laser-induced fluorescence of the ion during an optical excitation and amplification sequence. The laser detuning for the cooling stages is -10 MHz and for the amplification region it is set to +10 MHz.

the sharp drop in fluorescence in fig. 7.2.

After around 35 μs the laser is switched back on, although control of the AOM has been switched from VCO 1 to VCO 2, which has been set to the blue side of resonance, amplifying the motion induced by the initial radiation pressure kick. From the fluorescence profile the amplification of the motion can be seen during this blue-detuned stage. After a set time of 150 μs control is switched back to VCO 1, and the ion is cooled by the red-detuned laser. It takes another 150 μs for the motion of the ion to be cooled back to equilibrium.

7.1.4 Conclusions

This method provides a good demonstration of the optical excitation and amplification effects by using the radiation pressure force that acts on an ion in an intense laser field. It does, however, show that this sequence would not be suitable for amplifying when the state-dependent dipole force is used for the excitation. The limitation comes from not

being able to amplify for a long period of time, and that the damping part of the sequence is also a short amount of time. This means that in order to get enough signal to actually detect the force, the sequence has to be repeated many times. The more often the sequence has to be run, the more often the dipole force has to be applied. This needs to be reduced as much as possible, as exposing the ion to the dipole force for long periods of time will increase the probability of spontaneous decay of the nitrogen molecule.

7.2 Tuned Damping and switching techniques

7.2.1 Measurement principle

The aim now is to extend the sequence outlined in sec. 7.1 so that the oscillation of the ions remains for as long as possible without applying another excitation pulse. As in the previous method, this technique relies on the switching back and forth of the cooling laser for calcium from red to blue. For this method, two counter-propagating lasers are used so that two different detunings of 397 nm light can be applied simultaneously.

The sequence starts with Doppler cooling the ion. Next, this laser is switched off adiabatically to avoid excitation of the secular motion. The adiabatic switch-off is critical for ensuring that the sequence can be used for applying the dipole force excitation for the non-destructive state detection scheme. This is achieved by using a low-pass filter on the amplitude control for the VCO so that the frequency packet that contains the secular frequency of the ion crystal is suppressed.

After a period the second 397 nm laser is switched on. For the purposes of simulating the excitation from the dipole force, radiation pressure is used. Therefore this switch-on is rapid, so as to induce a radiation pressure 'kick'. When the sequence is used for the non-destructive state detection scheme, this switch-on will be adiabatic. The laser is blue-detuned for amplification of the motion from the initial excitation - whether this comes from radiation pressure or the laser-induced dipole force for state detection.

After the amplification period the motion then has to be damped out. This is where the sequence is extended in order to maintain the oscillation for a longer period without having to apply another excitation. Instead of applying an optimally tuned laser for cooling during this damping stage, there are two new approaches that can be taken. First of all is a tuned damping technique. Instead of switching off the blue-detuned laser used in the amplification stage during the damping stage, it can be left on simultaneously as the red-detuned cooling laser is adiabatically switched on (again, this is to ensure that

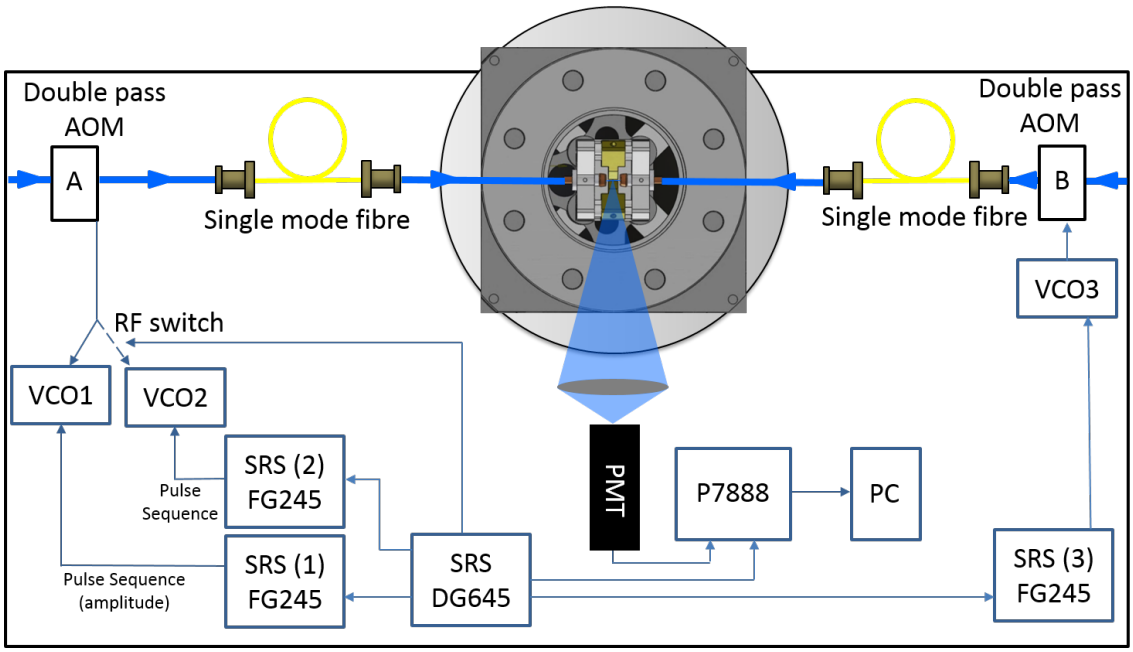

Figure 7.3: Full experimental setup for applying more complex laser pulse sequences. Two counter-propagating cooling lasers at 397 nm are used, aligned in the axial direction of the ion trap. Control of laser A is switched between two different VCOs which determine the frequency and amplitude of the beam. The AOM for laser B is controlled with one VCO. All three VCOs are frequency controlled with a DAQ (not included in this diagram for clarity), and the amplitude of each is controlled by separate programmable function generators, triggered by the delay generator. As previously, the fluorescence from the ion is collected with a PMT, and the photon arrival times counted with a P7888 counting module, triggered with the delay generator.

no additional radiation pressure 'kick' occurs at this stage). This now has the effect of increasing the time it takes to damp out the motion. Depending on the ratio of blue to red light intensity, there are three main scenarios; the system is over-damped - in which case we return to the previous sequence in sec. 7.1, the system is under-damped - in which case the motion continues to be amplified, or the system is balanced so that the oscillation time is extended for a far greater period.

The other approach is to switch between amplifying and cooling many times, so that the oscillation is not totally damped out during each cooling cycle. Instead, just before the oscillation is completely damped out, the blue-detuned laser is switched on so that the oscillation is re-amplified. This is continued for many damping-amplification cycles.

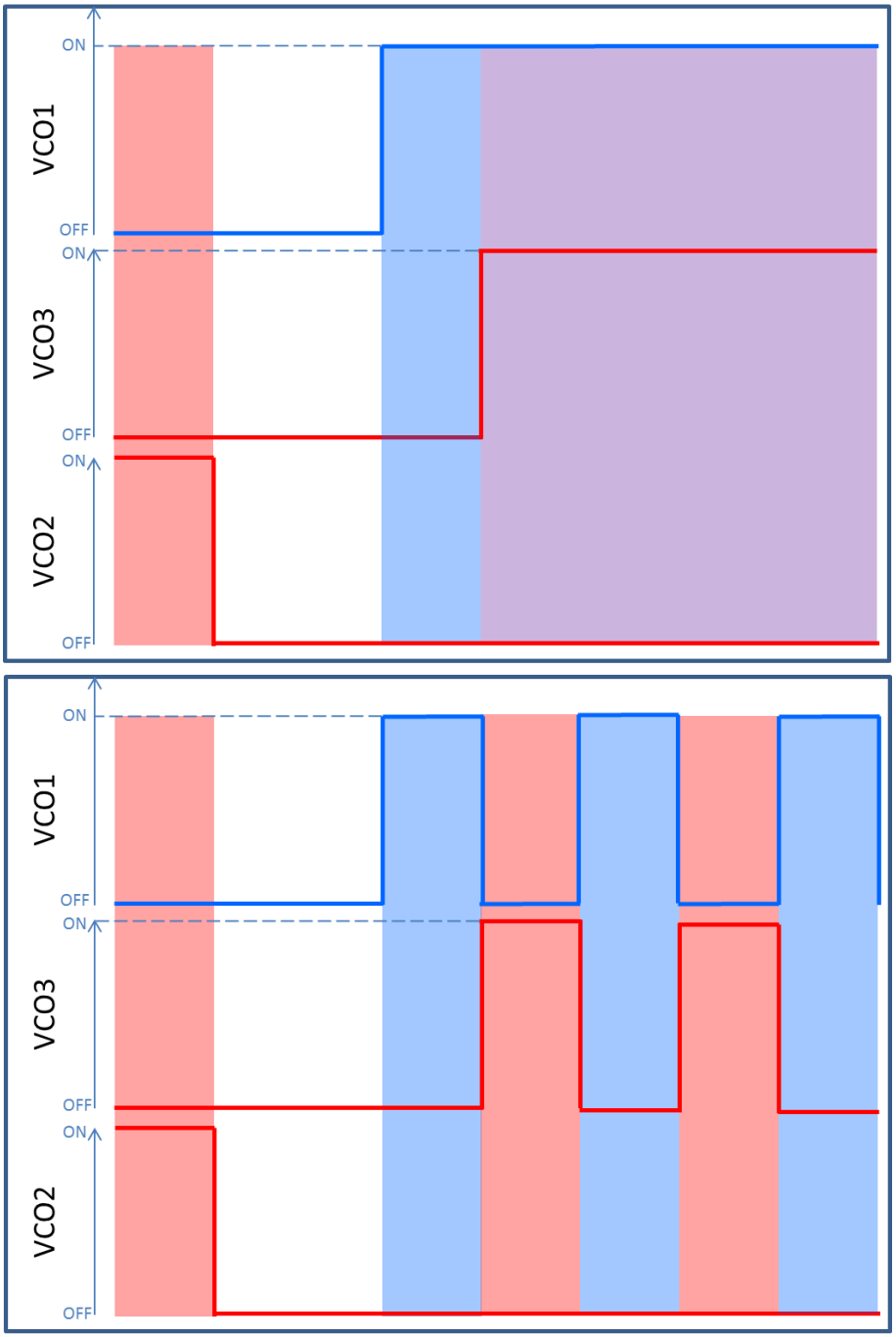

Figure 7.4: The two different sequences used. Both sequences first start with a cooling period using VCO 2, which is switched off adiabatically. VCO 1 is switched on to impart a radiation pressure-induced kick and amplify the motion. (Top) The tuned damping sequence. After some amplification time, VCO 3 is switched on adiabatically for the tuned damping part, shown in purple. (Bottom) The switching sequence. Instead of a tuned damping section, the sequence is switched from amplification to damping many times between VCO 1 and VCO 3 to sustain an oscillation. The switching for these two lasers is also adiabatic.

7.2.2 Experimental setup

The previous experimental setup for the optical excitation and amplification scheme is extended so that two counter-propagating lasers are used. One laser is switched between two different VCOs, and the other is held at a constant frequency for laser cooling. The entire scheme is controlled by the delay generator as before. The laser intensities are varied by use of three programmable function generators[4], which are triggered by the delay generator[5].

Two different sequences are explored in this chapter, although the programmable function generators allow for any sequences to be applied. The two sequences are shown in fig. 7.4.

It is important for both sequences that there is not a rapid increase or decrease in radiation pressure in places other than the excitation (which is the switch on of the blue-detuned laser). For example, in the tuned damping sequence the function generators that control the sequences of VCO 2 and VCO 3 have low-pass filters on the outputs, which blocks out the high frequency components and makes the switching slower, so as to prevent an optical excitation. A filter is also used on VCO 1 for the completely adiabatic sequences (that will be used with the dipole force as the optical excitation).

7.2.3 Phonon laser and tuned damping technique

This scheme is very similar to the simple optical kicking and amplification sequence in sec. 7.1. The first stages of cooling, rapid switching of the radiation pressure to induce an excitation of the motion, and then amplification by blue-detuning the laser are kept the same as before. The only change that is made is that the blue-detuned laser remains on for the cooling part of the sequence until the oscillation is damped out, as shown in fig 7.4 (top). The main aim is to extend out this damping period for as long as possible, so as to limit the number of excitations needed.

The damping stage needs to be carefully considered, due to the phonon laser effect [67]. If two lasers are applied simultaneously to the ion, with one detuned to the red side of resonance while the other is blue detuned, the ions' secular motion can be excited. Whether this occurs or not depends on the intensity of each of the lasers. The phonon laser effect undergoes a threshold behaviour, where there is a sudden jump to the regime in which ion excitation occurs.

[4]SRS DS345
[5]SRS DG645

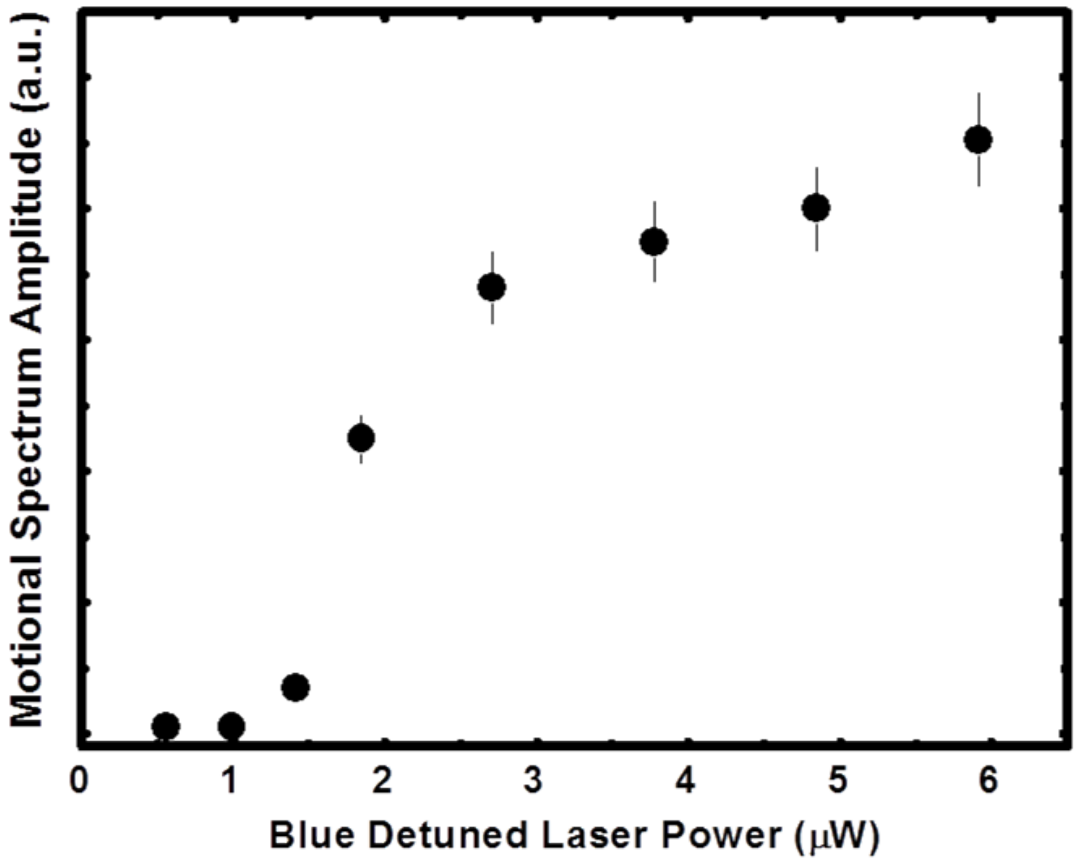

Figure 7.5: The motional spectrum amplitude as a function of the blue power when the blue detuning, red power, and red detuning are held constant. The oscillation amplitude is taken to be the mean height of the FFT peak obtained for three separate measurements, with the error bars being the standard deviation.

This threshold behaviour therefore has to be explored further. Although the main aim is to create a long period of oscillation with one excitation, there is another very important requirement. The chosen sequence has to work so that no oscillation is detectable when the sequence is used in the adiabatic regime, when no excitation is applied. This is so that when this sequence is used for the non-destructive state detection technique, the only excitation comes from the state-dependent dipole force laser, and not the sequence itself.

Figure 7.5 demonstrates the threshold nature of the phonon laser. For this, two counter propagating lasers are used, one is blue detuned, and the other is red detuned. The power and detuning of the red cooling laser are held constant, as well as the detuning for the blue laser. The trap confinement, and so the secular frequency, also remains constant for the measurement. The power of the blue detuned laser is increased, and the amplitude of the peak in the motional spectrum is measured. For the smaller powers, absolutely no oscillation can be seen. It is only when the power reaches a particular value that the

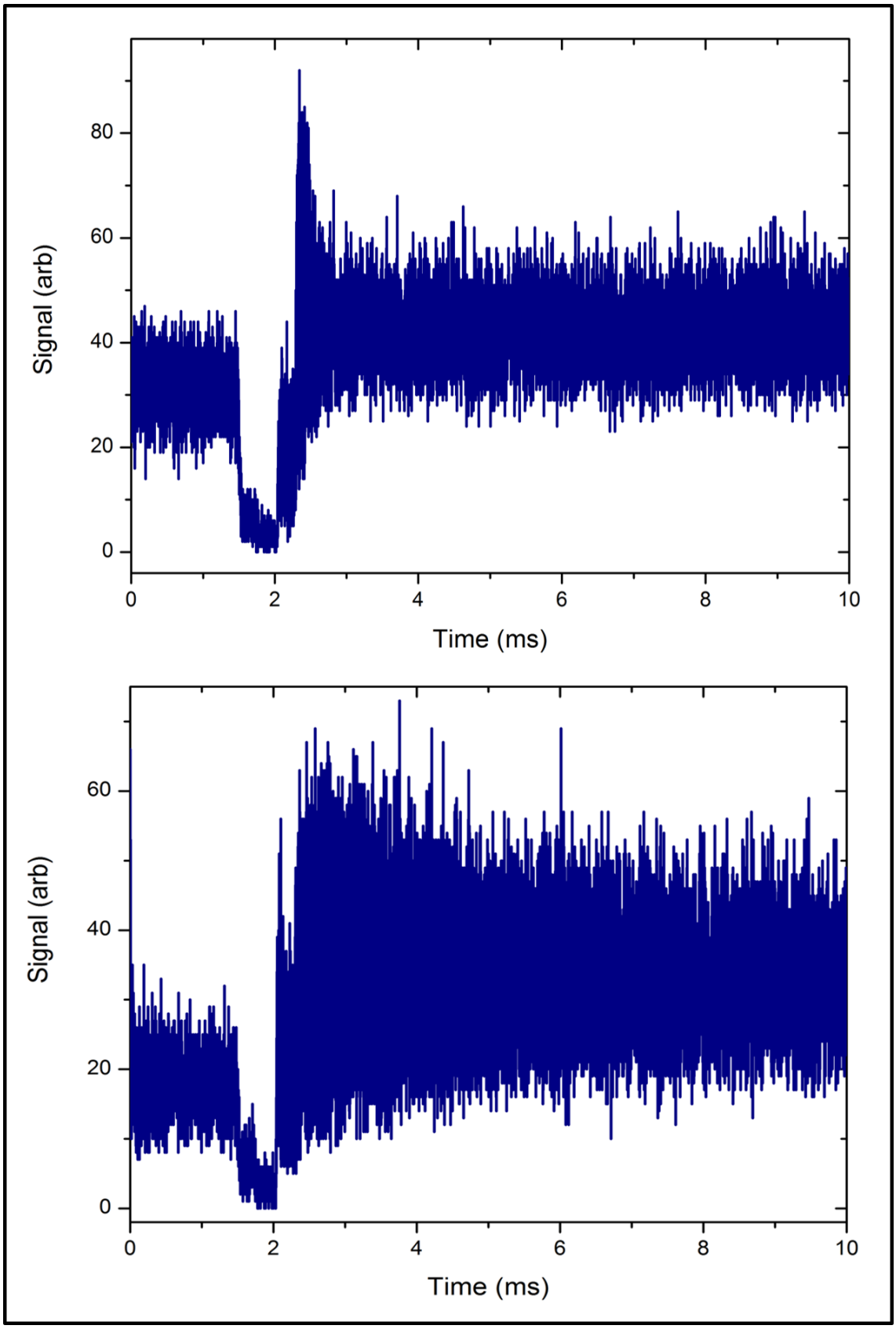

Figure 7.6: A cross correlation of photon arrival times between a starting trigger pulse and photon arrival times. This is the tuned damping sequence, which has been extended out for 10 ms. Each of the graphs demonstrate different amounts of damping out of the oscillation.

oscillation begins. Saturation of the transition means that amplitude reaches a maximum, where it flattens out. To prevent any excitation from this phonon laser effect, the laser parameters have to be set so that the system sits just below threshold.

Figure 7.6 shows the tuned damping sequence for when the parameters are set so that the system is overdamped (top) and just below threshold (bottom). The sequence has been extended for 10 ms, which is over ten times longer than the original sequence in fig. 7.2. For the overdamped sequence the oscillation dies out after the first millisecond of tuned damping, at a time of $\sim$3 ms from the trigger. However, for the case where the parameters sit just below the threshold for the phonon laser, the oscillation lasts for the full 10 ms.

7.2.4 Repeated switching technique

An alternative to the tuned damping sequence is to instead have a sequence whereby the damping and amplification stages are rapidly switched between, which is the sequence shown in fig. 7.4 (bottom). The main consideration for this sequence is to make sure that the oscillation is not damped out completely during any of the damping parts, so that is remains for as long as possible.

Figure 7.7 shows an example of the laser induced fluorescence during a repeated switching sequence. The sequence was extended out for 10 ms, although only 8 ms is shown in order to see the switching properly. More scattering events happen for the blue-detuned part, which is due to using more power in the blue-detuned laser than in the red-detuned laser. This is in order to try and avoid damping out the oscillation during the sequence.

This sequence has been characterised to find out how the oscillation amplitude changes with the power of the blue-detuned laser. The power and detuning of the red-detuned laser was held constant along with the detuning for the amplification laser. The power of the amplification laser was then stepped, and the amplitude in the motional spectrum measured, as shown in fig. 7.8.

Interestingly, there seems to be a threshold-like behaviour, similar to that of the phonon laser shown in fig. 7.5. When the blue power is very low, the initial radiation-pressure kick will be fairly small. The amplification stage is also not very effective, as a reduced power means less scattering events, and so there is no amplitude in the motional spectrum. It is only when the power in the laser is increased to 0.8 μW and above that any amplitude in the motional spectrum is seen. After reaching a maximum amplitude there is a levelling off as expected.

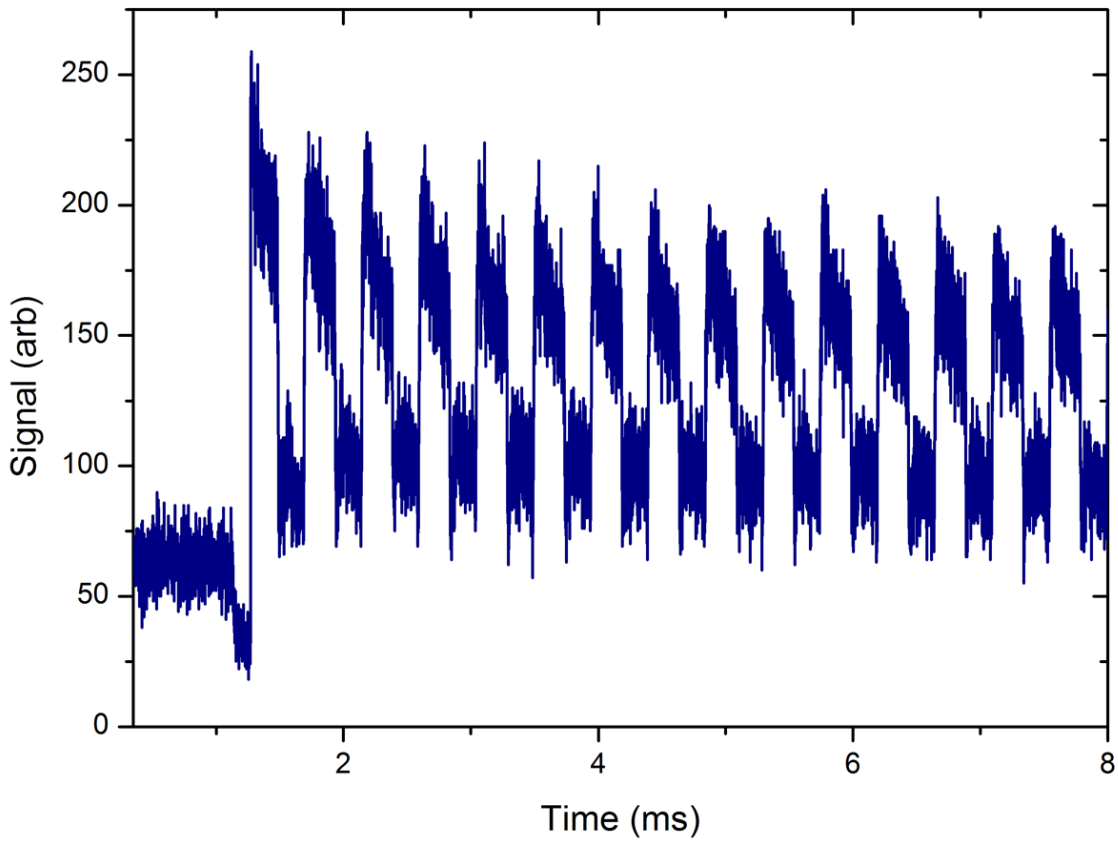

Figure 7.7: A cross correlation of photon arrival times with the trigger pulse for the repeated switching sequence, showing 8 ms of the 10 ms duration of the sequence.

7.2.5 Adiabatic switching and data analysis: Auto correlation vs. Cross correlation

The development of the pulse sequence has two main aims. The first is to amplify and then damp out the motion over as long a period of time as possible, to prolong the oscillation caused by an initial excitation. This is to reduce the amount of times the dipole force laser has to be applied. Secondly, there needs to be no oscillation caused by the sequence itself, and so it also has to be tested without an excitation at the start. This is to avoid getting any false positives for state detection.

The first part of both sequences that have been looked at is the laser switch off. During this time, there is no damping force on the ion as there is no cooling applied. This is vital for applying the dipole force excitation laser, and means that the ion receives the full excitation force with no damping. Next, the 397 nm laser is switched back on, but tuned to blue. In the test sequences that have appeared in this chapter so far, this has been the excitation pulse used to start the whole sequence. When the state-dependent excitation is applied instead, this 397 nm laser switch on has to be adiabatic, so as not to use the

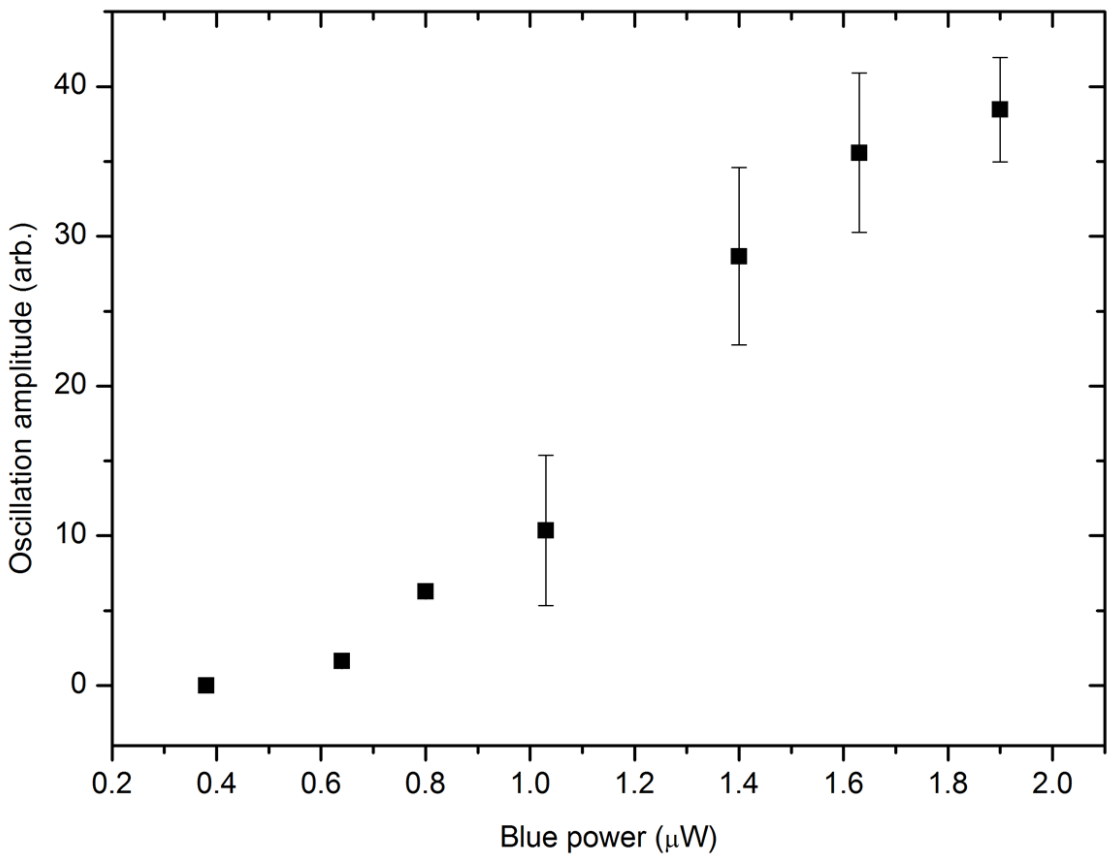

Figure 7.8: The oscillation amplitude as a function of the blue power when the blue detuning, red power, and red detuning are held constant. For this measurement the blue detuning was set at +20 MHz, with the red power and detuning set to 25.5 μ W and -5 MHz respectively. The oscillation amplitude is taken to be the mean height of the FFT peak obtained for three separate measurements, with the error bars being the standard deviation.

non-state dependent radiation force for excitation.

It has been found that the method of analysis has a strong bearing on how achievable this is, and is illustrated in fig. 7.9. For each of the four graphs exactly the same settings have been used. The only difference is that the sequence used for the top two graphs (a) and (c) uses a fast switch on radiation pressure excitation, and the bottom two (b) and (d) instead have no excitation applied, with the laser switch-on being adiabatic. The fluorescence has been analysed in two different ways, using cross-correlation and auto-correlation.

For the auto-correlation a large peak appears at the COM mode frequency of the ion crystal. The amplitude of oscillation is of the same magnitude, although for the adiabatic case the amplitude is a little smaller. For the cross correlation results, the kick graph (c)

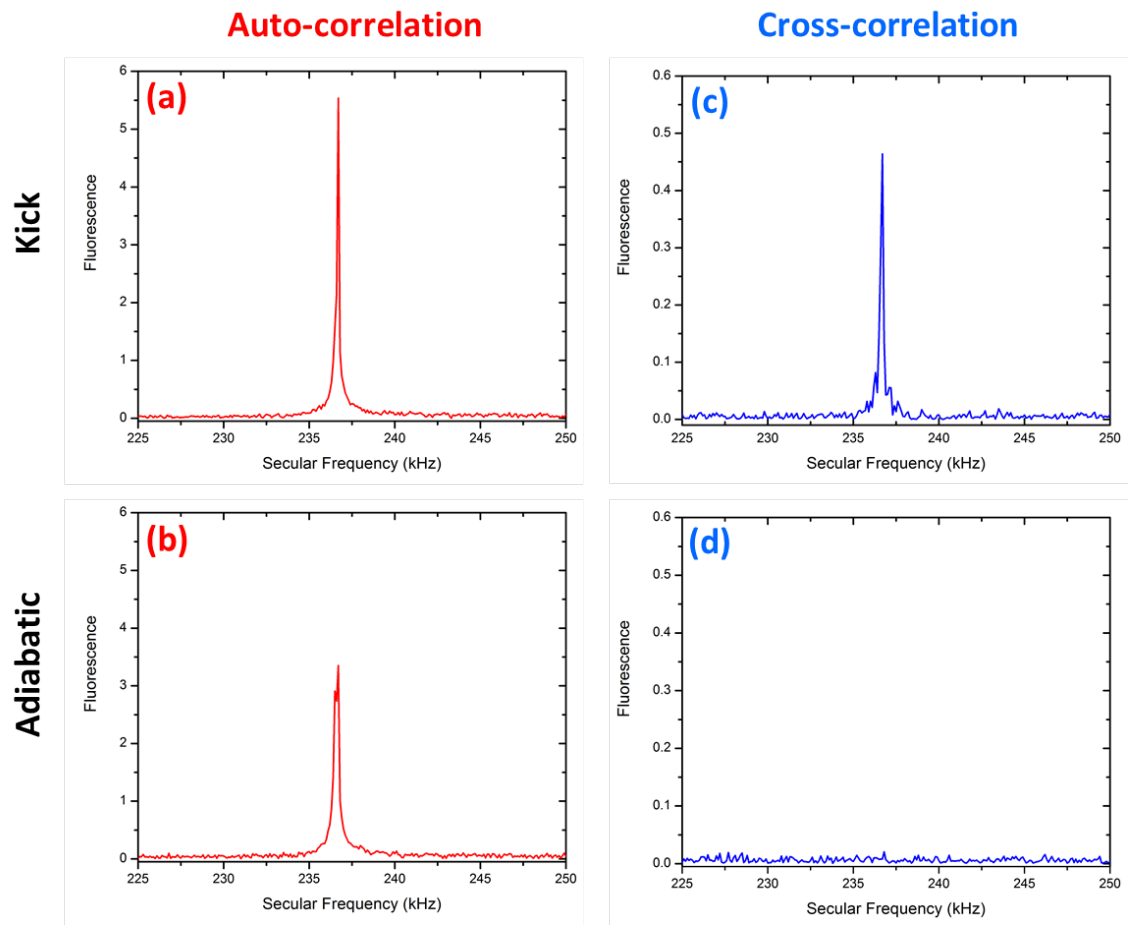

Figure 7.9: Examples of fast-Fourier transforms to demonstrate the difference between analysis with the cross-correlation and auto-correlation for both *kicking* and *adiabatic* cases. Power and detuning settings were kept constant for each of the measurements. For graphs (a) and (b), the auto-correlation is used. For (c) and (d) the cross-correlation has been used (note that the y-axis changes by a factor of 10 from auto- to cross-correlation). This demonstrates that although a larger signal is obtained for the auto-correlation, the cross-correlation will have to be used for the state detection measurement to avoid exciting the motion regardless of the state.

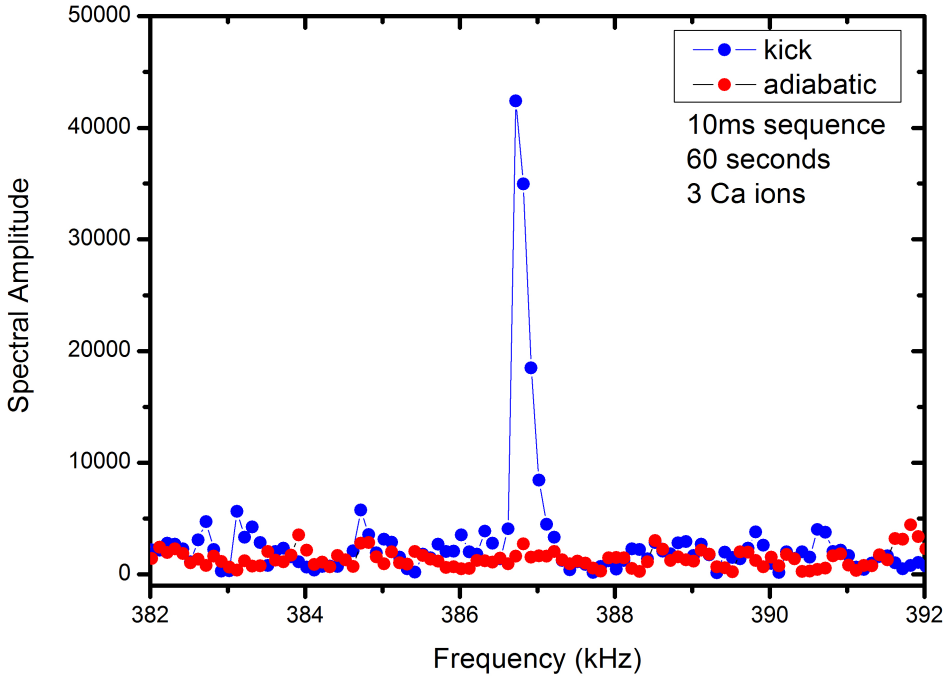

Figure 7.10: Fast-Fourier transforms of a cross correlated sequence for when the sequence has a radiation pressure kick (blue) and when it is completely adiabatic (red).

is an order of magnitude smaller, but, when the adiabatic case is used, there is no peak at all (part (d)). This means that for analysis, it is vital to use the cross correlation in order to avoid false positives during non-destructive state detection of nitrogen ions.

This is due to the requirement for the cross-correlation to have the same phase of oscillation for every cycle of the sequence. Blue-detuning the cooling laser will have the effect of exciting the secular motion, but without a well defined initial 'kick' the phase will be different for each cycle. Therefore, if the cross-correlation is used, the sum over each cycle cancels to zero. However, if the auto correlation is used, the phase information is not as critical, as this is a correlation of every photon arrival time with all of the other photon arrival times. And so, even is there is no fixed phase information for each cycle in the form of a 'kick', the FFT still reveals some amplitude at the secular frequency.

Figure. 7.10 shows a direct comparison for a sequence that includes an initial radiation pressure kick with a completely adiabatic sequence, both of which have been analysed using a cross-correlation.

7.3 Summary/Conclusions

A versatile technique for all-optical excitation, amplification and damping has been demonstrated. First of all, a simple sequence with short intervals of amplification and damping was used, with the laser-induced fluorescence collected via Doppler velocimetry. This established the working principles of such a sequence. However, the short time interval over which this sequence runs is not quite suitable for use in the non-destructive state detection scheme.

As a result the experimental setup was altered so that a second VCO-controlled cooling laser could be added for a more flexible arrangement, which allowed for more complex pulse sequences to be tested. Two sequences have been used; one of which has a tuned damping stage for extending out the oscillation of the ion, and the other switches rapidly between amplification and damping. Both sequences had a similar response and could be extended out for an order of magnitude larger than that of the original sequence in sec. 7.1. With such a time span it has been estimated that the sequence would need to run repeatedly over 15 s for a detectable signal. Over this time, if the dipole force laser is applied for 100 μs per sequence, there is a 50 % probability of spontaneous decay of the N_2^+. This is not suitable for the non-destructive scheme, and so further improvements have to be made to the sequence. An additional problem is that of the phase of the dipole force intensity gradient applied over this time span. Figure 7.11 shows the proposed method for applying an intensity gradient that beats at the COM mode frequency of the ion crystal, a walking wave interferometer. The 787 nm laser used for applying the dipole force to the molecular ion is overlapped with an 866 nm laser, which can be used as a repumper for laser cooling $^{40}Ca^+$, and confirms good alignment of the lasers with the ion crystal. The beam is then split into two separate arms, each of which is aligned into an AOM to shift the frequency so that the difference between the two arms is equal to the secular frequency of the ion crystal.

The two beams are then aligned through the ion trap so that they are counter-propagating in the axial direction. They are overlapped so as to create the walking wave for state-dependent motional excitation. So a crucial part to the technique is that the intensity gradient at the ion is always at the same phase if repeated kicking is used for a single measurement. It is unknown if the interferometer can maintain such stability over such a long period of time, but a preferred sequence would use only one dipole force 'kick' for a single measurement, to rule out any stability issues.

Therefore some further work on this sequence to try and extend it out for a single-shot

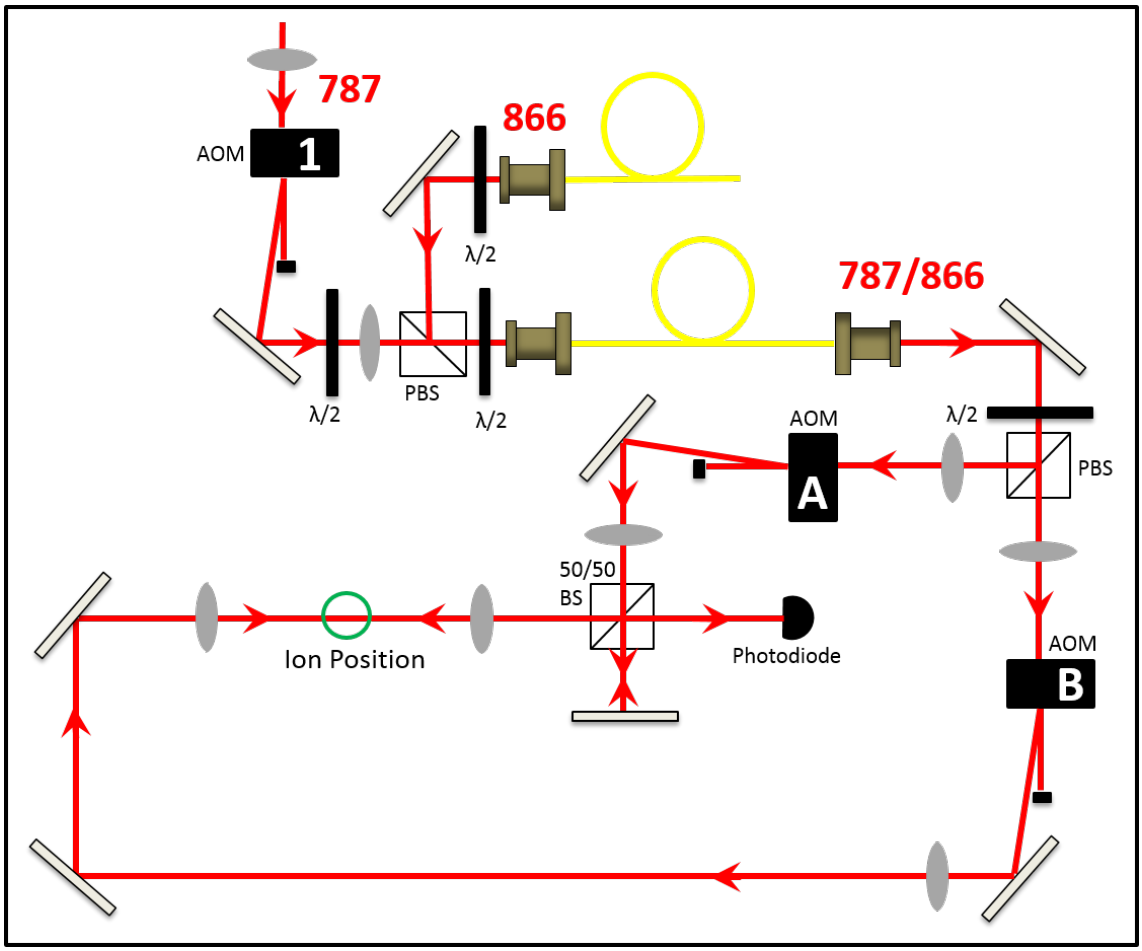

Figure 7.11: Setup of the proposed walking wave interferometer used to resonantly excite the motion of the Ca^+-N_2^+ Coulomb crystal.

measurement is required. A second VCO could be added to AOM B in fig. 7.3 which would enable a sequence where the amplification stage could be extended in a similar way to the damping.

Another important issue is the stability of the cooling laser. Although the cooling laser can be locked using the setup in chapter 4, the stability requirements could be aided by power broadening the cooling transition of the $^{40}Ca^+$. A broadened line would mean a smaller change in radiation pressure if there are any fluctuations at all. Of course, this would be limited by the desire to keep the ion crystal at a low temperature. It would be interesting to test the sequence for a well cooled ion compared to when the lineshape is broadened.

Chapter 8

Conclusion

8.1 Summary

In this thesis, experimental techniques for molecular ions in traps have been developed with the main aim of performing high resolution spectroscopy on N_2^+. These techniques also have a wider appeal to other fields for which molecular ions potentially play a central role, such as the study of cold chemical reactions, improved frequency standards and quantum computing.

A working ion trap has been set up and characterised with calcium ions, the working principles of which are described in sec. 2.1, with the complete trap and laser setup used illustrated in chapter 3. Calcium atoms are ionised with a resonant ionisation process and can be routinely trapped and laser cooled using this system.

In chapter 4, a technique for spectroscopy on dipole allowed transitions in trapped ions has been demonstrated on $^{40}Ca^+$, where it is possible to plot the full, symmetric lineshape of the the $4S_{1/2} \rightarrow 4P_{1/2}$ transition. By rapidly switching between short intervals of transition probing and optimal laser cooling, probing of regions where the ion is actively heated is achieved without distortion of the lineshape. Using this technique, good determination of where linecentre sits is possible, and the shape of the line can be analysed so that the Lorentzian and Gaussian contributions can be measured. Additional to this, a second probe can be introduced that is slightly detuned from the first, and a dispersive-like signal obtained. When the transition is probed repeatedly in this manner, the collected fluorescence can be used to generate an error signal for feedback to the cooling laser for stabilisation. From the measured Allan variance a frequency instability of better than 10^{-10} is obtained for an interrogation time of 1000 s. Frequency stabilisation of the cooling laser is vital for the techniques described in sec. 2.3.3 and chapter 7.

The ionisation scheme for nitrogen molecules and experimental setup for performing ionisation spectroscopy are described in chapter 5. The higher degree of complexity of molecular structure means that internal state preparation is more challenging. The 2+1 REMPI process used has the dual purpose of ionising N_2 for trap loading, and also preparing the molecule in the desired state, which is $X^2\Sigma_g^+(N = 0, \nu = 0)$. Ionisation spectroscopy has been performed on the $a^1\pi_g(\nu = 10) \longleftarrow X^2\Sigma_g^+(\nu = 0)$ band of N_2 using a time-of-flight (TOF) mass spectrometry setup. By using the PGopher simulation tool and literature values, the suitable transitions could be identified. An internal temperature of 300 K was obtained from the spectrum.

The source of the neutral nitrogen for the 2+1 REMPI scheme determines how efficient the process is. If the internal temperature of the N_2 is at room temperature, then there is a reduced population in the lower rotational states where the ionisation scheme starts from. Therefore an internal cooling scheme has to be employed, which is achieved by using a supersonic expansion as described in chapter 6. A molecular beamline system has been set up, and trap loading of N_2^+ which is sympathetically cooled by $^{40}Ca^+$ has been achieved, detection of which is carried out by using the technique of crystal weighing. Full characterisation of the beamline system is required, and has been started with the assembly of the beamline with the ionisation spectroscopy setup. Spectroscopy using the pulsed valve source has been demonstrated. Further work will include inserting the skimmers for additional analysis and alignment of the system.

The nature of the non-destructive state detection scheme for which the experiments in this thesis are precursors means that detection of very small forces applied to a single ion is vital. The scheme will employ the dipole force interaction from a laser, which can induce a force that is state-selective, as discussed in sec. 2.3.3. The force will be modulated at the frequency of the COM mode of motion of the $^{40}Ca^+$-N_2^+ Coulomb crystal. This means that N_2^+ prepared in a particular state will undergo resonant excitation of its motion (along with the $^{40}Ca^+$ coolant and readout ion), whereas N_2^+ prepared in any other state will not. Oscillations at the secular frequency can be detected using the Doppler velocimetry technique, for which the laser-induced fluorescence of the $^{40}Ca^+$ is used. The expected magnitude of the dipole force is on the order of zepto Newtons, as calculated in sec. 2.3.3. In order to make this force detectable, an amplification and tuned damping technique has been demonstrated in chapter 7, which can be utilised to extend out an initial weak excitation for over 10 ms. This will reduce the amount of time for which the dipole force laser is applied, and so reducing the probability of spontaneous decay from the molecule

which would incur the loss of the prepared state.

8.2 Outlook

All of the techniques outlined in this thesis can be used to contribute to the ultimate goal of performing high-resolution spectroscopy on N_2^+. Once the molecular beamline has been fully characterised, it can be used to provide internally cold neutral molecules to the ion trap, where previously loaded $^{40}Ca^+$ are in place. The 2+1 REMPI laser will be timed with the cold molecular beam so that state prepared N_2^+ are loaded, where sympathetic cooling via the laser cooled $^{40}Ca^+$ takes place. The presence of a loaded nitrogen ion can be inferred by the process of crystal weighing, which will then dictate if an additional loading attempt is required, or if the experiment can continue.

The non-destructive state detection scheme can then be used to determine if the load has yielded an N_2^+ in the $X^2\Sigma_g^+(N = 0, \nu = 0)$ state. The scheme for detecting the small motional excitation from the dipole force laser will extend out the oscillation without increasing the probability of losing the molecule's state. The $^{40}Ca^+$ cooling laser used for the amplification and tuned damping of the motion will be locked to the $4S_{1/2} \rightarrow 4P_{1/2}$ transition in a trapped $^{40}Ca^+$ in a separate ion trap system for stabilisation.

Once the successful load of an N_2^+ in the required state is confirmed, high-resolution spectroscopy can be implemented. The scheme for this has been proposed by Kajita *et. al.*, who have found that particular transitions in N_2^+ demonstrate good properties for detection of a possible time variation of the fundamental constant μ (the proton to electron mass ratio m_p/m_e) [30]. An important consideration for making precision measurements of transitions is how they are affected by the environment. Shifts due to environmental influences such as the Zeeman and Stark shifts incur systematic errors, which need to be kept at a minimum. For one of the proposed transitions, $(\nu = 2) \longleftarrow (\nu = 0)$ in the electronic state $X^2\Sigma_g^+$, the Zeeman, Stark, quadrupole and blackbody shifts have all been calculated to reveal smaller systematics than other proposed molecules, such as CaH^+ [89] and HD^+ [25]. Additionally, the very small natural linewidth of the $(\nu = 2) \longleftarrow (\nu = 0)$ transition is less than 0.1 Hz and is therefore ideal for high precision measurements. Furthermore, the spectroscopic method for measuring the chosen transitions means that the induced AC Stark shift from the lasers applied can be cancelled out. Raman spectroscopy can be employed for this. At specific 'magic' wavelengths, if the two lasers used for the Raman transition have the same power, then the Stark shifts cancel out to zero.

The techniques used for this will allow for precise determination of the transition

energies measured, which will lead to a better constraint on the variation of the constant μ. Furthermore, all of the techniques described here have a wider appeal to the field of molecular ions in physics and chemistry.

Bibliography

[1] N. W. McLachlan, *Theory and Application of Mathieu functions*. Oxford University Press, 1951. Cited on x, 12, 13

[2] J. M. Brown, *Molecular Spectroscopy*. Oxford University Press, 2003. Cited on xi, 36, 37, 40, 44, 45

[3] S. Opitz, D. Proch, T. Trickl, and K. Kompa, "State-selective ionization of nitrogen by resonance-enhanced three- and four-photon excitation," *Chemical Physics*, vol. 143, no. 2, pp. 305 – 323, 1990. Cited on xi, 48, 49, 50, 100, 103, 105

[4] A. Lofthus and P. H. Krupenie, "The spectrum of molecular nitrogen," *Journal of Physical and Chemical Reference Data*, vol. 6, no. 1, 1977. Cited on xi, 48, 103

[5] X. Tong, A. H. Winney, and S. Willitsch, "Sympathetic cooling of molecular ions in selected rotational and vibrational states produced by threshold photoionization," *Phys. Rev. Lett.*, vol. 105, p. 143001, Sep 2010. Cited on xv, 3, 4, 5, 49, 106, 107, 108, 127

[6] G. Scoles, *Atomic and Molecular Beam Methods: Volume 1*. Oxford University Press, 1988. Cited on xv, 109, 110, 112

[7] S. Willitsch, "Coulomb-crystallised molecular ions in traps: methods, applications, prospects," *International Reviews in Physical Chemistry*, vol. 31, no. 2, pp. 175–199, 2012. Cited on 1

[8] T. Rosenband, D. B. Hume, P. O. Schmidt, C. W. Chou, A. Brusch, L. Lorini, W. H. Oskay, R. E. Drullinger, T. M. Fortier, J. E. Stalnaker, S. A. Diddams, W. C. Swann, N. R. Newbury, W. M. Itano, D. J. Wineland, and J. C. Bergquist, "Frequency ratio of Al^+ and Hg^+ single-ion optical clocks; metrology at the 17th decimal place," *Science*, vol. 319, no. 5871, pp. 1808–1812, 2008. Cited on 1, 80

[9] H. S. Margolis, G. P. Barwood, G. Huang, H. A. Klein, S. N. Lea, K. Szymaniec, and P. Gill, "Hertz-level measurement of the optical clock frequency in a single $^{88}Sr^+$ ion," *Science*, vol. 306, no. 5700, pp. 1355–1358, 2004. Cited on 1, 80

[10] S. Schiller and V. Korobov, "Tests of time independence of the electron and nuclear masses with ultracold molecules," *Phys. Rev. A*, vol. 71, p. 032505, Mar 2005. Cited on 1, 2

[11] J. J. Hudson, B. E. Sauer, M. R. Tarbutt, and E. A. Hinds, "Measurement of the electron electric dipole moment using YbF molecules," *Phys. Rev. Lett.*, vol. 89, p. 023003, Jun 2002. Cited on 1, 2

[12] M. Quack, J. Stohner, and M. Willeke, "High-resolution spectroscopic studies and theory of parity violation in chiral molecules," *Annual Review of Physical Chemistry*, vol. 59, no. 1, pp. 741–769, 2008. PMID: 18173376. Cited on 1

[13] T. Zelevinsky, S. Kotochigova, and J. Ye, "Precision test of mass-ratio variations with lattice-confined ultracold molecules," *Phys. Rev. Lett.*, vol. 100, p. 043201, Jan 2008. Cited on 1, 2

[14] D. DeMille, S. Sainis, J. Sage, T. Bergeman, S. Kotochigova, and E. Tiesinga, "Enhanced sensitivity to variation of m_p/m_e in molecular spectra," *Phys. Rev. Lett.*, vol. 100, p. 043202, Jan 2008. Cited on 1

[15] S. Ospelkaus, K.-K. Ni, D. Wang, M. H. G. de Miranda, B. Neyenhuis, G. Quéméner, P. S. Julienne, J. L. Bohn, D. S. Jin, and J. Ye, "Quantum-state controlled chemical reactions of ultracold potassium-rubidium molecules," *Science*, vol. 327, no. 5967, pp. 853–857, 2010. Cited on 1

[16] T. T. Wang, M.-S. Heo, T. M. Rvachov, D. A. Cotta, and W. Ketterle, "Deviation from universality in collisions of ultracold $^6Li_2$ molecules," *Phys. Rev. Lett.*, vol. 110, p. 173203, Apr 2013. Cited on 1, 3

[17] S. Willitsch, M. T. Bell, A. D. Gingell, and T. P. Softley, "Chemical applications of laser- and sympathetically-cooled ions in ion traps," *Phys. Chem. Chem. Phys.*, vol. 10, pp. 7200–7210, 2008. Cited on 1, 2, 4, 25, 120

[18] D. DeMille, "Quantum computation with trapped polar molecules," *Phys. Rev. Lett.*, vol. 88, p. 067901, Jan 2002. Cited on 1

[19] K. Sheridan and M. Keller, "Weighing of trapped ion crystals and its applications," *New Journal of Physics*, vol. 13, no. 12, p. 123002, 2011. Cited on 1, 77

[20] M. Drewsen, A. Mortensen, R. Martinussen, P. Staanum, and J. L. Sørensen, "Nondestructive identification of cold and extremely localized single molecular ions," *Phys. Rev. Lett.*, vol. 93, p. 243201, Dec 2004. Cited on 1

[21] T. Nicholson, S. Campbell, R. Hutson, G. Marti, B. Bloom, R. McNally, W. Zhang, M. Barrett, M. Safronova, G. Strouse, W. Tew, and J. Ye, "Systematic evaluation of an atomic clock at 2 x 10^{-18} total uncertainty," *Nature Communications*, vol. 6, March 2015. Cited on 2

[22] M. de Angelis, M. Angonin, Q. Beaufils, C. Becker, A. Bertoldi, K. Bongs, T. Bourdel, P. Bouyer, V. Boyer, S. Drscher, H. Duncker, W. Ertmer, T. Fernholz, T. Fromhold, W. Herr, P. Krger, C. Krbis, C. Mellor, F. P. D. Santos, A. Peters, N. Poli, M. Popp, M. Prevedelli, E. Rasel, J. Rudolph, F. Schreck, K. Sengstock, F. Sorrentino, S. Stellmer, G. Tino, T. Valenzuela, T. Wendrich, A. Wicht, P. Windpassinger, and P. Wolf, "isense: A portable ultracold-atom-based gravimeter," *Procedia Computer Science*, vol. 7, pp. 334 – 336, 2011. Proceedings of the 2nd European Future Technologies Conference and Exhibition 2011 (FET 11). Cited on 2

[23] M. Godun, R. B. R. Nisbet-Jones, P. M. Jones, J. A. King, S. A. M. Johnson, L. S. Margolis, H. K. Szymaniec, N. Lea, S. K. Bongs, and P. Gill, "Frequency ratio of two optical clock transitions in $^{171}Yb^+$ and constraints on the time variation of fundamental constants," *Phys. Rev. Lett.*, vol. 113, p. 210801, Nov 2014. Cited on 2

[24] C. W. Chou, D. B. Hume, J. C. J. Koelemeij, D. J. Wineland, and T. Rosenband, "Frequency comparison of two high-accuracy Al^+ optical clocks," *Phys. Rev. Lett.*, vol. 104, p. 070802, Feb 2010. Cited on 2

[25] S. Schiller, D. Bakalov, and V. I. Korobov, "Simplest molecules as candidates for precise optical clocks," *Phys. Rev. Lett.*, vol. 113, p. 023004, Jul 2014. Cited on 2, 148

[26] P. Jansen, H. L. Bethlem, and W. Ubachs, "Perspective: Tipping the scales: Search for drifting constants from molecular spectra," *The Journal of Chemical Physics*, vol. 140, no. 1, pp. –, 2014. Cited on 2

[27] J. K. Webb, V. V. Flambaum, C. W. Churchill, M. J. Drinkwater, and J. D. Barrow, "Search for time variation of the fine structure constant," *Phys. Rev. Lett.*, vol. 82, pp. 884–887, Feb 1999. Cited on 2

[28] A. L. Wolf, S. A. van den Berg, C. Gohle, E. J. Salumbides, W. Ubachs, and K. S. E. Eikema, "Frequency metrology on the $4s^2S_{12}$-$4p^2P_{12}$ transition in $^{40}Ca^+$ for a comparison with quasar data," *Phys. Rev. A*, vol. 78, p. 032511, Sep 2008. Cited on 2, 82

[29] N. Huntemann, B. Lipphardt, C. Tamm, V. Gerginov, S. Weyers, and E. Peik, "Improved limit on a temporal variation of m_p/m_e from comparisons of Yb^+ and cs atomic clocks," *Phys. Rev. Lett.*, vol. 113, p. 210802, Nov 2014. Cited on 2

[30] M. Kajita, G. Gopakumar, M. Abe, M. Hada, and M. Keller, "Test of m_p/m_e changes using vibrational transitions in N_2^+," *Phys. Rev. A*, vol. 89, p. 032509, Mar 2014. Cited on 2, 6, 29, 148

[31] M. T. Bell and T. P. Softley, "Ultracold molecules and ultracold chemistry," *Molecular Physics*, vol. 107, no. 2, pp. 99–132, 2009. Cited on 2

[32] L. Ratschbacher, C. Zipkes, C. Sias, and M. Köhl, "Controlling chemical reactions of a single particle," *Nature Physics*, vol. 8, pp. 649 – 652, Sept. 2012. Cited on 3, 5

[33] R. V. Krems, "Molecules near absolute zero and external field control of atomic and molecular dynamics," *International Reviews in Physical Chemistry*, vol. 24, no. 1, pp. 99–118, 2005. Cited on 3

[34] I. S. Vogelius, L. B. Madsen, and M. Drewsen, "Blackbody-radiation assisted laser cooling of molecular ions," *Phys. Rev. Lett.*, vol. 89, p. 173003, Oct 2002. Cited on 3

[35] P. F. Staanum, K. Højbjerre, P. S. Skyt, A. K. Hansen, and M. Drewsen, "Rotational laser cooling of vibrationally and translationally cold molecular ions," *Nature*, vol. 6, pp. 271–274, Mar 2010. Cited on 3, 5, 120

[36] T. Schneider, B. Roth, H. Duncker, I. Ernsting, and S. Schiller, "All-optical preparation of molecular ions in the rovibrational ground state," *Nature*, vol. 6, pp. 275–278, Mar 2010. Cited on 3, 5, 120

[37] S. Willitsch and F. Merkt, "Rovibronic photoionization dynamics of asymmetric-top molecules," *International Journal of Mass Spectrometry*, vol. 245, no. 13, pp. 14 – 25, 2005. Cited on 3

[38] J. B. Wübbena, S. Amairi, O. Mandel, and P. O. Schmidt, "Sympathetic cooling of mixed-species two-ion crystals for precision spectroscopy," *Phys. Rev. A*, vol. 85, p. 043412, Apr 2012. Cited on 4

[39] D. Kielpinski, B. E. King, C. J. Myatt, C. A. Sackett, Q. A. Turchette, W. M. Itano, C. Monroe, D. J. Wineland, and W. H. Zurek, "Sympathetic cooling of trapped ions for quantum logic," *Phys. Rev. A*, vol. 61, p. 032310, Feb 2000. Cited on 4

[40] B. Roth, P. Blythe, and S. Schiller, "Motional resonance coupling in cold multispecies Coulomb crystals," *Phys. Rev. A*, vol. 75, p. 023402, Feb 2007. Cited on 4

[41] Y. Wan, F. Gebert, F. Wolf, and P. O. Schmidt, "Efficient sympathetic motional-ground-state cooling of a molecular ion," *Phys. Rev. A*, vol. 91, p. 043425, Apr 2015. Cited on 4

[42] S. Willitsch, M. T. Bell, A. D. Gingell, S. R. Procter, and T. P. Softley, "Cold reactive collisions between laser-cooled ions and velocity-selected neutral molecules," *Phys. Rev. Lett.*, vol. 100, p. 043203, Jan 2008. Cited on 4

[43] K. Dulitz, A. Tauschinsky, and T. P. Softley, "Zeeman deceleration of electron-impact-excited metastable helium atoms," *New Journal of Physics*, vol. 17, no. 3, p. 035005, 2015. Cited on 4

[44] A. K. Hansen, O. O. Versolato, L. Kłosowski, S. B. Kristensen, A. Gingell, M. Schwarz, A. Windberger, J. Ullrich, J. R. Crespo López-Urrutia, and M. Drewsen, "Efficient rotational cooling of coulomb-crystallized molecular ions by a helium buffer gas," *Nature*, vol. 508, pp. 76–79, Mar 2014. Cited on 4, 5, 120

[45] F. H. J. Hall and S. Willitsch, "Millikelvin reactive collisions between sympathetically cooled molecular ions and laser-cooled atoms in an ion-atom hybrid trap," *Phys. Rev. Lett.*, vol. 109, p. 233202, Dec 2012. Cited on 5, 120

[46] J. K. Thompson, S. Rainville, and D. E. Pritchard, "Cyclotron frequency shifts arising from polarization forces," *Nature*, vol. 430, May 2004. Cited on 5

[47] J. C. J. Koelemeij, B. Roth, and S. Schiller, "Blackbody thermometry with cold molecular ions and application to ion-based frequency standards," *Phys. Rev. A*, vol. 76, p. 023413, Aug 2007. Cited on 5

[48] P. O. Schmidt, T. Rosenband, C. Langer, W. M. Itano, J. C. Bergquist, and D. J. Wineland, "Spectroscopy using quantum logic," *Science*, vol. 309, no. 5735, pp. 749–752, 2005. Cited on 5

[49] F. Wolf, Y. Wan, J. C. Heip, F. Gebert, C. Shi, and P. O. Schmidt, "Quantum logic with molecular ions," *arXiv:1507.07511*, 2015. Cited on 5

[50] J. Mur-Petit, J. J. García-Ripoll, J. Pérez-Ríos, J. Campos-Martínez, M. I. Hernández, and S. Willitsch, "Temperature-independent quantum logic for molecular spectroscopy," *Phys. Rev. A*, vol. 85, p. 022308, Feb 2012. Cited on 5

[51] D. B. Hume, C. W. Chou, D. R. Leibrandt, M. J. Thorpe, D. J. Wineland, and T. Rosenband, "Trapped-ion state detection through coherent motion," *Phys. Rev. Lett.*, vol. 107, p. 243902, Dec 2011. Cited on 5, 32

[52] P. K. Ghosh, *Ion Traps*. International Series of Monographs in Physics, Oxford University Press, 1995. Cited on 8, 10

[53] E. Schrödinger, "Are there quantum jumps? part ii," *British Journal for the Philosophy of Science*, vol. 3, no. 11, pp. 233–242, 1952. Cited on 8

[54] W. Neuhauser, M. Hohenstatt, P. E. Toschek, and H. Dehmelt, "Localized visible Ba^+ mono-ion oscillator," *Phys. Rev. A*, vol. 22, pp. 1137–1140, Sep 1980. Cited on 8

[55] D. J. Griffiths, *Introduction to electrodynamics: Third edition*. Pearson Benjamin Cummings, 2008. Cited on 9

[56] H. Takahashi, A. Wilson, A. Riley-Watson, F. Oruevi, N. Seymour-Smith, M. Keller, and W. Lange, "An integrated fiber trap for single-ion photonics," *New Journal of Physics*, vol. 15, no. 5, p. 053011, 2013. Cited on 9

[57] A. Mokhberi and S. Willitsch, "Sympathetic cooling of molecular ions in a surface-electrode ion trap," *Phys. Rev. A*, vol. 90, p. 023402, Aug 2014. Cited on 9

[58] H. J. Metcalf and P. van der Straten, *Laser Cooling and Trapping*. Springer-Verlag New York, 1999. Cited on 15, 19, 21

[59] Nobelprize.org, *The Nobel prize in physics 1997*. Nobel Media AB 2014. Cited on 15

[60] C. J. Foot, *Atomic Physics*. Oxford University Press, 2005. Cited on 17, 29

[61] J. Weiner and P. T. Ho, *Light-Matter Interaction, Volume 1, Fundamentals and Applications*. John Wiley Sons Inc., 2003. Cited on 17

[62] F. L. Kien and K. Hakuta, *Density Operator and Applications in Nonlinear Optics*. Lecture Notes, University of Electro-Communications, Japan, 2004. Cited on 18

[63] M. A. Wilson, "Quantum state control of a single trapped strontium ion," PhD Thesis, University of Strathclyde, 2001. Cited on 25

[64] K. T. Sheridan, "Experimental techniques for cold chemistry and molecular spectroscopy in an ion trap," PhD Thesis, University of Sussex, 2012. Cited on 25, 26, 65

[65] G. Janik, W. Nagourney, and H. Dehmelt, "Doppler-free optical spectroscopy on the Ba^+ mono-ion oscillator," *J. Opt. Soc. Am. B*, vol. 2, pp. 1251–1257, Aug 1985. Cited on 26, 27

[66] W. Ketterle, *Atomic and Optical physics lecture notes: Chapter 9*. Center for Ultracold Atoms, MIT, 2006. Cited on 29

[67] K. Vahala, M. Herrmann, S. Knünz, V. Batteiger, G. Saathoff, T. W. Hänsch, and T. Udem, "A phonon laser," *Nature*, vol. 5, August 2009. Cited on 32, 136

[68] P. Atkins and R. Friedman, *Molecular Quantum Mechanics*. Oxford University Press, 2011. Cited on 34, 36, 38, 39

[69] J. M. Bransden and C. J. Joachain, *Physics of atoms and molecules*. Longman Group Ltd., 1983. Cited on 44

[70] S. T. Pratt, P. M. Dehmer, and J. L. Dehmer, "Photoelectron studies of resonant multiphoton ionization of molecular nitrogen," *The Journal of Chemical Physics*, vol. 81, no. 8, 1984. Cited on 49

[71] X. Tong, D. Wild, and S. Willitsch, "Collisional and radiative effects in the state-selective preparation of translationally cold molecular ions in ion traps," *Phys. Rev. A*, vol. 83, p. 023415, Feb 2011. Cited on 49

[72] Y. Wu, J. Ben, L. Li, L. Zheng, Y. Chen, and X. Yang, "Study of (2, 0) band of $A_u^2 - X_g^{2+}$ system of N_2^+ by optical heterodyne detected velocity modulation spectroscopy," *Chinese Journal of Chemical Physics*, vol. 20, no. 3, 2007. Cited on 51

[73] D. M. Lucas, A. Ramos, J. P. Home, M. J. McDonnell, S. Nakayama, J.-P. Stacey, S. C. Webster, D. N. Stacey, and A. M. Steane, "Isotope-selective photoionization for calcium ion trapping," *Phys. Rev. A*, vol. 69, p. 012711, Jan 2004. Cited on 68

[74] D. James, "Quantum dynamics of cold trapped ions with application to quantum computation," *Applied Physics B*, vol. 66, no. 2, pp. 181–190. Cited on 69

[75] J. H. Wesenberg, R. J. Epstein, D. Leibfried, R. B. Blakestad, J. Britton, J. P. Home, W. M. Itano, J. D. Jost, E. Knill, C. Langer, R. Ozeri, S. Seidelin, and D. J. Wineland, "Fluorescence during doppler cooling of a single trapped atom," *Phys. Rev. A*, vol. 76, p. 053416, Nov 2007. Cited on 80

[76] E. Brama, A. Mortensen, M. Keller, and W. Lange, "Heating rates in a thin ion trap for microcavity experiments," *Applied Physics B*, vol. 107, no. 4, pp. 945–954. Cited on 80

[77] C. F. Roos, M. Chwalla, K. Kim, M. Riebe, and R. Blatt, "'Designer atoms' for quantum metrology," *Nature*, vol. 443, pp. 316–319, July 2006. Cited on 80

[78] J. Stenger, C. Tamm, N. Haverkamp, S. Weyers, and H. R. Telle, "Absolute frequency measurement of the 435.5-nm $^{171}Yb^{+}$-clock transition with a kerr-lens mode-locked femtosecond laser," *Opt. Lett.*, vol. 26, pp. 1589–1591, Oct 2001. Cited on 80

[79] Y. Wan, F. Gebert, J. B. Wübbena, N. Scharnhorst, S. Amairi, I. D. Leroux, B. Hemmerling, N. Lörch, K. Hammerer, and P. O. Schmidt, "Precision spectroscopy by photon-recoil signal amplification," *Nature Communications*, vol. 5, Jan 2014. Cited on 81, 90

[80] C. Hempel, B. P. Lanyon, P. Jurcevic, R. Gerritsma, R. Blatt, and C. F. Roos, "Entanglement-enhanced detection of single-photon scattering events," *Nature Photonics*, vol. 7, pp. 630–633, May 2013. Cited on 81

[81] G. Clos, M. Enderlein, U. Warring, T. Schaetz, and D. Leibfried, "Decoherence-assisted spectroscopy of a single Mg^{+} ion," *Phys. Rev. Lett.*, vol. 112, p. 113003, Mar 2014. Cited on 81

[82] M. Herrmann, V. Batteiger, S. Knünz, G. Saathoff, T. Udem, and T. W. Hänsch, "Frequency metrology on single trapped ions in the weak binding limit: The $3S_{1/2} - 3P_{3/2}$ transition in $^{24}Mg^{+}$," *Phys. Rev. Lett.*, vol. 102, p. 013006, Jan 2009. Cited on 81

[83] R. Drullinger, D. Wineland, and J. Bergquist, "High-resolution optical spectra of laser cooled ions," *Applied physics*, vol. 22, no. 4, pp. 365–368. Cited on 81

[84] W. Nagourney, G. Janik, and H. Dehmelt, "Linewidth of single laser-cooled $^{24}Mg^{+}$ ion in radiofrequency trap," *Proceedings of the National Academy of Sciences*, vol. 80, no. 2, pp. 643–646, 1983. Cited on 81

[85] R. Nicolaescu, E. S. Fry, and T. Walther, "Generation of near-fourier-transform-limited high-energy pulses in a chain of fiber–bulk amplifiers," *Opt. Lett.*, vol. 26, pp. 13–15, Jan 2001. Cited on 107

[86] M. Putignano, "Supersonic gas-jet based beam profile monitor," PhD Thesis, University of Liverpool, 2012. Cited on 109

[87] R. E. March, "An introduction to quadrupole ion trap mass spectrometry," *Journal of Mass Spectrometry*, vol. 32, pp. 351–369, Feb 1997. Cited on 119

[88] K. Sheridan, N. Seymour-Smith, A. Gardner, and M. Keller, "Optical broadband excitation of the motional state of trapped ions," *EPJD*, vol. 66, p. 289, 2012. Cited on 129

[89] M. Kajita and M. Abe, "Frequency uncertainty estimation for the $^{40}CaH^{+}$ vibrational transition frequencies observed by raman excitation," *Journal of Physics B: Atomic, Molecular and Optical Physics*, vol. 45, no. 18, p. 185401, 2012. Cited on 148